SOME DIVERSE DIRECTIONS IN HIGHER ORDER COMPACT METHODOLOGY

by

Bidyut B. Gogoi

Department of Mathematics
Indian Institute of Technology, Guwahati, INDIA
December 2014

SOME DIVERSE DIRECTIONS IN HIGHER ORDER COMPACT METHODOLOGY

A Thesis Submitted

for the Award of the Degree of

Doctor of Philosophy

by

Bidyut Bikash Gogoi

to the

DEPARTMENT OF MATHEMATICS

INDIAN INSTITUTE OF TECHNOLOGY, GUWAHATI

December, 2014

DECLARATION

It is certified that the work contained in this thesis entitled **"Some Diverse Directions in Higher Order Compact Methodology"** has done by me, under the supervision of **Dr. Jiten C. Kalita**, Professor, Department of Mathematics, Indian Institute of Technology Guwahati for the award of the degree of Doctor of Philosophy and this work has not been submitted elsewhere for a degree.

December, 2014

Bidyut Bikash Gogoi
Roll No. 09612313
Department of Mathematics
Indian Institute of Technology Guwahati

CERTIFICATE

It is certified that the work contained in this thesis entitled **"Some Diverse Directions in Higher Order Compact Methodology"** by **Bidyut Bikash Gogoi,** a student of Department of Mathematics, Indian Institute of Technology Guwahati, for the award of the degree of Doctor of Philosophy has been carried out under my supervision and this work has not been submitted elsewhere for a degree.

December, 2014

Dr. Jiten Chandra Kalita
Professor
Department of Mathematics
Indian Institute of Technology Guwahati

To My Mother

***Late Kalpana Gogoi*, for her love, sacrifice and devotion.**

Acknowledgement

First and foremost, I would like to express my deep and sincere gratitude to my thesis supervisor, **Prof. Jiten C. Kalita** for guiding me through my research; his careful guidance, constructive criticisms and valuable suggestions proved very stimulating and helpful. I am deeply indebted to him for his utmost care and making me feel free to express my views. Without his help, the work could not have been accomplished. Special thanks to his family for making me feel like a family member. I would never forget about his constant inspiration and love throughout my research days. It would be really unfair enough not to state that he is truly a good friend, philosopher and a great guide for someone like me. Without his frequent advice, I would have probably never endeavour to carry out valuable research activites.

I owe my thanks to the members of my doctoral committee Prof. Rajen Kumar Sinha and Dr. Siddhartha Pratim Chakrabarty (Department of Mathematics) and Prof. Anoop Kumar Dass (Department of Mechanical Engineering) for their helpful criticism and in overseeing the advancement of my work. I take this opportunity to express my gratitude to all the faculty members of the Department of Mathematics who have offered help directly or indirectly at different stages during my research work. My sincere thanks are due to Mr. Santanu Majumdar and Mr. Pranpratim Borgohain for their technical support, Mr. Sridhar Samal and Mr. Phatik Kumar of the Department of Mathematics for their assistance in all official matters.

Special thanks to Dr. M. Prabhakar, Assistant Professor, Indian Institute of Technology Ropar, Department of Mathematics, Punjab, India for his constant support during my M.Sc and encouraging me for pursuing Ph. D.

I gladly acknowledge the Indian Institute of Technology Guwahati and the Council of Scientific and Industrial Research (CSIR) for providing fellowship during the period of my Ph.D. programme.

I take this opportunity to convey my gratefulness to my friends and co-researchers for all their timely help, encouragement and support. My love and

thanks to my friends Ravi, Biswajit, Debajit, Gowrishankar, Himadri, Santu, Murali, Dinesh, Pratibhamoy, Arnab, Jitender, Kalyan, Kaushik, Jayanta, Sougata, Shubh, Hassan, Shibsankar, Debopam, Barun and Puneet. I acknowledge their company for making my life at IIT Guwahati an extremely comfortable one. My heartfelt thanks to my senior Dr. Shuvam Sen, Associate professor, Department of Mathematical Sciences, Tezpur University, Tezpur for his friendship, brotherly love, care, valuable suggestions and help throughout this work.

This work would have not been possible without the strong moral support and the unfailing faith of my parents, my mother Late Kalpana Gogoi and my father Mr. Bhakti Ram Gogoi, which have sustained me throughout this endeavour. I would like to thank my elder sisters Jinu and Rina, and my brother-in-laws for their pampering love and care. They have been a source of inspiration throughout my life and I dedicate this thesis to them. Special thanks to my litte cousin brother Jatin Gogoi, who has been all along with me to support in my day-to-day activities. I am also thankful to my parent-in-laws for always playing a supportive role in my life.

Lastly, I would like to convey my deepest love to my wife Nabanita for her love, sacrifice, devotion, encouragement and patience for supporting me to carry out my Ph. D work. Thanks to her for being always with me in every step of this journey and beyond.

Bidyut Bikash Gogoi

Indian Institute of Technology
Guwahati

Abstract

This dissertation is concerned with the application of some existing compact finite difference schemes to hitherto unexplored areas and further development of some new higher-order compact (HOC) schemes. A global stability analysis of the staggered lid-driven cavity flow for both parallel and antiparallel motion of the lids is carried out with a recently developed HOC scheme. To the best of our knowledge, this is the very first attempt to carry out the analysis of the flow stability inside a staggered cavity. Some more complicated flows are then analyzed, where the biharmonic formulation of the Navier-Stokes (N-S) equations is utilized for the first time. In doing so, a most recently developed pure streamfunction based compact scheme has been employed, again for the first time. This approach is seen to drastically reduce the computational effort vis-a-vis the ψ-ω and the primitive variable formulation of the N-S equations, specifically in computing the critical parameters from the generalized eigenvalue problem. Next, a family of implicit HOC finite difference schemes is developed for the transient three-dimensional (3D) convection-diffusion-reaction equations. They efficiently capture solutions of fluid flow problems governed by any of these fundamental processes. The results obtained for flows of varying complexities governed by the 3D incompressible N-S equations are in excellent agreement with established numerical results. The 2D formulation of one of these schemes is then applied to problems in Mathematical Biology to study pattern formation occuring in nature. Various patterns have been recognized with different model problems and in particular, spikes, spots, stripes and labyrinths patterns are obtained. Finally, a new family of HOC schemes has been developed for the 1D Euler equations of Gas Dynamics (compressible flows). These schemes produce highly accurate results and are seen to capture shocks and discontinuities very well on much coarser grids.

Contents

List of Figures

List of Tables

NOMENCLATURE

ψ	streamfunction
ω	vorticity
ν	kinematic viscosity
δ	perturbation parameter
λ	eigenvalue
λ_r	Real-part pf eigenvalue λ
λ_i	Imaginary-part pf eigenvalue λ
λ_c	Critical eigenvalue
θ	angle of incidence
$\delta_x, \delta_y, \delta_z$	central difference operators in x-, y- and z-directions respectively
δ_t^+	forward time-difference operator
β	modified wave number ($k_m h$)
ς	weighted average parameter
μ_U, μ_V	decay coefficients of activator and inhibitor respectively
ρ_a, ρ_b	inflow of activator and inhibitor respectively
ρ	density
γ	Gas Dynamic constant

h	mesh step-length in x-direction
$\triangle t$	time step-length
a	Diffusion coefficient
c	convection coefficient along x-direction
d	convection coefficient along y-direction
L	characteristic Length
Re	Reynolds number $\left(\frac{U_0 L}{\nu}\right)$
p	pressure
u	horizontal velocity component in Cartesian co-ordinates
v	vertical velocity component in Cartesian co-ordinates
∇^2	Laplacian operator
f	forcing function
i, j	indices along x- and y- and directions respectively
k	mesh step-length in y-direction
t	time
l	mesh step-length in z-direction
Re_c	Critical Reynolds number
T	temperature
m	momentum
S	Entropy
E	internal energy

∇^4	biharmonic operator
$\hat{a}$	projected width of the cylinder
C_D	drag coefficient
$C_{\hat{L}}$	lift coefficient
A	characteristic area
D	drag force
$\hat{L}$	lift force
St	Strouhal number
f_s	shedding frequency
e	reaction coefficient
k_m	wave number
Pe	Peclet number
G	amplification factor
U	concentration of the activator
V	concentration of the inhibitor
D_u	diffusion coefficient of the activator
D_v	diffusion coefficient of the inhibitor
F	feed rate
$\tilde{k}$	degrading rate
P_0	stagnation value of pressure
T_0	stagnation value of temperature
CFL	Courant-Friedrich-Lewy number
M	mach number

Chapter 1

INTRODUCTION

1.1 General Background

Numerical simulation of fluid motion has been the prime subject of research for applied mathematicians in the last few decades. Most of these physical phenomena are described with mathematical models that govern fundamental processes like convection, diffusion and reaction. Such models encompass equations that are either ordinary differential equations (ODE) or partial differential equations (PDE). However, many of the PDEs like the Navier-Stokes equations or the Euler equations do not possess any analytical solution and therefore one has to espouse to the numerical methods. The major difficulty in solving these equations is primarily because of the fact that they consist of nonlinear terms. Because of non-linearity, these models are considerably difficult for direct computation and as such suitable numerical strategies have been adopted by researchers from time to time. Computational fluid dynamics (CFD) research mainly revolves around methods like the finite difference method (FDM), finite volume method (FVM), finite element method (FEM), spectral method, Lattice Boltzmann method (LBM) etc. Amongst these methods, the finite difference methods have always been the prime choice for investigators as they are simple and easier to implement, compared to the other methods.

Finite difference methods are one of the simplest and of the oldest methods for numerically solving differential equations. In the year 1768, it was first described by Leonhard Euler in the one dimensional space and was extended to the two dimensional space by C. Runge in 1908. However, the advent of finite difference techniques in numerical applications began only in the early 1950s and their development was stimulated by the emergence of computers that offered a convenient framework for dealing with complex problems of science and technology. Theoretical results have also been obtained during the last five decades which helps in establishing the accuracy, stability and convergence of the FDM for partial differential equations. The basic methodology in FDM deals in approximating the differential operators appearing in the governing equations by replacing the derivatives using differential quotients and setting up a grid. To accomplish that, the problem domain is partitioned in space and time and approximations of the solution are computed. This results in a system of algebraic equations (finite difference equations) which can be solved with the aid of some matrix solution algorithm.

Finite difference approximations to derivatives are mainly based on Taylor series expansion of the variables at the nodal points. The accuracy of the scheme is determined by the leading term of the truncation error (TE) of this expansion. For instance, the difference scheme is said to be accurate of order m or $O(h^m)$, if this TE is asymtotically proportional to h^m, where h is the distance between neighbouring nodes and m depends on the form of the difference operator. Because of their easiness and straight-forwardness in applications, the $O(h^2)$ central difference schemes are quite standard in applications and often yield quite good results on reasonable meshes when the solution is well behaved. Therefore, the $O(h^2)$ methods have been the most widely used finite difference method for constructing discrete approximations to linear PDEs. However, for problems like the convection dominated flows, the solution may exhibit some oscillatory behaviour if the mesh is not sufficiently refined. But mesh refinement invariably leads to an increase in the system size by bringing in additional points into the system. This leads to an increase in the memory requirements and hence more CPU time is required for obtaining such solutions numerically on a computer. So traditional central difference scheme has

$m = 2$. If we increase this order of accuracy m, the stencil size increases which results in increase band-width of the coefficient matrix. As both mesh refinement and increased band-width of coefficient matrix increases the arithmetic operations, neither a lower-order accurate method on a fine mesh nor a higher-order accurate one on a larger stencil could be computationally economical. This has necessitated the development of schemes which are higher-order accurate on a compact stencil.

A finite difference scheme is termed as compact if it utilizes only the nodal points that are located directly adjacent to the node about which the finite difference approximations have been taken. In addition to this, if it possesses a spatial accuracy greater than two, then it is termed as an higher-order compact (HOC) method. The combined effect of its higher order accuracy and compactness of stencils yields not only highly accurate numerical solutions on grids which are relatively coarser but also provides a greater computational efficiency.

1.2 Motivation

Existing literature manifests that Higher Order Compact (HOC) schemes that have been developed so far were mainly confined to simulation of incompressible viscous flows. But one important issue that needs attention is its applications and developments on some more diverse fields. Of late, global two-dimensional stability analysis of incompressible viscous flows has been an interesting topic among the researchers. However, to the best of our knowledge, there is no literature to discuss global two-dimensional stability analysis of incompressible viscous flows with an HOC approach. Again, in the three dimensional space, some HOC schemes have been developed for the convection-diffusion equation but for the convection-diffusion-reaction equation, it is considerably less. A careful study on pattern formation in Mathematical Biology reveals that a plethora of numerical methods exist for simulating pattern formation in nature. But most of them are atmost second order accurate in

space and time. In this context, it seems important to check how the HOC schemes behave when they are incorporated for simulating pattern formations in nature. Moreover, only a few HOC schemes have been developed so far for problems in Gas Dynamics (compressible flows), for the Euler equations in particular. Application of HOC schemes for these problems has challenges and is replete with many interesting possibilities. These are the major motivating factors behind this work, which is concerned with addressing these issues.

1.3 Literature Review

A careful undermining into the existing literature reveals that numerous researchers adopted different strategies for achieving higher-order compactness of finite difference schemes. In 1982, Gartland Jr. [52] adopted the discrete weighted mean approximation approach for developing HOC methods for convection-diffusion equations. This was followed by the works of Wilkes *et al.* [119] in 1983 where they have used upwind differencing to obtain HOC methods for elliptic flow problems. In 1984, Gupta *et al.* [42] developed yet another HOC method by applying series expansion to the differential equations. Later on, some more HOC methods have been developed. Among them, the notable ones include Dennis and Hudson [21] who used transformation that invloves expanding the exponential of a definite integral of the convective coefficient of the concerned PDEs, the fourth order compact scheme of Li *et al.* [70], weighted modified PDE method of Noye *et al.* [83, 84], upwind differencing HOC method of Yanwen *et al.* [124] and HOC upwind schemes by Sesterhenn [97] using a characteristic-type formulation of the Navier-Stokes (N-S) equations.

Higher-order compact finite difference methods can also be obtained by adding the leading terms of the TE of the central difference approximation in the finite difference equation. These leading terms of the TE can be approximated by using the original differential equation as the auxilliary equation and substituting them in the finite difference equation to obtain the desired HOC

method. Throughout our present work, we have adopted this mechanism. These methods are mainly based on ideas first used by Lax and Wendroff [6, 47, 53], wherein they used the original PDE to approximate the second-order time derivative in a Taylor series expansion with time accuracies of $O(\triangle t)$ and $O(\triangle t^2)$. In 1988, Mackinnon and Carey [73] for the first time proposed a spatial implementation of this temporal Lax-Wendroff idea. This work was followed by Mackinnon and Johnson [74], Abarbanel and Kumar [1], Wong *et al.* [120], Dukowicz *et al.* [23], Spotz and Carey [105, 106], Kalita *et al.* [41, 55, 56, 57, 60, 86] etc. Some of the pioneering works of HOC methods in three dimensional (3D) include the works carried out by Ananthakrishnaih [5], Ge *et al.* [30], Gupta and Kouatchou [40], Mohamed *et al.* [78], Spotz and Carey [107], Turkel *et al.* [115], Zhai *et al.* [126] and Zhang [127].

Global two-dimensional stability analysis of incompressible viscous flows has been investigated by numerous researchers. So far, the major problem of discussion in global stability analysis is the famous lid-driven cavity (LDC) flow on a square domain. Gustafson and Halasi [43, 44] and Goodrich *et al.* [34] simulated the full time-dependent Navier-Stokes equations and found that the steady flow loses its stability via a Hopf bifurcation. In their recent work, Auteri *et al.* [10] have taken account of the corner singularities in the flow computation for the simple LDC problem and managed to narrow the range of values of the critical Reynolds number (Re_c) when a Hopf bifurcation takes place. In 1995, Poliashenko *et al.* [89] reviewed some interesting techniques that can be used to study the stability of the steady state problem and compute the bifurcations using all those techniques. Aidun *et al.* [3] and Fortin *et al.* [29] solved the two-dimensional eigenvalue problem numerically and compared the critical Reynolds numbers and frequencies from the eigenvalue analysis with the simulations of the unsteady equations. Peng *et al.* [88] in 2003, used a seventh order upwind biased method for the spatial discretization of the convective term and a sixth-order central method for the spatial discretization of the diffusive term and found the critical Re_c for the simple LDC problem on a square cavity. Recently in 2009, Bopanna and Gajjar [16] carried out a global two-dimensional stability analysis of the 2D simple lid-driven cavity using an accurate numerical technique based on a hybrid scheme

with spectral collocation and higher-order finite differences.

Till date, several HOC schemes have been proposed for the convection-diffusion equation, a majority of which very aptly handle the two-dimensional (2D) incompressible N–S equations. However, higher-order compact schemes for the more generalized convection-diffusion-reaction equation have been relatively scarce. The convection-diffusion-reaction model problem is a very important problem in science and engineering as it describes all the three fundamental phenomena in transport, viz. convection, diffusion and reaction. Some of its practical applications include constitutive equations (convection-diffusion equation) for modeling turbulent quantities like k and ϵ [49], Helmholtz equation (diffusion-reaction equation) for modeling the exterior acoustics [45] and Mickens-type convection-reaction equation in combustion models [7]. The solution of convection-diffusion-reaction dates from earlier to 1990s [118]. With the advent of higher-order compact methods in the numerical field, few HOC schemes have been proposed for the convection-diffusion-reaction equations [71, 92] but simulations were performed mostly for the two-dimensional model problem. In the three dimensional space, some HOC schemes have been developed for the convection-diffusion equation but for the convection-diffusion-reaction equation, it is relatively scarce.

Study on pattern formation dates to 1952, when the British Mathematician, Alan Turing, in his pioneering work [113] described a reaction-diffusion model for morphogen concentrations. This model hypothesizes the existence of two different molecules, an activator and an inhibitor. In nature, various pattern formations occur due to the variation of concentration of morphogens within each cell, which, both react and diffuse within the system owing to instabilities. A variety of species exhibits remarkable types of patterns in their skins, shapes or sizes. Patterns imitating the spots in leopards, spikes in cactus, stripes in zebras etc. has created tremendous interest amongst researchers and biologists. These pattern formation mechanisms are actually governed by simple mathematical models of reaction and diffusion. Researchers have carried out different startegies for solving such equations and in the process several spatial and temporal patterns are observed. In recent years, spatial pattern forma-

tion has become a crucial area of research in developmental biology. In 1993, Murray [79] suggested an alternative mechanism for spatial patterning by a mechanochemical approach. Both the models of Turing [113] and Murray [79] have been extensively studied and it has been observed that they can simulate many patterns that are seen in the nature. In particular, the effects of domain size and non-linearities and stability of solutions has also been analysed. Consequently, it has been observed that the absence of quadratic non-linearities in the reaction kinetics favors stripes, but the presence of quadratic terms favors spots (Bard [25]; Nagorcka *et al.* [80]). Literature suggests that researchers working on pattern formation mainly employed the central difference schemes. It is because they are computationally easier to implement and they handle the boundary conditions in a straightforward way. So, most of the existing numerical works pertaining to pattern formation revolve around numerical methods which are of atmost second order accurate in space in time.

There have been several attempts on developing numerical schemes for the Euler equations of Gas Dynamics. A majority of these existing numerical methods lack accuracy, for example, the AUSM, HLLC solver, Godunov, Rusanov, Lax-Friedrich, Lax-Wendroff, MacCormack methods etc. In 1988, Saul Abarbanel and Ajay Kumar [1] proposed a compact higher-order method for the simulation of Euler equations. This scheme was of fourth order spatial accuracy which was followed by the works of Deng *et al.* [20], Elfaghi *et al.* [24], Mohamad *et al.* [77] and Stipcich *et al.* [108]. However, all of them are only first order accurate in time.

1.4 Objectives

The main aim of the present work is to discuss the application and development of higher-order compact methods on some more diverse fields, viz. stability analysis of incompressible viscous flows, pattern formations in Mathematical Biology, simulation of Euler equations of Gas Dynamics which represent compressible flows etc. We intended to apply some of the existing HOC schemes to

analyse the global 2D stability of incompressible viscous flows, which include the staggered lid driven cavity flow, the square LDC flow, the cross LDC flow and the flow past an inclined square cylinder. Moreover, we proposed some new HOC schemes for the transient 3D convection-diffusion-reaction equations and the 3D cubical LDC has been studied. These schemes were further trimmed down to solve the transient two-dimensional convection-diffusion-reaction equations which are then applied to some of the well-known model problems for pattern formation in Mathematical Biology. Lastly, we propose a new HOC scheme for solving the one-dimensional (1D) Euler equations of Gas Dynamics. This has been later on applied to some of the well-known 1D problems on Gas Dynamics and excellent comparison with the existing results have been observed.

1.5 The Work

The present dissertation is concerned with some more diverse directions in HOC methodology. In this context, we have attempted to carry out an investigation of application and development of higher-order compact methods in some new directions.

Firstly, we apply an existing HOC scheme [56] for the ψ-ω formulation of the N-S equations to analyse the global two-dimensional stability of the flow inside a two-sided 2D staggered LDC with both paralllel and anti-parallel motions of lids. Existing literature reveals that prior to our attempt, no global stability analysis has been carried out for the two-sided 2D lid-driven staggered cavity flow. A fourth order spatially accurate and second order temporally accurate compact scheme is used to discretize the two-dimensional Navier–Stokes equations governing the flow as well as the perturbed equations leading to the generalized eigenvalue problem. Estimates of the critical parameters are found for several grids and extensive grid convergence study is performed to accurately identify them. Computation is performed for a wide range of Reynolds numbers (Re) on either side of the critical values in the range $50 \leq Re \leq 12,000$.

For flows below the critical Reynolds number Re_c, our numerical results are compared with established steady-state results and an excellent agreement is obtained in all the cases. For Reynolds numbers above Re_c, phase plane and spectral density analysis confirmed the existence of periodic and chaotic flow patterns.

The second part of our work embodies an investigation of flow stabilities in some incompressible viscous fluid flow problems, namely, the simple (one-sided) square LDC, the two-sided cross LDC flows and the flow past an inclined square cylinder. In order to accomplish this, we utilize the spatially and temporally second order accurate biharmonic formulation of the 2D incompressible Navier-Stokes equations developed by Kalita and Gupta [59]. Critical parameters have been studied with the help of eigenvalue analysis and results have been reported. It has been observed that there is a reasonable agreement with established results for the square cavity and the inclined square cylinder problem, while for the two-sided cross cavity, it's global stability analysis has been carried out for the first time and new results are observed.

Next, we have developed a class of fourth order spatially accurate higher order compact schemes for the transient three-dimensional convection-diffusion-reaction equations. The proposed schemes are second or lower order accurate in time depending on the choice of a weighted average parameter. We have also carried out a convergence analysis in order to establish the spatial and temporal accuracy of the schemes in the discrete Euclidean norm (L^2-norm). To test the efficiency of the proposed schemes, they are applied to unsteady three-dimensional convection-diffusion-reaction problems with both constant as well as variable convection-reaction coefficients and results obtained are found to be superbly in agreement with the analytical solutions. Further, to check the robustness of the proposed schemes, we apply them to the benchmark problem of 3D lid-driven cubical cavity flow governed by the unsteady Navier-Stokes (N-S) equations and compare our results with established numerical results, which gives us an excellent comparison.

The next part of our work deals with the introduction of a new family of

implicit higher-order compact finite difference method for numerically simulating biological pattern formation in reaction-diffusion systems. In order to focus deeply into the fundamental aspects of the proposed scheme, dispersion-dissipation analysis and Fourier stability analysis have been provided. Validation of our scheme has been justified on application to well known results in the existing literature. Later on, effectiveness of our schemes have been tested by applying them to three different well known model problems. In the process, simulation of various patterns, viz. spikes, spots, stripes and labyrinths have been observed, exemplifying the robustness of the schemes developed by us.

Lastly, we develop a new class of higher-order compact schemes for the one dimensional (1D) Euler equations of Gas Dynamics. These implicit schemes are fourth order accurate in space and at most second order accurate in time. To test the efficiency of our proposed schemes, we apply them to three different shock tube problem of gas dynamics, including the famous SOD shock tube problem. In all the cases, for a much coarser grid, our computed numerical solutions are found to be in excellent match with the exact solutions. Overall the schemes are found to be very efficient and accurate.

Almost all of the above computations were carried out on a HCL Desktop PC with corei5@3ghz processor and 4gb ddr3 ram.

1.6 Organization of the Thesis

The present dissertation has been arranged in eight chapters. Chapter 2 briefly discusses the basics of the numerical schemes used in the work. Chapter 3 describes the global two-dimensional stability analysis of the flow inside a two-sided 2D staggered LDC with an HOC approach via the ψ-ω formulation of the 2D incompressible Navier-Stokes equations. Chapter 4 describes the global two-dimensional stability analysis of some incompressible viscous flows with yet another approach - the biharmonic formulation (ψ-v) of the 2D incom-

pressible N-S equations. Chapter 5 describes the class of HOC schemes developed for the transient three-dimensional convection-diffusion-reaction equations with a theoretical convergence analysis of the schemes. Chapter 6 describes the class of HOC schemes developed for the reaction-diffusion systems in Mathematical Biology with a dispersion-dissipation analysis and stability analysis of the schemes. Development of a new class of HOC schemes for the one-dimensional Euler equations of Gas Dynamics has been discussed in Chapter 7. Chapter 8 summarizes and comments on the whole work and discusses scope for future work.

Chapter 2

FOUNDATIONS OF THE SCHEMES USED

This chapter briefly describes the procedure for the development of compact schemes [74, 105] for 2D steady-state Navier-Stokes (N-S) equations on uniform grids. The technique employed here is the utilization of the original PDE, as mentioned in chapter 1, to replace some of the derivatives appearing in the truncation error obtained from finite difference approximation. Throughout the present work, we will basically follow two different approaches, the ψ-ω and the ψ-v formulation of the N-S equations. Let us discuss both of these approaches one by one.

2.1 2D steady-state convection-diffusion equations

At the outset, let us consider the 2D steady-state convection-diffusion equation for a transport ϕ on some domain Ω with boundary $\partial\Omega$ as

$$-a\nabla^2\phi + u(x,y)\frac{\partial\phi}{\partial x} + v(x,y)\frac{\partial\phi}{\partial y} = s(x,y), \quad (x,y) \in \Omega \tag{2.1a}$$

$$\phi(x,y) = \phi_0(x,y), \quad (x,y) \in \partial\Omega \tag{2.1b}$$

here a is a constant positive diffusion coefficient, u and v are the convective velocities along x- and y- directions respectively, s is the source term such as the body force and ∇^2 is the Laplacian operator given by

$$\nabla^2 \equiv \frac{\partial^2}{\partial x^2} + \frac{\partial^2}{\partial y^2}.$$

Equation (2.1a) represents almost all problems of fluid dynamics which involve convection and diffusion of flow variables like mass, energy, heat, vorticity etc. With proper choice of parameters, this equation may also be used to represent the complete 2D steady-state Navier-Stokes equations.

Most of the times numerical simulation of fluid flow problems has been performed by non-dimensionalizing the governing equation(s). In order to non-dimensionalize equation (2.1a), we choose a characteristic length L, a characteristic velocity U_0 and a characteristic value Φ of ϕ and letting

$$\phi^* = \frac{\phi}{\Phi}, \quad u^* = \frac{u}{U_0}, \quad v^* = \frac{v}{U_0}, \quad x^* = \frac{x}{L} \text{ and } y^* = \frac{y}{L}. \tag{2.2}$$

Using these, the non-dimensional 2D steady-state convection-diffusion equation can therefore be written as (omitting the asterisk)

$$-\nabla^2\phi + c(x,y)\frac{\partial\phi}{\partial x} + d(x,y)\frac{\partial\phi}{\partial y} = f(x,y), \tag{2.3}$$

where the diffusion coefficient is unity and

$$c(x,y) = \frac{U_0 L}{a} u(x,y)$$

and

$$d(x,y) = \frac{U_0 L}{a} v(x,y)$$

are the ratios of convection to diffusion along x- and y- directions respectively

and

$$f(x,y) = \frac{L^2}{a\Phi} s(x,y)$$

is the forcing function. Depending on the fluid flow situations, the term

$$\frac{U_0 L}{a}$$

represents different parameters. However, in problems governed by the Navier-Stokes equations, this term represents the Reynolds number (Re). To formulate HOC schemes for the convection-diffusion equation, we have assumed that c, d, f and ϕ are sufficiently smooth so that they are atleast twice differentiable.

2.2 2D steady-state Navier-Stokes equations

The 2D steady-state N-S equations in the traditional primitive variable formulation can be written in the non-dimensional form as

$$\frac{\partial u}{\partial x} + \frac{\partial v}{\partial y} = 0, \tag{2.4a}$$

$$u\frac{\partial u}{\partial x} + v\frac{\partial u}{\partial y} = -\frac{\partial p}{\partial x} + \frac{1}{Re}\nabla^2 u, \tag{2.4b}$$

$$u\frac{\partial v}{\partial x} + v\frac{\partial v}{\partial y} = -\frac{\partial p}{\partial y} + \frac{1}{Re}\nabla^2 v, \tag{2.4c}$$

where u and v are the velocities along x- and y-directions and p is the pressure; Re is the Reynolds number and ∇^2 is the Laplacian operator.

Though the primitive variable formulation accurately represents the fluid flow phenomena, its direct solution is normally difficult to obtain due to the pressure term in equations (2.4b) and (2.4c).

2.3 HOC scheme for the ψ-ω formulation of the Navier-Stokes equations

Partly in order to avoid handling the pressure variable, an alternative formulation of (2.4) using streamfunction ψ and vorticity ω has been used for several decades. The ψ-ω formulation of (2.4) can be written as

$$-\frac{1}{\mathrm{Re}}\left(\omega_{xx}+\omega_{yy}\right)+\left(u\omega_x+v\omega_y\right)=0, \tag{2.5a}$$

$$\psi_{xx}+\psi_{yy}=-\omega(x,y). \tag{2.5b}$$

with

$$u=\psi_y, \quad \text{and} \quad v=-\psi_x, \tag{2.6}$$

and

$$\omega=v_x-u_y. \tag{2.7}$$

To construct an HOC formulation for the system (2.5), we first consider the 2D steady-state convection-diffusion equation given by (2.3) and construct its HOC formulation.

Choose the solution domain in such a way that it can be divided into rectangular sub-regions where each sub-region can be further divided into uniform meshes of square cells of which each vertex serves as a node and the distance between two succesive node is a constant, say h. Let $[x_0,x_m]\times[y_0,y_n]$ be the rectangular domain, then for $\phi_{ij}=\phi(x_i,y_j)=\phi(x_0+ih,y_0+jh);\quad 0\le i\le m, 0\le j\le n$, the central difference approximation to (2.3) turns out to be of the form

$$-\delta_x^2\phi_{ij}-\delta_y^2\phi_{ij}+c\delta_x\phi_{ij}+d\delta_y\phi_{ij}-\tau_{ij}=f_{ij}, \tag{2.8}$$

where the truncation error τ_{ij} is of the form

$$\tau_{ij}=\frac{h^2}{12}\left[2\left(c\frac{\partial^3\phi}{\partial x^3}+d\frac{\partial^3\phi}{\partial y^3}\right)-\left(\frac{\partial^4\phi}{\partial x^4}+\frac{\partial^4\phi}{\partial y^4}\right)\right]_{ij}+O(h^4) \tag{2.9}$$

Now in order to obtain a fourth order compact finite difference scheme for (2.3), we compactly approximate [73, 74] each of the derivatives appearing in (2.9) to $O(h^2)$. To accomplish this, we treat the original PDE (2.3) as an auxiliary relation that can be differentiated to yield expressions for higher derivatives. Then the derivatives appearing on the right hand side of Equation (2.9) can be compactly approximated as

$$\frac{\partial^3\phi}{\partial x^3} = -\frac{\partial^3\phi}{\partial x\partial y^2} + c\frac{\partial^2\phi}{\partial x^2} + \frac{\partial c}{\partial x}\frac{\partial\phi}{\partial x} + d\frac{\partial^2\phi}{\partial x\partial y} + \frac{\partial d}{\partial x}\frac{\partial\phi}{\partial y} - \frac{\partial f}{\partial x} \tag{2.10}$$

$$\frac{\partial^3\phi}{\partial y^3} = -\frac{\partial^3\phi}{\partial x^2\partial y} + c\frac{\partial^2\phi}{\partial x\partial y} + \frac{\partial c}{\partial y}\frac{\partial\phi}{\partial x} + d\frac{\partial^2\phi}{\partial y^2} + \frac{\partial d}{\partial y}\frac{\partial\phi}{\partial y} - \frac{\partial f}{\partial y} \tag{2.11}$$

$$\begin{aligned}\frac{\partial^4\phi}{\partial x^4} = &-\frac{\partial^4\phi}{\partial x^2\partial y^2} + c\frac{\partial^3\phi}{\partial x^3} + 2\frac{\partial c}{\partial x}\frac{\partial^2\phi}{\partial x^2} + \frac{\partial^2 c}{\partial x^2}\frac{\partial\phi}{\partial x} + d\frac{\partial^3\phi}{\partial x^2\partial y}\\ &+ 2\frac{\partial d}{\partial x}\frac{\partial^2\phi}{\partial x\partial y} + \frac{\partial^2 d}{\partial x^2}\frac{\partial\phi}{\partial y} - \frac{\partial^2 f}{\partial x^2}\end{aligned} \tag{2.12}$$

$$\begin{aligned}\frac{\partial^4\phi}{\partial y^4} = &-\frac{\partial^4\phi}{\partial x^2\partial y^2} + c\frac{\partial^3}{\partial x\partial y^2} + 2\frac{\partial c}{\partial y}\frac{\partial^2\phi}{\partial x\partial y} + \frac{\partial^2 c}{\partial y^2}\frac{\partial\phi}{\partial x} + d\frac{\partial^3\phi}{\partial y^3}\\ &+ 2\frac{\partial d}{\partial y}\frac{\partial^2\phi}{\partial y^2} + \frac{\partial^2 d}{\partial y^2}\frac{\partial\phi}{\partial y} - \frac{\partial^2 f}{\partial y^2}\end{aligned} \tag{2.13}$$

Substituting equations (2.10)-(2.13) in equation (2.9), the truncation error at the (i,j)-th node is given by

$$\begin{aligned}\tau_{ij} = &\frac{h^2}{12}\left[-2\left\{\frac{\partial^4\phi}{\partial x^2\partial y^2} + c\frac{\partial^3}{\partial x\partial y^2} + d\frac{\partial^3\phi}{\partial x^2\partial y} + \left(\frac{\partial c}{\partial y} + \frac{\partial d}{\partial x} - cd\right)\frac{\partial^2\phi}{\partial x\partial y}\right\}\right.\\ &+ \left(c^2 - 2\frac{\partial c}{\partial x}\right)\frac{\partial^2\phi}{\partial x^2} + \left(d^2 - 2\frac{\partial d}{\partial y}\right)\frac{\partial^2\phi}{\partial y^2} - \left(\frac{\partial^2 c}{\partial x^2} + \frac{\partial^2 c}{\partial y^2} - c\frac{\partial c}{\partial x} - d\frac{\partial c}{\partial y}\right)\frac{\partial\phi}{\partial x}\\ &\left.- \left(\frac{\partial^2 d}{\partial x^2} + \frac{\partial^2 d}{\partial y^2} - c\frac{\partial d}{\partial x} - d\frac{\partial d}{\partial y}\right)\frac{\partial\phi}{\partial y} - \left(\frac{\partial^2 f}{\partial x^2} + \frac{\partial^2 f}{\partial y^2} - c\frac{\partial f}{\partial x} - d\frac{\partial f}{\partial y}\right)\right]_{ij}\\ &+ O(h^4)\end{aligned} \tag{2.14}$$

Note that all the derivatives and cross-derivatives appearing in the RHS of equation (2.14) have $O(h^2)$ approximations. For instance

$$\left.\frac{\partial^4\phi}{\partial x^2\partial y^2}\right|_{ij} = \delta_x^2\delta_y^2\phi_{ij} - \frac{h^2}{12}\left[\frac{\partial^6\phi}{\partial x^4\partial y^2} + \frac{\partial^6\phi}{\partial x^2\partial y^4}\right]_{ij} + O(h^4) \tag{2.15}$$

Substituting these types of $O(h^4)$ approximations for all the derivatives appearing in equation (2.14), we can arrive at the following fourth order accurate HOC scheme for equation (2.1)

$$\begin{aligned} &- \alpha_{ij}\delta_x^2\phi_{ij} - \beta_{ij}\delta_y^2\phi_{ij} + C_{ij}\delta_x\phi_{ij} + D_{ij}\delta_y\phi_{ij} \\ &- \frac{h^2}{6}[\delta_x^2\delta_y^2 - c_{ij}\delta_x\delta_y^2 - d_{ij}\delta_x^2\delta_y - \gamma_{ij}\delta_x\delta_y]\phi_{ij} = F_{ij}, \end{aligned} \tag{2.16}$$

where δ_x and δ_y are the first and δ_x^2 and δ_y^2 are the second order central difference operators along x- and y-directions respectively.

The coefficients α_{ij}, β_{ij}, γ_{ij}, C_{ij}, D_{ij} and F_{ij} appearing in equation (2.16) are as follows:

$$\alpha_{ij} = 1 + \frac{h^2}{12}(c_{ij}^2 - 2\delta_x c_{ij}),$$

$$\beta_{ij} = 1 + \frac{h^2}{12}(d_{ij}^2 - 2\delta_y d_{ij}),$$

$$\gamma_{ij} = \delta_y c_{ij} - c_{ij}d_{ij} + \delta_x d_{ij},$$

$$C_{ij} = c_{ij} + \frac{h^2}{12}(\delta_x^2 + \delta_y^2 - c_{ij}\delta_x - d_{ij}\delta_y)c_{ij},$$

$$D_{ij} = d_{ij} + \frac{h^2}{12}(\delta_x^2 + \delta_y^2 - c_{ij}\delta_x - d_{ij}\delta_y)d_{ij},$$

$$F_{ij} = f_{ij} + \frac{h^2}{12}(\delta_x^2 + \delta_y^2 - c_{ij}\delta_x - d_{ij}\delta_y)f_{ij},$$

Now, consider the streamfunction-vorticity formulation given by (2.5). Putting $\phi = \omega$, $c(x,y) = Reu(x,y)$, $d(x,y) = Rev(x,y)$ and $f(x,y) = 0$ in equation

(2.1) and following the above outline procedure we can obtain the fourth order compact formulation for the vorticity transport equation (2.5a). In a similar manner, letting $\phi = \psi$, $c(x, y) = 0$, $d(x, y) = 0$ and $f(x, y) = \omega$, we have the fourth order compact formulation for the streamfunction equation (2.5b). Note that in order to derive HOC schemes for unsteady equations, the time derivative is considered as a part of the source term in equation (2.3), which later on is approximated again with finite difference schemes. This would be discussed in detail in chapter 3 and 5.

2.4 Compact scheme for the ψ-v formulation of the Navier-Stokes equations

Although the streamfunction-vorticity (ψ-ω) formulation has been quite popular amongst the researchers, who, over the last several decades employed it to analyse new methods for the numerical solutions of a variety of fluid flow problems, a certain difficulty is associated with this type of formulation which lies in the specification of vorticity values at the no-slip boundaries. Since the vorticity (ω) is defined through the Poisson equation $-\omega = \psi_{xx} + \psi_{yy}$, it needs to be solved discretely on the boundaries so that boundary values of the vorticity can be specified for the vorticity transport equation when this formulation is utilized. But the vorticity values on the boundaries are generally unspecified and therefore one has to carry out some numerical approximations in order to specify the boundary values of vorticity.

In order to avoid this difficulty, another alternative formulation [41, 90] of equation (2.4) can be derived by substituting ψ for ω from equation (4.1) in equation (4.2). This results in a fourth-order partial differential equation as:

$$\nabla^4\psi - Re\left(v\nabla^2 u - u\nabla^2 v\right) = 0 \tag{2.17}$$

with

$$u(x, y) = \psi_y \text{ and } v(x, y) = -\psi_x \tag{2.18}$$

where

$$\nabla^4\psi = \frac{\partial^4\psi}{\partial x^4} + 2\frac{\partial^4\psi}{\partial x^2\partial y^2} + \frac{\partial^4\psi}{\partial y^4} \tag{2.19}$$

Using equations (2.18)-(2.19), equation (2.17) may be written in the expanded form as

$$\frac{\partial^4\psi}{\partial x^4} + 2\frac{\partial^4\psi}{\partial x^2\partial y^2} + \frac{\partial^4\psi}{\partial y^4} - Re\,u\left[\frac{\partial^3\psi}{\partial x^3} + \frac{\partial^3\psi}{\partial x\partial y^2}\right] + Re\,v\left[\frac{\partial^3\psi}{\partial x^2\partial y} + \frac{\partial^3\psi}{\partial y^3}\right] = 0 \tag{2.20}$$

This formulation is known as the streamfunction-velocity formulation or bi-harmonic formulation of the 2D Navier-Stokes equations.

The prime advantages of using this formulation are:

1. Avoids difficulties associated with primitive variables u, v, p.
2. Avoids difficulties associated with vorticity boundary conditions in the ψ-ω approach.
3. Iterations involve only the single variable ψ.
4. Reduces the computational effort and costs.

Treating the velocities u and v in equation (2.20) as locally fixed at the grid point (x, y), Gupta and Kalita [41] uses their *Mathematica* code and developed the following compact finite difference scheme for the 2D steady Navier-Stokes equations

$$\begin{aligned}&\psi_{i-1,j-1} - 8\psi_{i,j-1} + \psi_{i+1,j-1} - 8\psi_{i-1,j} + 28\psi_{i,j} - 8\psi_{i+1,j} + \psi_{i-1,j+1} - 8\psi_{i,j+1}\\ &\psi_{i+1,j+1} - 3h(u_{i,j-1} - u_{i,j+1} + v_{i+1,j} - v_{i-1,j}) - 0.5Reh^2\{v_{i,j}(u_{i+1,j} + u_{i-1,j}\\ &+ u_{i,j+1} + u_{i,j-1}) - u_{i,j}(v_{i+1,j} + v_{i-1,j} + v_{i,j+1} + v_{i,j-1})\} = 0\end{aligned} \tag{2.21}$$

where

$$u_{i,j} = \frac{3}{4h}(\psi_{i,j+1} - \psi_{i,j-1}) - \frac{1}{4}(u_{i,j+1} - u_{i,j-1}) \tag{2.22}$$

$$v_{i,j} = -\frac{3}{4h}(\psi_{i+1,j} - \psi_{i-1,j}) - \frac{1}{4}(v_{i+1,j} - v_{i-1,j}) \tag{2.23}$$

Equations (4.9) and (4.9) are derived using the definitions of the velocities u and v given by equation (2.18).

In the present work, we will employ the finite difference scheme (2.21) to approximate the streamfunction-velocity formulation of the 2D Navier-Stokes equations. These compact schemes forms the basis of the first part of our work which discusses their applications in the global stability analysis of incompressible viscous flows. The later part of our work introduces some new HOC schemes which are applicable for the 3D Navier-Stokes equations and the Euler equations of Gas Dynamics. All these discussions will be carried out in the subsequent chapters.

Chapter 3

GLOBAL 2D STABILITY ANALYSIS OF THE TWO-SIDED STAGGERED LDC FLOW WITH AN HOC APPROACH

3.1 Introduction

Almost all of the Higher Order Compact schemes that have been developed so far are mainly used for numerical simulation of fluid flow problems. One can see an increasing trend in the use of such schemes over the years. To the best of our knowledge, HOC schemes have not yet been utilized for analyzing the global stability of fluid flows. In this chapter, we utilize the recently developed HOC scheme by Kalita *et al.* [56] to carry out a global two-dimensional (2D) stability analysis of the two-sided 2D staggered lid-driven cavity flow [1].

For a long time, flows in cavities have been a major topic of research for mathematicians and engineers. The LDC problem is a frequently used benchmark

[1] A part of this work has been published in *Computers and Mathematics with Applications* [58]

problem for the assessment of numerical methods for solving the Navier-Stokes (N-S) equations, because it displays almost all fluid mechanical phenomena for incompressible viscous flows in the simplest of geometric settings. Therefore, the dynamics of fluid in LDCs have been one of the mainstays of computational fluid dynamics research over the last few decades, particularly for establishing newly developed numerical schemes [31, 41, 57, 55, 60, 105]. In recent years, double driven staggered LDC has become a major topic of interest among the researchers. The double driven staggered LDC is a slightly modified version of the the simple two-sided LDC, which was probably first studied in length by Kuhlmann and Wanschura [66], and later on by their co-workers [4, 15]. The two-sided staggered LDC which can be thought of as two superimposed lid-driven square cavities diagonally offset by 40%, was first introduced by Hinatsu and Ferziger in 1991 [46] and many interesting results on the flow structures followed soon. A more detailed analysis of the flow was carried out by Zhou *et al.* [129] in 2003 with discrete singular convolution (DSC) approximation, where they have obtained benchmark quality solutions over the range of Reynolds numbers between 50 and $3,200$ with the top and bottom lids moving in antiparallel motion. This was followed by Nithiarasu and Liu [82] in 2005 who investigated this problem for the antiparallel motion of the lids and as a potential benchmark problem by using an artificial compressibility-based characteristic-based split scheme. Recently in 2010, Tekic *et al.* [111] have simulated the flows in staggered LDC, for both antiparallel and parallel motion with the aid of Lattice Boltzmann Simulation.

In the last three decades, the higher-order compact finite difference methods for two-dimensional flows have gained a lot of popularity amongst the researchers and since then many specialized techniques have been developed for different fluid flow problems. In 2002, Kalita *et al.* [56] proposed a class of implicit HOC schemes for solving the unsteady two-dimensional convection-diffusion equation with variable convection coefficients. These schemes were seen to be very effective in handling fluid flow problems governed by 2D incompressible Navier-Stokes (N-S) equations. In this chapter, we apply one of these schemes to simulate the two-sided staggered lid-driven cavity problem governed by the 2D N-S equations. Analogous to the work of Kalita *et al.* [56], we simulate

the flows inside the cavity by considering the streamfunction-vorticity (ψ-ω) formulation of the 2D N-S equations. The flow pattern is then investigated using the HOC scheme mentioned above ([56]) and results of the HOC simulation for both parallel and antiparallel motion of lids are compared with the data from existing literatures. Excellent comparison is obtained in both the cases.

Despite the growing popularity of the 2D staggered two-sided LDC amongst the researchers in the last two decades, one aspect of this study that has not attracted the attention of the researchers is the global 2D stability analysis of the flow. This may be attributed to the fact that simulation of the unsteady equations and obtaining accurate values of the critical parameters for which the stability is lost, in general are difficult tasks and computationally very expensive. On the contrary, stability analysis of the simple 2D Lid Driven Cavity problem has been investigated by a number of researchers on a square cavity. One may refer to the work of Gustafson and Halasi [43, 44], Goodrich *et al.* [34], Auteri *et al.* [10], Aidun *et al.* [3], Poliashenko and Aidun [89], Fortin *et al.* [29], Peng *et al.* [88], Tiesinga *et al.* [112], Cadou *et al.* [17], Sahin *et al.* [94] etc. More recently, Bopanna and Gajjar [16] carried out global stability analysis of the 2D simple LDC using an accurate numerical technique based on a hybrid scheme with spectral collocation in the y-direction and higher-order finite differences in the x-direction. But despite the presence of quite a number of global stability analysis study for the one sided square LDC problem in the literature, to the best of our knowledge, no global 2D stability analysis has been carried out for the two-sided 2D lid-driven staggered cavity flow so far. In our present study, we carry out a global two-dimensional stability analysis of the staggered LDC, both for parallel and antiparallel motion of lids, with grid aspect ratio unity by following the same strategy adopted in [16]. However, in contrast to their hybrid scheme, we have employed the HOC scheme proposed by Kalita *et al.* [56] to simulate the steady state flow and then utilized the same scheme to investigate the stability of the flow in the staggered lid-driven cavity by solving the generalized 2D eigenvalue problem obtained from the linearized unsteady equations.

3.2 The Problem

The problem considered here is the diagonally symmetric, two-sided staggered LDC with the top and bottom lids moving at equal velocity as shown in Figure 3.1.

We have followed the same configuration as in Tekic *et al.* [111]. Essentially, it can be thought of as two superimposed square lid-driven cavities of length L, diagonally offset by 40%, i.e. $0.4L$. Here, we assumed that the velocities at the top and bottom lids to be U and $-U$ respectively, for antiparallel motion, while it is taken as U at both the lids for parallel motion.

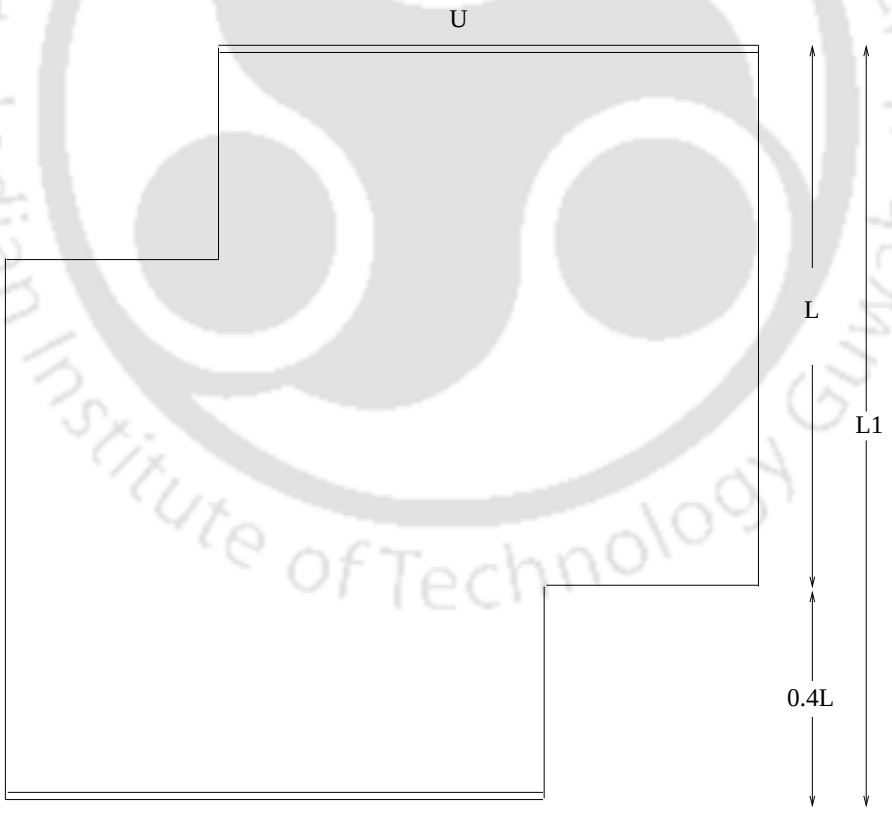

(a) − U (antiparallel motion)
(b) U (parallel motion)

Figure 3.1: A two-sided Staggered Lid-Driven Cavity.

The flow inside the cavity is governed by the unsteady 2D N-S equations which in non-dimensional form, can be written as

$$\frac{\partial u}{\partial x} + \frac{\partial v}{\partial y} = 0, \tag{3.1a}$$

$$\frac{\partial u}{\partial t} + u\frac{\partial u}{\partial x} + v\frac{\partial u}{\partial y} = -\frac{\partial p}{\partial x} + \frac{1}{Re}\nabla^2 u, \tag{3.1b}$$

$$\frac{\partial v}{\partial t} + u\frac{\partial v}{\partial x} + v\frac{\partial v}{\partial y} = -\frac{\partial p}{\partial y} + \frac{1}{Re}\nabla^2 v, \tag{3.1c}$$

Here u and v are the velocities along x- and y-directions and p is the pressure; Re is the Reynolds number defined as UL/ν, where ν is the kinematic viscosity of the fluid; U is the velocity of the lid and $L = 1.4$ is the width of the cavity which are used to non-dimensionalize the velocity and length-scale variables, respectively. For the present configuration, we have taken the non-dimensional velocity U as 1.

Introducing streamfunction ψ and vorticity ω, the above equations can be written as

$$\omega_t - \frac{1}{\mathrm{Re}}\left(\omega_{xx} + \omega_{yy}\right) + (u\omega_x + v\omega_y) = 0, \tag{3.2}$$

$$\psi_{xx} + \psi_{yy} = -\omega(x, y). \tag{3.3}$$

with

$$u = \psi_y, \quad \text{and} \quad v = -\psi_x, \tag{3.4}$$

and

$$\omega = v_x - u_y. \tag{3.5}$$

The boundary conditions for the antiparallel motion are given by

$$\begin{aligned}
&\psi = 0 \text{ and } \psi_y = -1 \text{ for } y = 0, \quad 0 \le x \le 1 \\
&\psi = 0 \text{ and } \psi_x = 0 \quad \text{for } x = 1, \quad 0 \le y \le 0.4 \\
&\psi = 0 \text{ and } \psi_y = 0 \quad \text{for } y = 0.4, \ 1 \le x \le 1.4 \\
&\psi = 0 \text{ and } \psi_x = 0 \quad \text{for } x = 1.4, \ 0.4 \le y \le 1.4
\end{aligned} \tag{3.6}$$

$$\begin{aligned}
&\psi = 0 \text{ and } \psi_y = 1 \quad \text{for } y = 1.4,\ 0.4 \le x \le 1.4 \\
&\psi = 0 \text{ and } \psi_x = 0 \quad \text{for } x = 0.4,\ 1 \le y \le 1.4 \\
&\psi = 0 \text{ and } \psi_y = 0 \quad \text{for } y = 1,\ 0 \le x \le 0.4 \\
&\psi = 0 \text{ and } \psi_x = 0 \quad \text{for } x = 0,\ 0 \le y \le 1
\end{aligned} \tag{3.7}$$

The boundary conditions for the parallel motion are same as (3.7), except that the first condition must be replaced by

$$\psi = 0 \text{ and } \psi_y = 1 \text{ for } y = 0, \quad 0 \le x \le 1$$

These boundary conditions clearly indicate that flow singularities exist at the corners with coordinates $(0, 0)$, $(1.0, 0)$, $(0.4, 1.4)$ and $(1.4, 1.4)$.

3.2.1 The Numerical Scheme

In order to discretize the governing equations (3.2)-(3.3), we use the HOC scheme developed by Kalita *et al.* [56] for the unsteady convection-diffusion equation for variable convection coefficients. The scheme is briefly discussed below.

The unsteady two-dimensional convection-diffusion equation for a transport variable ϕ in some domain can be written as

$$a\frac{\partial \phi}{\partial t} - \nabla^2 \phi + c(x,\ y,\ t)\frac{\partial \phi}{\partial x} + d(x,\ y,\ t)\frac{\partial \phi}{\partial y} = g(x,\ y,\ t) \tag{3.8}$$

where a is a constant, c and d are the convection coefficients, and g is a forcing function. The $(9, 9)$ HOC scheme by Kalita *et al.* [56] for this equation with accuracy $O((\triangle t)^2,\ h^4,\ k^4)$ is given by:

$$a\left[1+\frac{h^2}{12}(\delta_x^2-c_{ij}\delta_x)+\frac{k^2}{12}(\delta_y^2-d_{ij}\delta_y)\right]\delta_t^+\phi_{ij}^n-$$
$$\frac{1}{2}\left[\alpha_{ij}\delta_x^2+\beta_{ij}\delta_y^2-C_{ij}\delta_x-D_{ij}\delta_y+\frac{h^2+k^2}{12}(\delta_x^2\delta_y^2-c_{ij}\delta_x\delta_y^2-d_{ij}\delta_x^2\delta_y-\gamma_{ij}\delta_x\delta_y)\right]$$
$$(\phi_{ij}^n+\phi_{ij}^{n+1})=\frac{1}{2}(G_{ij}^n+G_{ij}^{n+1}) \tag{3.9}$$

where δ_t^+ denotes the forward difference operator for time with uniform step length $\triangle t$, and δ_x, δ_y are the first order and δ_x^2, δ_y^2 are the second order central difference operators in the space directions x and y with uniform step lengths h and k respectively.

The coefficients α_{ij}, β_{ij}, γ_{ij}, C_{ij}, D_{ij} and G_{ij} are given by:

$$\alpha_{ij}=\frac{h^2}{12}(c_{ij}^2-2\delta_x c_{ij}) \tag{3.10}$$

$$\beta_{ij}=\frac{h^2}{12}(d_{ij}^2-2\delta_y d_{ij}) \tag{3.11}$$

$$\gamma_{ij}=\frac{2}{h^2+k^2}(h^2\delta_x d_{ij}+k^2\delta_y c_{ij}-c_{ij}d_{ij}) \tag{3.12}$$

$$C_{ij}=[1+\frac{h^2}{12}(\delta_x^2-c_{ij}\delta_x)+\frac{k^2}{12}(\delta_y^2-d_{ij}\delta_y)]c_{ij} \tag{3.13}$$

$$D_{ij}=[1+\frac{h^2}{12}(\delta_x^2-c_{ij}\delta_x)+\frac{k^2}{12}(\delta_y^2-d_{ij}\delta_y)]d_{ij} \tag{3.14}$$

$$G_{ij}=[1+\frac{h^2}{12}(\delta_x^2-c_{ij}\delta_x)+\frac{k^2}{12}(\delta_y^2-d_{ij}\delta_y)]g_{ij} \tag{3.15}$$

Here, it is assumed that the convection coefficients c, d and the forcing function g are sufficiently smooth.

In order to solve the ψ-ω formulation of N-S equations using (3.9), we employ an outer-inner iteration procedure and for reaching steady state, a time

marching strategy is adopted. In a typical outer temporal cycle, we discretize equation (3.2) using (3.9) with $a = Re$, $c = Reu$, $d = Rev$ and $g = 0$. Once ω is obtained, we compute ψ by discretizing (3.3) with the steady state version of (3.9). Thus on setting $\phi = \psi$, $c = d = 0 = \delta_t^+ \phi_{ij}$ and $g = -\omega$, the fourth order compact approximation of the Poisson equation (3.3) becomes

$$\left[\delta_x^2 + \delta_y^2 + \frac{1}{12}(h^2 + k^2)\delta_x^2\delta_y^2\right]\psi_{ij} = \left[1 + \frac{h^2}{12}\delta_x^2 + \frac{k^2}{12}\delta_y^2\right]\omega_{ij}. \tag{3.16}$$

3.2.2 Approximation of the vorticity boundary conditions

The value of the streamfunction ψ is taken to be zero along all the boundaries while the vorticity boundary condition is derived using a fourth order compact scheme for the Neumann boundary condition. For example, on the leftmost wall ($x = 0$, $0 \leq y \leq 1$), the approximation for ω can be found from the relation $v = -[(\partial\psi)/(\partial x)]$ and equations (3.2), (3.4) and (3.5) as

$$-\delta_x^+\psi_{0j} - \left[\frac{h}{2} + \frac{h^2}{6}\delta_x^+ - \frac{h^3}{24}(Rev_{0j}\delta_y - \delta_y^2)\right]\omega_{0j} = v_{0j} - \frac{h^3}{24}(\delta_x^+\delta_y^2 v_{0j} - \delta_t^+\omega_{0j}) \tag{3.17}$$

where the suffixes 0 and j stand for the leftmost wall and the vertical index respectively. Using equation (3.7) and $v = -[(\partial\psi)/(\partial x)]$ we obtain an explicit expression for ω on the leftmost wall as

$$\omega_{0j}^{n+1} = \frac{24\triangle t}{h^3}\left[-\frac{\psi_{1j}^n}{h} - \frac{h}{2}\omega_{0j}^n - \frac{h}{6}(\omega_{1j}^n - \omega_{0j}^n) - \frac{h}{24}(\omega_{0j+1}^n - 2\omega_{0j}^n + \omega_{0j-1}^n)\right] + \omega_{0j}^n \tag{3.18}$$

Vorticities on the other walls can be found in a similar way and for the corners, we use a third order approximation as outlined in [105].

After discretization, the vorticity equation (3.2) and the streamfunction equation (3.3) reduce to the single matrix form of the type

$$A\boldsymbol{\phi} = \boldsymbol{B} \tag{3.19}$$

where the coefficient matrix A is an asymmetric sparse matrix with each row containing at most nine non-zero entries, $\boldsymbol{\phi}$ is the unknown vector (ψ or ω) and $\boldsymbol{B}$ is the vector of known (source) terms. For a grid of size $m \times n$, A is of size $mn \times mn$, and $\boldsymbol{\phi}$ and $\boldsymbol{B}$ are mn-component vectors.

The next step now is to solve equation (3.19); as the coefficient matrix A is not generally diagonally dominant, conventional solvers such as Gauss-Seidel cannot be used. For both the vorticity and streamfunction equation, the resulting matrix equations are solved using BiCGStab [63, 101], which constitutes the inner iterations. Once (3.3) is solved, u and v in (3.4) are calculated using a fourth order compact formula (see ref. [56]). This constitutes one outer iteration cycle. For the inner iterations, the computations were stopped when the norm of the residual vector $\boldsymbol{r} = \boldsymbol{B} - A\boldsymbol{\phi}$ ($\boldsymbol{\phi}$ being either ψ or ω) arising out of equation (3.19) fell below 10^{-6}. Steady state was assumed to reach when the maximum ω-error between two successive outer temporal iteration steps was smaller than the tolerance limit 0.5×10^{-6}.

3.2.3 The Algorithm

The algorithm for computing the flow inside the cavity by solving the ψ-ω formulation of the N-S equations can be summarized as follows:

1. Initialize $\psi^{(n)}$, $\omega^{(n)}$, $u^{(n)}$ and $v^{(n)}$ for $n = 0$ with zero everywhere except at the boundaries where values from equations (3.7) and(3.17) are to be used.

2. Solve the vorticity transport equation of (3.2) by using the HOC formulation (3.9).

3. Solve the stream-function (ψ) equation of (3.3), using (3.16).

   In both 2 and 3, solve the algebraic system of equations of the form (3.19) till the l_2 norm of the residual, that is $||\boldsymbol{B} - A\boldsymbol{\phi}||_2 < 10^{-6}$ ($\boldsymbol{\phi}$ being either ψ or ω).

4. Compute $u^{(n+1)}$ and $v^{(n+1)}$ from (3.4) using the fourth order compact approximation of Kalita *et al.* [56].

5. If $\max|\omega^{(n+1)} - \omega^{(n)}| < 0.5 \times 10^{-6}$ steady state is reached, stop computation; else repeat steps 2 to 4 until convergence.

In the above $(n+1)$ and (n) stand for the $(n+1)^{th}$ and $(n)^{th}$ time levels, respectively.

Flow simulations are carried out using uniform grids of sizes 71×71, 85×85, 99×99, 106×106, 141×141 and 211×211 with a time step $\triangle t = 0.01$ in the range of Reynolds numbers $50 \leq Re \leq 12,000$ for both the antiparallel and parallel motion of the lid. In the cases where steady state is achievable, a time marching strategy is adopted till a steady state is reached. In all the computations for this problem except in section 3.5, the data from the previous lower Reynolds numbers were used as the initial data except for $Re = 50$, where zero initial data was used. Unless otherwise mentioned, all the qualitative and quantitative results presented here are from computations on a 211×211 grid.

3.3 Validation of the code

To the best of our knowledge, no global stability analysis is available for the flow in a staggered cavity. Therefore, the validation of the present algorithm is first done through a comparison exercise for a a certain range of Reynolds numbers for which reliable qualitative and quantitative numerical results [82, 111, 129] are available so that the confidence resulting from accurate validation of our numerical results with the established ones could be carried over to the threshold region where computation of the flow could be very delicate.

3.3.1 Antiparallel motion

We present numerical results for the antiparallel motion of the top and bottom lids in Figures 3.2-3.5 and Table 3.1. Figure 3.2 shows a side by side comparison of our computed steady state streamlines for $Re = 50$, 100, 400 and $1,000$

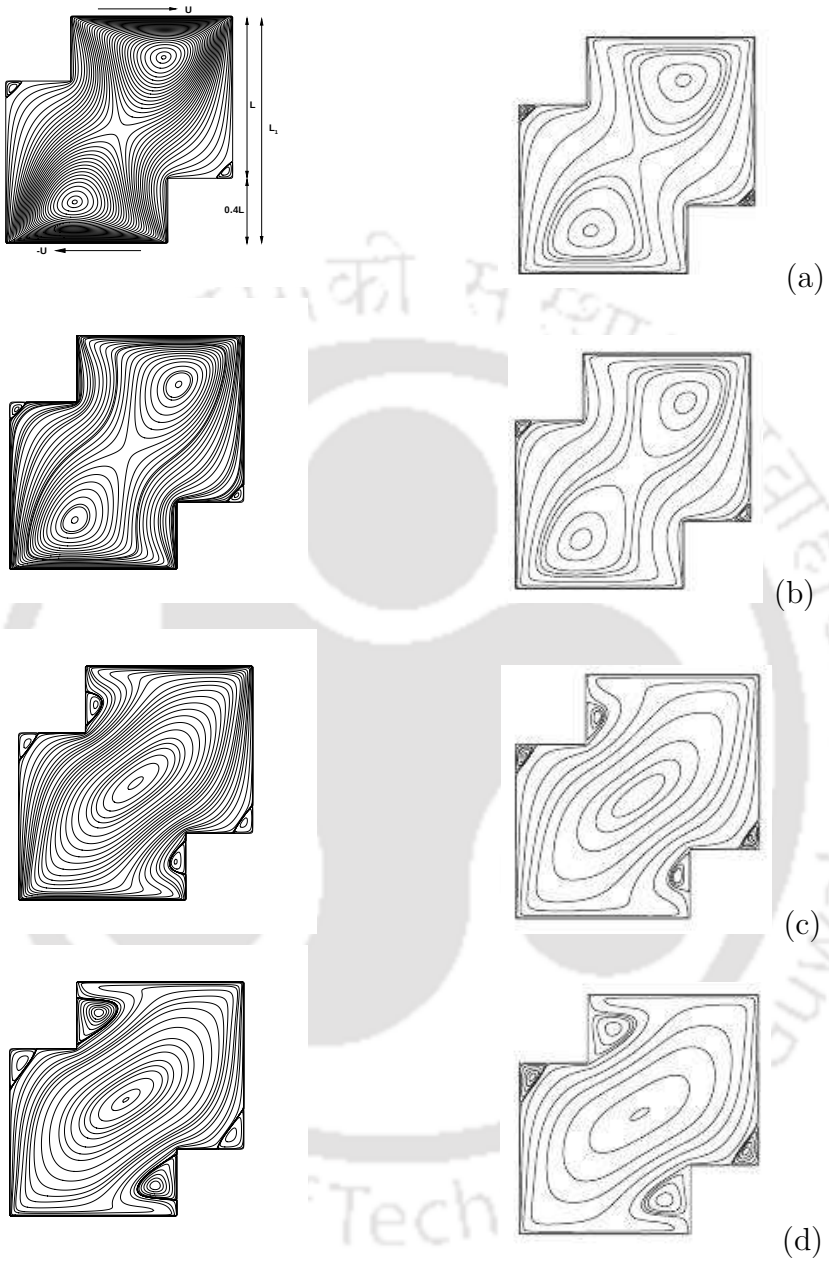

Figure 3.2: *Comparison of streamlines from the present computation (left column) on a* 211×211 *grid with those of Zhou* et al. *[129] (right column) at : (a)*$Re = 50$*, (b)*$Re = 100$*, (c)*$Re = 400$ *and (d)* $Re = 1,000$ *- antiparallel motion.*

on a grid of size 211×211 with those of Zhou *et al.* [129]. As can be seen from

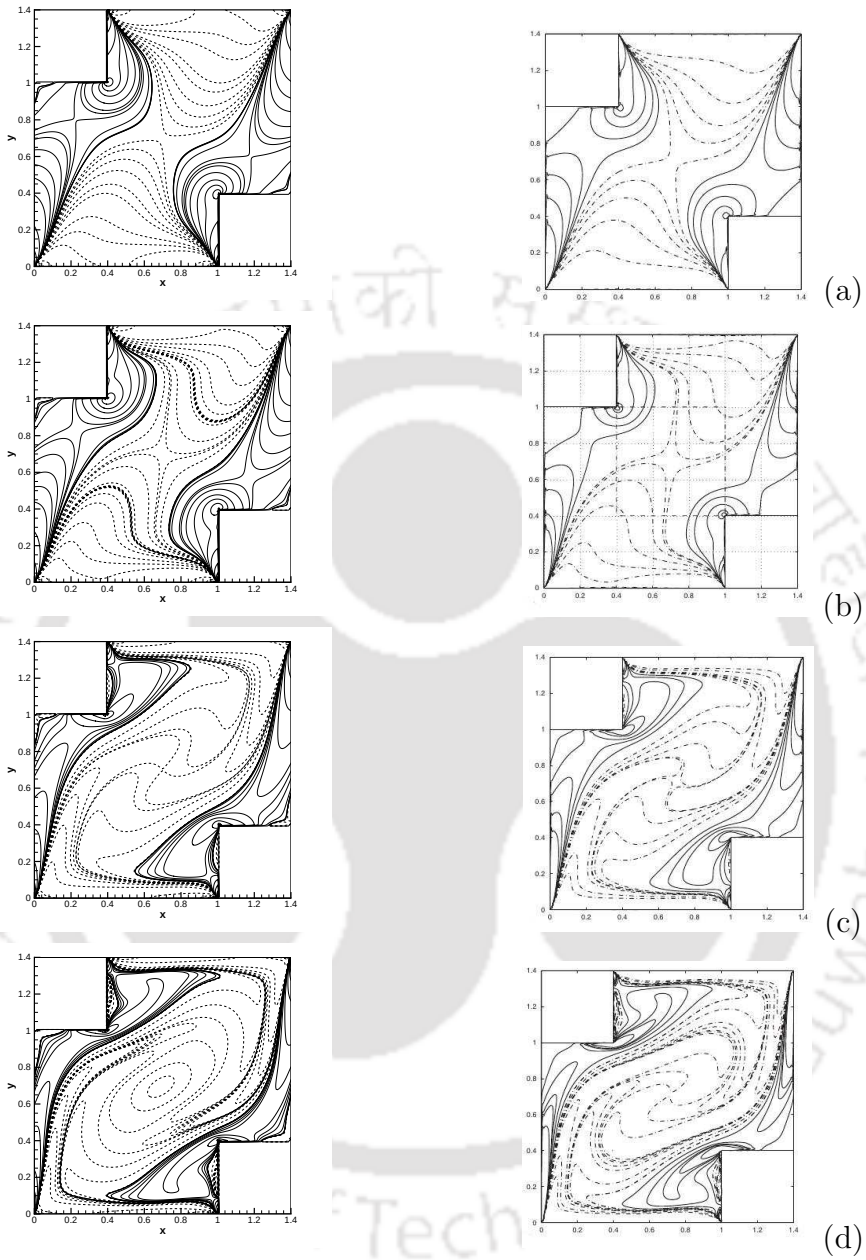

Figure 3.3: *Comparison of vorticity contours from the present computation (left column) on a* 211×211 *grid with those of Zhou* et al. *[129] (right column) at :* $(a)Re = 50$, $(b)Re = 100$, $(c)Re = 400$ *and (d)* $Re = 1,000$ *- antiparallel motion.*

the figures, the flow is symmetrical about the longer and shorter diagonals of the cavity and our simulations are very close to the ones obtained by Zhou *et*

Table 3.1: *Location and vorticity values in the centres of primary and secondary vortices - antiparallel motion.*

		Primary vortex		First secondary vortex		Second secondary vortex	
Re	References	(x_{c1}, y_{c1})	ω_1	(x_{c2}, y_{c2})	ω_2	(x_{c3}, y_{c3})	ω_3
50	Zhou *et al.* [129]	(0.9781, 1.1600)	-3.05843	(1.3556, 0.4405)	0.02395		
		(0.4219, 0.2518)	-3.05670	(0.0444, 0.9595)	0.02394		
	Liu *et al.* [82]	(0.9776, 1.1478)	-3.07633	(1.3566, 0.4446)	0.02786		
		(0.4263, 0.2473)	-3.10055	(0.0424, 0.9569)	0.02587		
	Tekic *et al.* [111]	(0.9637, 1.1551)	-4.2768	(1.3484, 0.4476)	0.0304		
		(0.4494, 0.2543)	-4.2920	(0.0460, 0.9543)	0.0412		
	Present study	(0.9733, 1.1400)	-2.97225	(1.3533, 0.4400)	0.02905		
		(0.4266, 0.2467)	-3.09339	(0.0466, 0.9533)	0.03649		
100	Zhou *et al.* [129]	(1.0172, 1.1091)	-2.7239	(1.3556, 0.4486)	0.04399		
		(0.3828, 0.2889)	-2.7231	(0.0444, 0.9514)	0.04401		
	Liu *et al.* [82]	(1.0114, 1.1035)	-2.69993	(1.3566, 0.4446)	0.03975		
		(0.3865, 0.2894)	-2.73231	(0.0424, 0.9569)	0.03695		
	Tekic *et al.* [111]	(1.0031, 1.1382)	-4.0616	(1.3502, 0.4457)	0.0384		
		(0.4082, 0.2693)	-4.1610	(0.0460, 0.9543)	0.0537		
	Present study	(1.0066, 1.1000)	-2.6259	(1.3533, 0.4400)	0.041889		
		(0.3866, 0.2933)	-2.6933	(0.0400, 0.9600)	0.032549		
400	Zhou *et al.* [129]	(0.7000, 0.7000)	-1.54842	(1.3500, 0.4656)	0.15569	(0.4703, 1.1625)	1.38495
				(0.0500, 0.9344)	0.15777	(0.9219, 0.2375)	1.38140
	Liu *et al.* [82]	(0.6995, 0.6966)	-1.60552	(1.3483, 0.4688)	0.19767	(0.4772, 1.1610)	1.70971
				(0.0569, 0.9400)	0.19385	(0.9232, 0.2385)	1.69442
	Tekic *et al.* [111]	(0.6822, 0.6859)	-2.1999	(1.3522, 0.4607)	0.1192	(0.4382, 1.1345)	1.3786
				(0.0554, 0.9506)	0.1574	(0.9824, 0.2862)	0.8613
	Present study	(0.7000, 0.6933)	-1.57755	(1.3400, 0.4600)	0.22630	(0.4600, 1.1600)	1.3849
				(0.0533, 0.9333)	0.2160	(0.9333, 0.2200)	1.5292
1000	Zhou *et al.* [129]	(0.7000, 0.7000)	-1.41562	(1.3250, 0.4844)	0.53846	(0.5484, 1.2000)	2.38557
				(0.0750, 0.9063)	0.53813	(0.7256, 0.2000)	2.38559
	Liu *et al.* [82]	(0.6895, 0.6969)	-1.52363	(1.3221, 0.4836)	0.65005	(0.5505, 1.2071)	2.73409
				(0.0753, 0.9142)	0.63326	(0.8523, 0.2015)	2.60588
	Tekic *et al.* [111]	(0.7004, 0.7001)	-2.0834	(1.3331, 0.4830)	0.5761	(0.5301, 1.1962)	3.3958
				(0.0714, 0.9229)	0.5667	(0.8726, 0.2059)	3.4679
	Present study	(0.6867, 0.6933)	-1.54962	(1.3266, 0.4733)	0.5511	(0.5333, 1.2133)	2.59822
				(0.0667, 0.9133)	0.5673	(0.8600, 0.1800)	2.68074

al. [129]. One can also see the appearance of two more secondary vortices on the top left and bottom right sides of the cavity for $Re = 400$ and $1,000$. With increase in Re, the corner vortices grow in size. The corresponding vorticity contours for the same range of Reynolds numbers shown in Figure 3.3 where the solid and dotted lines correspond to positive and negative values of the vorticity. From the figure, it is clear that the flow patterns depicted by the vorticity contours are very close to the ones computed by Zhou *et al.* [129]. Note that though the locations of the primary and secondary vortices match

very well with the ones obtained by [82, 111, 129] (see Table 3.1), the vorticity values obtained by [111] at the centers of these vortices differs reasonably from the ones obtained by the present computation and [82, 129]. However, in all aspects, our results match very well with [82] and [129]. The data from Table 3.1 clearly indicates that the vortices located at symmetrically opposite locations with respect to the diagonals are of almost equal strength.

We have also presented the streamlines and vorticity contours for $Re = 215$ and 225 in Figure 3.4. From the figure, it is evident that somewhere between $Re = 215$ and 225, the top right and bottom left primary vortices coalesce to form a single primary vortex.

In Figure 3.5, we compare our computed horizontal velocity along the vertical centerline and the vertical velocity along the horizontal centerline of the cavity for these Re with those obtained by Zhou *et al.* [129]. Note that in their computation, Zhou *et al.* [129] used a $1,12,429$ point grid which is equivalent to a grid of size 335×335. On the other hand, with a grid of size 211×211, we were able to match the results of Zhou *et al.* [129] including the steep velocity gradients for the higher Reynolds number as is obvious from the figure. These graphs also reconfirms the symmetric pattern of the flow for the range of Reynolds number considered here.

3.3.2 Parallel motion

Next, we compute the flow for the parallel motion of lids, and then we compare our steady state results with that of Tekic *et al.* [111] for the range of Reynolds number $50 \leq Re \leq 3,200$ in Figures 3.6 and 3.7 and Tables 3.2 and 3.3. We once again present a side by side comparison of streamfunction and vorticity contours with those of Tekic *et al.* in Figures 3.6 and 3.7 respectively. In the left column of Figure 3.6, we plot the streamlines obtained from our numerical experiments and on the right column of the same figure, the corresponding streamlines obtained by Tekic *et al.* [111] have been illustrated. Similarly in Figure 3.7, we have shown a comparison of our vorticity contour plots with those of Tekic *et al.* [111]. From the figures, one can see an excellent match

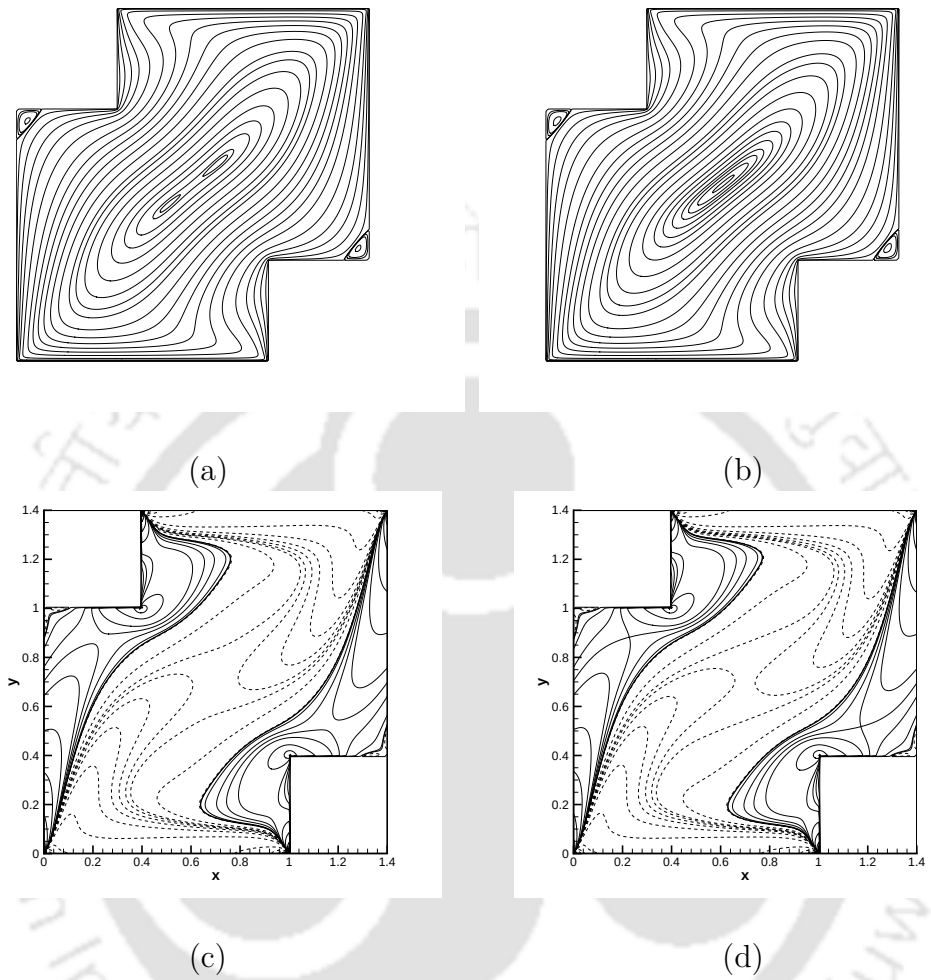

Figure 3.4: *Antiparallel motion of the lids : Streamlines at* $(a)Re = 215$, $(b)Re = 225$ *and vorticity contours at* $(c)Re = 215$, *(d)* $Re = 225$.

between our obtained numerical results and theirs.

Moreover, it is noteworthy that our computed streamlines clearly reveal the secondary vortices in the extreme top left corner of the cavity in the range of $50 \leq Re \leq 400$ and the extreme bottom right corner tertiary vortices in the range $400 \leq Re \leq 3,200$; these vortices were visibly absent in the figures resulting from the simulation of Tekic *et al.* [111]. Note that the second secondary vortex for $Re = 1,000$ was not clearly visible in their simulation (see Table 3.2 also). Again, contrary to the antiparallel motion, no symmetry

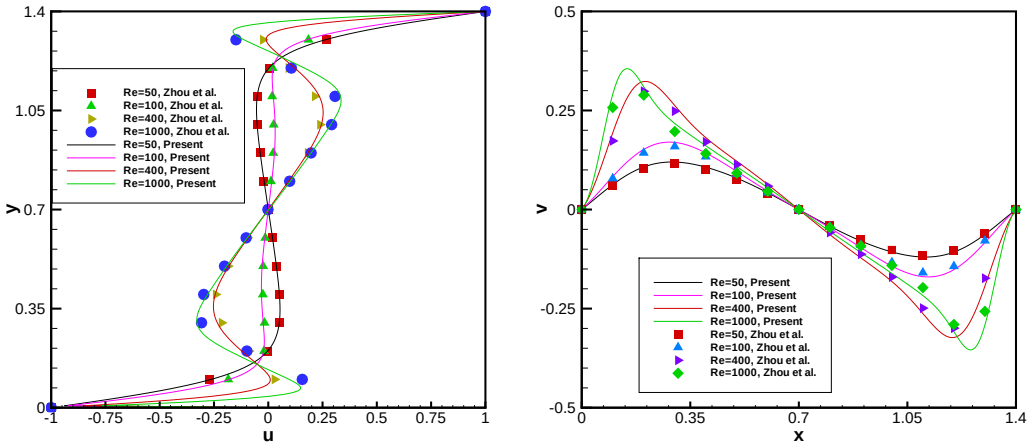

(a) (b)

Figure 3.5: *The velocity profiles (a) u- and (b) v- along the vertical and horizontal centrelines for antiparallel motion.*

was observed in the flow pattern. Unlike antiparallel motion, one can see the presence of two primary vortices for the whole range of Re for which the flow has been computed. With increase in Re (which is visible from $Re = 3,200$ onwards here, see the instantaneous streamlines for $Re = 5,000$ and $12,000$ in Figure 3.23(b), (d) as well), one can see the presence of a secondary vortex at the extreme bottom left corner of the cavity. The locations and strengths of the primary and secondary vortices are presented in Table 3.2 and compared with those of [111]. As in antiparallel motion, although excellent comparison is obtained for the location of the vortices, there is reasonable difference in the vorticity values thereat. In Table 3.3, we present the strengths and locations of the tertiary vortices in the range $400 \leq Re \leq 3,200$.

In Figure 3.8, we present the graphs of the horizontal velocity along the vertical centerline and the vertical velocity along the horizontal centerline of the cavity for $50 \leq Re \leq 1,000$ and compare them with the results of [111].

As no quantitative data is available for the parallel motion for comparison, we also provide a table for the horizontal velocity along the vertical centerline

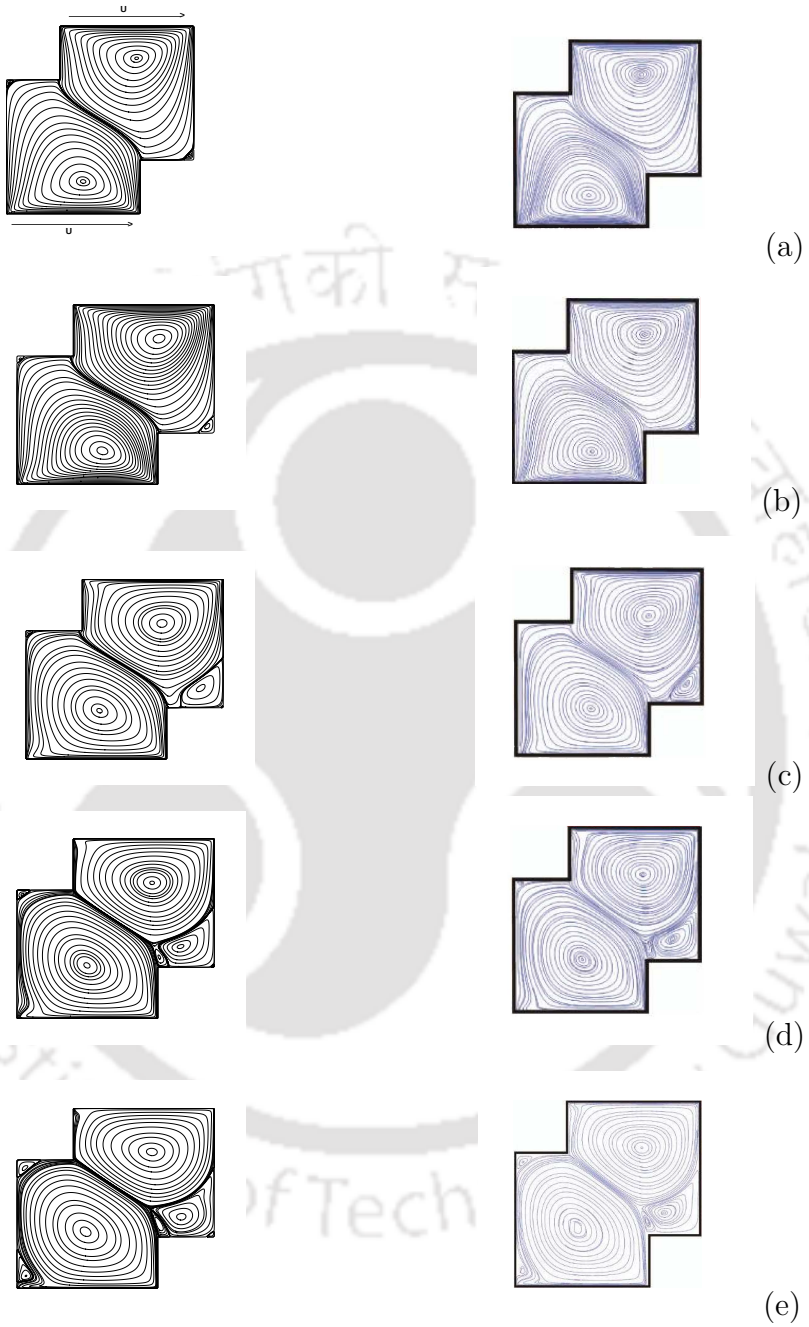

Figure 3.6: *Comparison of streamlines from the present computation (left column) on a* 211×211 *grid with those of Tekic* et al. *[111] (right column): (a)* $Re = 50$*, (b)*$Re = 100$*, (c)*$Re = 400$*, (d)*$Re = 1,000$ *and (e)*$Re = 3,200$ *- parallel motion.*

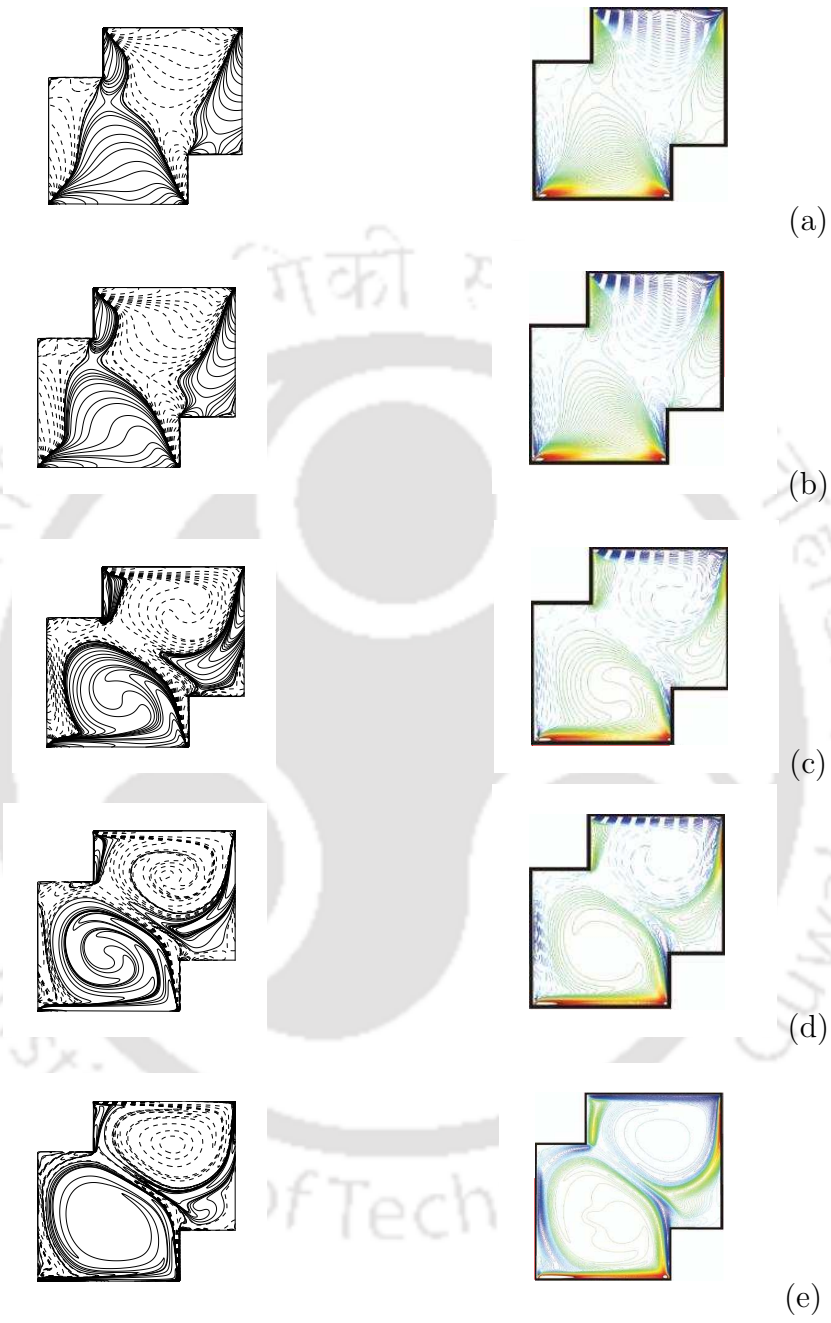

Figure 3.7: *Comparison of vorticity contours from the present computation (left column) on a* 211×211 *grid with those of Tekic* et al. *[111] (right column): (a)* $Re = 50$*, (b)*$Re = 100$*, (c)*$Re = 400$*, (d)*$Re = 1,000$ *and (e)*$Re = 3,200$ *- parallel motion.*

Table 3.2: *Locations and vorticity values in the centres of primary and secondary vortices - parallel motion.*

		Primary vortex		First secondary vortex		Second secondary vortex	
Re	References	(x_{c1}, y_{c1})	ω_1	(x_{c2}, y_{c2})	ω_2	(x_{c3}, y_{c3})	ω_3
50	Tekic *et al.* [111]	(0.9599, 1.1607)	-4.5273	(1.3671, 0.4419)	0.0136		
		(0.5602, 0.2468)	4.5478				
	Present study	(0.9733, 1.1533)	-3.2847	(1.3667, 0.4333)	0.0126	(0.0267, 0.9733)	-0.01352
		(0.5733, 0.2400)	3.2901				
100	Tekic *et al.* [111]	(0.9994, 1.1532)	-4.5648	(1.3634, 0.4569)	0.0281		
		(0.5978, 0.2581)	4.6025				
	Present study	(1.0066, 1.1333)	-3.1256	(1.3467, 0.4533)	0.0304	(0.0267, 0.9800)	-0.01139
		(0.6066, 0.2600)	3.1952				
400	Tekic *et al.* [111]	(0.9899, 1.0631)	-3.7700	(1.2770, 0.5508)	0.4138		
		(0.5508, 0.3650)	3.5793				
	Present study	(0.9666, 1.0533)	-2.6766	(1.2400, 0.5533)	0.5567	(0.0266, 0.9800)	-0.03596
		(0.5200, 0.3800)	2.4421				
1000	Tekic *et al.* [111]	(0.9712, 1.0556)	-3.3564	(1.1945, 0.5677)	1.2599	(0.0460, 0.9918)	-0.09768
		(0.5114, 0.4138)	3.2437				
	Present study	(0.9800, 1.0467)	-2.6786	(1.1600, 0.5599)	1.2422	(0.0400, 0.9667)	-0.17516
		(0.5000, 0.4133)	2.2425	(1.0067, 0.4800)	-3.1476		
3200	Tekic *et al.* [111]	(0.9655, 1.0575)	-3.1081	(1.1363, 0.5621)	2.2066	(0.0647, 0.9506)	-0.9889
		(0.4738, 0.4457)	2.4533	(1.0068, 0.4982)	-6.2375	(0.0629, 0.1229)	1.6397
	Present study	(0.9600, 1.0600)	-2.2292	(1.1666, 0.5600)	1.4287	(0.0600, 0.9400)	-1.1413
		(0.4866, 0.4400)	1.8408	(1.0067, 0.5000)	-5.3363	(0.0666, 0.1000)	-2.2852

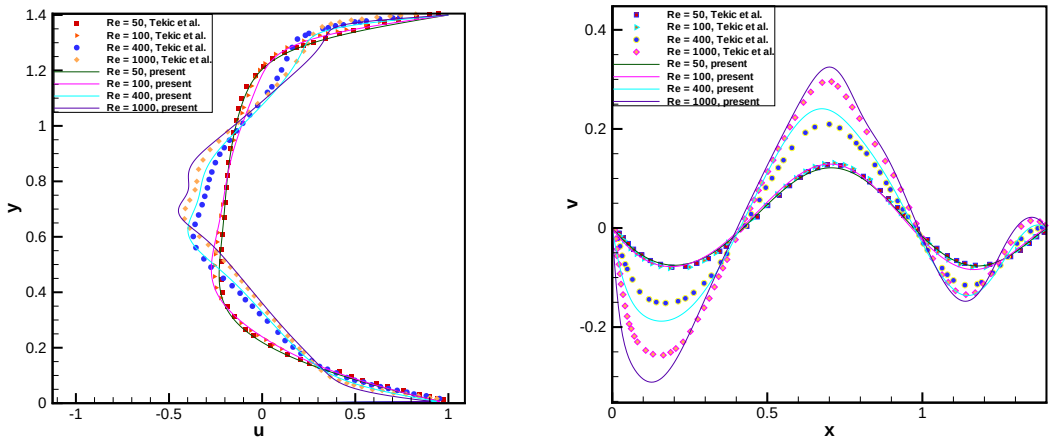

(a) (b)

Figure 3.8: *The velocity profiles (a) u- and (b) v- along the vertical and horizontal centrelines for parallel motion.*

Table 3.3: *Locations and vorticity values in the centres of tertiary vortices - parallel motion.*

	Tertiary vortex	
Re	$(x_{c4},\ y_{c4})$	ω_4
400	(1.3933, 0.4067)	-0.00153
1000	(1.3867, 0.4133)	-0.01202
3200	(1.3800, 0.4200)	-0.03591

and vertical velocity along the horizontal centerline for $50 \leq Re \leq 3,200$ in Tables 3.4 and 3.5.

Table 3.4: *Effect of Reynolds number on the horizontal velocity (u) along mid width ($x = 0.7$) - parallel motion.*

y-co-ordinate	$Re = 50$	$Re = 100$	$Re = 400$	$Re = 1000$	$Re = 3200$
0.0	1.00000	1.00000	1.00000	1.00000	1.00000
0.1	-0.01919	-0.02246	-0.06161	-0.09481	-0.10018
0.2	-0.05959	-0.06730	-0.15300	-0.18269	-0.14196
0.3	-0.10351	-0.11562	-0.23887	-0.22815	-0.17596
0.4	-0.14388	-0.16184	-0.31147	-0.26854	-0.21254
0.5	-0.17906	-0.20252	-0.36913	-0.32525	-0.26229
0.6	-0.20330	-0.22786	-0.39641	-0.40565	-0.32793
0.7	-0.20881	-0.22911	-0.36467	-0.45116	-0.41164
0.8	-0.19554	-0.21107	-0.31599	-0.35215	-0.41357
0.9	-0.17211	-0.18847	-0.31590	-0.37945	-0.40107
1.0	-0.14442	-0.16464	-0.31503	-0.40774	-0.47234
1.1	-0.10808	-0.12658	-0.26027	-0.35513	-0.41351
1.2	-0.06129	-0.07092	-0.13818	-0.17020	-0.13106
1.3	-0.01806	-0.01962	-0.02814	-0.01920	-0.00808
1.4	1.00000	1.00000	1.00000	1.00000	1.00000

Table 3.5: *Effect of Reynolds number on the vertical velocity (v) along mid height (y = 0.7) - parallel motion.*

x-co-ordinate	$Re = 50$	$Re = 100$	$Re = 400$	$Re = 1000$	$Re = 3200$
0.0	0.00000	0.00000	0.00000	0.00000	0.00000
0.1	-0.05165	-0.03817	-0.02150	-0.03165	-0.04522
0.2	-0.13412	-0.09514	-0.07787	-0.10280	-0.09860
0.3	-0.19037	-0.15761	-0.13903	-0.15773	-0.13992
0.4	-0.19904	-0.19689	-0.18826	-0.19775	-0.17211
0.5	-0.17344	-0.19171	-0.24495	-0.22958	-0.20197
0.6	-0.14233	-0.16012	-0.28731	-0.27453	-0.23944
0.7	-0.12644	-0.13707	-0.24152	-0.32736	-0.30348
0.8	-0.13364	-0.14131	-0.22787	-0.28699	-0.30922
0.9	-0.16256	-0.17036	-0.26052	-0.31043	-0.30737
1.0	-0.20179	-0.20712	-0.27262	-0.27563	-0.23330
1.1	-0.22689	-0.22666	-0.25880	-0.24439	-0.18923
1.2	-0.20185	-0.20230	-0.21267	-0.20680	-0.15319
1.3	-0.09589	-0.10510	-0.12221	-0.12646	-0.10433
1.4	0.00000	0.00000	0.00000	0.00000	0.00000

3.4 Hydrodynamic Stability Analysis

The stability of the flow may be determined by performing a normal mode analysis. Here, the total flow in terms of $\psi(x,\ y,\ t)$ and $\omega(x,\ y,\ t)$ may be expressed as a combination of its steady flow and perturbation introduced as ([16])

$$\begin{aligned} \psi(x,\ y,\ t) &= \overline{\psi}(x,\ y) + \delta\tilde{\psi}(x,\ y)e^{\lambda t} \text{ and} \\ \omega(x,\ y,\ t) &= \overline{\omega}(x,\ y) + \delta\tilde{\omega}(x,\ y)e^{\lambda t} \end{aligned} \tag{3.20}$$

where δ is a small constant prefactor to the perturbations $\tilde{\psi}(x,\ y)$ and $\tilde{\omega}(x,\ y)$ with $\delta \ll 1$ and $\overline{\psi}(x,\ y)$ and $\overline{\omega}(x,\ y)$ denote the steady state values of the streamfunction and the vorticity respectively. Substituting the above form into equations (3.2) and (3.3) and collecting the like order terms we will get a set of equations for the steady flow and the linear stability equations.

The steady equations and their boundary conditions are as follows:

$$\nabla^2\overline{\psi} = -\overline{\omega} \tag{3.21a}$$

$$\overline{\psi}_y\overline{\omega_x} - \overline{\psi}_x\overline{\omega}_y = \frac{1}{Re}\nabla^2\overline{\omega} \tag{3.21b}$$

$$\begin{aligned}
&\overline{\psi} = 0 \text{ and } \overline{\psi}_y = -1 \text{ for } y = 0, \quad 0 \le x \le 1\\
&\overline{\psi} = 0 \text{ and } \overline{\psi}_x = 0 \quad \text{for } x = 1, \quad 0 \le y \le 0.4\\
&\overline{\psi} = 0 \text{ and } \overline{\psi}_y = 0 \quad \text{for } y = 0.4, \ 1 \le x \le 1.4\\
&\overline{\psi} = 0 \text{ and } \overline{\psi}_x = 0 \quad \text{for } x = 1.4, \ 0.4 \le y \le 1.4\\
&\overline{\psi} = 0 \text{ and } \overline{\psi}_y = 1 \quad \text{for } y = 1.4, \ 0.4 \le x \le 1.4\\
&\overline{\psi} = 0 \text{ and } \overline{\psi}_x = 0 \quad \text{for } x = 0.4, \ 1 \le y \le 1.4\\
&\overline{\psi} = 0 \text{ and } \overline{\psi}_y = 0 \quad \text{for } y = 1, \quad 0 \le x \le 0.4\\
&\overline{\psi} = 0 \text{ and } \overline{\psi}_x = 0 \quad \text{for } x = 0, \quad 0 \le y \le 1
\end{aligned} \tag{3.21c}$$

Likewise, the stability equations (in linear order of the small parameter δ) and their boundary conditions are:

$$\nabla^2\tilde{\psi} = -\tilde{\omega} \tag{3.22a}$$

$$\lambda\tilde{\omega} + \overline{\psi}_y\tilde{\omega_x} - \overline{\psi}_x\tilde{\omega}_y + \tilde{\psi}_y\overline{\omega_x} - \tilde{\psi}_x\overline{\omega}_y = \frac{1}{Re}\nabla^2\tilde{\omega} \tag{3.22b}$$

$$\begin{aligned}
&\tilde{\psi} = 0 \text{ and } \tilde{\psi}_y = 0 \text{ for } y = 0, \quad 0 \le x \le 1\\
&\tilde{\psi} = 0 \text{ and } \tilde{\psi}_x = 0 \quad \text{for } x = 1, \quad 0 \le y \le 0.4\\
&\tilde{\psi} = 0 \text{ and } \tilde{\psi}_y = 0 \quad \text{for } y = 0.4, \ 1 \le x \le 1.4\\
&\tilde{\psi} = 0 \text{ and } \tilde{\psi}_x = 0 \quad \text{for } x = 1.4, \ 0.4 \le y \le 1.4\\
&\tilde{\psi} = 0 \text{ and } \tilde{\psi}_y = 0 \quad \text{for } y = 1.4, \ 0.4 \le x \le 1.4\\
&\tilde{\psi} = 0 \text{ and } \tilde{\psi}_x = 0 \quad \text{for } x = 0.4, \ 1 \le y \le 1.4\\
&\tilde{\psi} = 0 \text{ and } \tilde{\psi}_y = 0 \quad \text{for } y = 1, \quad 0 \le x \le 0.4\\
&\tilde{\psi} = 0 \text{ and } \tilde{\psi}_x = 0 \quad \text{for } x = 0, \quad 0 \le y \le 1
\end{aligned} \tag{3.22c}$$

For parallel motion of the lids, we simply replace the first equation of (3.21(c))

by

$$\overline{\psi} = 0 \text{ and } \overline{\psi}_y = 1 \text{ for } y = 0, \quad 0 \leq x \leq 1$$

The steady state formulation of (3.9) is used to solve the steady equations (3.21) to obtain the values of $\overline{\psi}$ and $\overline{\omega}$, which are then substituted in the stability equations (3.22) to find $\tilde{\psi}$, $\tilde{\omega}$ and λ. The same steady state formulation of (3.9) is again used to solve the stability equations (3.22). After discretization, those equations lead to a generalized eigenvalue problem that is solved to find $\tilde{\psi}$, $\tilde{\omega}$ and λ for different Re. In general, the eigenvalues λ can be real ($\lambda = \lambda_r$) or complex ($\lambda = \lambda_r \pm i\lambda_i$, where $i = \sqrt{-1}$). The stability of the flow depends on the sign of the largest value of λ_r.

At one particular value of Re, a pair of complex conjugate eigenvalues of crosses the imaginary axis which leads the basic flow to lose stability and a one parameter family of periodic solution bifurcates from the stationary solution. Such a bifurcation is called a Hopf bifurcation which refers to the local death or birth of a periodic solution from an equilibrium point. When $\lambda_r < 0$, the fixed point is a stable focus. When λ crosses the imaginary axis and $\lambda_r > 0$, the fixed point becomes an unstable focus, with orbits spiralling out.

The global stability analysis of the staggered LDC problem, for both antiparallel and parallel motion of lids, on various uniform grids of sizes 71×71, 85×85, 99×99, 106×106, 141×141 and 211×211, are discussed briefly in the following subsection.

3.4.1 2D Global Stability Analysis : Results and Discussion

The stability equations (3.22) with the steady state HOC formulation as discussed in the previous section, turns out to be of the form

$$A_1 \, \widetilde{\boldsymbol{\omega}} \; + \; A_2 \, \widetilde{\boldsymbol{\psi}} \; = \; 0 \tag{3.23a}$$

$$A_3\,\widetilde{\boldsymbol{\omega}} \;+\; A_4\,\widetilde{\boldsymbol{\psi}} \;=\; Re\lambda\,A_5\,\widetilde{\boldsymbol{\omega}}. \tag{3.23b}$$

Now, we have the following eigenvalue problem

$$\begin{bmatrix} A_1 & A_2 \\ A_3 & A_4 \end{bmatrix} \begin{bmatrix} \widetilde{\boldsymbol{\omega}} \\ \widetilde{\boldsymbol{\psi}} \end{bmatrix} = Re\lambda \begin{bmatrix} 0 & 0 \\ A_5 & 0 \end{bmatrix} \begin{bmatrix} \widetilde{\boldsymbol{\omega}} \\ \widetilde{\boldsymbol{\psi}} \end{bmatrix} \tag{3.24}$$

which can also be expressed as a generalized eigenvalue problem

$$A\boldsymbol{\phi} = \mu B\boldsymbol{\phi}, \tag{3.25}$$

where $\mu = Re\lambda$, $\boldsymbol{\phi} = \begin{bmatrix} \widetilde{\boldsymbol{\omega}} \\ \widetilde{\boldsymbol{\psi}} \end{bmatrix}$ and A and B are block diagonal matrices as shown in Figure 3.9. The component blocks A_1 and A_5 are penta-diagonal matrices and A_2, A_3 and A_4 are nona-diagonal matrices. Equation (3.25) is solved for eigenvalue λ and eigenvector $\boldsymbol{\phi}$ using the freely available software package ARPACK [68].

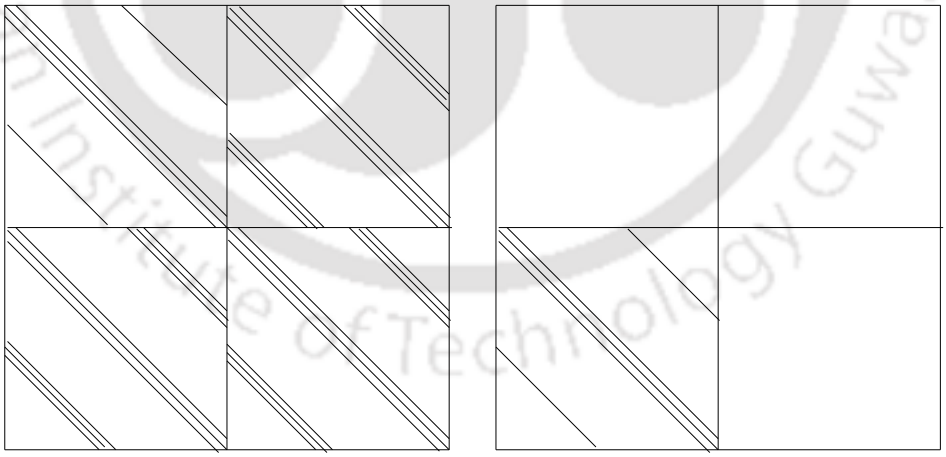

(a) (b)

Figure 3.9: *Structure of block matrices (a) A and (b) B.*

Numerical experiments were carried out on the staggered LDC to determine the critical Reynolds number Re_c. We begin the search with $Re = 500$ and

5,000. The algorithm used was

1. Compute the stationary solution for a given Re from equations (3.21).
2. Substitute that solution in equations (3.22) and compute the eigenvalues.
3. If no eigenvalue with positive real part exists, increase the Reynolds number Re by ΔRe and return to step 1.
4. If eigenvalue with positive real part exists, then reduce the value of the Reynolds number Re and return to step 1.

Repeat the above algorithm, until there exists only one pair of purely imaginary eigenvalues for which the corresponding Re is termed as Re_c and the eigenvalues as critical eigenvalues λ_c. At this critical Reynolds number Re_c, Hopf bifurcation occurs. If the eigenvalue spectrum shift towards the imaginary axis i.e. if the real part of eigenvalue increases with the increases in Re, the flow tends to bifurcate as the real part of eigenvalue approaches zero and Hopf bifurcation occurs.

Note that in the algorithm described above, the step size ΔRe in Reynolds number was initially set as 500. Once an eigenvalue crossing the imaginary axis was found within the range of this ΔRe, the value of ΔRe was further reduced to 100, 50, 10, 5, 1 and finally to 0.1.

3.4.1.1 Antiparallel Motion

In Table 3.6, we tabulate the results consisting of the critical values Re_c and λ_c for antiparallel motion. From the table, it is clear that with increase in grid size, both Re_c and λ_c converge towards fixed values. We observe that Re_c increases with the increase in grid size which was also observed by Peng *et al.* [88] for simple LDC flow as well. However, one should also keep in mind that the dependence of Re_c on grid size also depends upon the method used [10, 16, 29, 76, 89, 95]. The real and imaginary parts of the streamfunction and vorticity perturbation eigenvectors corresponding to $\lambda_c = \pm 1.411i$ and $Re_c = 2,162.6$ on the grid of size 211×211 are shown in Figures 3.10 and 3.11

Table 3.6: Critical parameters for antiparallel motion where the first Hopf bifurcation occurs.

grid size	critical Re (Re_c)	critical eigenvalue (λ_c)
71×71	2119.6	$3.40 \times 10^{-7} \pm 1.464i$
85×85	2143.1	$2.65 \times 10^{-8} \pm 1.448i$
99×99	2154.7	$1.17 \times 10^{-9} \pm 1.432i$
106×106	2155.3	$1.02 \times 10^{-9} \pm 1.428i$
141×141	2160.8	$7.81 \times 10^{-10} \pm 1.419i$
211×211	2162.6	$1.03 \times 10^{-10} \pm 1.411i$

(a) (b)

Figure 3.10: *Contours of the (a) real and (b) imaginary parts of the stream-function eigenvector at* $Re_c = 2162.6$ *on grid of size* 211×211 *- antiparallel motion.*

(a) (b)

Figure 3.11: *Contours of the (a) real and (b) imaginary parts of the vorticity eigenvector at* $Re_c = 2162.6$ *on grid of size* 211×211 *- antiparallel motion.*

respectively.

In Table 3.7, we show the eigenvalue λ_c which is closest to the imaginary axis for Reynolds numbers $500 \leq Re \leq 5,000$ on the finest grid 211×211.

Table 3.7: *Antiparallel motion: Reynolds number verses the eigenvalue closest to imaginary axis (*211×211 *grid).*

Reynolds Number	λ_r ($\times 10^{-5}$)	λ_i
500	-27.785	± 1.363i
800	-11.193	± 1.370i
1000	-9.167	± 1.377i
1200	-7.458	± 1.382i
1500	-5.765	± 1.391i
2000	-4.669	± 1.403i
2100	-2.146	± 1.407i
2125	-1.152	± 1.410i
2150	-0.573	±1.413i
2155	-0.327	± 1.417i
2160	-0.077	± 1.419i
2162	-0.014	± 1.419i
2162.5	-0.000000294	± 1.411i
2162.6	0.0000103	± 1.411i
2164	0.028	±1.409i
2165	0.047	± 1.408i
2166	0.109	± 1.406i
2170	1.214	± 1.4051i
2180	2.218	± 1.4049i
2250	4.896	± 1.4018i
2500	7.234	± 1.3976i
5000	11.315	± 1.3727i

In Figure 3.12(a), we depict the 1000 eigenvalues used to eventually determine the critical parameter, which according to our computation on a grid of size 211×211 was found to be $Re_c = 2,162.6$. In Figure 3.12(b), we show a zoomed version of these eigenvalues in the neighborhood of the imaginary axis and one can clearly see the eigenvalues that correspond to the Hopf bifurcation.

In Figure 3.13, we plot the time history of u-velocity at the mid-point of the

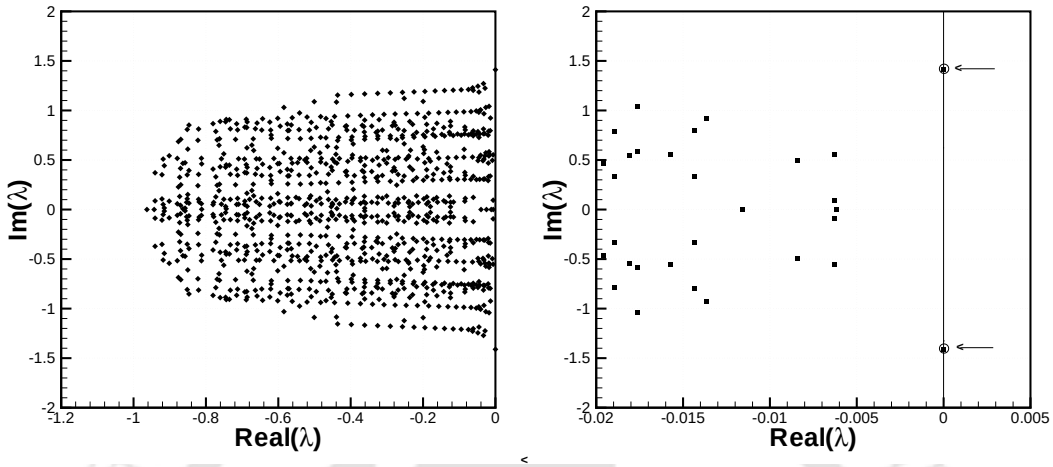

(a) (b)

Figure 3.12: *Plots showing a) 1000 eigenvalues and b) few eigenvalues near the imaginary axis for $Re_c = 2162.6$ (211 × 211 grid).*

cavity and its close-up view at this critical Reynolds number. The power spectral density and the phase diagram of u-v velocity are presented in Figure 3.14. From the figures it is clear that the flow is periodic at this Reynolds number.

3.4.1.2 Parallel Motion

As in antiparallel motion, we tabulate the eigenvalue λ_c which is closest to the imaginary axis for Reynolds numbers $500 \leq Re \leq 5,000$ in Table 3.8 and the observation is analogous to that of antiparallel motion. Similar is the observation on the results consisting of the critical values Re_c and λ_c on the same grid sizes in Table 3.9. Here a much higher value of $Re_c = 4,074.3$ is obtained with corresponding $\lambda_c = \pm 0.5822i$.

The real and imaginary parts of the streamfunction and vorticity perturbation eigenvectors corresponding to the critical values on the grid of size 211 × 211 are shown in Figures 3.15 and 3.16 respectively.

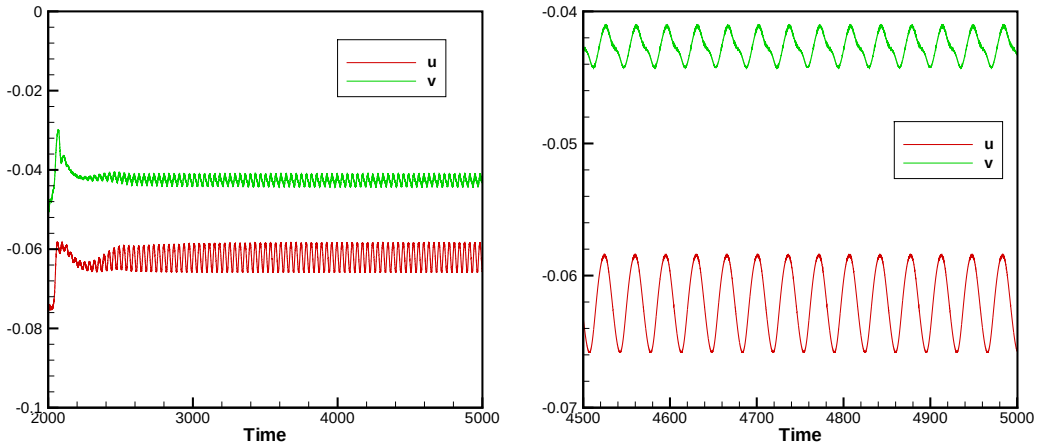

(a) (b)

Figure 3.13: *(a) Evolution of u and v with t and (b) a snapshot of the same signal for antiparallel motion corresponding to the critical Reynolds number monitored at the mid-point of the cavity.*

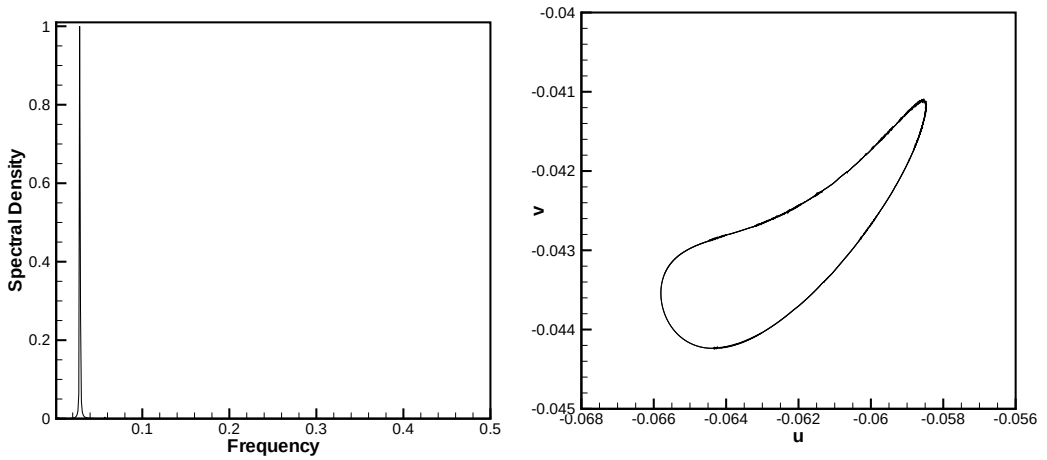

(a) (b)

Figure 3.14: *(a) Power spectral density, (b) Phase portrait of u vs v for antiparallel motion corresponding to the critical Reynolds number.*

The eigenvalue plots for parallel motion on a grid of size 211×211 correspond-

Table 3.8: *Parallel motion: Reynolds number verses the eigenvalue closest to imaginary axis (*211×211 *grid).*

Reynolds Number	λ_r ($\times 10^{-5}$)	λ_i
500	-58.126	± 0.5656i
1000	-57.877	±0.5685i
1500	-54.724	±0.5708i
2000	-49.229	±0.5729i
2500	-43.945	±0.5747i
3000	-34.692	±0.5765i
3500	-23.456	±0.5781i
4000	-9.043	±0.5797i
4050	-0.726	±0.5808i
4060	-0.254	±0.5818i
4070	-0.029	±0.5826i
4074.2	-0.0001	±0.5823i
4074.3	0.0000212	±0.5822i
4075	0.00069	±0.5821i
4080	0.0097	±0.5816i
4100	0.0874	±0.5805i
4500	1.276	±0.5780i
5000	2.913	±0.5749i

Table 3.9: Critical parameters for parallel motion where the first Hopf bifurcation occurs.

grid size	critical Re (Re_c)	critical eigenvalue (λ_c)
71×71	4016.4	$1.04 \times 10^{-9} \pm 0.5971i$
85×85	4034.66	$9.98 \times 10^{-10} \pm 0.5902i$
99×99	4048.25	$8.96 \times 10^{-10} \pm 0.5864i$
106×106	4050.7	$8.13 \times 10^{-10} \pm 0.5855i$
141×141	4069.5	$4.67 \times 10^{-10} \pm 0.5837i$
211×211	4074.3	$2.12 \times 10^{-10} \pm 0.5822i$

ing to $Re = 4,074.3$ are depicted in Figure 3.17.

As in antiparallel motion, in Figure 3.18, we plot the time history of u-velocity at the mid-point and its close-up view at the critical Reynolds number. The power spectral density and the phase diagram of u-v velocity is presented in

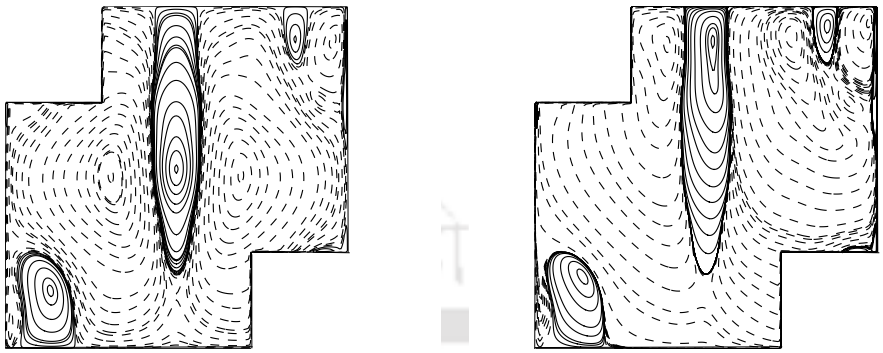

(a) (b)

Figure 3.15: *Contours of the (a) real and (b) imaginary parts of the stream-function eigenvector at* $Re_c = 4074.3$ *on grid of size* 211×211 *- parallel motion.*

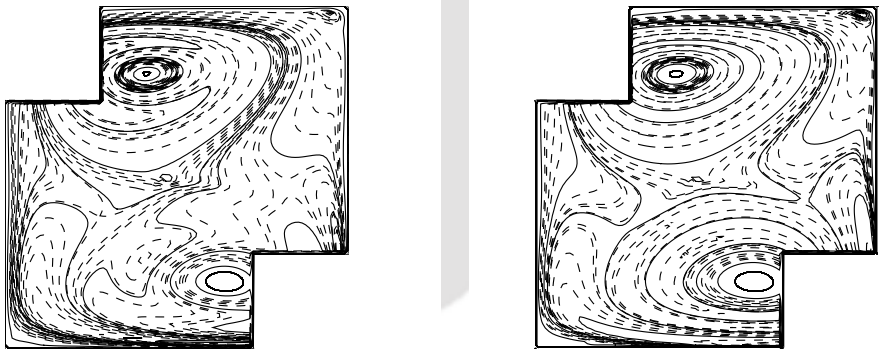

(a) (b)

Figure 3.16: *Contours of the (a) real and (b) imaginary parts of the vorticity eigenvector at* $Re_c = 4074.3$ *on grid of size* 211×211 *- parallel motion.*

Figure 3.19. As in antiparallel motion, these figures indicate a periodic flow at the Reynolds number for parallel motion as well.

Note that the simulations pertaining to flow corresponding to the critical Reynolds numbers in Figures 3.13, 3.14, 3.18 and 3.19 were performed by

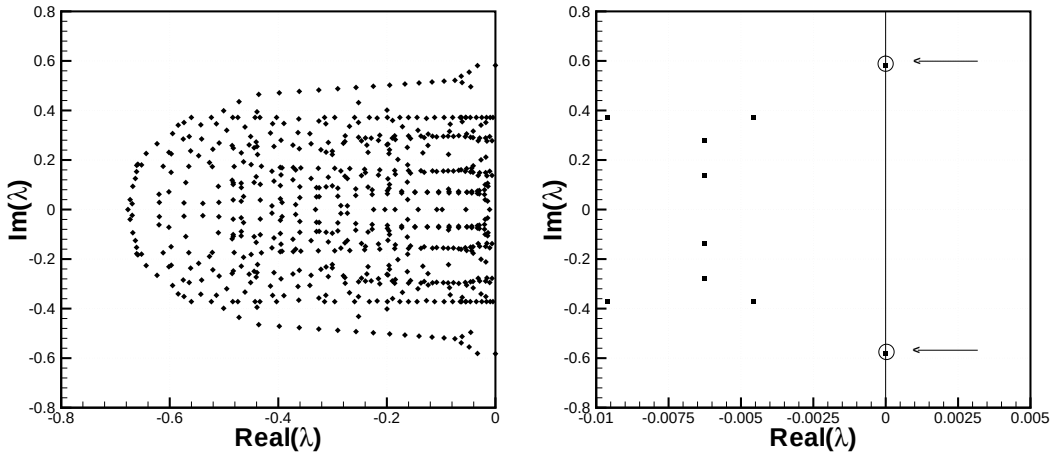

(a) (b)

Figure 3.17: *Plots showing (a) 400 eigenvalues and (b) few eigenvalues near the imaginary axis for* $Re_c = 4074.3$ *(*211×211 *grid) - parallel motion.*

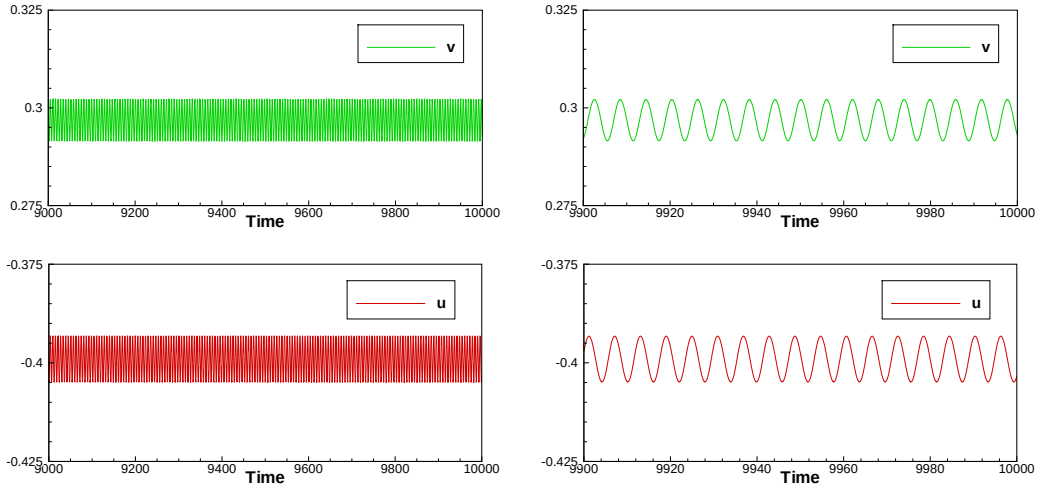

(a) (b)

Figure 3.18: *Evolution of* u *and* v *with* t *(left) and a snapshot of the same signal (right) for parallel motion corresponding to the critical Reynolds number monitored at the mid-point of the cavity.*

using zero initial data at the interior of the cavity.

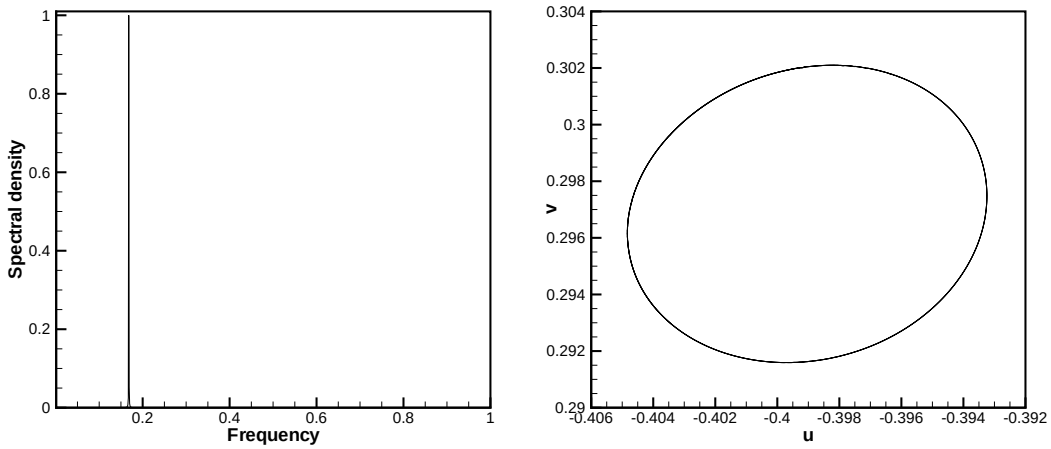

(a) (b)

Figure 3.19: *(a) Power spectral density and (b) Phase portrait of u vs v for parallel motion corresponding to the critical Reynolds number.*

3.4.1.3 Convergence of the eigenvalue problem

As seen above, in order to find out the Re_c, one must find out the λ_c by solving a generalized eigenvalue problem; the convergence of the eigenvalue problem is extremely sensitive to the grid resolution. In order to establish the credibility of our Re_c computation, we plot six equally spaced phases of the streamlines on grids of sizes 106×106 and 211×211 corresponding to the eigenmode over one period $T = \frac{2\pi}{\lambda_i}$ given by

$$Real\left(e^{(\lambda_r+\lambda_i)t}(Y_r + iY_i)\right) = e^{\lambda_r t}\left(Y_r \cos\lambda_i t - Y_i \sin\lambda_i t\right)$$

where λ_r and λ_i are the real and imaginary parts of the critical eigenvalue λ_c and, $Y_r + iY_i$ is the complex eigenvector corresponding to the critical eigenvalue λ_c. They are presented in Figures 3.20 and 3.21 for antiparallel and parallel motions respectively. Note that unlike [95], no adjustment in the phase was required for synchronizing oscillations between the coarser and finer grids. Here the dotted lines represent negative contour values. From these figures it is clear that the spatial and temporal structures of these most sensitive

eigenmodes are very close to each other and all the salient features of the flow are accurately captured on a grid as coarse as 106×106. The wiggles observed in some places of the cavity for the parallel motion on 106×106 stems out of the fact that the critical Reynolds number for the parallel motion is much higher than that of the antiparallel motion and as such requires much finer grid to resolve the smaller scales that are archetypal of flows at higher Re.

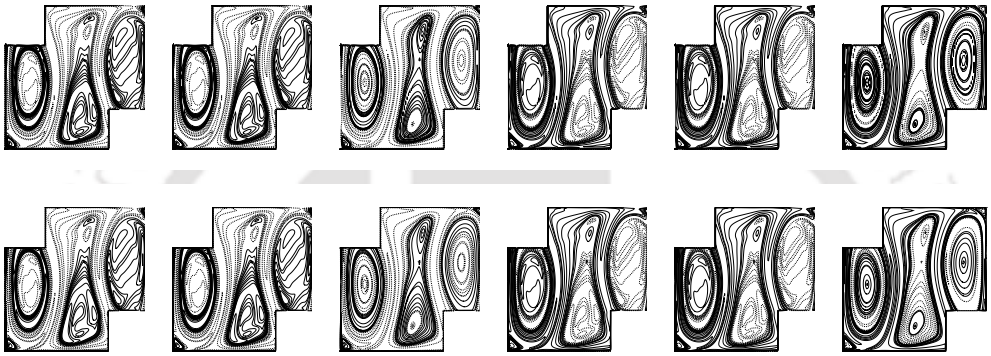

Figure 3.20: Streamlines of the eigenmode corresponding to the critical eigenvalues for the antiparallel motion on 106×106 (top) and 211×211 (bottom) grids over one period at interval $\frac{T}{6}$.

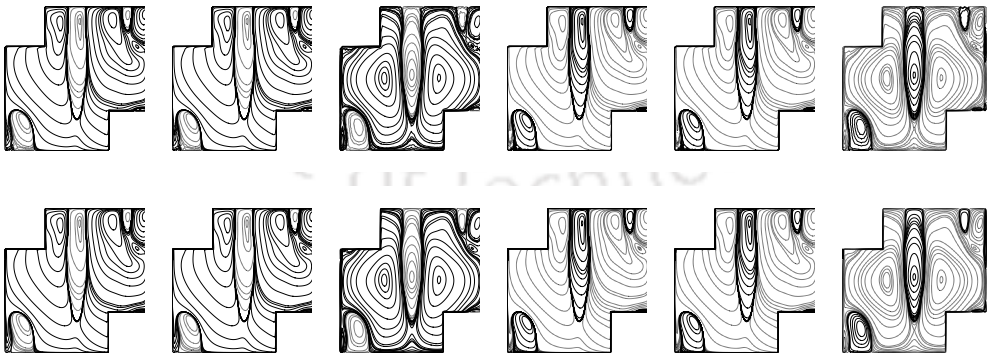

Figure 3.21: Streamlines of the eigenmode corresponding to the critical eigenvalues for the parallel motion on 106×106 (top) and 211×211 (bottom) grids over one period at interval $\frac{T}{6}$.

3.4.1.4 Extrapolation of the critical data

We now extrapolate the critical Reynolds number values obtained on the finest two grids, namely 141×141 and 211×211 from Tables 3.6 and 3.9. We have used Richardson's extrapolation formula given by ([48])

$$\text{Improved value} = Re_c(h_f) + \frac{1}{R^n - 1}\left(Re_c(h_f) - Re_c(h_c)\right)$$

where $R = \dfrac{h_c}{h_f}$, the ratio of the step sizes h_c, h_f on coarser and finer grids respectively and n is the order of accuracy of the numerical method used.

With this, the extrapolated values of the critical Reynolds numbers for the antiparallel and parallel motion are estimated as 2163.043 and 4075.482 respectively. Treating these values as the exact values of the critical Re, we estimate the numerical rate of convergence of the scheme used in the present computation by the following formula

$$\frac{\ln(\text{error}_\text{c}/\text{error}_\text{f})}{\ln(h_c/h_f)}$$

where error_c, error_f are the errors in the critical Reynolds numbers computed on coarser and finer grids respectively. For both parallel and the antiparallel motion, the numerical convergence rate turns out to be 4.000, which is exactly the theoretical rate of convergence.

3.4.1.5 Interpolation of the critical data

Now, we will try to fit the datas obtained on the 211×211 grid, for both the antiparallel and parallel motion of lids into the Lagrangian interpolation polynomial. Meanwhile, it is noteworthy that in order to estimate the critical Reynolds number, the extrapolation was carried out using two different step sizes and their corresponding critical Reynolds number. But in the interpolation we have used the real part of eigenvalues obtained for different Reynolds number on the finest grid. After interpolation, we found that the critical Reynolds number are $2,162.604$ and $4,074.303$ for the antiparallel and

parallel motion respectively. Figure 3.22 shows the curve for the Lagrangian interpolation polynomial, which has been determined from the datas obtained on the 211×211 grid, for both the antiparallel and parallel motion.

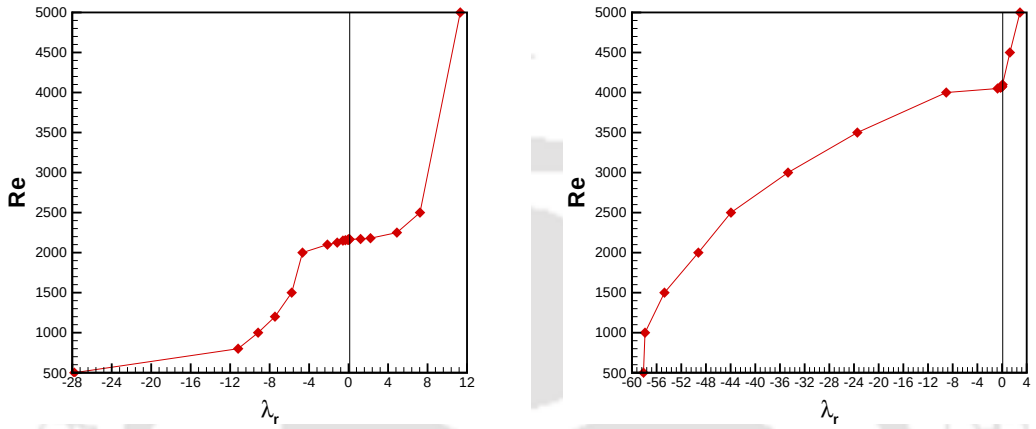

(a) (b)

Figure 3.22: *Lagrangian interpolation curve for the obtained data, which gives (a) antiparallel motion; (b) parallel motion (grid size* 211×211*).*

From the figure, one can see that the critical Reynolds numbers (Re_c) obtained from the Lagrange interpolation polynomial is in very close agreement with our predicted values of Re_c for both the antiparallel and parallel motion of lids of the staggered lid driven cavity flow.

3.5 Periodic flow for higher Reynolds number

Having obtained the critical Reynolds numbers Re_c for both the antiparallel and parallel motions of the lids, we compute the flow beyond Re_c in order to have more insights into the nature of the flow in the high Re regime. For this purpose, we have chosen Re values $5,000$ and $12,000$ for both the parallel and antiparallel motion. In all the cases, computation was started from rest and continued till a non-dimensional time $t = 10,000$ was reached. We present our results in Figures 3.23-3.26.

Figures 3.23(a) and (b) show the instantaneous streamlines for $Re = 5,000$

for the antiparallel and parallel motion of the lids respectively at the instants

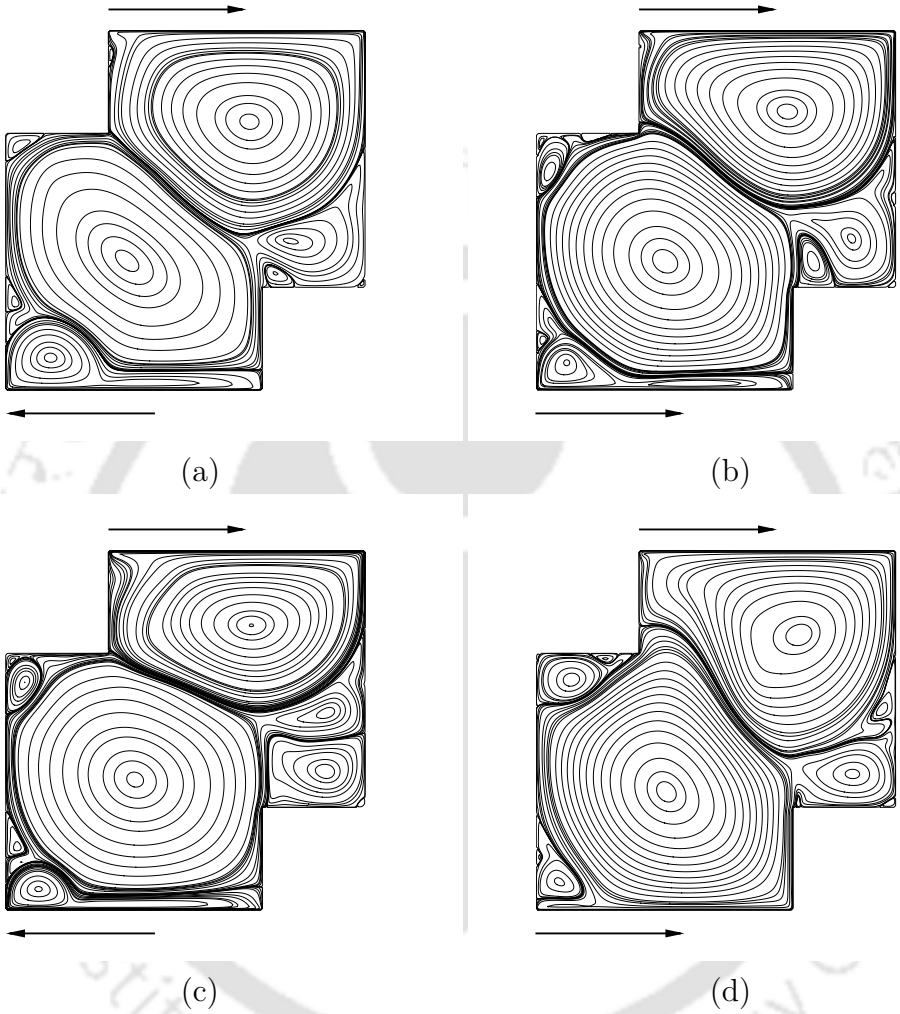

Figure 3.23: *Instantaneous streamlines for (a) $Re = 5,000$, antiparallel motion, (b) $Re = 5,000$, parallel motion, (c) $Re = 12,000$, antiparallel motion, and (d) $Re = 12,000$, parallel motion.*

corresponding to the circled locations of the phase diagrams in Figures 3.25(a)-(b); the instants were chosen such that the v-velocity was maximum at the monitoring points. In Figures 3.23(c) and (d), we present the instantaneous streamlines for $Re = 12,000$ for the antiparallel and parallel motion respectively at the instant $t = 10,000$. From the figures it is clear that with increasing Reynolds number, the number of recirculation zones also increases.

In Figure 3.24, the time histories of u and v velocities at the mid point of the cavity (except for the antiparallel motion for $Re = 5,000$ where we have chosen the point $(0.537, 1.201)$ at the top-left corner). The phase plane trajec-

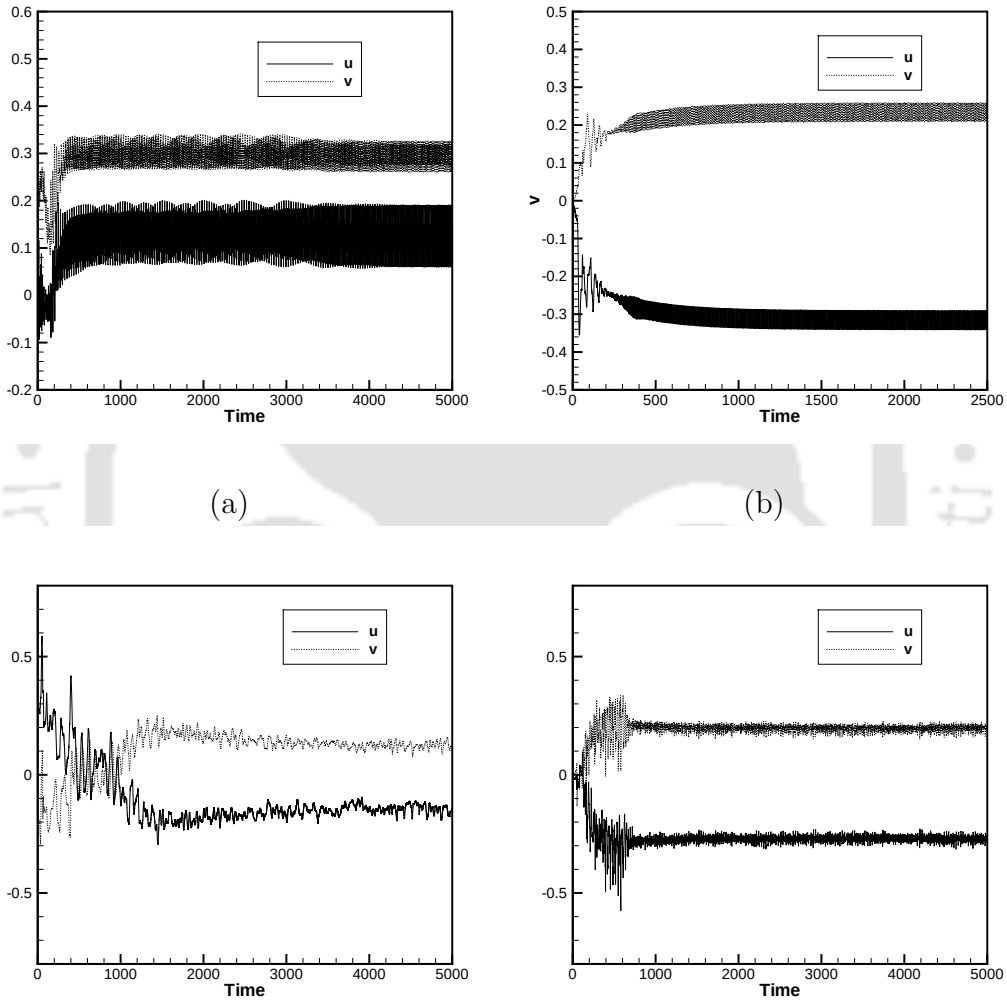

Figure 3.24: *History of u and v-velocity at a chosen point inside the cavity: (a) $Re = 5,000$, antiparallel motion; monitored at the point $(0.537,\ 1.201)$ and (b) $Re = 5,000$, parallel motion (monitored at the mid-point), (c) $Re = 12,000$, antiparallel motion (monitored at the mid-point), (d) $Re = 12,000$, parallel motion (monitored at the mid-point).*

tories over the last part of the time range of the flow computation in Figures 3.25(a)-(b) and the corresponding power-spectra plots in Figures 3.26(a)-(b) for $Re = 5,000$ leans towards a periodic motion for both the parallel and antiparallel motions.

At $Re = 12,000$, for both the parallel and antiparallel motion, the flow is chaotic as can be clearly seen from Figures 3.24(c)-(d), 3.25(c)-(d) and 3.26(c)-(d). The time histories of u and v velocities do not follow a specific pattern and the frequency is spread all over the time range. The phase plane trajectories in Figures 3.25(c)-(d) shown over the whole time-range for which the flow is computed reveals a chaotic motion, thus leaning towards a chaotic state.

Note that in most systems, as is the case for the lid driven cavity, the 3D instabilities have a much lower critical Reynolds number than the 2D perturbations. Recent studies (e. g. [27]) have suggested that there exist qualitative differences in the transition from steady to oscillatory 2D and 3D lid-driven flows. As such, the 3D version of the two-sided staggered cavity flow is likely to unfold some more interesting features than its 2D counterpart.

3.6 Conclusion

In this work, we have applied a recently developed HOC scheme for 2-D convection-diffusion equations to study the global two-dimensional stability of the flow inside the two-sided staggered LDC, for both parallel and antiparallel motions of the lids. To the best of our knowledge, no global stability analysis is available in the literature for the flow in a two-sided lid-driven staggered cavity. We have provided algorithms for computing the critical parameters resulting from the generalized eigenvalue problem and also for computing the flow in general. In the process, we have also computed the flow for a wide range of Reynolds number in the region $50 \leq Re \leq 12,000$. Extensive grid convergence study was carried out to identify the most sensitive eigenvalue leading to the detection of the critical Reynolds number Re_c. The study reveals that the critical Reynolds number for the parallel motion of lids is significantly higher

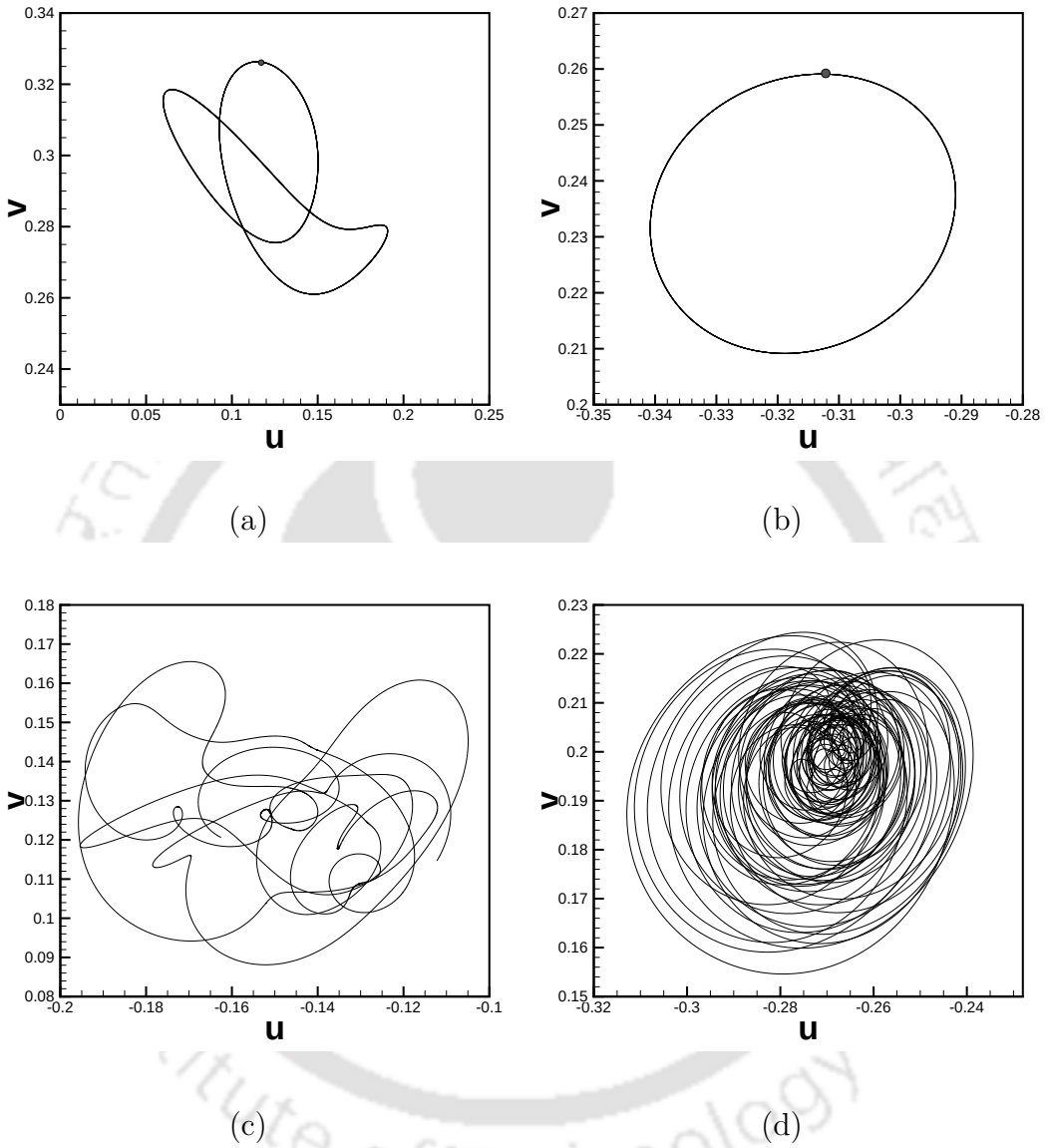

Figure 3.25: *The phase plane of u and v-velocity at the points corresponding to Figure 3.24: (a) $Re = 5,000$ $(5,400 \leq t \leq 5,500)$, antiparallel motion, (b) $Re = 5,000$ $(4,950 \leq t \leq 5,000)$, parallel motion, (c) $Re = 12,000$ $(9,500 \leq t \leq 10,000)$, antiparallel motion, and (d) $Re = 12,000$ $(4,500 \leq t \leq 5,000)$, parallel motion. The circled locations in (a) and (b) correspond to the instants at which the streamlines are drawn for Figures 3.23(a) and (b) respectively.*

in contrast to its antiparallel motion, which signifies that for parallel motion of the lids the flow loses its stability at a much higher value of the critical

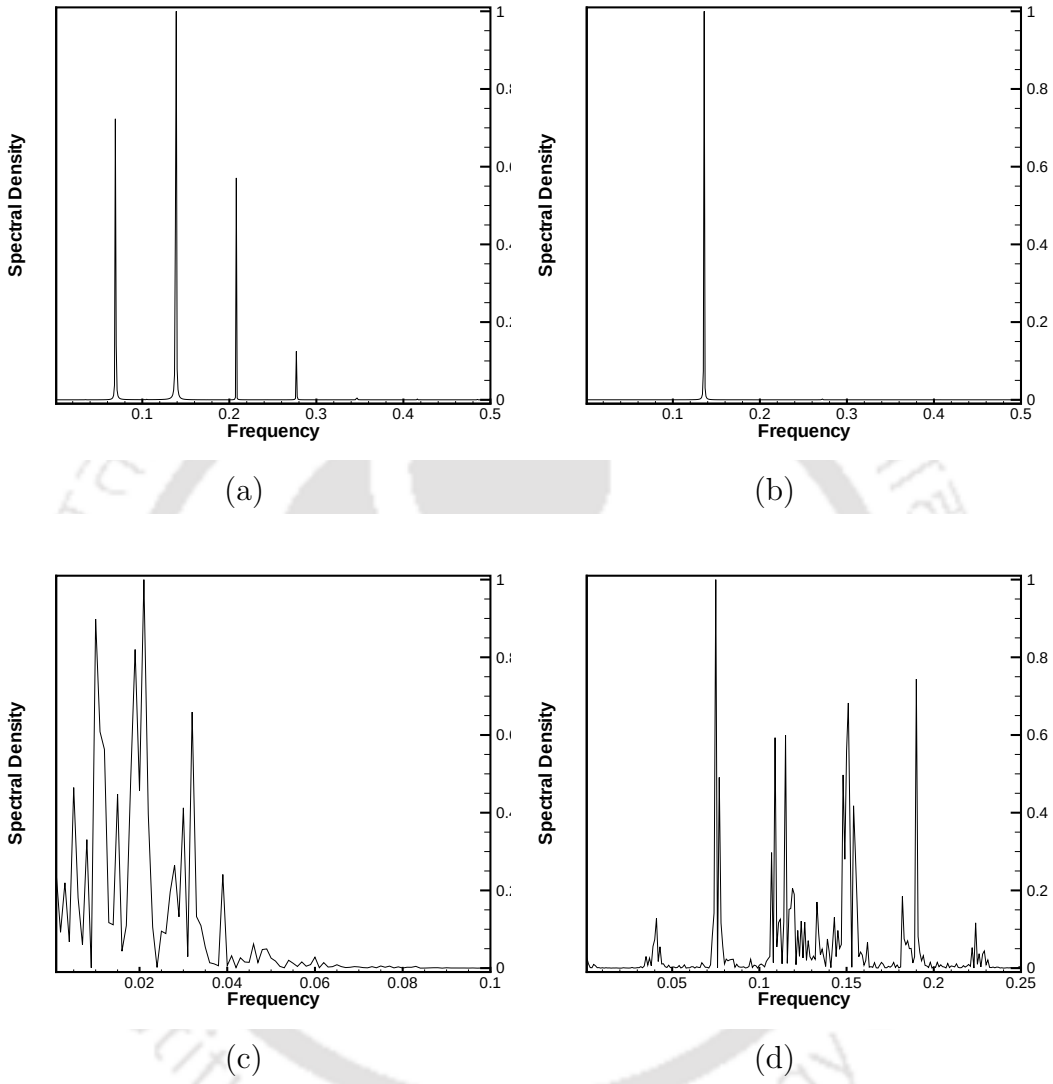

Figure 3.26: *Power spectra of u-velocity: (a)* $Re = 5,000$ *(*$4,500 \leq t \leq 5,500$*), antiparallel motion, (b)* $Re = 5,000$ *(*$4,000 \leq t \leq 5,000$*), parallel motion, (c)* $Re = 12,000$ *(*$9,000 \leq t \leq 10,000$*), antiparallel motion, and (d)* $Re = 12,000$ *(*$4,000 \leq t \leq 5,000$*), parallel motion.*

parameter (here, the Reynolds number); extrapolation and Lagrange interpolation of the data further justify this fact. It is found that for the antiparallel motion, the flow loses its stability at a relatively low $Re_c = 2163.043$ against a much higher value 4075.482 for the parallel motion. Our numerical results are

compared with available results in the literature for the steady state flow and satisfactory comparison is obtained in all the cases. For the unsteady flow, in order to study the asymptotic behaviour of the flow, computations were continued till a non-dimensional time $t = 10,000$ was reached. Phase plane and spectral density analysis confirms that at moderately high Re the flow is periodic while at high Re, it shows a disorderly nature leaning towards a chaotic state.

Chapter 4

A BIHARMONIC APPROACH FOR THE STABILITY ANALYSIS OF INCOMPRESSIBLE VISCOUS FLOWS

4.1 Introduction

In chapter 3, we have discussed the global two-dimensional stability of the staggered lid-driven cavity flow with HOC schemes using the ψ-ω approach. This approach was seen to yield very accurate results for the type of flow considered. However, the presence of two variables (namely ψ and ω) invariably resulted in a much larger matrix vector computation in the generalized eigenvalue problem, apart from the usual computational time in obtaining the steady state solutions for the flow variables considered. In this chapter, we introduce the global stability analysis of incompressible viscous flows by the pure streamfunction (biharmonic) [90] formulation of the N-S equations [1]. As would be seen later, this approach drastically reduces the CPU time for com-

[1] A part of this work has been published in the *Proceedings of the International Conference on Computer Aided Engineering (CAE 2013), IIT Madras, Chennai, India* [32]

puting the eigenvalue and the corresponding eigenvectors for the generalized eigenvalue problem. A brief description of the biharmonic formulation of the steady state Navier-Stokes equations has already been provided in section 2.4 of chapter 2.

The unsteady form of the biharmonic formulation can be derived in the following way. Recall the unsteady form of the ψ-ω formulation of the Navier-Stokes equation:

$$\psi_{xx} + \psi_{yy} = -\omega(x, y). \tag{4.1}$$

$$\omega_t + u\omega_x + v\omega_y = \frac{1}{Re}(\omega_{xx} + \omega_{yy}), \tag{4.2}$$

where $(x, y) \in \Omega$, Re is the non-dimensional Reynolds number (Re) and the velocity components are defined as

$$u(x, y) = \psi_y \text{ and } v(x, y) = -\psi_x. \tag{4.3}$$

This ψ-ω formulation has been very popular and it has been widely used by researchers over the years to validate newly established numerical methods for the numerical simulations of a variety of fluid flow problems. The major difficulty with this formulation lies in the specification of vorticity values at the no-slip boundaries. The vorticity ω, which can be defined through the Poisson equation $-\omega = \psi_{xx} + \psi_{yy}$ needs to be solved discretely on the boundaries so that the boundary values of the vorticity can be specified for the vorticity transport equation when this formulation is employed.

To overcome this difficulty, yet another alternative formulation can be derived by substituting ψ for ω from equation (4.1) in equation (4.2). This results in a fourth-order partial differential equation as follows:

$$\frac{\partial}{\partial t}\left(-\nabla^2\psi\right) + \nabla^4\psi - Re\left(v\nabla^2 u - u\nabla^2 v\right) = 0 \tag{4.4}$$

where

$$\nabla^4\psi = \frac{\partial^4\psi}{\partial x^4} + 2\frac{\partial^4\psi}{\partial x^2\partial y^2} + \frac{\partial^4\psi}{\partial y^4} \tag{4.5}$$

Using equations (4.3) and (4.5), equation (4.4) may be written in the expanded form as

$$-Re\left[\frac{\partial}{\partial t}\left(\nabla^2\psi\right)\right]+\frac{\partial^4\psi}{\partial x^4}+2\frac{\partial^4\psi}{\partial x^2\partial y^2}+\frac{\partial^4\psi}{\partial y^4}-Re(\psi_y)\left[\frac{\partial^3\psi}{\partial x^3}+\frac{\partial^3\psi}{\partial x\partial y^2}\right]$$
$$+Re(\psi_x)\left[\frac{\partial^3\psi}{\partial x^2\partial y}+\frac{\partial^3\psi}{\partial y^3}\right]=0 \tag{4.6}$$

This formulation is known as the biharmonic or pure streamfunction formulation of the unsteady 2D Navier-Stokes equations.

4.1.1 The Numerical Scheme

In order to discretize equations of the form (4.6), we use the compact scheme developed by Kalita and Gupta [59] for the time-dependent Navier-Stokes equations in biharmonic form. The scheme is briefly discussed below.

The biharmonic formulation of the steady state Navier-Stokes equations in some domain Ω can be written as

$$\nabla^4\psi-Re\left(v\nabla^2u-u\nabla^2v\right)=f \tag{4.7}$$

where f is the forcing function.

The second-order compact formulation for (4.7) on a uniform grid of step-length h in both x- and y-directions is given by [59] as

$$\begin{aligned}&\psi_{i-1,j-1} - 8\psi_{i,j-1} + \psi_{i+1,j-1} - 8\psi_{i-1,j} + 28\psi_{i,j} - 8\psi_{i+1,j} + \psi_{i-1,j+1} - 8\psi_{i,j+1}\\ &\psi_{i+1,j+1} - 3h(u_{i,j-1} - u_{i,j+1} + v_{i+1,j} - v_{i-1,j}) - 0.5Reh^2\{v_{i,j}(u_{i+1,j} + u_{i-1,j}\\ &+ u_{i,j+1} + u_{i,j-1}) - u_{i,j}(v_{i+1,j} + v_{i-1,j} + v_{i,j+1} + v_{i,j-1})\} = \frac{h^4}{2} f_{i,j} \qquad (4.8)\end{aligned}$$

The velocities u and v can be obtained from equation (4.3) using fourth order central difference approximations

$$u_{i,j} = \frac{3}{4h}(\psi_{i,j+1} - \psi_{i,j-1}) - \frac{1}{4}(u_{i,j+1} - u_{i,j-1}) \qquad (4.9)$$

$$v_{i,j} = -\frac{3}{4h}(\psi_{i+1,j} - \psi_{i-1,j}) - \frac{1}{4}(v_{i+1,j} - v_{i-1,j}) \qquad (4.10)$$

Using forward differences for the time-derivative, an implicit finite difference approximation for equation (4.6) may be written as

$$\begin{aligned}&0.5Reh^2\left[\psi_{i+1,j}^{(n+1)} + \psi_{i,j+1}^{(n+1)} + \psi_{i-1,j}^{(n+1)} + \psi_{i,j-1}^{(n+1)} - 4\psi_{i,j}^{(n+1)}\right]\\ =\ & 0.5Reh^2\left[\psi_{i+1,j}^{(n)} + \psi_{i,j+1}^{(n)} + \psi_{i-1,j}^{(n)} + \psi_{i,j-1}^{(n)} - 4\psi_{i,j}^{(n)}\right]\\ &+ \triangle t\left[\psi_{i-1,j-1}^{(n)} - 8\psi_{i,j-1}^{(n)} + \psi_{i+1,j-1}^{(n)} - 8\psi_{i-1,j}^{(n)}\right.\\ &+ 28\psi_{i,j}^{(n)} - 8\psi_{i+1,j}^{(n)} + \psi_{i-1,j+1}^{(n)} - 8\psi_{i,j+1}^{(n)} + \psi_{i+1,j+1}^{(n)}\\ &- 3h(u_{i,j-1}^{(n)} - u_{i,j+1}^{(n)} + v_{i+1,j}^{(n)} - v_{i-1,j}^{(n)})\\ &- 0.5Reh^2\{v_{i,j}^{(n)}(u_{i+1,j}^{(n)} + u_{i-1,j}^{(n)} + u_{i,j+1}^{(n)} + u_{i,j-1}^{(n)})\\ &\left.- u_{i,j}^{(n)}(v_{i+1,j}^{(n)} + v_{i-1,j}^{(n)} + v_{i,j+1}^{(n)} + v_{i,j-1}^{(n)})\}\right] \qquad (4.11)\end{aligned}$$

The above formulation is of $O(h^2, \triangle t)$ accurate. The superscripts (n) and $(n+1)$ represent the values at the n- and $(n+1)$-th time levels respectively.

Kalita and Gupta [59] also proposed a more general formulation with the introduction of a weighted average parameter μ such that $t_\mu = (1-\mu)t^n + \mu t^{n+1}$ for $0 \leq \mu \leq 1$.

This formulation is as follows

$$
\begin{aligned}
& 0.5Reh^2\left[\psi_{i+1,j}^{(n+1)}+\psi_{i,j+1}^{(n+1)}+\psi_{i-1,j}^{(n+1)}+\psi_{i,j-1}^{(n+1)}-4\psi_{i,j}^{(n+1)}\right] \\
= \;& 0.5Reh^2\left[\psi_{i+1,j}^{(n)}+\psi_{i,j+1}^{(n)}+\psi_{i-1,j}^{(n)}+\psi_{i,j-1}^{(n)}-4\psi_{i,j}^{(n)}\right] \\
& +\triangle t(1-\mu)\left[\psi_{i-1,j-1}^{(n)}-8\psi_{i,j-1}^{(n)}+\psi_{i+1,j-1}^{(n)}-8\psi_{i-1,j}^{(n)}\right. \\
& +28\psi_{i,j}^{(n)}-8\psi_{i+1,j}^{(n)}+\psi_{i-1,j+1}^{(n)}-8\psi_{i,j+1}^{(n)}+\psi_{i+1,j+1}^{(n)} \\
& -3h(u_{i,j-1}^{(n)}-u_{i,j+1}^{(n)}+v_{i+1,j}^{(n)}-v_{i-1,j}^{(n)}) \\
& -0.5Reh^2\{v_{i,j}^{(n)}(u_{i+1,j}^{(n)}+u_{i-1,j}^{(n)}+u_{i,j+1}^{(n)}+u_{i,j-1}^{(n)}) \\
& \left.-u_{i,j}^{(n)}(v_{i+1,j}^{(n)}+v_{i-1,j}^{(n)}+v_{i,j+1}^{(n)}+v_{i,j-1}^{(n)})\}\right] \\
& +\triangle t\mu\left[\psi_{i-1,j-1}^{(n+1)}-8\psi_{i,j-1}^{(n+1)}+\psi_{i+1,j-1}^{(n+1)}-8\psi_{i-1,j}^{(n+1)}\right. \\
& +28\psi_{i,j}^{(n+1)}-8\psi_{i+1,j}^{(n+1)}+\psi_{i-1,j+1}^{(n+1)}-8\psi_{i,j+1}^{(n+1)}+\psi_{i+1,j+1}^{(n+1)} \\
& -3h(u_{i,j-1}^{(n+1)}-u_{i,j+1}^{(n+1)}+v_{i+1,j}^{(n+1)}-v_{i-1,j}^{(n+1)}) \\
& -0.5Reh^2\{v_{i,j}^{(n+1)}(u_{i+1,j}^{(n+1)}+u_{i-1,j}^{(n+1)}+u_{i,j+1}^{(n+1)}+u_{i,j-1}^{(n+1)}) \\
& \left.-u_{i,j}^{(n+1)}(v_{i+1,j}^{(n+1)}+v_{i-1,j}^{(n+1)}+v_{i,j+1}^{(n+1)}+v_{i,j-1}^{(n+1)})\}\right] \qquad (4.12)
\end{aligned}
$$

Altering the values of μ gives us a family of integrators, for instance $\mu = 0.5$ gives us a Crank-Nicholson type discretization with second order accuracy in time and space. In all our simulations, we will use this particular type of formulation. The system of equations resulting from equation (4.12) may be written in matrix form as

$$A\Psi^{(n+1)} = \mathbf{f}(\Psi^{(n)}, u^{(n)}, v^{(n)}, u^{(n+1)}, v^{(n+1)}). \qquad (4.13)$$

Here the coefficient matrix A is an asymmetric sparse matrix and for an $m \times n$ grid, A is of dimension $mn \times mn$. All the vectors $\Psi^{(n+1)}, \Psi^{(n)}, \mathbf{f}, u^{(n)}, v^{(n)}, u^{(n+1)}$ and $v^{(n+1)}$ are mn-component vectors. Note that equation (4.13) contains u and v at the $(n+1)$-rh time level and as such some special strategy is required to solve this equation. Following is the algorithm for solving equation (4.13):

1. Initialize $\Psi^{(n+1)}, u^{(n+1)}$ and $v^{(n+1)}$ (with $\Psi^{(n)}, u^{(n)}, v^{(n)}$).

2. Set $\Psi_{old}^{(n+1)} = \Psi^{(n+1)}$.

3. Determine $\Psi^{(n+1)}$ using equation (4.13).
4. Determine $u^{(n+1)}$ and $v^{(n+1)}$ using equations (4.9) and (4.10).
5. If max $|\Psi^{(n+1)} - \Psi^{(n+1)}_{old}|$ < tolerance limit, then stop; else repeat steps 2-5 until convergence.

In order to solve the unsteady Navier–Stokes equations using the formulation mentioned above, an outer–inner iteration procedure has been adopted. In a typical outer temporal cycle, we discretize equation (4.6) using (4.12). The resulting system of algebraic equations is then solved by using the BiCGStab [63, 101] method. The BiCGStab constitutes the inner iteration cycles. Once (4.12) is solved, u and v are calculated using equations (4.9) and (4.10). This constitutes one outer iteration cycle. The inner iterative procedure is continued until the steady state is achieved. The steady state was assumed to reach when the maximum ψ-error between two successive outer temporal iteration steps was smaller than 0.5×10^{-6}.

4.2 Hydrodynamic stability analysis

As described in chapter 3, once again the total flow $\psi(x, y, t)$ can be expressed as a combination of its steady flow and flow perturbation as

$$\psi(x, y, t) = \overline{\psi}(x, y) + \delta\tilde{\psi}(x, y)e^{\lambda t} \tag{4.14}$$

where δ is a small constant prefactor to the perturbation $\tilde{\psi}(x, y)$ with $\delta \ll 1$ and $\overline{\psi}(x, y)$ denotes the steady-state value of the streamfunction. Substituting (4.14) in (4.6) and collecting the like order terms, we get a set of equations for the steady flow and flow perturbation as follows

Steady equations

$$\begin{aligned}\frac{\partial^4\overline{\psi}}{\partial x^4} + 2\frac{\partial^4\overline{\psi}}{\partial x^2\partial y^2} + \frac{\partial^4\overline{\psi}}{\partial y^4} - Re(\overline{\psi}_y)\left[\frac{\partial^3\overline{\psi}}{\partial x^3} + \frac{\partial^3\overline{\psi}}{\partial x\partial y^2}\right] \\ + Re(\overline{\psi}_x)\left[\frac{\partial^3\overline{\psi}}{\partial x^2\partial y} + \frac{\partial^3\overline{\psi}}{\partial y^3}\right] = 0\end{aligned} \tag{4.15}$$

Stability equations

$$\begin{aligned}\frac{\partial^4\tilde{\psi}}{\partial x^4}+2\frac{\partial^4\tilde{\psi}}{\partial x^2\partial y^2}+\frac{\partial^4\tilde{\psi}}{\partial y^4}-Re(\overline{\psi}_y)\left[\frac{\partial^3\tilde{\psi}}{\partial x^3}+\frac{\partial^3\tilde{\psi}}{\partial x\partial y^2}\right] \\ +Re(\overline{\psi}_x)\left[\frac{\partial^3\tilde{\psi}}{\partial x^2\partial y}+\frac{\partial^3\tilde{\psi}}{\partial y^3}\right]-Re(\tilde{\psi}_y)\left[\frac{\partial^3\overline{\psi}}{\partial x^3}+\frac{\partial^3\overline{\psi}}{\partial x\partial y^2}\right] \\ +Re(\tilde{\psi}_x)\left[\frac{\partial^3\overline{\psi}}{\partial x^2\partial y}+\frac{\partial^3\overline{\psi}}{\partial y^3}\right]=\lambda Re\left[\frac{\partial^2\tilde{\psi}}{\partial x^2}+\frac{\partial^2\tilde{\psi}}{\partial y^2}\right]\end{aligned} \tag{4.16}$$

The boundary conditions for the steady equation depend on the problem concerned while the stability equations follow homogeneous boundary conditions.

Firstly, we utilize (4.8) to solve the steady equation (4.15) and obtain the value of $\overline{\psi}$, which is then substituted in the stability equation (4.16) to find $\tilde{\psi}$ and λ. (4.8) is again used to solve the stability equation (4.16). Similar to the ψ-ω approach described in chapter 3, this equation after discretization leads to a generalized eigenvalue problem (GEVP) which can be solved to find the values of $\tilde{\psi}$ and λ for different values of Re. Owing to the phenomenon of Hopf bifurcation, for a particular Reynolds number, a pair of complex conjugate eigenvalues crosses the imaginary axis which leads the basic flow to lose stability and a one parameter family of periodic solution bifurcates from the stationary solution.

The stability equations (4.16) with the steady state formulation of (4.12) turns out to be of the form

$$P\tilde{\psi}=\lambda ReQ\tilde{\psi} \tag{4.17}$$

where P is a tridecagonal matrix while Q is a pentadiagonal matrix as shown in the Figure 4.1.

This is a generalized eigenvalue problem. We solve equation (4.17) to find eigenvalue λ and eigenvector $\tilde{\psi}$ employing the freely available software package ARPACK [68].

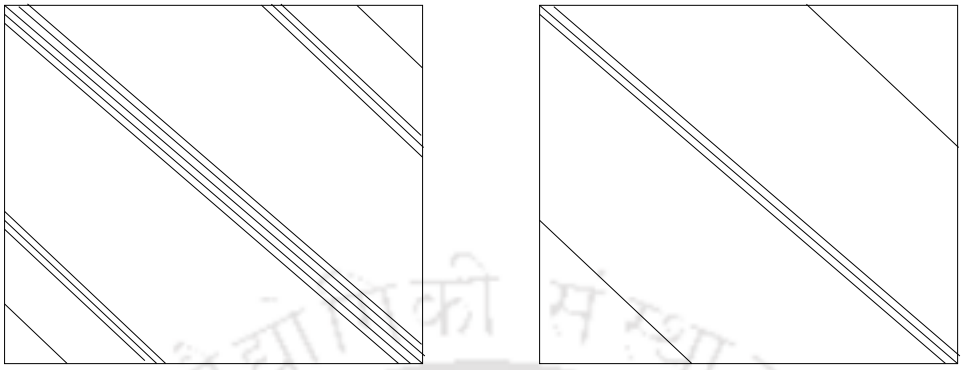

(a) (b)

Figure 4.1: *Structure of Matrices (a) P, (b) Q.*

In the numerical experiments performed here, the same methodology is followed in order to find the critical eigenvalue and the critical Reynolds number (Re_c).

Note that for the generalized eigenvalue problem the matrices P and Q (obtained from equation (4.17)) are of dimension $3mn \times 3mn$ in primitive variable formulation, $2mn \times 2mn$ in the $\psi - \omega$ approach, while the pure streamfunction formulation results in only matrices of dimension $mn \times mn$. Moreover the steady-state equation(s) resulting from the normal mode analysis in this approach has one and two lesser equations than the $\psi - \omega$ and primitive variable approaches respectively. So using the biharmonic approach not only reduces the computational effort significantly but is also much economical compared to the other two approaches.

4.3 Numerical examples

Three problems of different configurations have been considered here. The first problem considered here is the famous simple LDC flow, which has been extensively used as a benchmark problem for validating numerical codes. Moreover, several results are available on its global stability in the literature. As such this problem will also act as a validation exercise for our algorithm. The next two problems considered are the two-sided cross LDC flow, and the flow past

an inclined square cylinder for which no global stability analysis is available to the best of our knowledge. All these three problems are governed by the unsteady 2D incompressible Navier-Stokes equations. We are going to discuss about the flow instabilities in each of these problems one by one.

4.3.1 Simple lid-driven cavity flow on a square

Figure 4.2 shows a simple lid-driven cavity defined on $0 \leq x,\ y \leq 1$.

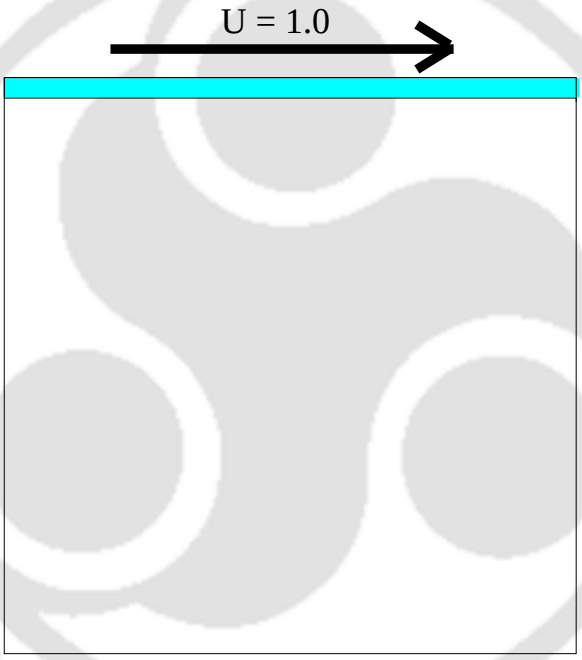

Figure 4.2: *Simple Lid-Driven Cavity.*

The top wall of the cavity at $y = 1$ is moving from left to right whic is the force behind setting the fluid into motion. The velocities on this wall are $u = 1$ and $v = 0$, whereas on the other walls, $u = v = 0$. Simple lid-driven cavity flows have been discussed by numerous researchers on a square cavity [2, 3, 10, 16, 17, 29, 31, 34, 41, 43, 44, 55, 56, 57, 86]. Literature also suggests that its global stability has been analysed by numerous researchers and various techniques have been employed with several established numerical methods [16, 17, 29, 58, 88, 89, 94, 112].

The stability analysis of the simple LDC flow has been performed using two different grids of size 129×129 and 501×501. In Table 4.1, we have shown the eigenvalue λ_c which is closest to the imaginary axis for Reynolds numbers $200 \leq Re \leq 10,000$ on a grid of size 501×501. From the table, one can easily deduce that our estimated value of the critical Reynolds number is 8025.9.

A comprehensive study reveals that the value of the critical parameter (here critical Reynolds number) for the simple lid-driven cavity flow lies in the range 7704-8031.93 [16, 17, 29, 88, 89, 94, 112] and our critical value lies very well within that range.

Table 4.1: *Reynolds number vs eigenvalue closest to imaginary axis on a* 501×501 *grid (square LDC flow).*

Reynolds Number (Re)	Eigenvalue (λ_c)
200	$-46.811 \times 10^{-5} \pm 2.80098i$
2000	$-18.619 \times 10^{-5} \pm 2.81265i$
5000	$-4.872 \times 10^{-5} \pm 2.81398i$
7000	$-1.756 \times 10^{-5} \pm 2.81527i$
8000	$-6.203 \times 10^{-6} \pm 2.81639i$
8025.9	$\mathbf{-2.340 \times 10^{-7} \pm 2.81642i}$
8050	$9.654 \times 10^{-7} \pm 2.81639i$
8250	$3.122 \times 10^{-6} \pm 2.81621i$
8500	$5.146 \times 10^{-5} \pm 2.81443i$
9000	$8.229 \times 10^{-5} \pm 2.81286i$
10000	$1.775 \times 10^{-4} \pm 2.80374i$

In Figure 4.3(a), we have depicted the eigenvalue spectrum at the critical Reynolds number. A pair of complex conjugate eigenvalues crossing the imaginary axis of the complex-plane and causing the flow in the cavity to be neutrally stable are clearly shown in Figure 4.3(b).

Figure 4.4 shows how a pair of eigenvalues approaches and crosses the imaginary axis of the complex plane respectively before and after arriving at the critical Reynolds number (Re_c).

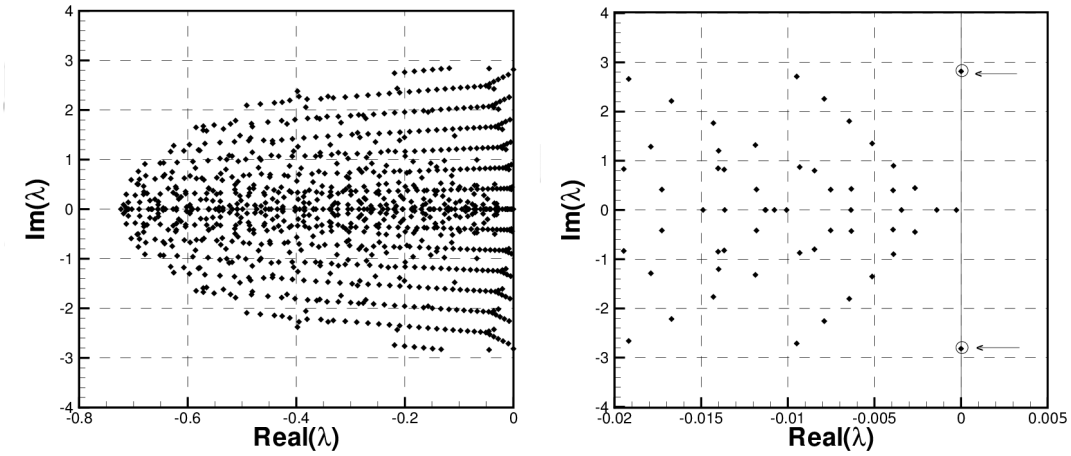

(a) (b)

Figure 4.3: *Plots showing a) 1000 eigenvalues and b) few eigenvalues near the imaginary axis for* $Re_c = 8025.9$ *(*501×501 *grid).*

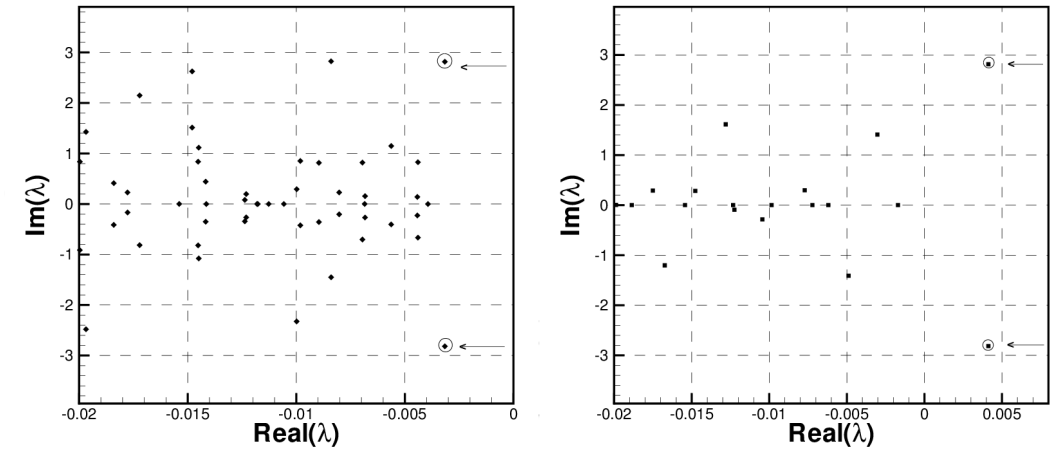

(a) (b)

Figure 4.4: *Plots showing few eigenvalues near the imaginary axis for (a)* $Re = 8000$ *and (b)* $Re = 8500$ *(*501×501 *grid).*

Table 4.2 shows the critical parameters obtained with different numerical methods for the square LDC flow. From the table, one can see that our results are in very good agreement with the established ones, particularly to Bopanna and Gajjar [16]. This is also exemplified by Figure 4.5, which shows the real and

imaginary parts of the streamfunction perturbation eigenvector corresponding to $\lambda_c = \pm 2.81642i$ and $Re_c = 8025.9$ on a 501×501 grid. These patterns are very similar to the ones obtained by Bopanna and Gajjar [16].

Table 4.2: *Comparison of critical parameters with existing literatures for the square LDC flow.*

Researcher	Re_c	λ_c	Method
Peng *et al.*[88]	7704.0	—	DNS
Poliashenko *et al.*[89]	7763.4	$\pm 2.8634i$	FEM
Fortin *et al.*[29]	8000.0	$5.4773 \times 10^{-5} \pm 2.8356i$	FEM
Tiesinga *et al.*[112]	8375.0	$9.0 \times 10^{-4} \pm 2.7640i$	PDECONT
Cadou *et al.*[17]	7890.0	$\pm 2.7646i$	FEM
Sahin *et al.*[94]	8031.93	—	FVM
Bopanna *et al.*[16]	8026.6	$2.61939 \times 10^{-6} \pm 2.8356i$	FDM in x-dir. and SC in y-dir.
Present Study	8025.9	$2.340 \times 10^{-7} \pm 2.8164i$	FDM (ψ-v)

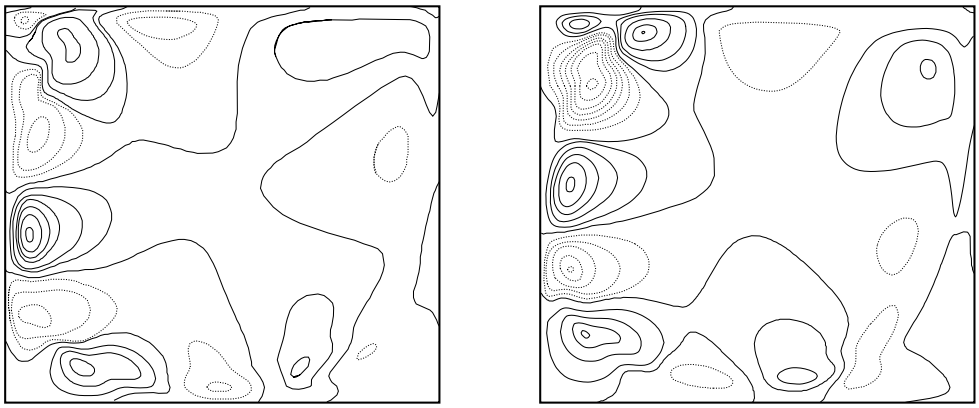

(a) (b)

Figure 4.5: *Streamfunction eigenvector on a* 501×501 *grid at* $Re_c = 8025.9$ *(a) Real-part, (b) Imaginary-part.*

In Table 4.3, we compare the CPU times taken by the ARPACK package while solving equation (4.17) for the generalized eigenvalue problem by the ψ-ω and ψ-v formulations. As expected, the current approach computes the eigenvalues at a pace twice (or more) that of the ψ-ω formulation, as the length of the

perturbed vector $\tilde{\psi}$ in (4.17) is half of that occurring in the ψ-ω formulation. We also present the eigenvalue closest to the imaginary axis corresponding to different Reynolds numbers. A close look at the table reveals the extreme closeness of the imaginary parts of λ_c for each of the Re considered here by both these approaches confirming the accuracy of the critical parameters.

Table 4.3: *CPU time comparison of the eigenvalue problem by the ψ-ω and ψ-v approach.*

Re	ψ-ω		ψ-v	
	Eigenvalue	CPU time	Eigenvalue	CPU time
200	$-4.926 \times 10^{-5} \pm 2.79814i$	5295	$-4.6811 \times 10^{-5} \pm 2.80098i$	2549
5000	$-7.558 \times 10^{-5} \pm 2.81276i$	5529	$-4.8720 \times 10^{-5} \pm 2.81398i$	2591
8000	$-1.294 \times 10^{-5} \pm 2.81552i$	6077	$-6.203 \times 10^{-6} \pm 2.81639i$	2648
8025.9	$-5.176 \times 10^{-6} \pm 2.81597i$	6122	$-2.340 \times 10^{-7} \pm 2.81642i$	2676
8500	$3.895 \times 10^{-5} \pm 2.81486i$	6378	$5.146 \times 10^{-5} \pm 2.81443i$	2725
10000	$9.972 \times 10^{-5} \pm 2.79845i$	6578	$1.775 \times 10^{-4} \pm 2.80374i$	2817

Figure 4.6(a) shows the instantaneous streamline patterns at the critical Reynolds number $Re_c = 8025.9$ and 4.6(b) shows the corresponding post-processed vorticity contour.

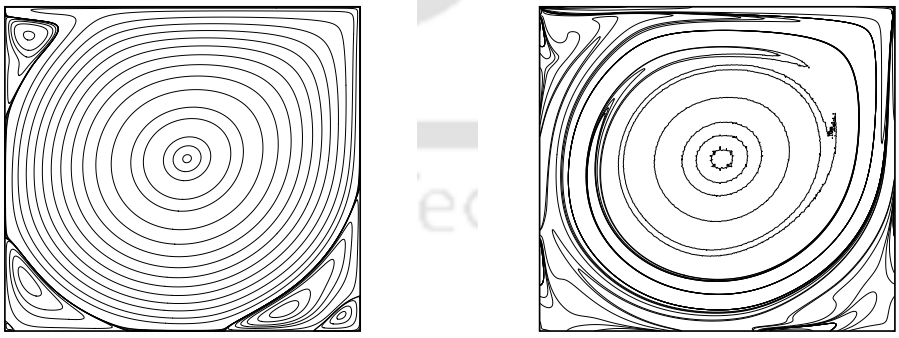

(a) (b)

Figure 4.6: *(a) Instantaneous streamline patterns at $Re_c = 8025.9$ on a 501×501 grid, (b) The post-processed vorticity contours at $Re_c = 8025.9$ on 501×501 grid - simple LDC flow.*

4.3.2 Two-sided cross lid-driven cavity flow

Our next example is the cross lid-driven cavity flow with two facing lids moving in antiparallel direction as shown in Figure 4.7. It shows a complex cross-sectional profile which is a symmetrized version of the staggered lid-driven cavity described in chapter 3. The velocities on the top wall are $u = 1$ and $v = 0$ while the velocities on the bottom wall are $u = -1$ and $v = 0$. The velocities on all the other walls are $u = v = 0$.

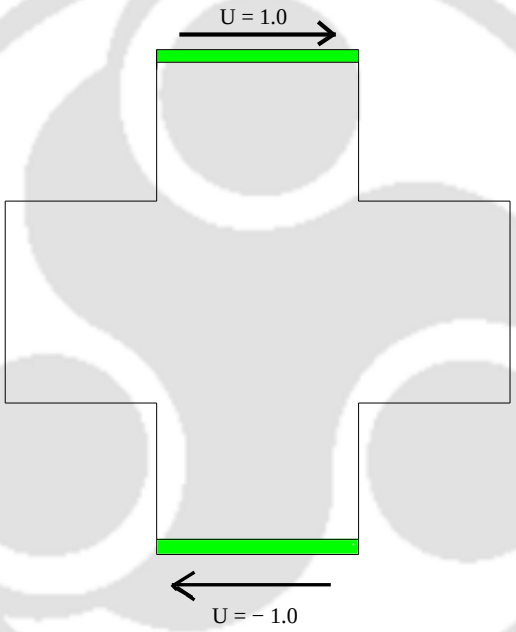

Figure 4.7: *Cross Lid-Driven Cavity.*

The cross lid-driven cavity flow has been proposed and is probably discussed only by Vicente *et al.* [116]. In their work [116], Vicente *et al.* described a linear three-dimensional global stability analysis of the cross lid-driven cavity flow. However, the 2D global stability analysis of the cross LDC has not yet been carried out and we, in the present work, for the first time carry out its global 2D stability analysis. To accomplish that, we once again employed the same techniques analogous to the ones employed for the simple LDC flow.

Since, the numerical method described here has not been utilized to simulate the flow patterns inside the cross LDC flow, we perform a validation study of

the code on the cross lid-driven cavity flow through a comparison exercise for a certain range of Reynolds numbers for which reliable qualitative and quantitative numerical results are available. Our numerical results are presented in Figure 4.8 and table 4.4. Figure 4.8 shows a side by side comparison of our computed steady state streamlines for $Re = 200$, 500 and $1,000$ on a grid of size 141×141 with those of Vicente *et al.* [116]. From the figure, one can confirm that our results agree quite well with those of [116] and it is also evident that our numerical solution shows four secondary vortices at the four corners at extreme left and extreme right which were visibly absent in Vicente *et al.* [116] for such small Re. This appearance becomes more and more apparent with the increase in Re as can be seen from the figure.

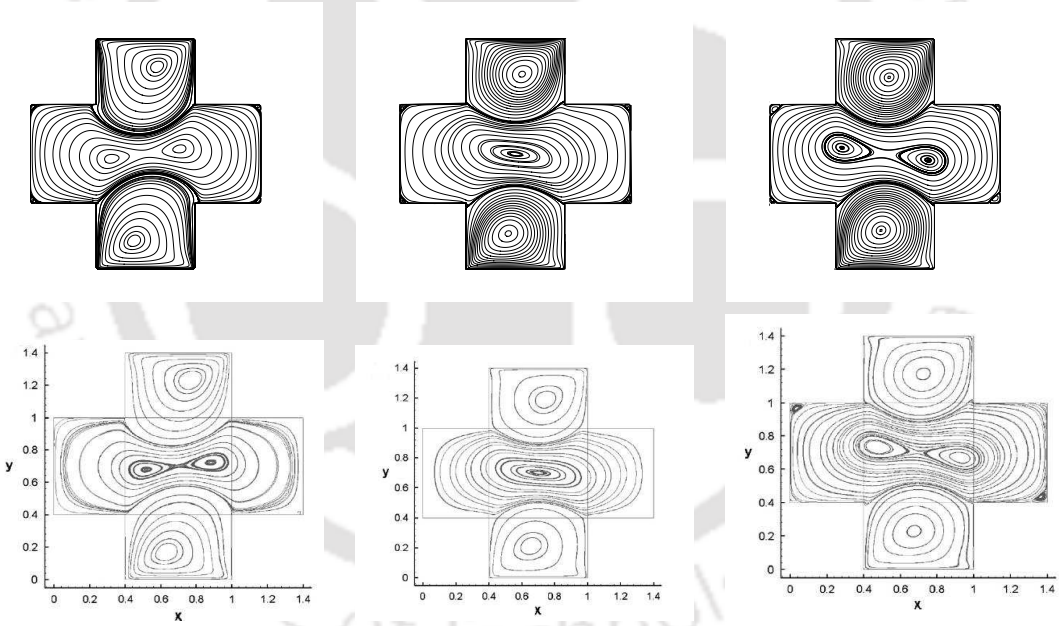

Figure 4.8: *Streamline contours for the Cross Lid-Driven Cavity : Present study (top) at* $Re = 200$ *(left),* $Re = 500$ *(middle) and* $Re = 1000$ *(right) and Vicente* et al. *[116] (bottom) at* $Re = 200$ *(left),* $Re = 500$ *(middle) and* $Re = 1000$ *(right) (*99×99 *Grid).*

Table 4.4 shows the locations of the primary, secondary and tertiary vortices for the cross lid-driven cavity flow. From the table, once again we can see that our results match very well with the ones obtained by [116].

Table 4.4: *Locations and vorticity values in the centres of primary, secondary and tertiary vortices - cross lid-driven cavity flow.*

		Primary vortices		Secondary vortices		Tertiary vortices	
Re	References	(x_{c1}, y_{c1})	ω_1	(x_{c2}, y_{c2})	ω_2	(x_{c3}, y_{c3})	ω_3
200	Vicente *et al.* [116]	(0.7707, 1.2326)	-5.03919	(0.5164, 0.6778)	0.33976		
		(0.6293, 0.1673)	-5.04023	(0.8836, 0.7221)	0.33968		
	Present study	(0.7701, 1.2300)	-5.17089	(0.4801, 0.6660)	0.34357	(0.0203, 0.9802)	-0.00239
		(0.6302, 0.1699)	-5.21263	(0.9192, 0.7317)	0.34384	(1.3800, 0.9800)	-0.00216
						(0.0200, 0.4199)	-0.00215
						(1.3804, 0.4202)	-0.00239
500	Vicente *et al.* [116]	(0.7431, 1.1876)	-4.27435	(0.7, 0.7)	0.67221		
		(0.6569, 0.2122)	-4.27317				
	Present study	(0.7400, 1.1800)	-4.1550	(0.7000, 0.7000)	0.68049	(0.0200, 0.9799)	-0.00439
		(0.6600, 0.2200)	-4.1601			(1.3800, 0.9800)	-0.00441
						(0.0200, 0.4200)	-0.00445
						(1.3800, 0.4199)	-0.00439
1000	Vicente *et al.* [116]	(0.7255, 0.1721)	-3.93792	(0.4701, 0.7322)	0.73701		
		(0.6745, 0.2278)	-3.93796	(0.9299, 0.6676)	0.73707		
	Present study	(0.7229, 0.1684)	-3.91785	(0.4700, 0.7399)	0.77277	(0.0300, 0.9699)	-0.02253
		(0.6800, 0.2369)	-3.92424	(0.9600, 0.6600)	0.74568	(1.3800, 0.9800)	-0.01058
						(0.0200, 0.4200)	-0.01067
						(1.3700, 0.4299)	-0.02247

Now we proceed on to carry out the global 2D stability analysis of the cross lid-driven cavity flow, For carrying out the stability analysis we consider the 211×211 grid. In Table 4.5, the *Re* verses eigenvalue closest to imaginary axis are presented.

Table 4.5: *Reynolds number vs eigenvalue closest to imaginary axis on a* 211×211 *grid (cross LDC flow).*

Reynolds Number (Re)	Eigenvalue (λ_c)
200	$-32.735 \times 10^{-5} \pm 0.48667i$
500	$-29.226 \times 10^{-5} \pm 0.48769i$
1000	$-18.102 \times 10^{-5} \pm 0.48858i$
2000	$-2.740 \times 10^{-5} \pm 0.49034i$
2041.7	$\mathbf{0.1120 \times 10^{-6} \pm 0.49612i}$
2500	$2.987 \times 10^{-6} \pm 0.49243i$
3000	$1.086 \times 10^{-5} \pm 0.49075i$
4000	$3.752 \times 10^{-5} \pm 0.49002i$
5000	$5.891 \times 10^{-5} \pm 0.48961i$
10000	$9.674 \times 10^{-5} \pm 0.48872i$

From the table, it is evident that for the cross LDC flow, the Re_c value lies

very close to 2041.7. Therefore, it is clear that for the cross lid-driven cavity flow, the predicted Re_c value is 2041.7 and $\lambda_c = 0.1120 \times 10^{-6} \pm 0.49612i$.

The real and imaginary parts of the streamfunction perturbation eigenvectors corresponding to the critical values on the grid of size 211×211 are shown in Figure 4.9 and the eigenvalue plots for the cross lid-driven cavity flow on a grid of size 211×211 corresponding to $Re = 2041.7$ are depicted in Figure 4.10. One interesting feature which can be observed from the streamfunction perturbation eigenvectors is the appearance of opposite bands of contour lines across the four interior mid-corners of the cavity.

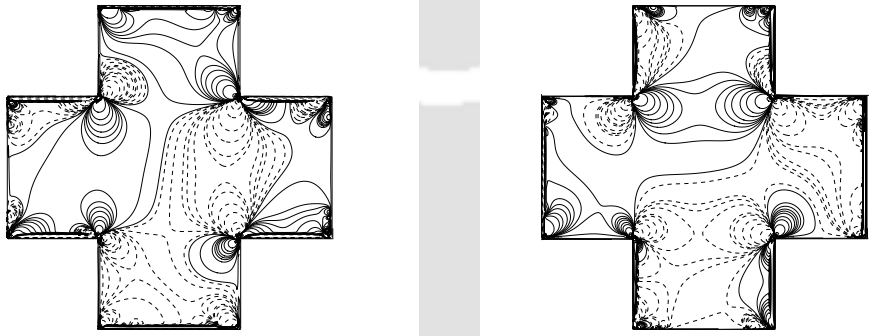

(a) (b)

Figure 4.9: *Streamfunction eigenvector on a* 211×211 *grid at* $Re_c = 2041.7$ *(a) Real-part, (b) Imaginary-part.*

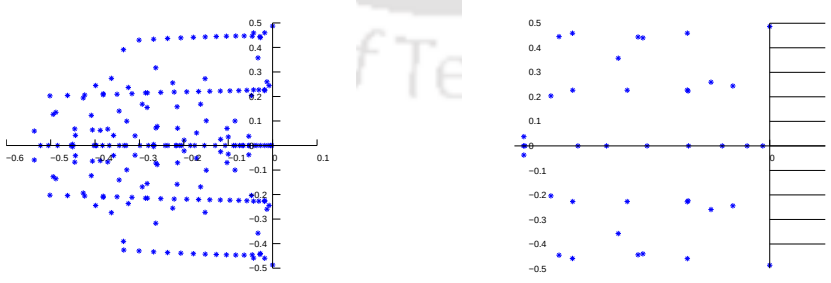

(a) (b)

Figure 4.10: *Plots showing a) 1000 eigenvalues and b) few eigenvalues near the imaginary axis for* $Re_c = 2041.7$ *(*211×211 *grid - cross LDC flow).*

Figure 4.11(a) shows the instantaneous streamline patterns at the critical Reynolds number $Re_c = 2041.7$ and 4.11(b) shows the corresponding post-processed vorticity contours.

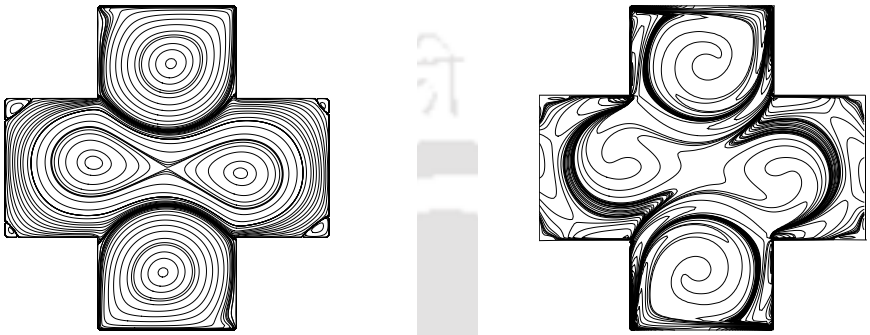

(a) (b)

Figure 4.11: *(a) Instantaneous streamline patterns at* $Re_c = 2041.7$ *on a* 211×211 *grid, (b) The post-processed vorticity contours at* $Re_c = 2041.7$ *on* 211×211 *grid - cross LDC flow.*

4.3.3 Flow past an inclined square cylinder

Our last example is the flow past an inclined square cylinder as depicted in Figure 4.12.

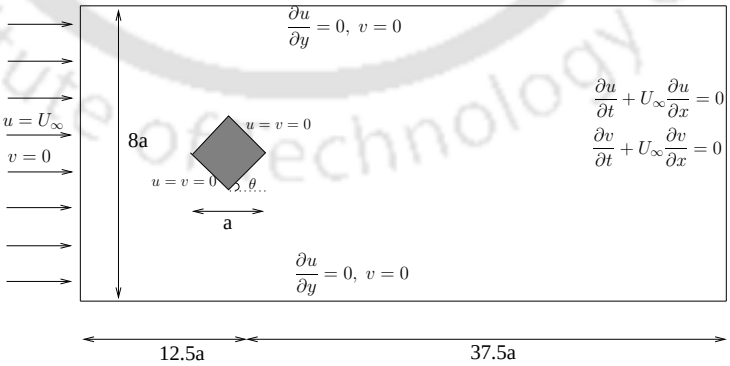

Figure 4.12: *Flow past an inclined square cylinder.*

The figure shows a fixed square cylinder placed in an infinite domain with an angle of incidence $\theta = 45^o$ at constant free-stream velocity U_∞; we assume

incompressible flow with constant fluid flow properties. The Reynolds number is defined as $Re = \dfrac{U_\infty \hat{a}}{\nu}$, where $\hat{a}$ is the projected width of the cylinder in the streamwise direction and ν is the kinematic viscosity of the fluid. On the surface of the cylinder, no-slip boundary condition is imposed where $u = v = 0$. At the inlet of the computational domain, a Dirichlet boundary condition $u = U_\infty,\ v = 0$ is used while at the outlet, we have employed a convective boundary condition such that $\dfrac{\partial \phi}{\partial t} + U_\infty \dfrac{\partial \phi}{\partial x} = 0$ with ϕ standing for u, v or ψ. A slip boundary condition $\dfrac{\partial u}{\partial y} = 0$ and $v = 0$ is used on the other boundaries. The entire computational domain is defined as $-12.5\hat{a} \leq x \leq 37.5\hat{a}$ and $-4\hat{a} \leq y \leq 4\hat{a}$ with the center of the square cylinder being at the origin.

To perform simulations we consider a grid of size 1001×161 and for analysing the stability of the fluid flow we begin our search with $Re = 40$ and 60 and followed the same algorithm as in the first two problems. However, we choose the step size of Reynolds number (ΔRe) to be 10 initially, which is later on followed by $\Delta Re = 5,\ 1.0,\ 0.5$ and finally 0.1.

Our results are shown in Table 4.6 and Figures 4.13-4.19. Table 4.6 shows the eigenvalues λ_c closest to the imaginary axis for Reynolds numbers in the range $40 \leq Re \leq 60$ on a grid of size 1001×161.

Table 4.6: *Reynolds number vs eigenvalue closest to imaginary axis on a* 1001×161 *grid.*

Reynolds Number (Re)	Eigenvalue (λ_c)
40	$-21.307 \times 10^{-7} \pm 0.020953i$
40.5	$-9.864 \times 10^{-7} \pm 0.021349i$
40.6	$-1.065 \times 10^{-8} \pm 0.021698i$
40.7	$\mathbf{1.783 \times 10^{-9} \pm 0.022567i}$
41	$-4.968 \times 10^{-8} \pm 0.022474i$
42	$-7.530 \times 10^{-8} \pm 0.022349i$
42.5	$2.879 \times 10^{-7} \pm 0.022332i$
45	$6.741 \times 10^{-7} \pm 0.022287i$
50	$1.004 \times 10^{-6} \pm 0.021964i$
60	$5.693 \times 10^{-6} \pm 0.020705i$

From the table, one can conclude that the critical Reynolds number for this flow is 40.7. The Re_c value found by us interestingly lies between the ones found by Yoon *et al.* [125] ($Re = 39$) and Sohankar *et al.* [104] ($Re = 42$).

The real and imaginary parts of the streamfunction eigenvector corresponding to $\lambda_c = \pm 0.022567i$ and $Re_c = 40.7$ on the 1001×161 grid are shown in Figures 4.13 and 4.14 respectively.

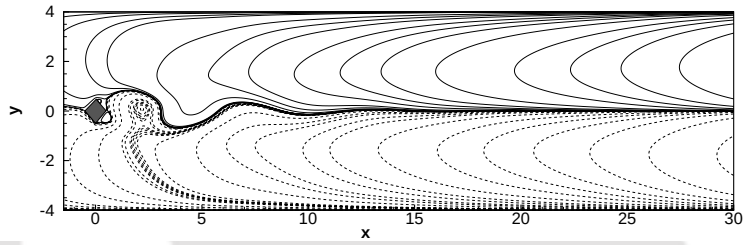

Figure 4.13: *Real part of streamfunction eigenvector on a* 1001×161 *grid at* $Re_c = 40.7$

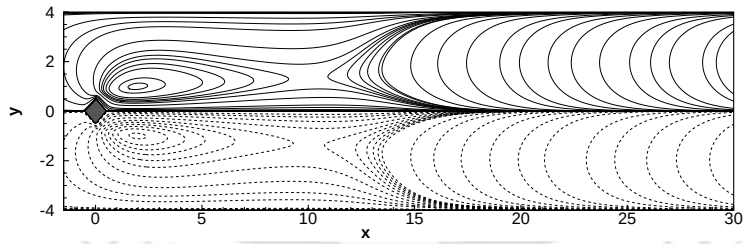

Figure 4.14: *Imaginary part of streamfunction eigenvector on a* 1001×161 *grid at* $Re_c = 40.7$

In Figure 4.15(a), we have shown the eigenvalue spectrum at the critical Reynolds number, $Re_c = 40.7$. Once again, a pair of purely imaginary eigenvalues can be clearly seen from the Figure 4.15(b).

In Figures 4.16 and 4.17, we show the streamline and vorticity contours respectively for Reynolds numbers 40, 40.7, 50 and 60. As can be seen from Figures 4.16(a) and 4.17(a), for $Re < Re_C$, the flow reaches steady-state and

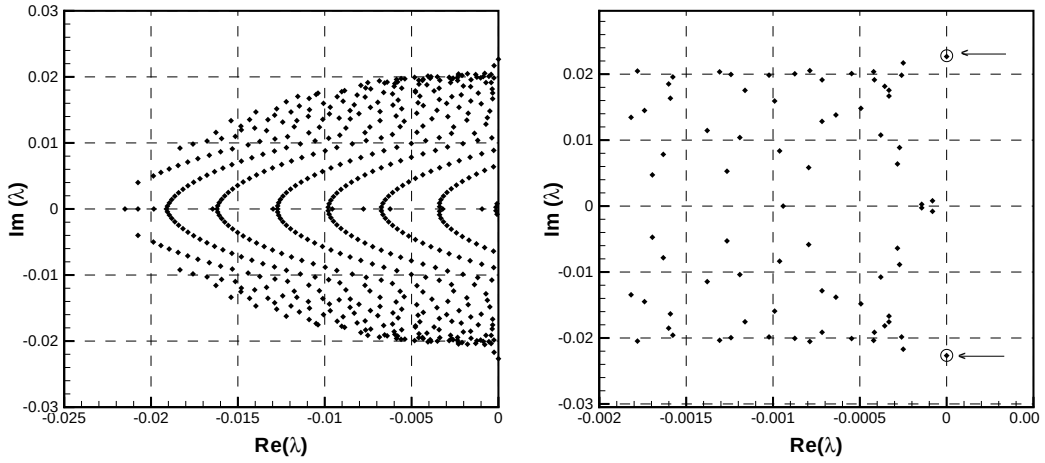

(a) (b)

Figure 4.15: *Plots showing a) 1000 eigenvalues and b) few eigenvalues near the imaginary axis for* $Re_c = 40.7$ *(*1001×161 *grid).*

symmetric flow can be observed. For $Re \geq Re_C$ (see Figures 4.16(b)-(d) and 4.17(b)-(d)), the flow eventually settles into a periodic nature leading to the shedding of vortices which can be clearly seen from these figures. Note that, in actual computation for $Re = 40.7$, the flow was perturbed in order to trigger asymmetry into the flow [61], while for $Re = 50$ and 60, the asymmetry set into the flow naturally. We also compute the drag and lift coefficients C_D and C_F, which are computed by using the following formulas

$$C_D = \frac{D}{\frac{1}{2}\rho U_\infty^2 A} \quad \text{and} \quad C_{\hat{L}} = \frac{\hat{L}}{\frac{1}{2}\rho U_\infty^2 A},$$

where D and $\hat{L}$ are the drag and lift forces respectively, ρ is the density of the fluid and A is the characteristic area. Here D and $\hat{L}$ are computed using momentum balance of the forces in a very small area $[-2, 2] \times [-2, 2]$ surrounding the cylinder.

We show the evolution of the drag and lift coefficients for $Re = 40.7$, 50 and 60 in Figure 4.18, which again depicts the eventual periodic flow patterns. Finally in Figure 4.19, we show the power spectral density for Reynolds numbers 40.7

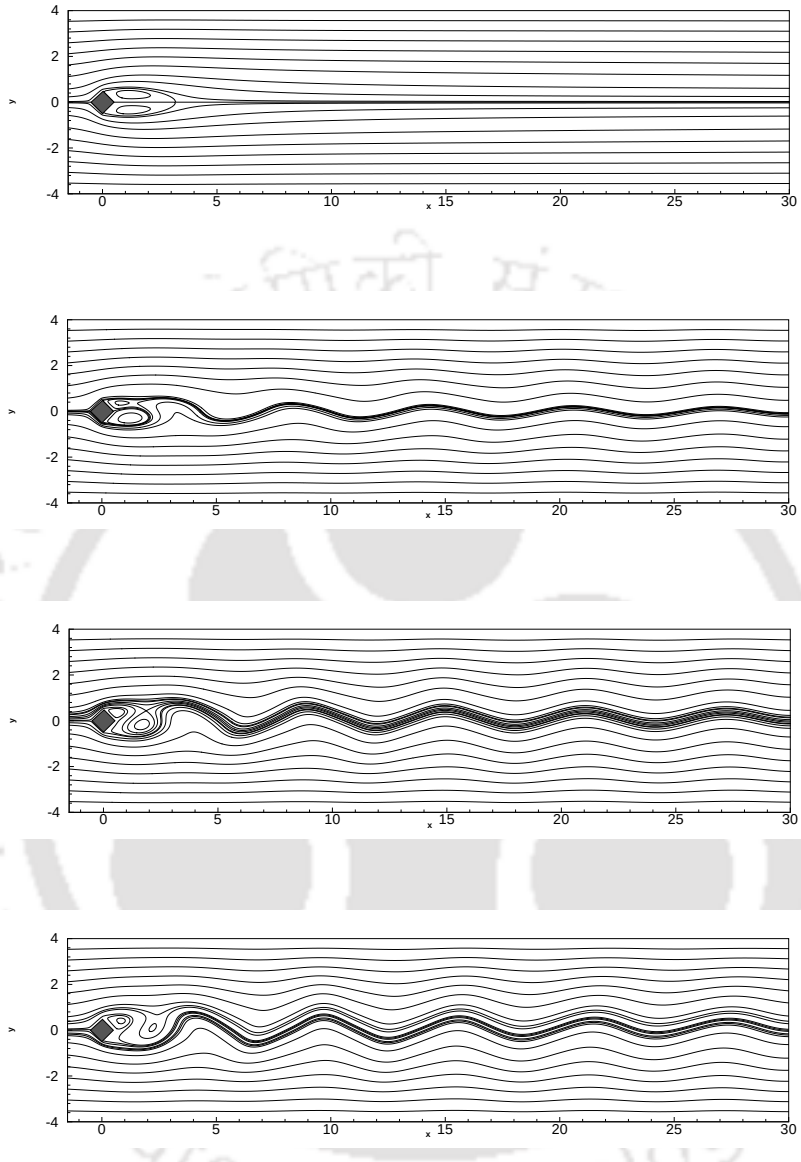

Figure 4.16: *Streamlines for the flow past an inclined square cylinder: steady-state for (a) $Re = 40$, and periodic flow for (b) $Re = 40.7$, (c) $Re = 50$ and (d) $Re = 60$.*

and 60, which corresponds to Strouhal numbers 0.15 and 0.16 respectively. The Strouhal number St is defined as $St = \dfrac{f_s \hat{a}}{U_\infty}$, where f_s is the shedding frequency, which is obtained from the spectral density analysis of the time history of the lift coefficient $C_{\hat{L}}$.

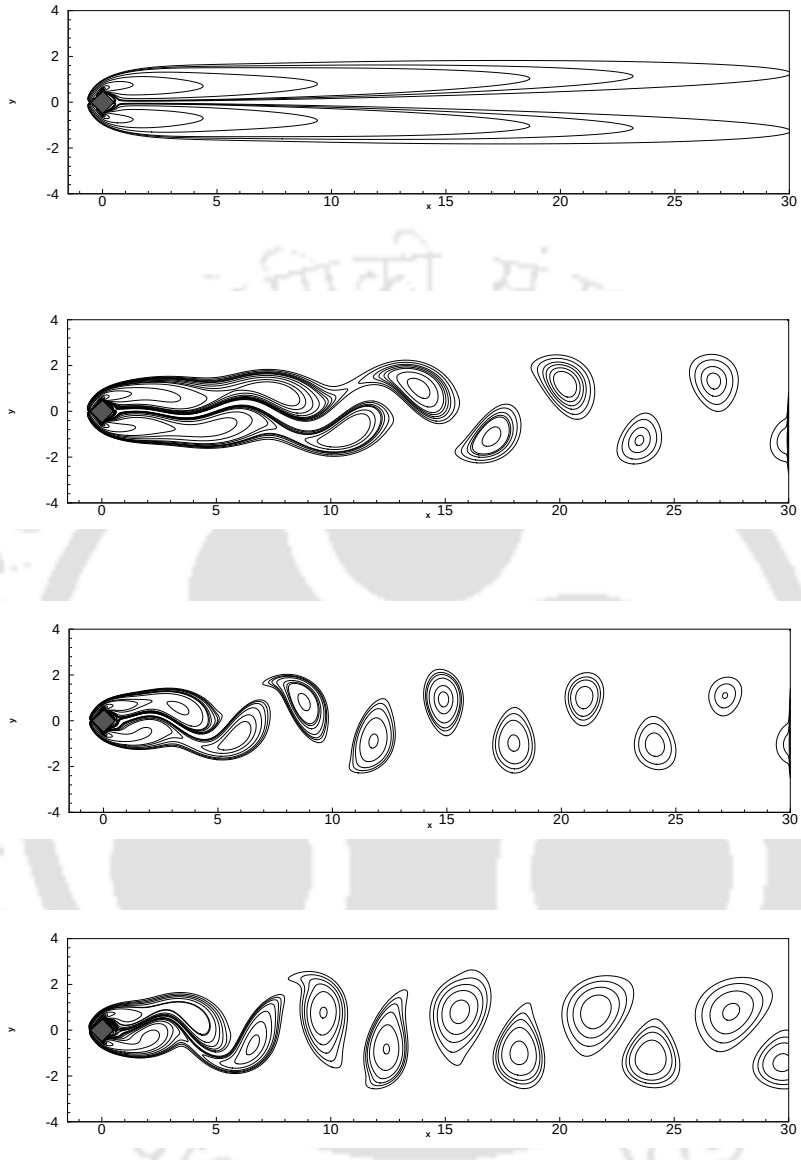

Figure 4.17: *Vorticity contours for the flow past an inclined square cylinder: steady-state for (a)* $Re = 40$*, and periodic flow for (b)* $Re = 40.7$*, (c)* $Re = 50$ *and (d)* $Re = 60$*.*

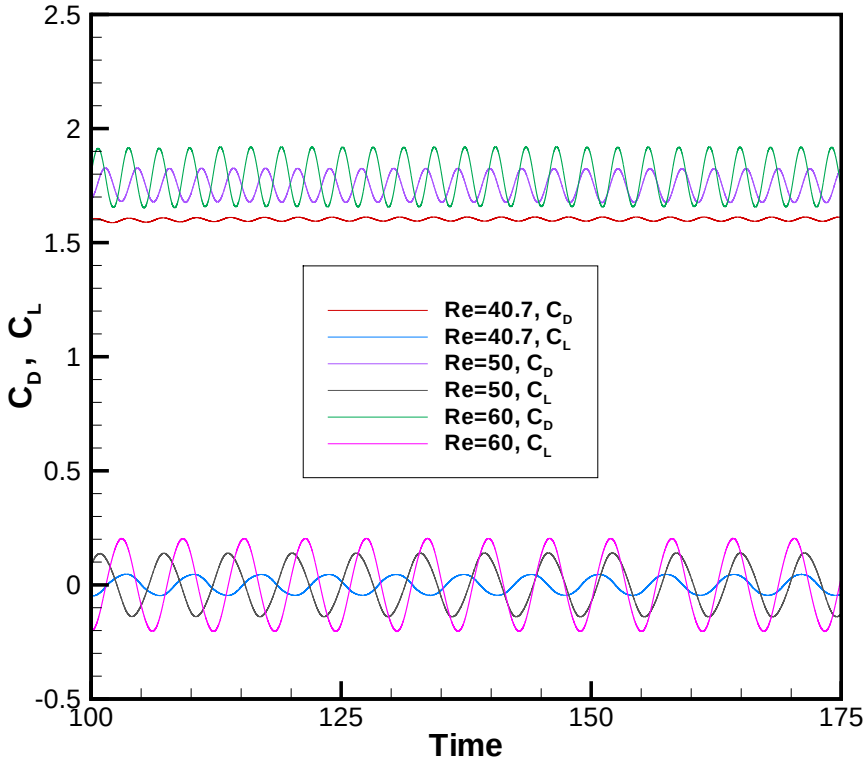

Figure 4.18: *Evolution of* C_D *and* $C_{\hat{L}}$ *for* $Re = 40.7$, 50 *and* 60.

4.4 Conclusion

In this chapter, we, for the first time employed the biharmonic formulation of the Navier-Stokes equations to study the global two-dimensional stability of incompressible viscous fluid flow problems. In the preceeding chapter, we have already analyzed the stability of flow inside a two-sided staggered LDC, for the both the parallel and anti-parallel motions of the lids using the ψ-ω formulation of the Navier-Stokes equations. However, in contrast to that, in this work we have used the pure streamfunction formulation of the N-S equations which reduces the governing equations into a single fourth order partial differential equation. The main advantage of this approach is that it drastically reduces the computational effort needed to solve the stability

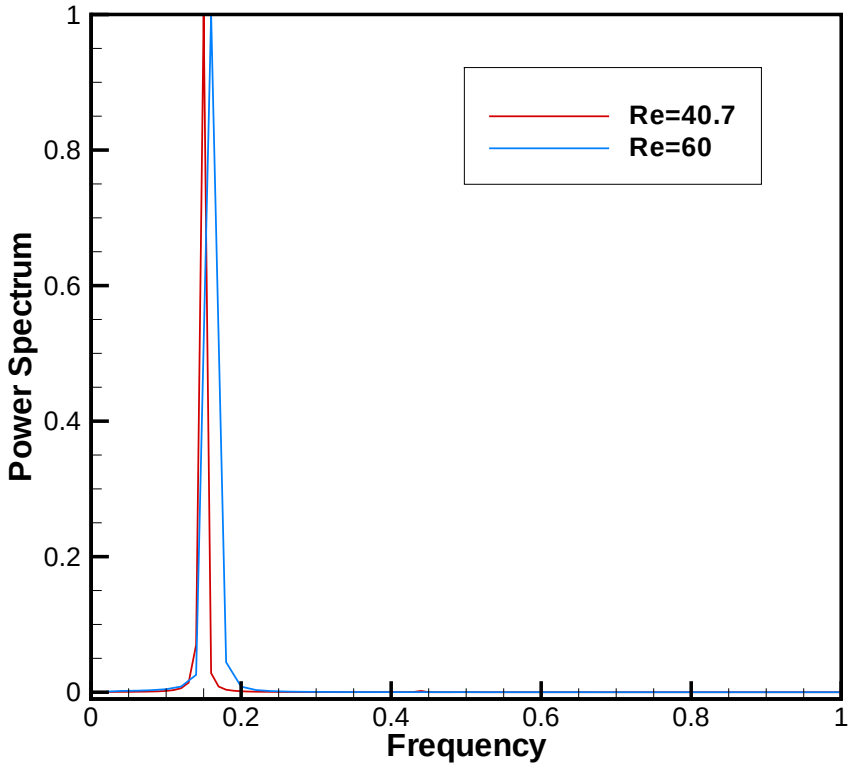

Figure 4.19: *Power spectral density of (a) the critical Reynolds number* $Re_c = 40.7$ *and (b)* $Re = 60$.

equations. This approach is applied to three fluid flow problems. For the first and the third problem, viz. the simple LDC flow and the flow past an inclined square cylinder, our results are very close to the established results. On the other hand, for the flow in the cross LDC problem, our approach is probably the first attempt to understand the 2D global stability for this problem. This approach, because of the computational economy of the generalized eigenvalue problem, may prove to be very useful in analyzing the global stability of more complex fluid flows.

Chapter 5

HOC SCHEMES FOR THE TRANSIENT 3D CONVECTION-DIFFUSION-REACTION EQUATIONS

5.1 Introduction

This chapter describes the development of a class of higher-order compact schemes with weighted time discretization for the transient three-dimensional (3D) convection-diffusion-reaction equations for variable convection and reaction coefficients. A class of fourth order spatially accurate implicit schemes for the governing set of equations are developed in line with the scheme of Reference [56]. One of the major features in determining the efficiency of a transient scheme is the temporal accuracy and one of our proposed scheme is temporally second order accurate. In order to focus deeply into the major aspects of our proposed schemes, we provide some fundamental studies, namely, the convergence analysis, dispersion-dissipation analysis and Fourier stability analysis. To test the robustness, accuracy and efficiency of the proposed schemes, we have applied it to four pertinent test cases for which numerical and/or analyt-

ical results are available. It is observed that these schemes very aptly handle problems governed by the transient 3D convection-diffusion-reaction equations including the 3D incompressible N-S equations.

The transient 3D convection-diffusion-reaction equation may be written as

$$a\frac{\partial\phi}{\partial t} - \nabla^2\phi + p(x,y,z,t)\frac{\partial\phi}{\partial x} + q(x,y,z,t)\frac{\partial\phi}{\partial y} + r(x,y,z,t)\frac{\partial\phi}{\partial z} + e(x,y,z,t)\phi(x,y,z,t) = f(x,y,z,t) \tag{5.1}$$

for the unknown transport variable $\phi(x,y,z,t)$ in a cubical domain $\Omega \subset \mathbb{R}^3$ with boundary $\partial\Omega$ and initial and boundary conditions of the form

I.C.: $\phi(x,y,z,0) = \phi_0(x,y,z), \qquad (x,y,z) \in \Omega$

B.C.: $\phi(x,y,z,t) = g(x,y,z,t), \qquad (x,y,z) \in \partial\Omega, \;\; t \in (0,T]$

where $a(>0)$ is a constant, $p(x,y,z,t)$, $q(x,y,z,t)$ and $r(x,y,z,t)$ are the convection coefficients, $e(x,y,z,t)$ is the reaction coefficient and $f(x,y,z,t)$ is the forcing function and $(0,T]$ is the time interval, with T being the final time. The functions $\phi_0(x,y,z)$, $f(x,y,z,t)$ and $g(x,y,z,t)$ are all assumed to be sufficiently smooth so that they are atleast twice differnetiable. With proper choice of parameters a, p, q, r, e and f, the above equation also represents the complete Navier-Stokes (N-S) equations in 3D.

5.2 Basic formulation and numerical procedure

The steady state form of equation (5.1) (considering ϕ, p, q, r, e and f to be independent of t) is,

$$-\nabla^2\phi + p(x,y,z)\frac{\partial\phi}{\partial x} + q(x,y,z)\frac{\partial\phi}{\partial y} + r(x,y,z)\frac{\partial\phi}{\partial z} + e(x,y,z)\phi(x,y,z) = f(x,y,z) \tag{5.2}$$

On the assumption that the domain under consideration is cubical, we construct a uniform cartesian mesh of steps h, k and l in the x-, y- and z-directions respectively and consequently the standard central difference approximation

to equation (5.2) at the (i, j, k)-th node is given by

$$(-\delta_x^2 - \delta_y^2 - \delta_z^2 + p\delta_x + q\delta_y + r\delta_z + e)\phi_{ijk} - \tau_{ijk} = f_{ijk}, \tag{5.3}$$

Here ϕ_{ijk} represents $\phi(x_i, y_j, z_k)$; δ_x, δ_x^2, δ_y, δ_y^2 and δ_z, δ_z^2 being the first and second order central difference operators along x-, y- and z-directions respectively.

The truncation error τ_{ijk} is as follows

$$\begin{aligned}\tau_{ijk} &= \left[\frac{h^2}{12}\left(2p\frac{\partial^3\phi}{\partial x^3} - \frac{\partial^4\phi}{\partial x^4}\right) + \frac{k^2}{12}\left(2q\frac{\partial^3\phi}{\partial y^3} - \frac{\partial^4\phi}{\partial y^4}\right) + \frac{l^2}{12}\left(2r\frac{\partial^3\phi}{\partial z^3} - \frac{\partial^4\phi}{\partial z^4}\right)\right]_{ijk} \\ &+ O(h^4, k^4, l^4).\end{aligned} \tag{5.4}$$

For obtaining a fourth order compact finite difference scheme for (5.2), we follow the procedure discussed in section 2.3 of chapter 2. Following that, we compactly approximate each of the derivatives of the leading term of equation (5.4) to $O(h^2, k^2, l^2)$. For example, the first term can be approximated as:

$$\begin{aligned}\left.\frac{\partial^3\phi}{\partial x^3}\right|_{ijk} &= \left[-\frac{\partial^3\phi}{\partial x\partial y^2} - \frac{\partial^3\phi}{\partial x\partial z^2} + p\frac{\partial^2\phi}{\partial x^2} + \frac{\partial p}{\partial x}\frac{\partial\phi}{\partial x} + q\frac{\partial^2\phi}{\partial x\partial y} + \frac{\partial q}{\partial x}\frac{\partial\phi}{\partial y}\right. \\ &\quad \left. + r\frac{\partial^2\phi}{\partial x\partial z} + \frac{\partial r}{\partial x}\frac{\partial\phi}{\partial z} + e\frac{\partial\phi}{\partial x} + \frac{\partial e}{\partial x}\phi - \frac{\partial f}{\partial x}\right]_{ijk} \\ &= \left[-\delta_x\delta_y^2 - \delta_x\delta_z^2 + p_{ijk}\delta_x^2 + \delta_x p_{ijk}\delta_x + q_{ijk}\delta_x\delta_y + \delta_x q_{ijk}\delta_y\right. \\ &\quad \left. + r_{ijk}\delta_x\delta_z + \delta_x r_{ijk}\delta_z + e_{ijk}\delta_x + \delta_x e_{ijk}\right]\phi_{ijk} - \delta_x f_{ijk} + O(h^2, k^2, l^2)\end{aligned} \tag{5.5}$$

Now, replacing the derivatives in equation (5.4) with approximations such as equation (5.5) and substituting for τ_{ijk} as described in (5.3), we obtain an $O(h^4, k^4, l^4)$ approximation for equation (5.2) on a nineteen-point stencil.

5.2.1 Constant reactive and convective coefficients

If the convective coefficients p, q and r and the reactive coefficient e are constants, the derivatives of p, q, r and e appearing in equation (5.4) vanishes

and from equation (5.3), we have the following HOC scheme

$$\begin{aligned}&[-A\delta_x^2 - B\delta_y^2 - C\delta_z^2 + P\delta_x + Q\delta_y + R\delta_z - D\delta_x\delta_y - E\delta_y\delta_z - F\delta_z\delta_x\\&+ H\delta_x\delta_y^2 + K\delta_x^2\delta_y - L\delta_x^2\delta_y^2 + M\delta_y\delta_z^2 + N\delta_y^2\delta_z - O\delta_y^2\delta_z^2 + S\delta_x^2\delta_z\\&+ T\delta_x\delta_z^2 - U\delta_z^2\delta_x^2 + G]\phi_{ijk} = W \qquad (5.6)\end{aligned}$$

where the coefficients A, B, C, P, Q, R, D, E, F, H, K, L, M, N, O, S, T, U, G and W are as follows:

$$A = 1+\frac{h^2}{12}(p^2-e);\quad B = 1+\frac{k^2}{12}(q^2-e);\quad C = 1+\frac{l^2}{12}(r^2-e);\quad P = p-\frac{h^2}{12}pe;$$

$$Q = q-\frac{k^2}{12}qe;\quad R = r-\frac{l^2}{12}re;\quad D = \frac{(h^2+k^2)}{12}pq;\quad E = \frac{(k^2+l^2)}{12}qr;$$

$$F = \frac{(l^2+h^2)}{12}rp;\quad H = \frac{(h^2+k^2)}{12}p;\quad K = \frac{(h^2+k^2)}{12}q;\quad L = \frac{(h^2+k^2)}{12};$$

$$M = \frac{(k^2+l^2)}{12}q;\quad N = \frac{(k^2+l^2)}{12}r;\quad O = \frac{(k^2+l^2)}{12};\quad S = \frac{(l^2+h^2)}{12}r;$$

$$T = \frac{(l^2+h^2)}{12}p;\quad U = \frac{(l^2+h^2)}{12};\quad G = e;\quad W = f$$

5.2.2 Variable reactive and convective coefficients

If the convective coefficients p, q and r and the reactive coefficient e are variables, then we have the following HOC schemes

$$\begin{aligned}&[-A_{ijk}\delta_x^2 - B_{ijk}\delta_y^2 - C_{ijk}\delta_z^2 + P_{ijk}\delta_x + Q_{ijk}\delta_y + R_{ijk}\delta_z - D_{ijk}\delta_x\delta_y \qquad (5.7)\\&-E_{ijk}\delta_y\delta_z - F_{ijk}\delta_z\delta_x + H_{ijk}\delta_x\delta_y^2 + K_{ijk}\delta_x^2\delta_y - L_{ijk}\delta_x^2\delta_y^2 + M_{ijk}\delta_y\delta_z^2\\&+N_{ijk}\delta_y^2\delta_z - O_{ijk}\delta_y^2\delta_z^2 + S_{ijk}\delta_x^2\delta_z + T_{ijk}\delta_x\delta_z^2 - U_{ijk}\delta_z^2\delta_x^2 + G_{ijk}]\phi_{ijk} = W_{ijk}\end{aligned}$$

where the coefficients A_{ijk}, B_{ijk}, C_{ijk}, P_{ijk}, Q_{ijk}, R_{ijk}, D_{ijk}, E_{ijk}, F_{ijk}, H_{ijk}, K_{ijk}, L_{ijk}, M_{ijk}, N_{ijk}, O_{ijk}, S_{ijk}, T_{ijk}, U_{ijk}, G_{ijk} and W_{ijk} are as follows:

$$
\begin{aligned}
A_{ijk} &= 1+\frac{h^2}{12}(p_{ijk}^2-2\delta_x p_{ijk}-e_{ijk}),\\
B_{ijk} &= 1+\frac{k^2}{12}(q_{ijk}^2-2\delta_y q_{ijk}-e_{ijk}),\\
C_{ijk} &= 1+\frac{l^2}{12}(r_{ijk}^2-2\delta_z r_{ijk}-e_{ijk}),\\
P_{ijk} &= \left[1+\frac{h^2}{12}(\delta_x^2-p_{ijk}\delta_x)+\frac{k^2}{12}(\delta_y^2-q_{ijk}\delta_y)+\frac{l^2}{12}(\delta_z^2-r_{ijk}\delta_z)\right]p_{ijk}\\
&+ \frac{h^2}{12}(2\delta_x e_{ijk}-e_{ijk}p_{ijk}),\\
Q_{ijk} &= \left[1+\frac{h^2}{12}(\delta_x^2-p_{ijk}\delta_x)+\frac{k^2}{12}(\delta_y^2-q_{ijk}\delta_y)+\frac{l^2}{12}(\delta_z^2-r_{ijk}\delta_z)\right]q_{ijk},\\
&+ \frac{k^2}{12}(2\delta_y e_{ijk}-e_{ijk}q_{ijk}),\\
R_{ijk} &= \left[1+\frac{h^2}{12}(\delta_x^2-p_{ijk}\delta_x)+\frac{k^2}{12}(\delta_y^2-q_{ijk}\delta_y)+\frac{l^2}{12}(\delta_z^2-r_{ijk}\delta_z)\right]r_{ijk},\\
&+ \frac{l^2}{12}(2\delta_z e_{ijk}-e_{ijk}r_{ijk}),\\
D_{ijk} &= \frac{(h^2+k^2)}{12}(p_{ijk}q_{ijk})-\frac{1}{6}(h^2\delta_x q_{ijk}+k^2\delta_y p_{ijk}),\\
E_{ijk} &= \frac{(k^2+l^2)}{12}(q_{ijk}r_{ijk})-\frac{1}{6}(k^2\delta_y r_{ijk}+l^s 2\delta_z q_{ijk}),\\
F_{ijk} &= \frac{(l^2+h^2)}{12}(r_{ijk}p_{ijk})-\frac{1}{6}(l^2\delta_z p_{ijk}+h^2\delta_x r_{ijk}),\\
H_{ijk} &= \frac{(h^2+k^2)}{12}p_{ijk},\quad K_{ijk}=\frac{(h^2+k^2)}{12}q_{ijk},\quad L_{ijk}=\frac{(h^2+k^2)}{12},\\
M_{ijk} &= \frac{(k^2+l^2)}{12}q_{ijk},\quad N_{ijk}=\frac{(k^2+l^2)}{12}r_{ijk},\quad O_{ijk}=\frac{(k^2+l^2)}{12},\\
S_{ijk} &= \frac{(l^2+h^2)}{12}r_{ijk},\quad T_{ijk}=\frac{(l^2+h^2)}{12}p_{ijk},\quad U_{ijk}=\frac{(l^2+h^2)}{12},\\
G_{ijk} &= \left[1+\frac{h^2}{12}(\delta_x^2-p_{ijk}\delta_x)+\frac{k^2}{12}(\delta_y^2-q_{ijk}\delta_y)+\frac{l^2}{12}(\delta_z^2-r_{ijk}\delta_z)\right]e_{ijk}\quad \text{and}\\
W_{ijk} &= \left[1+\frac{h^2}{12}(\delta_x^2-p_{ijk}\delta_x)+\frac{k^2}{12}(\delta_y^2-q_{ijk}\delta_y)+\frac{l^2}{12}(\delta_z^2-r_{ijk}\delta_z)\right]f_{ijk}
\end{aligned}
$$

Throughout our discussion, we have assumed that the convection coefficients p, q, r, the reaction coefficients e and the forcing function f are sufficiently smooth so that they are at least twice differentiable and their derivatives are known analytically or their discrete approximations are known.

5.2.3 The transient form of the convection-diffusion-reaction equation

For the transient case, we consider the coefficients p, q, r and e and the forcing function f to be functions of x, y, z and t. The expression on the right hand side of the transient equation (5.1) can now be written as of the form $f(x,y,z,t) - a[(\partial\phi)/(\partial t)]$ and if we use forward difference approximation for $[(\partial\phi)/(\partial t)]$ with a time step $\triangle t$, we can approximate the equation (5.1) with the help of equation (5.7) as follows

$$
\begin{aligned}
& a\left[1+\overbrace{\frac{h^2}{12}(\delta_x^2 - p_{ijk}\delta_x) + \frac{k^2}{12}(\delta_y^2 - q_{ijk}\delta_y) + \frac{l^2}{12}(\delta_z^2 - r_{ijk}\delta_z)}\right]\delta_t^+\phi_{ijk}^n - A_{ijk}\delta_x^2\phi_{ijk}^n \\
& - B_{ijk}\delta_y^2\phi_{ijk}^n - C_{ijk}\delta_z^2\phi_{ijk}^n + P_{ijk}\delta_x\phi_{ijk}^n + Q_{ijk}\delta_y\phi_{ijk}^n + R_{ijk}\delta_z\phi_{ijk}^n - D_{ijk}\delta_x\delta_y\phi_{ijk}^n \\
& - E_{ijk}\delta_y\delta_z\phi_{ijk}^n - F_{ijk}\delta_z\delta_x\phi_{ijk}^n + H_{ijk}\delta_x\delta_y^2\phi_{ijk}^n + K_{ijk}\delta_x^2\delta_y\phi_{ijk}^n - L_{ijk}\delta_x^2\delta_y^2\phi_{ijk}^n \\
& + M_{ijk}\delta_y\delta_z^2\phi_{ijk}^n + N_{ijk}\delta_y^2\delta_z\phi_{ijk}^n - O_{ijk}\delta_y^2\delta_z^2\phi_{ijk}^n + S_{ijk}\delta_x^2\delta_z\phi_{ijk}^n + T_{ijk}\delta_x\delta_z^2\phi_{ijk}^n \\
& - U_{ijk}\delta_z^2\delta_x^2\phi_{ijk}^n + G_{ijk}\phi_{ijk}^n = W_{ijk}^n
\end{aligned}
\tag{5.8}
$$

where δ_t^+ is the forward difference operator and the superscript n stands for the n-th time level. Equation (5.8) can thus be rewritten as

$$
\begin{aligned}
& \sum_{i_1=-1}^{1}\sum_{j_1=-1}^{1}\sum_{k_1=-1}^{1}\alpha_{i+i_1,j+j_1,k+k_1}\phi_{i+i_1,j+j_1,k+k_1}^{n+1} = \\
& \sum_{i_1=-1}^{1}\sum_{j_1=-1}^{1}\sum_{k_1=-1}^{1}\beta_{i+i_1,j+j_1,k+k_1}\phi_{i+i_1,j+j_1,k+k_1}^{n} + 12W_{ijk}^n
\end{aligned}
\tag{5.9}
$$

where $\alpha_{i+i_1,j+j_1,k+k_1} = \beta_{i+i_1,j+j_1,k+k_1} = 0$ when all three indices i_1 , j_1 and k_1 are non-zero simultaneously, and $\alpha_{i+i_1,j+j_1,k+k_1} = 0$ when two of the indices i_1 , j_1 and k_1 are non-zero simultaneously. Here α and β are functions of the coefficients a, p, q, r and e appearing in equation (5.1) and may be written as

$$
\alpha_{i+i_1,j+j_1,k+k_1} = q_{i+i_1,j+j_1,k+k_1} \tag{5.10a}
$$

$$\beta_{i+i_1,j+j_1,k+k_1} = 12p_{i+i_8 1,j+j_1,k+k_1} + q_{i+i_1,j+j_1,k+k_1}, \tag{5.10b}$$

where

$$p_{i-1,j-1.k} = -\frac{D_{ijk}}{4hk} - \frac{H_{ijk}}{2hk^2} - \frac{K_{ijk}}{2h^2k} - \frac{L_{ijk}}{h^2k^2}, \qquad q_{i-1,j-1.k} = 0,$$

$$p_{i,j-1.k-1} = -\frac{E_{ijk}}{4kl} - \frac{M_{ijk}}{2kl^2} - \frac{N_{ijk}}{2k^2l} - \frac{O_{ijk}}{k^2l^2}, \qquad q_{i,j-1.k-1} = 0,$$

$$p_{i-1,j.k-1} = -\frac{F_{ijk}}{4lh} - \frac{S_{ijk}}{2lh^2} - \frac{T_{ijk}}{2l^2h} - \frac{U_{ijk}}{l^2h^2}, \qquad q_{i-1,j.k-1} = 0,$$

$$p_{i-1,j.k} = -\frac{A_{ijk}}{h^2} - \frac{P_{ijk}}{2h} + \frac{H_{ijk}}{hk^2} + \frac{T_{ijk}}{hl^2} + \frac{2L_{ijk}}{h^2k^2} + \frac{2U_{ijk}}{l^2h^2}, \qquad q_{i-1,j.k} = a\left(1 + \frac{p_{ijk}h}{2}\right),$$

$$p_{i,j-1.k} = -\frac{B_{ijk}}{k^2} - \frac{Q_{ijk}}{2k} + \frac{K_{ijk}}{h^2k} + \frac{M_{ijk}}{kl^2} + \frac{2L_{ijk}}{h^2k^2} + \frac{2O_{ijk}}{k^2l^2}, \qquad q_{i,j-1.k} = a\left(1 + \frac{q_{ijk}k}{2}\right),$$

$$p_{i,j.k-1} = -\frac{C_{ijk}}{l^2} - \frac{R_{ijk}}{2l} + \frac{N_{ijk}}{k^2l} + \frac{S_{ijk}}{h^2l} + \frac{2O_{ijk}}{k^2l^2} + \frac{2U_{ijk}}{l^2h^2}, \qquad q_{i,j.k-1} = a\left(1 + \frac{r_{ijk}l}{2}\right),$$

$$p_{i+1,j-1.k} = \frac{D_{ijk}}{4hk} + \frac{H_{ijk}}{2hk^2} - \frac{K_{ijk}}{2h^2k} - \frac{L_{ijk}}{h^2k^2}, \qquad q_{i+1,j-1.k} = 0,$$

$$p_{i,j+1.k-1} = \frac{E_{ijk}}{4kl} + \frac{M_{ijk}}{2kl^2} - \frac{N_{ijk}}{2k^2l} - \frac{O_{ijk}}{k^2l^2}, \qquad q_{i,j+1.k-1} = 0,$$

$$p_{i-1,j.k+1} = \frac{F_{ijk}}{4lh} + \frac{S_{ijk}}{2lh^2} - \frac{T_{ijk}}{2l^2h} - \frac{U_{ijk}}{l^2h^2}, \qquad q_{i-1,j.k+1} = 0,$$

$$p_{i,j.k} = \frac{2A_{ijk}}{h^2} + \frac{2B_{ijk}}{k^2} + \frac{2C_{ijk}}{l^2} - \frac{4L_{ijk}}{h^2k^2} - \frac{4O_{ijk}}{k^2l^2} - \frac{4U_{ijk}}{l^2h^2} + G_{ijk}, \qquad q_{i,j.k} = 6a,$$

$$p_{i+1,j.k} = -\frac{A_{ijk}}{h^2} + \frac{P_{ijk}}{2h} - \frac{H_{ijk}}{hk^2} - \frac{T_{ijk}}{hl^2} + \frac{2L_{ijk}}{h^2k^2} + \frac{2U_{ijk}}{l^2h^2}, \qquad q_{i+1,j.k} = a\left(1 - \frac{p_{ijk}h}{2}\right),$$

$$p_{i,j+1.k} = -\frac{B_{ijk}}{k^2} + \frac{Q_{ijk}}{2k} - \frac{K_{ijk}}{h^2k} - \frac{M_{ijk}}{kl^2} + \frac{2L_{ijk}}{h^2k^2} + \frac{2O_{ijk}}{k^2l^2}, \qquad q_{i,j+1.k} = a\left(1 - \frac{q_{ijk}k}{2}\right),$$

$$p_{i,j.k+1} = -\frac{C_{ijk}}{l^2} + \frac{R_{ijk}}{2l} - \frac{N_{ijk}}{k^2l} - \frac{S_{ijk}}{h^2l} + \frac{2O_{ijk}}{k^2l^2} + \frac{2U_{ijk}}{l^2h^2}, \qquad q_{i,j.k+1} = a\left(1 - \frac{r_{ijk}l}{2}\right),$$

$$p_{i-1,j+1.k} = \frac{D_{ijk}}{4hk} - \frac{H_{ijk}}{2hk^2} + \frac{K_{ijk}}{2h^2k} - \frac{L_{ijk}}{h^2k^2}, \qquad q_{i-1,j+1.k} = 0,$$

$$p_{i,j-1.k+1} = \frac{E_{ijk}}{4kl} - \frac{M_{ijk}}{2kl^2} + \frac{N_{ijk}}{2k^2l} - \frac{O_{ijk}}{k^2l^2}, \qquad q_{i,j-1.k+1} = 0,$$

$$p_{i+1,j.k-1} = \frac{F_{ijk}}{4lh} - \frac{S_{ijk}}{2lh^2} + \frac{T_{ijk}}{2l^2h} - \frac{U_{ijk}}{l^2h^2}, \qquad q_{i+1,j.k-1} = 0,$$

$$p_{i+1,j+1.k} = -\frac{D_{ijk}}{4hk} + \frac{H_{ijk}}{2hk^2} + \frac{K_{ijk}}{2h^2k} - \frac{L_{ijk}}{h^2k^2}, \qquad q_{i+1,j+1.k} = 0,$$
$$p_{i,j+1.k+1} = -\frac{E_{ijk}}{4kl} + \frac{M_{ijk}}{2kl^2} + \frac{N_{ijk}}{2k^2l} - \frac{O_{ijk}}{k^2l^2}, \qquad q_{i,j+1.k+1} = 0,$$
$$p_{i+1,j.k+1} = -\frac{F_{ijk}}{4lh} + \frac{S_{ijk}}{2lh^2} + \frac{T_{ijk}}{2l^2h} - \frac{U_{ijk}}{l^2h^2}, \qquad q_{i+1,j.k+1} = 0.$$

Introducing a weighted average parameter ς via forward time approximation of $[(\partial\phi)/(\partial t)]$ such that $t_\varsigma = (1-\varsigma)t^n + \varsigma t^{n+1}$ for $0 \leq \varsigma \leq 1$, we obtain a class of integrators; for instance, for $\varsigma = 0$, we have the forward Euler approximation, $\varsigma = 1$ gives backward Euler, while $\varsigma = 0.5$ gives the Crank-Nicholson. With these, $\alpha_{i+i_1,j+j_1,k+k_1}$ and $\beta_{i+i_1,j+j_1,k+k_1}$ appearing in equation (5.9) can be written as $\alpha_{i+i_1,j+j_1,k+k_1} = 12\varsigma p_{i+i_1,j+j_1,k+k_1} + q_{i+i_1,j+j_1,k+k_1}$ and $\beta_{i+i_1,j+j_1,k+k_1} = 12(\varsigma-1)p_{i+i_1,j+j_1,k+k_1} + q_{i+i_1,j+j_1,k+k_1}$ respectively, and the term W^n_{ijk} on the right hand side of equation (5.9) takes the form $\varsigma W^{n+1}_{ijk} + (1-\varsigma)W^n_{ijk}$. Thus we have equation (5.9) as the HOC finite-difference approximation for the transient 3D convection-diffusion-reaction equation with fourth order spatial accuracy. Because of the operator under the brace in equation (5.8), all such schemes with varied values of ς are implicit with order of accuracy as $O((\triangle t)^s, h^4, k^4, l^4)$, where $s \leq 2$. We should also note that for $\varsigma = 0$, the difference stencil requires nineteen points in the n-th and seven points in the $(n+1)$-th time level resulting in a HOC scheme which we termed as a (19, 7) scheme. Likewise, with replacements for ς as 0.5 and 1, we derive a (19, 19) and a (7, 19) scheme respectively. The stencils required in these type of formulations are illustrated in Figure 5.1.

With the help of these p's and q's, the equation (5.9) can now be written in matrix form as

$$A\boldsymbol{\phi}^{n+1} = \boldsymbol{g}(\boldsymbol{\phi}^n) + \boldsymbol{W}^n \tag{5.11}$$

here the matrix A is an asymmetric sparse matrix and on a grid of size $m \times n \times p$, size of A is $mnp \times mnp$, and ϕ^{n+1}, $g(\phi^n)$ and W^n are mnp-component vectors. Conventional solvers like Gauss-Seidel cannot be used for solving equation (5.11) as in general, the matrix A is not diagonally dominant. In cartesian co-

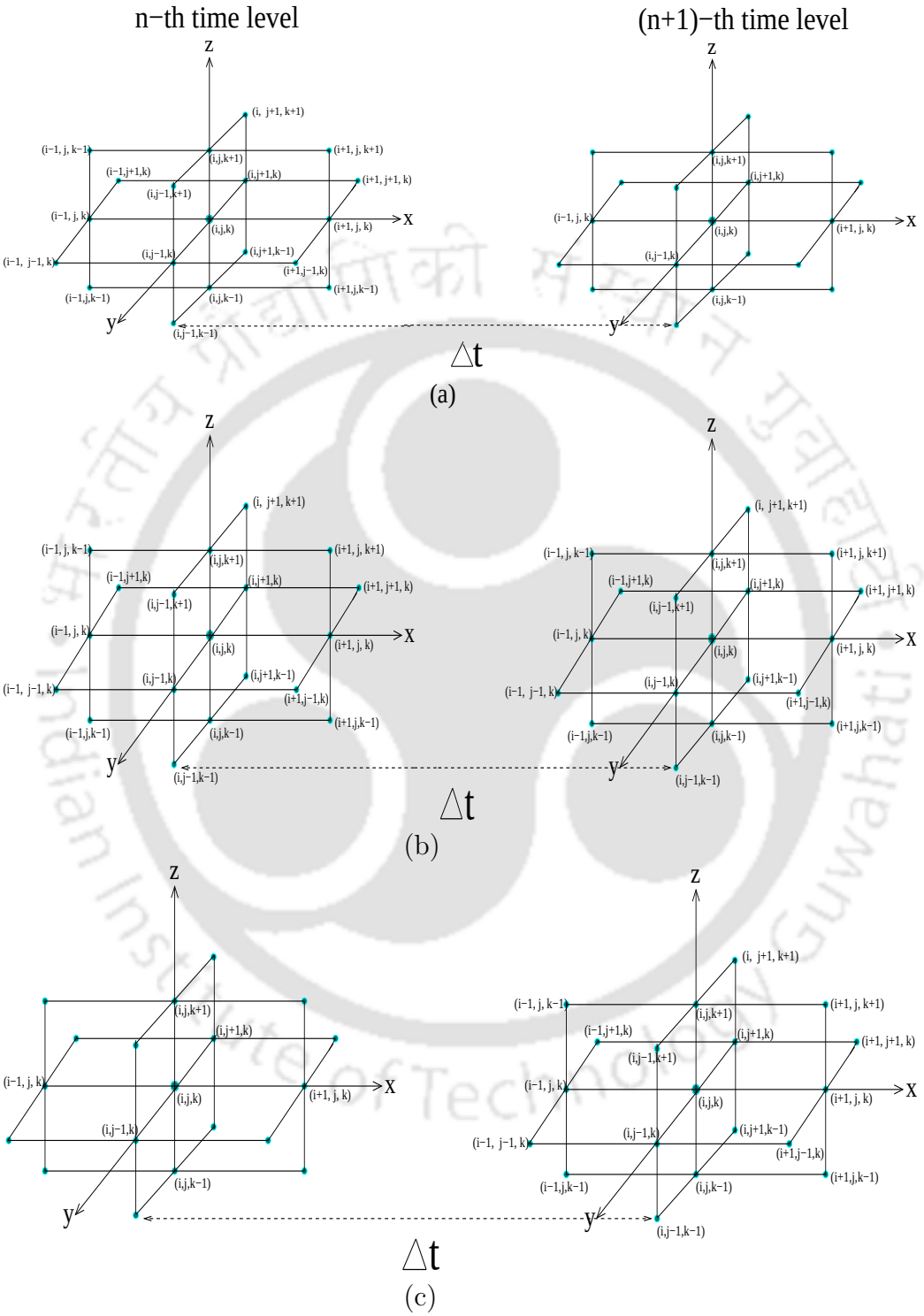

Figure 5.1: Unsteady HOC stencils for (a) $\varsigma = 0$, (b) $\varsigma = 0.5$ and (c) $\varsigma = 1.0$

ordinates, some of the associated matrices are symmetric and positive definite on a uniform grid, which allows algorithms like conjugate-gradient (CG) [63] to be used. But the matrices may not be necessarily symmetric due to the variable coefficients of the derivatives appearing in equation (5.1), therefore in order to solve (5.11), we use the Biconjugate Gradient Stabilized method (BiCGStab) [63] without any preconditioning.

5.2.4 Implementation on N-S equations:

The transient 3D incompressible N-S equations in non-dimensional form may be wriiten as

$$\frac{\partial u}{\partial t}+u\frac{\partial u}{\partial x}+v\frac{\partial u}{\partial y}+w\frac{\partial u}{\partial z}-\frac{1}{Re}\left(\frac{\partial^2 u}{\partial x^2}+\frac{\partial^2 u}{\partial y^2}+\frac{\partial^2 u}{\partial z^2}\right)=-\frac{\partial p}{\partial x}, \tag{5.12a}$$

$$\frac{\partial v}{\partial t}+u\frac{\partial v}{\partial x}+v\frac{\partial v}{\partial y}+w\frac{\partial v}{\partial z}-\frac{1}{Re}\left(\frac{\partial^2 v}{\partial x^2}+\frac{\partial^2 v}{\partial y^2}+\frac{\partial^2 v}{\partial z^2}\right)=-\frac{\partial p}{\partial y}, \tag{5.12b}$$

$$\frac{\partial w}{\partial t}+u\frac{\partial w}{\partial x}+v\frac{\partial w}{\partial y}+w\frac{\partial w}{\partial z}-\frac{1}{Re}\left(\frac{\partial^2 w}{\partial x^2}+\frac{\partial^2 w}{\partial y^2}+\frac{\partial^2 w}{\partial z^2}\right)=-\frac{\partial p}{\partial z}, \tag{5.12c}$$

$$\frac{\partial u}{\partial x}+\frac{\partial v}{\partial y}+\frac{\partial w}{\partial z}=0. \tag{5.13}$$

where t is the time, p is the pressure, $Re=\frac{U_0 L}{\nu}$ is the Reynolds number, L is some characteristic length, U_0 is some characteristic velocity and ν is the kinematic viscosity.

To solve this system numerically, we discretize (5.12) using (5.9) with $a=Re$, $p=Reu$, $q=Rev$, $r=Rew$, $e=0$ and f standing for either

$$-Re\frac{\partial p}{\partial x}, -Re\frac{\partial p}{\partial y} \text{ or } -Re\frac{\partial p}{\partial z}.$$

Since analytical expressions for p are unknown, the pressure gradients must be approximated numerically. To accomplish that, we use central difference approximations at the interior and standard one sided first order approximations at the boundaries. However, in order to obtain a fourth order fully compact

approximation, one can use the strategy applied in [56] for the gradient source term. Once this system is solved, we can differentiate the velocities with respect to x, y and z and add them to obtain the pressure Poisson equation (PPE) given as

$$\nabla^2 p = \xi \tag{5.14}$$

where

$$\begin{aligned}\xi = &- \left(uu_x + vu_y + wu_z\right)_x - \left(uv_x + vv_y + wv_z\right)_y - \left(uw_x + vw_y + ww_z\right)_z \\ &- D_t + \frac{1}{Re}(D_{xx} + D_{yy} + D_{zz})\end{aligned} \tag{5.15}$$

and

$$D = u_x + v_y + w_z$$

is the dilation at each grid point. PPE (5.14) has been solved by a numerous approaches [2, 6, 37, 51, 53, 60, 91, 110]. But the boundary conditions for pressure is not known explicitly and hence solving the PPE for p is an extremely strenuous task even for low Reynolds numbers and more frequently, some pressure correction strategies need to be applied to rectify the pressure values at each time step in such a way that the momentum equation becomes valid. Therefore we have adopted the modified compressibility technique proposed by Cortes and Miller [18]. In this approach, the continuity equation is modified as

$$\frac{p}{\lambda} + \left(\frac{\partial u}{\partial x} + \frac{\partial v}{\partial y} + \frac{\partial w}{\partial z}\right) = 0 \tag{5.16}$$

where λ is a small number. On computing pressure at each time level, momentum equations (5.12) are solved using (5.11) as described earlier and D is computed. If $|D|_{max}$ is less than a prescribed tolerance limit, one can move to the next time level; otherwise pressure is corrected as

$$p_{new} = p_{old} - \lambda D \tag{5.17}$$

The above procedure is repeated continuously until $|\nabla \cdot V|_{max}$ (where $V = (u, v, w)$) falls below a prescribed tolerance limit or the number of inner iteration equals to a pre-determined value. This criteria of controlling the dilation

value D will allow the method to satisfy the continuity equation (5.13) at each time level. Also, since an explicit expression is available for pressure, seeking boundary conditions for pressure is no longer a requirement. Thus implementation of this approach is not only faster than PPE approach, but is also very simple and straightforward.

5.3 Fundamental studies

This section encompasses the fundamental aspects of the proposed schemes viz. convergence analysis, dispersion-dissipation analysis and stability analysis. Let us discuss them one by one.

5.3.1 Convergence analysis:

Consider equation (5.1) with the convective coefficients p. q and r and the reactive coefficient e as constants. To perform the convergence analysis of the schemes assume $a = 1$ subject to the initial condition

$$\phi(x, y, z, 0) = \phi_0(x, y, z), \quad (x, y, z) \in \Omega \cup \partial\Omega \tag{5.18}$$

and with the boundary condition

$$\phi(x, y, z, t) = \text{constant}, \quad (x, y, z) \in \partial\Omega, \quad t > 0, \tag{5.19}$$

where $\phi_0(x, y, z)$ is a known smooth function and $\partial\Omega$ is the boundary of the finite domain Ω.

Thence as discussed in the previous section, our finite difference scheme for this problem is the one given by (5.8) but with constant coefficients.

Lemma 5.3.1. *There exists a lower bound $\mathcal{C}$ to all the coefficients appearing in equation (5.8) at all grid points, where $\mathcal{C}$ is a real number.*

Equivalently, there exists a real constant $\mathcal{C}$ such that $\mathcal{C} \lesssim V$, where V may be any of the coefficients appearing in equation (5.8).

Proof. Since all of the coefficients A, B, C, P, Q, R, D, E, F, H, K, L, M, N, O, S, T, U, G and W, appearing in equation (5.8) are real numbers, they have finite values, so the proof of the above lemma follows. □

Next, let us introduce some useful notations.

For the sake of our discussions in the current section, let us assume that $h = \triangle x = \triangle y = \triangle z$ and $\tau = \triangle t$.

Denote the grid points as (x_i, y_j, z_k), where $x_i = x_a + ih$, $y_j = y_a + jh$, $z_k = z_a + kh$ and $[x_a, x_b] \times [y_a, y_b] \times [z_a, z_b]$ is the domain under consideration with the index sets given as

$I_x = \{i | i = 0, 1, 2, \ldots, I\}$, $I_x^o = \{i | i = 1, 2, \ldots, I-1\}$, where $I = (x_b - x_a)/h + 1$,

$I_y = \{j | j = 0, 1, 2, \ldots, J\}$,

$I_y^o = \{j | j = 1, 2, \ldots, J-1\}$, where $J = (y_b - y_a)/h + 1$,

$I_z = \{k | k = 0, 1, 2, \ldots, K\}$,

$I_z^o = \{k | k = 1, 2, \ldots, K-1\}$, where $K = (z_b - z_a)/h + 1$.

For grid functions of the form $\phi = \{\phi_{ijk}^n | (i, j, k) \in I_x \times I_y \times I_z, n = 0, 1, 2, \ldots, N\}$ (N is the total number of time steps), we have the following finite difference operators:

$\delta_x \phi_{ijk}^n = \frac{1}{2h}(\phi_{i+1jk}^n - \phi_{i-1jk}^n), \quad i \neq I;$

$\delta_x^2 \phi_{ijk}^n = \frac{1}{h^2}(\phi_{i+1jk}^n - 2\phi_{ijk}^n + \phi_{i-1jk}^n), \quad i \in I_x^o;$

$\delta_y \phi_{ijk}^n = \frac{1}{2h}(\phi_{ij+1k}^n - \phi_{ij-1k}^n), \quad j \neq J;$

$\delta_y^2 \phi_{ijk}^n = \frac{1}{h^2}(\phi_{ij+1k}^n - 2\phi_{ijk}^n + \phi_{ij-1k}^n), \quad j \in I_y^o;$

$\delta_z \phi_{ijk}^n = \frac{1}{2h}(\phi_{ijk+1}^n - \phi_{ijk-1}^n), \quad k \neq K;$

$\delta_z^2 \phi_{ijk}^n = \frac{1}{h^2}(\phi_{ijk+1}^n - 2\phi_{ijk}^n + \phi_{ijk-1}^n), \quad k \in I_z^o;$

$\nabla_h \phi_{ijk}^n = (\delta_x, \delta_y, \delta_z)\phi_{ijk}^n, \quad \nabla_{h^2} \phi_{ijk}^n = (\delta_x^2, \delta_y^2, \delta_z^2)\phi_{ijk}^n, \quad i \neq I, j \neq J, k \neq K;$

$\nabla_{h^2}^2 \phi_{ijk}^n = (\delta_x^2\delta_y^2, \delta_y^2\delta_z^2, \delta_z^2\delta_x^2)\phi_{ijk}^n, \quad i \neq I, j \neq J, k \neq K;$

$\delta_t^+ \phi_{ijk}^n = \frac{1}{\tau}(\phi_{ijk}^{n+1} - \phi_{ijk}^n), \quad n \neq N; \quad \delta_t \phi_{ijk}^n = \frac{1}{2\tau}(\phi_{ijk}^{n+1} - \phi_{ijk}^{n-1}), \quad n \neq 0, N;$

$\delta_t^2 \phi_{ijk}^n = \frac{1}{\tau^2}(\phi_{ijk}^{n+1} - 2\phi_{ijk}^n + \phi_{ijk}^{n-1}), \quad n \neq 0, N;$

$\mathcal{A}_h \phi_{ijk}^n = \{1 + \frac{h^2}{12}(\delta_x^2 - p\delta_x + \delta_y^2 - q\delta_y + \delta_z^2 - r\delta_z)\}\phi_{ijk}^n; \; i \in I_x^o, j \in I_y^o, k \in I_z^o.$

Further, let Φ^n_{ijk} be the numerical approximation of $\phi(x_i, y_j, z_k, t_n)$, then utilizing the average parameter ς in equation (5.8), coefficients of the form $A\delta_x^2\phi^n_{ijk}$ can be replaced by $\varsigma A\delta_x^2\phi^{n+1}_{ijk} + (1-\varsigma)A\delta_x^2\phi^n_{ijk}$. Likewise, we replace for the other terms as well.

With these replacements, the finite difference scheme can now be written as

$$\begin{aligned}
& \mathcal{A}_h\delta_t^+\Phi^n_{ijk} + (-\varsigma A)\delta_x^2\Phi^{n+1}_{ijk} - \{(1-\varsigma)A\}\delta_x^2\Phi^n_{ijk} + (-\varsigma B)\delta_y^2\Phi^{n+1}_{ijk} \\
- & \{(1-\varsigma)B\}\delta_y^2\Phi^n_{ijk} + (-\varsigma C)\delta_z^2\Phi^{n+1}_{ijk} - \{(1-\varsigma)C\}\delta_z^2\Phi^n_{ijk} + (\varsigma P)\delta_x\Phi^{n+1}_{ijk} \\
- & \{(\varsigma-1)P\}\delta_x\Phi^n_{ijk} + (\varsigma Q)\delta_y\Phi^{n+1}_{ijk} - \{(\varsigma-1)Q\}\delta_y\Phi^n_{ijk} + (\varsigma R)\delta_z\Phi^{n+1}_{ijk} \\
- & \{(\varsigma-1)R\}\delta_z\Phi^n_{ijk} + (-\varsigma D)\delta_x\delta_y\Phi^{n+1}_{ijk} - \{(1-\varsigma)D\}\delta_x\delta_y\Phi^n_{ijk} \\
+ & (-\varsigma E)\delta_y\delta_z\Phi^{n+1}_{ijk} - \{(1-\varsigma)E\}\delta_y\delta_z\Phi^n_{ijk} + (-\varsigma F)\delta_z\delta_x\Phi^{n+1}_{ijk} \\
- & \{(1-\varsigma)F\}\delta_z\delta_x\Phi^n_{ijk} + (\varsigma H)\delta_x\delta_y^2\Phi^{n+1}_{ijk} - \{(\varsigma-1)H\}\delta_x\delta_y^2\Phi^n_{ijk} \\
+ & (\varsigma K)\delta_x^2\delta_y\Phi^{n+1}_{ijk} - \{(\varsigma-1)K\}\delta_x^2\delta_y\Phi^n_{ijk} + (-\varsigma L)\delta_x^2\delta_y^2\Phi^{n+1}_{ijk} \\
- & \{(1-\varsigma)L\}\delta_x^2\delta_y^2\Phi^n_{ijk} + (\varsigma M)\delta_y\delta_z^2\Phi^{n+1}_{ijk} - \{(\varsigma-1)M\}\delta_y\delta_z^2\Phi^n_{ijk} \\
+ & (\varsigma N)\delta_y^2\delta_z\Phi^{n+1}_{ijk} - \{(\varsigma-1)N\}\delta_y^2\delta_z\Phi^n_{ijk} + (-\varsigma O)\delta_y^2\delta_z^2\Phi^{n+1}_{ijk} \\
- & \{(1-\varsigma)O\}\delta_y^2\delta_z^2\Phi^n_{ijk} + (\varsigma S)\delta_x^2\delta_z\Phi^{n+1}_{ijk} - \{(\varsigma-1)S\}\delta_x^2\delta_z\Phi^n_{ijk} \\
+ & (\varsigma T)\delta_x\delta_z^2\Phi^{n+1}_{ijk} - \{(\varsigma-1)T\}\delta_x\delta_z^2\Phi^n_{ijk} + (-\varsigma U)\delta_z^2\delta_x^2\Phi^{n+1}_{ijk} \\
- & \{(1-\varsigma)U\}\delta_z^2\delta_x^2\Phi^n_{ijk} + (\varsigma G)\Phi^{n+1}_{ijk} - \{(\varsigma-1)G\}\Phi^n_{ijk} = W
\end{aligned} \tag{5.20}$$

Define the initial approximations as

$$\Phi^0_{ijk} = \phi_0(x_i, y_j, z_k), \tag{5.21}$$

where $i \in I_x, j \in I_y, k \in I_z$ and $\phi_0(x_i, y_j, z_k) = \phi(x_i, y_j, z_k, 0)$

Also consider that,

$$\Phi^1_{ijk} = \phi_0(x_i, y_j, z_k) + \tau\phi_1(x_i, y_j, z_k),\ (i,j,k) \in I_x \times I_y \times I_z, \tag{5.22}$$

where $\phi^n_{ijk} = \phi(x_i, y_j, z_k, t_n)$ and $\phi_1(x_i, y_j, z_k) = \phi_t(x_i, y_j, z_k, 0)$.

Remark 5.3.2. By virtue of lemma 5.3.1, it follows that there exists a real constant $\mathcal{K}$ such that $\mathcal{K} \lesssim |\varsigma|\xi^{n+1}$ and $\mathcal{K} \lesssim |\varsigma - 1|\xi^{n}$, where ξ_{ijk} can be either of the coefficients A, B, C, P, Q, R, D, E, F, H, K, L, M, N, O, S, T, U or G.

Now, let us consider the space, $\mathcal{S} := \{\phi = \phi_{ijk} | (i,j,k) \in I_x \times I_y \times I_z\} \subseteq \mathbb{R}^{(I+1)\times(J+1)\times(K+1)}$ and the inner product and discrete norms defined over $\mathcal{S}$ as $\langle \phi_1,\ \phi_2 \rangle = h^3 \sum_{i=1}^{I-1} \sum_{j=1}^{J-1} \sum_{k=1}^{K-1} (\phi_1)_{ijk} (\phi_2)_{ijk}$, where $\phi_1, \phi_2 \in \mathcal{S}$,

$$
\begin{aligned}
\|\phi\| &= \langle \phi,\ \phi \rangle^{\frac{1}{2}}, \\
\|\delta_x \phi\| &= \left(8h^3 \sum_{i=0}^{I-1} \sum_{j=1}^{J-1} \sum_{k=1}^{K-1} |\delta_x \phi_{ijk}|^2 \right)^{\frac{1}{2}}, & \|\phi\|_\infty &= \max_{(i,j,k) \in I_x \times I_y \times I_z} |\phi_{ijk}|, \\
\|\delta_z \phi\| &= \left(8h^3 \sum_{i=1}^{I-1} \sum_{j=1}^{J-1} \sum_{k=0}^{K-1} |\delta_z \phi_{ijk}|^2 \right)^{\frac{1}{2}}, & \|\delta_y \phi\| &= \left(8h^3 \sum_{i=1}^{I-1} \sum_{j=0}^{J-1} \sum_{k=1}^{K-1} |\delta_y \phi_{ijk}|^2 \right)^{\frac{1}{2}}, \\
& & \|\nabla_h \phi\| &= \left(\|\delta_x \phi\|^2 + \|\delta_y \phi\|^2 + \|\delta_z \phi\|^2 \right)^{\frac{1}{2}}, \\
\|\delta_x^2 \phi\| &= \left(h^6 \sum_{i=0}^{I-1} \sum_{j=1}^{J-1} \sum_{k=1}^{K-1} |\delta_x^2 \phi_{ijk}|^2 \right)^{\frac{1}{2}}, & \|\delta_y^2 \phi\| &= \left(h^6 \sum_{i=1}^{I-1} \sum_{j=0}^{J-1} \sum_{k=1}^{K-1} |\delta_y^2 \phi_{ijk}|^2 \right)^{\frac{1}{2}}, \\
\|\delta_z^2 \phi\| &= \left(h^6 \sum_{i=1}^{I-1} \sum_{j=1}^{J-1} \sum_{k=0}^{K-1} |\delta_z^2 \phi_{ijk}|^2 \right)^{\frac{1}{2}}, & \|\nabla_{h^2} \phi\| &= \left(\|\delta_x^2 \phi\|^2 + \|\delta_y^2 \phi\|^2 + \|\delta_z^2 \phi\|^2 \right)^{\frac{1}{2}}, \\
\|\delta_x^2 \delta_y^2 \phi\| &= \left(h^{12} \sum_{i=0}^{I-1} \sum_{j=1}^{J-1} \sum_{k=1}^{K-1} |\delta_x^2 \delta_y^2 \phi_{ijk}|^2 \right)^{\frac{1}{2}}, & \|\delta_y^2 \delta_z^2 \phi\| &= \left(h^{12} \sum_{i=1}^{I-1} \sum_{j=0}^{J-1} \sum_{k=1}^{K-1} |\delta_y^2 \delta_z^2 \phi_{ijk}|^2 \right)^{\frac{1}{2}}, \\
\|\delta_z^2 \delta_x^2 \phi\| &= \left(h^{12} \sum_{i=1}^{I-1} \sum_{j=1}^{J-1} \sum_{k=0}^{K-1} |\delta_z^2 \delta_x^2 \phi_{ijk}|^2 \right)^{\frac{1}{2}}, & \|\nabla_{h^2}^2 \phi\| &= \left(\|\delta_x^2 \delta_y^2 \phi\|^2 + \|\delta_y^2 \delta_z^2 \phi\|^2 + \|\delta_z^2 \delta_x^2 \phi\|^2 \right)^{\frac{1}{2}}.
\end{aligned}
$$

Lemma 5.3.3. *If ϕ^{n-1}, ϕ^n, $\phi^{n+1} \in \mathcal{S}$, then we have*

$$
\frac{1}{\tau} \left(\langle \mathcal{A}_h \phi^{n+1},\ \phi^{n+1} \rangle - \langle \mathcal{A}_h \phi^n,\ \phi^n \rangle \right) \leq \langle \mathcal{A}_h \delta_t^+ \phi^n,\ \delta_t^+ \phi^n \rangle \tag{5.23}
$$

Proof. Since,

$$\begin{aligned}\langle \mathcal{A}_h\delta_t^+\phi^n,\ \delta_t^+\phi^n\rangle &= \langle \mathcal{A}_h\frac{\phi^{n+1}-\phi^n}{\tau},\ \frac{\phi^{n+1}-\phi^n}{\tau}\rangle\\ &= \frac{1}{\tau^2}\langle \mathcal{A}_h(\phi^{n+1}-\phi^n),\ (\phi^{n+1}-\phi^n)\rangle[\because \mathcal{A}_h \text{ is linear}]\\ &= \frac{1}{\tau^2}\{\langle \mathcal{A}_h\phi^{n+1},\ \phi^{n+1}\rangle - \langle \mathcal{A}_h\phi^{n+1},\ \phi^n\rangle\\ &\qquad - \langle \mathcal{A}_h\phi^n,\ \phi^{n+1}\rangle + \langle \mathcal{A}_h\phi^n,\ \phi^n\rangle\}\end{aligned}$$

Similarly, we have

$$\begin{aligned}\langle \mathcal{A}_h\delta_t^+\phi^{n-1},\ \delta_t^+\phi^{n-1}\rangle = \frac{1}{\tau^2}\{&\langle \mathcal{A}_h\phi^n,\ \phi^n\rangle - \langle \mathcal{A}_h\phi^n,\ \phi^{n-1}\rangle\\ &- \langle \mathcal{A}_h\phi^{n-1},\ \phi^n\rangle + \langle \mathcal{A}_h\phi^{n-1},\ \phi^{n-1}\rangle\}\end{aligned}$$

Therefore, using the definition of $\mathcal{A}_h$, property of symmetry of $\langle \phi^n,\ \phi^{n+1}\rangle$ and considering the unit vectors as $\frac{\phi}{\|\phi\|^2}$, the proof of the lemma follows. □

In order to analyse convergence of the difference scheme, let us define the local truncation error $r^n \in \mathcal{S}$ as follows

$$\begin{aligned}r_{ijk}^n &= \mathcal{A}_h\delta_t^+\phi_{ijk}^n + (-\varsigma A)\delta_x^2\phi_{ijk}^{n+1} - \{(1-\varsigma)A\}\delta_x^2\phi_{ijk}^n + (-\varsigma B)\delta_y^2\phi_{ijk}^{n+1}\\ &- \{(1-\varsigma)B\}\delta_y^2\phi_{ijk}^n + (-\varsigma C)\delta_z^2\phi_{ijk}^{n+1} - \{(1-\varsigma)C\}\delta_z^2\phi_{ijk}^n + (\varsigma P)\delta_x\phi_{ijk}^{n+1}\\ &- \{(\varsigma-1)P\}\delta_x\phi_{ijk}^n + (\varsigma Q)\delta_y\phi_{ijk}^{n+1} - \{(\varsigma-1)Q\}\delta_y\phi_{ijk}^n + (\varsigma R)\delta_z\phi_{ijk}^{n+1}\\ &- \{(\varsigma-1)R\}\delta_z\phi_{ijk}^n + (-\varsigma D)\delta_x\delta_y\phi_{ijk}^{n+1} - \{(1-\varsigma)D\}\delta_x\delta_y\phi_{ijk}^n + (-\varsigma E)\delta_y\delta_z\phi_{ijk}^{n+1}\\ &- \{(1-\varsigma)E\}\delta_y\delta_z\phi_{ijk}^n + (-\varsigma F)\delta_z\delta_x\phi_{ijk}^{n+1} - \{(1-\varsigma)F\}\delta_z\delta_x\phi_{ijk}^n + (\varsigma H)\delta_x\delta_y^2\phi_{ijk}^{n+1}\\ &- \{(\varsigma-1)H\}\delta_x\delta_y^2\phi_{ijk}^n + (\varsigma K)\delta_x^2\delta_y\phi_{ijk}^{n+1} - \{(\varsigma-1)K\}\delta_x^2\delta_y\phi_{ijk}^n + (-\varsigma L)\delta_x^2\delta_y^2\phi_{ijk}^{n+1}\\ &- \{(1-\varsigma)L\}\delta_x^2\delta_y^2\phi_{ijk}^n + (\varsigma M)\delta_y\delta_z^2\phi_{ijk}^{n+1} - \{(\varsigma-1)M\}\delta_y\delta_z^2\phi_{ijk}^n + (\varsigma N)\delta_y^2\delta_z\phi_{ijk}^{n+1}\\ &- \{(\varsigma-1)N\}\delta_y^2\delta_z\phi_{ijk}^n + (-\varsigma O)\delta_y^2\delta_z^2\phi_{ijk}^{n+1} - \{(1-\varsigma)O\}\delta_y^2\delta_z^2\phi_{ijk}^n + (\varsigma S)\delta_x^2\delta_z\phi_{ijk}^{n+1}\\ &- \{(\varsigma-1)S\}\delta_x^2\delta_z\phi_{ijk}^n + (\varsigma T)\delta_x\delta_z^2\phi_{ijk}^{n+1} - \{(\varsigma-1)T\}\delta_x\delta_z^2\phi_{ijk}^n + (-\varsigma U)\delta_z^2\delta_x^2\phi_{ijk}^{n+1}\\ &- \{(1-\varsigma)U\}\delta_z^2\delta_x^2\phi_{ijk}^n + (\varsigma G)\phi_{ijk}^{n+1} - \{(\varsigma-1)G\}\phi_{ijk}^n + W,\end{aligned} \tag{5.24}$$

where $(i,j,k)\in I_x^o \times I_y^o \times I_z^o$, and $1 \le n \le N-1$.

Using Taylor Series expansion, we have

$$r^o_{ijk} = \frac{\phi^1_{ijk} - \phi_0(x_i, y_j, z_k)}{\tau} - \phi_1(x_i, y_j, z_k), \quad \forall (i,j,k) \in I^o_x \times I^o_y \times I^o_z \tag{5.25}$$

Also we have the following

$$|\delta^+_x r^0_{ijk}| \lesssim \tau^2, \quad |\delta^+_y r^0_{ijk}| \lesssim \tau^2, \quad |\delta^+_z r^0_{ijk}| \lesssim \tau^2, \quad |r^n_{ijk}| \lesssim \tau^2, \tag{5.26}$$

where $(i,j,k) \in I^o_x \times I^o_y \times I^o_z$ and $0 \leq n \leq N$.

Let the error function $e^n \in \mathcal{S}$ be defined as

$$e^n_{ijk} = \phi^n_{ijk} - \Phi^n_{ijk}, \quad (i,j,k) \in I_x \times I_y \times I_z, \quad 0 \leq n \leq N. \tag{5.27}$$

Lemma 5.3.4. *For any grid function $\phi \in \mathcal{S}$, we have*

$$|\langle \mathcal{A}_h \phi, \ \phi \rangle| \leq \|\phi\|^2 \tag{5.28}$$

Proof. From the defintion of $\mathcal{A}_h \phi$ and use of diiferential operators, it follows that

$$|\langle \mathcal{A}_h \phi, \ \phi \rangle| \leq |\langle \phi, \ \phi \rangle|$$

Now, the proof of the above lemma follows from the definition of inner product and Cauchy-Schwarz inequality. □

Theorem 5.3.5. *If $\phi \in C^{6,6,6,3}([x_a, x_b] \times [y_a, y_b] \times [z_a, z_b] \times [0, T])$, and if h and τ are sufficiently small, then the solution of the finite difference problem (5.20)-(5.21)-(5.22) converges to the solution of the initial continuous problem (5.1)-(5.18)-(5.19) with order $O(\tau^2 + h^4)$ in the discrete L^2 norm for Φ^n, i.e.*

$$\|e^n\| + \|\nabla_h e^n\| + \|\nabla_{h^2} e^n\| + \|\nabla^2_{h^2} e^n\| \lesssim \tau^2 + h^4, \quad 0 \leq n \leq N. \tag{5.29}$$

Proof. Let us adopt an induction argument to proof that (5.29) holds for every

non-negative integer less than N. From equation (5.20) and remark (5.3.2), it is obvious that (5.29) holds for $n = 0$. For $(i, j, k) \in I_x^o \times I_y^o \times I_z^o$, we have

$$|e_{ijk}^1| = |\phi_{ijk}^1 - \Phi_{ijk}^1| = |\tau r_{ijk}^0| \lesssim \tau^3, \;\; |\delta_t^+ e_{ijk}^0| = |r_{ijk}^0| \lesssim \tau^2, \;\; \text{and} \tag{5.30a}$$

$$|\delta_x^+ e_{ijk}^1| \lesssim \tau |\delta_x^+ r_{ijk}^0| \lesssim \tau^3 \lesssim \tau^2, \tag{5.30b}$$

Likewise, we have

$$|\delta_y^+ e_{ijk}^1| \lesssim \tau^2 \text{ and } |\delta_z^+ e_{ijk}^1| \lesssim \tau^2 \tag{5.30c}$$

Equation (5.30) clearly implies that (5.29) holds for $n = 1$. Using the triangle inequality, when τ and h are sufficiently small, we have

$$|\Phi_{ijk}^1| \leq |\phi_{ijk}^1| + |e_{ijk}^1| \leq C_o + C(\tau^2 + h^2) \leq 1 + C_o, \;\; (i, j, k) \in I_x \times I_y \times I_z \tag{5.31}$$

where $C_o = \max\limits_{0 \leq t \leq T} \|\phi(\cdot, \cdot, \cdot, t)\|_{L^\infty(\Omega)}$.

We assume that (5.29) is valid for $0 \leq n \leq m - 1 < N - 1$, then we will show that it is still valid for $n = m$. Now, adding (5.20) and (5.24), we have the following error equation for the error function $e^n \in \mathcal{S}$

$$\begin{aligned}
&\mathcal{A}_h \delta_t^+ e_{ijk}^n + (-\varsigma A)\delta_x^2 e_{ijk}^{n+1} - \{(1-\varsigma)A\}\delta_x^2 e_{ijk}^n + (-\varsigma B)\delta_y^2 e_{ijk}^{n+1} \\
- \;& \{(1-\varsigma)B\}\delta_y^2 e_{ijk}^n + (-\varsigma C)\delta_z^2 e_{ijk}^{n+1} - \{(1-\varsigma)C\}\delta_z^2 e_{ijk}^n + (\varsigma P)\delta_x e_{ijk}^{n+1} \\
- \;& \{(\varsigma-1)P\}\delta_x e_{ijk}^n + (\varsigma Q)\delta_y e_{ijk}^{n+1} - \{(\varsigma-1)Q\}\delta_y e_{ijk}^n + (\varsigma R)\delta_z e_{ijk}^{n+1} \\
- \;& \{(\varsigma-1)R\}\delta_z e_{ijk}^n + (-\varsigma D)\delta_x\delta_y e_{ijk}^{n+1} - \{(1-\varsigma)D\}\delta_x\delta_y e_{ijk}^n + (-\varsigma E)\delta_y\delta_z e_{ijk}^{n+1} \\
- \;& \{(1-\varsigma)E\}\delta_y\delta_z e_{ijk}^n + (-\varsigma F)\delta_z\delta_x e_{ijk}^{n+1} - \{(1-\varsigma)F\}\delta_z\delta_x e_{ijk}^n + (\varsigma H)\delta_x\delta_y^2 e_{ijk}^{n+1} \\
- \;& \{(\varsigma-1)H\}\delta_x\delta_y^2 e_{ijk}^n + (\varsigma K)\delta_x^2\delta_y e_{ijk}^{n+1} - \{(\varsigma-1)K\}\delta_x^2\delta_y e_{ijk}^n + (-\varsigma L)\delta_x^2\delta_y^2 e_{ijk}^{n+1} \\
- \;& \{(1-\varsigma)L_{ijk}^n\}\delta_x^2\delta_y^2 e_{ijk}^n + (\varsigma M)\delta_y\delta_z^2 e_{ijk}^{n+1} - \{(\varsigma-1)M\}\delta_y\delta_z^2 e_{ijk}^n + (\varsigma N)\delta_y^2\delta_z e_{ijk}^{n+1} \\
- \;& \{(\varsigma-1)N\}\delta_y^2\delta_z e_{ijk}^n + (-\varsigma O)\delta_y^2\delta_z^2 e_{ijk}^{n+1} - \{(1-\varsigma)O\}\delta_y^2\delta_z^2 e_{ijk}^n + (\varsigma S)\delta_x^2\delta_z e_{ijk}^{n+1} \\
- \;& \{(\varsigma-1)S\}\delta_x^2\delta_z e_{ijk}^n + (\varsigma T)\delta_x\delta_z^2 e_{ijk}^{n+1} - \{(\varsigma-1)T\}\delta_x\delta_z^2 e_{ijk}^n + (-\varsigma U)\delta_z^2\delta_x^2 e_{ijk}^{n+1} \\
- \;& \{(1-\varsigma)U\}\delta_z^2\delta_x^2 e_{ijk}^n + (\varsigma G)e_{ijk}^{n+1} - \{(\varsigma-1)G\}e_{ijk}^n = r_{ijk}^n, \;\; (i, j, k) \in I_x^o \times I_y^o \times I_z^o
\end{aligned}$$

Assuming τ and h to be sufficiently small and considering (5.29) for $1 \leq n \leq$

$m-1$, we have the following estimate

$$\|\Phi^n\|_\infty \leq \|\phi^n\|_\infty + \|e^n\|_\infty \leq C_o + 1, \;\; 1 \leq n \leq m-1. \tag{5.32}$$

Let us consider the case when $\varsigma = 0.5$. Throughout this section, we will consider the case only where $\varsigma = 0.5$.

Now, computing the inner product of (5.32) with $\delta_t^+ e^n$ and considering remark (5.3.2) and lemma (5.3.3), we have

$$\begin{aligned}
&\frac{1}{\tau}(\langle \mathcal{A}_h e^{n+1},\ e^{n+1}\rangle - \frac{1}{\tau}\langle \mathcal{A}_h e^n,\ e^n\rangle + \mathcal{K}\langle(\delta_x^2+\delta_y^2+\delta_z^2+\delta_x+\delta_y+\delta_z+\delta_x\delta_y+\delta_y\delta_z \\
&+\delta_z\delta_x+\delta_x\delta_y^2+\delta_x^2\delta_y+\delta_x^2\delta_y^2+\delta_y\delta_z^2+\delta_y^2\delta_z+\delta_y^2\delta_z^2+\delta_z\delta_x^2+\delta_z^2\delta_x+\delta_z^2\delta_x^2+1)e^{n+1}, \\
&\delta_t^+ e^n\rangle \leq \langle r^n,\ \delta_t^+ e^n\rangle + \mathcal{K}\langle(\delta_x^2+\delta_y^2+\delta_z^2+\delta_x+\delta_y+\delta_z+\delta_x\delta_y+\delta_y\delta_z+\delta_z\delta_x \\
&+\delta_x\delta_y^2+\delta_x^2\delta_y+\delta_x^2\delta_y^2+\delta_y\delta_z^2+\delta_y^2\delta_z+\delta_y^2\delta_z^2+\delta_z\delta_x^2+\delta_z^2\delta_x+\delta_z^2\delta_x^2+1)e^n,\ \delta_t^+ e^n\rangle
\end{aligned} \tag{5.33}$$

Upon simplifying and transposing, we have

$$\begin{aligned}
&(\langle \mathcal{A}_h e^{n+1},\ e^{n+1}\rangle + \mathcal{K}\tau^2(\|\delta_x^2 e^{n+1}\|^2 + \|\delta_y^2 e^{n+1}\|^2 + \|\delta_z^2 e^{n+1}\|^2 + \|\delta_x e^{n+1}\|^2 \\
&+ \|\delta_y e^{n+1}\|^2 + \|\delta_z e^{n+1}\|^2 + \|\delta_x\delta_y e^{n+1}\|^2 + \|\delta_y\delta_z e^{n+1}\|^2 + \|\delta_z\delta_x e^{n+1}\|^2 \\
&+ \|\delta_x\delta_y^2 e^{n+1}\|^2 + \|\delta_x^2\delta_y e^{n+1}\|^2 + \|\delta_x^2\delta_y^2 e^{n+1}\|^2 + \|\delta_y\delta_z^2 e^{n+1}\|^2 + \|\delta_y^2\delta_z e^{n+1}\|^2 \\
&+ \|\delta_y^2\delta_z^2 e^{n+1}\|^2 + \|\delta_z\delta_x^2 e^{n+1}\|^2 + \|\delta_z^2\delta_x e^{n+1}\|^2 + \|\delta_z^2\delta_x^2 e^{n+1}\|^2 + \|e^{n+1}\|^2) \\
&\leq\ \tau^2(\|r^n\|^2 - \|e^{n+1}\|^2 + \|e^n\|^2) + \mathcal{K}\tau^2(\|\delta_x^2 e^n\|^2 + \|\delta_y^2 e^n\|^2 \\
&+ \|\delta_z^2 e^n\|^2 + \|\delta_x e^n\|^2 + \|\delta_y e^n\|^2 + \|\delta_z e^n\|^2 + \|\delta_x\delta_y e^n\|^2 + \|\delta_y\delta_z e^n\|^2 + \|\delta_z\delta_x e^n\|^2 \\
&+ \|\delta_x\delta_y^2 e^n\|^2 + \|\delta_x^2\delta_y e^n\|^2 + \|\delta_x^2\delta_y^2 e^n\|^2 + \|\delta_y\delta_z^2 e^n\|^2 + \|\delta_y^2\delta_z e^n\|^2 + \|\delta_y^2\delta_z^2 e^n\|^2 \\
&+ \|\delta_z\delta_x^2 e^n\|^2 + \|\delta_z^2\delta_x e^n\|^2 + \|\delta_z^2\delta_x^2 e^n\|^2 + \|e^n\|^2) + (\langle \mathcal{A}_h e^n,\ e^n\rangle
\end{aligned} \tag{5.34}$$

Define G^n as follows:

$$\begin{aligned}
G^n \;=\; &(\langle \mathcal{A}_h e^n,\ e^n\rangle + \tau^2\|e^n\|^2 + \mathcal{K}\tau^2(\|\delta_x^2 e^n\|^2 + \|\delta_y^2 e^n\|^2 + \|\delta_z^2 e^n\|^2 + \|\delta_x e^n\|^2 \\
+\; &\|\delta_y e^n\|^2 + \|\delta_z e^n\|^2 + \|\delta_x\delta_y e^n\|^2 + \|\delta_y\delta_z e^n\|^2 + \|\delta_z\delta_x e^n\|^2 + \|\delta_x\delta_y^2 e^n\|^2 \\
+\; &\|\delta_x^2\delta_y e^n\|^2 + \|\delta_x^2\delta_y^2 e^n\|^2 + \|\delta_y\delta_z^2 e^n\|^2 + \|\delta_y^2\delta_z e^n\|^2 + \|\delta_y^2\delta_z^2 e^n\|^2 + \|\delta_z\delta_x^2 e^n\|^2 \\
+\; &\|\delta_z^2\delta_x e^n\|^2 + \|\delta_z^2\delta_x^2 e^n\|^2 + \|e^n\|^2),\;\; 0 \leq n \leq m-1
\end{aligned} \tag{5.35}$$

Then equation (5.34) can be written as

$$G^{n+1} - G^n \lesssim \tau^2(\|r^n\|^2) + \mathcal{K}\tau^2(G^{n+1} + G^n),\ 0 \leq n < m-1. \tag{5.36}$$

This together with Gronwall's inequality [22, 38] gives

$$G^{n+1} \lesssim [G^0 + \tau^2 \sum_{l=1}^{n+1}(\|r^l\|^2)]e^{4CT}. \tag{5.37}$$

Equation (5.37), concurrently with lemma 5.3.4 and equation (5.30) gives the following estimates

$$\|e^m\| + \|\nabla_h e^m\| + \|\nabla_{h^2} e^m\| + \|\nabla^2_{h^2} e^m\| + \text{ some other terms } \lesssim \tau^2 + h^4. \tag{5.38}$$

which ultimately shows that, by principle of mathematical induction, we have

$$\|e^n\| + \|\nabla_h e^n\| + \|\nabla_{h^2} e^n\| + \|\nabla^2_{h^2} e^n\| \lesssim \tau^2 + h^4,\ \ 0 \leq n \leq N. \tag{5.39}$$

This completes the proof. □

5.3.2 Dispersion-dissipation analysis:

To discuss the dispersion and dissipation characteristics of the proposed schemes, consider the model unsteady convection-diffusion-reaction equation in one-dimension with a homogeneous source term

$$\phi_t + U\phi_x - K\phi_{xx} + C\phi = 0 \tag{5.40}$$

Subject to initial condition $\phi(x,0) = e^{ik_m x}(i = \sqrt{-1})$, it is easy to verify that (5.40) has a solution of the form

$$\phi(x,t) = e^{-(Kk_m^2 + C)t} e^{ik_m(x-Ut)} \tag{5.41}$$

where k_m is the wave number.

Applying the $O(\triangle t^2, h^4)$ approximation (keeping $\varsigma = 0.5$) discussed in the previous section to the model equation (5.40), we have

$$\left[1+\left(\frac{h^2}{12}-\frac{K\triangle t}{2}\right)\left(\delta_x^2-\frac{U}{K}\delta_x\right)+\frac{C\triangle t}{2}\right]\phi_i^{n+1}-\frac{h^2\triangle t}{24}\left[\left(\frac{U^2}{K}-C\right)\delta_x^2+\frac{UC}{K}\delta_x\right]\phi_i^{n+1}$$
$$=\left[1+\left(\frac{h^2}{12}+\frac{K\triangle t}{2}\right)\left(\delta_x^2-\frac{U}{K}\delta_x\right)-\frac{C\triangle t}{2}\right]\phi_i^{n}+\frac{h^2\triangle t}{24}\left[\left(\frac{U^2}{K}-C\right)\delta_x^2+\frac{UC}{K}\delta_x\right]\phi_i^{n}$$

After discretization, this can be compactly written as

$$A_1\phi_{i-1}^{n+1}+A_2\phi_i^{n+1}+A_3\phi_{i+1}^{n+1}=a_1\phi_{i-1}^{n}+a_2\phi_i^{n}+a_3\phi_{i+1}^{n} \tag{5.42}$$

where

$$A_1=\frac{1}{12}-\frac{\nu}{2Pe}+\frac{Pe}{24}-\frac{\nu}{4}-\frac{Pe\nu}{24}+\frac{R\nu}{24}+\frac{PeR\nu}{48}$$
$$A_2=\frac{5}{6}+\frac{\nu}{Pe}+\frac{Pe\nu}{12}+\frac{5R\nu}{12}$$
$$A_3=\frac{1}{12}-\frac{\nu}{2Pe}-\frac{Pe}{24}+\frac{\nu}{4}-\frac{Pe\nu}{24}+\frac{R\nu}{24}-\frac{PeR\nu}{48}$$
$$a_1=\frac{1}{12}+\frac{\nu}{2Pe}+\frac{Pe}{24}+\frac{\nu}{4}+\frac{Pe\nu}{24}-\frac{R\nu}{24}-\frac{PeR\nu}{48}$$
$$a_2=\frac{5}{6}-\frac{\nu}{Pe}-\frac{Pe\nu}{12}-\frac{5R\nu}{12}$$
$$a_3=\frac{1}{12}+\frac{\nu}{2Pe}-\frac{Pe}{24}-\frac{\nu}{4}+\frac{Pe\nu}{24}-\frac{R\nu}{24}+\frac{PeR\nu}{48}$$

Here $\nu=\frac{U\triangle t}{h}$ is the Courant number, $R=\frac{Ch}{U}$ and $Pe=\frac{Uh}{K}$ is the Peclet number. Since the amplitude and phase errors have been introduced because of the discretization, the exact solution of (5.42) is assumed to take the form as described in [98] as

$$\phi(x,t)=e^{-(Kk_m^2+C)\frac{k_r}{\beta^2}t}e^{ik_m(x-U\frac{k_i}{\beta}t)} \tag{5.43}$$

where $\beta=k_mh$ is the modified wave number.

The amplitude and phase errors can now be measured with the help of k_r and k_i respectively. We can analyze the dispersive and dissipative characteristics of the scheme by substituting (5.43) in (5.42) for ϕ_i and $\phi_{i\pm1}$.

On simplifying, the values of k_r and k_i may be obtained as

$$k_r = -\frac{P}{\nu\{(1/Pe) + (R/\beta^2)\}}, \tag{5.44}$$

$$k_i = \frac{Q}{\nu} \tag{5.45}$$

where

$$P = ln\left[\sqrt{\left(\frac{F_1A - F_2B}{A^2+B^2}\right)^2 + \left(\frac{F_1B + F_2A}{A^2+B^2}\right)^2}\right] \tag{5.46}$$

$$Q = tan^{-1}\left(\frac{F_1B + F_2A}{F_1A - F_2B}\right) \tag{5.47}$$

with $A = (A_1 + A_3)cos\beta + A_2$, $B = (A_1 - A_3)sin\beta$, $F_1 = (a_1 + a_3)cos\beta + a_2$ and $F_2 = (a_1 - a_3)sin\beta$. To analyse the dissipation and dispersion errors of our proposed scheme, in Figure 5.2, we have shown plots of k_r and k_i against β^2 and β respectively, keeping $R = 1$.

Ideally, for a scheme without dissipation and dispersion errors, k_r and k_i match perfectly with β^2 and β respectively. From the figure, it is clear that in the low Re regime, this matching is perfect for smaller value of ν. This matching becomes less effective with the increase in Peclet number and wave number. However from our figure, it is clear that our proposed scheme is less dissipative (as can be seen from Figures 5.2(a), 5.2(c) and 5.2(e)) but dispersive nature increases in the high Pe region (as suggested by Figures 5.2(b), 5.2(d) and 5.2(f)).

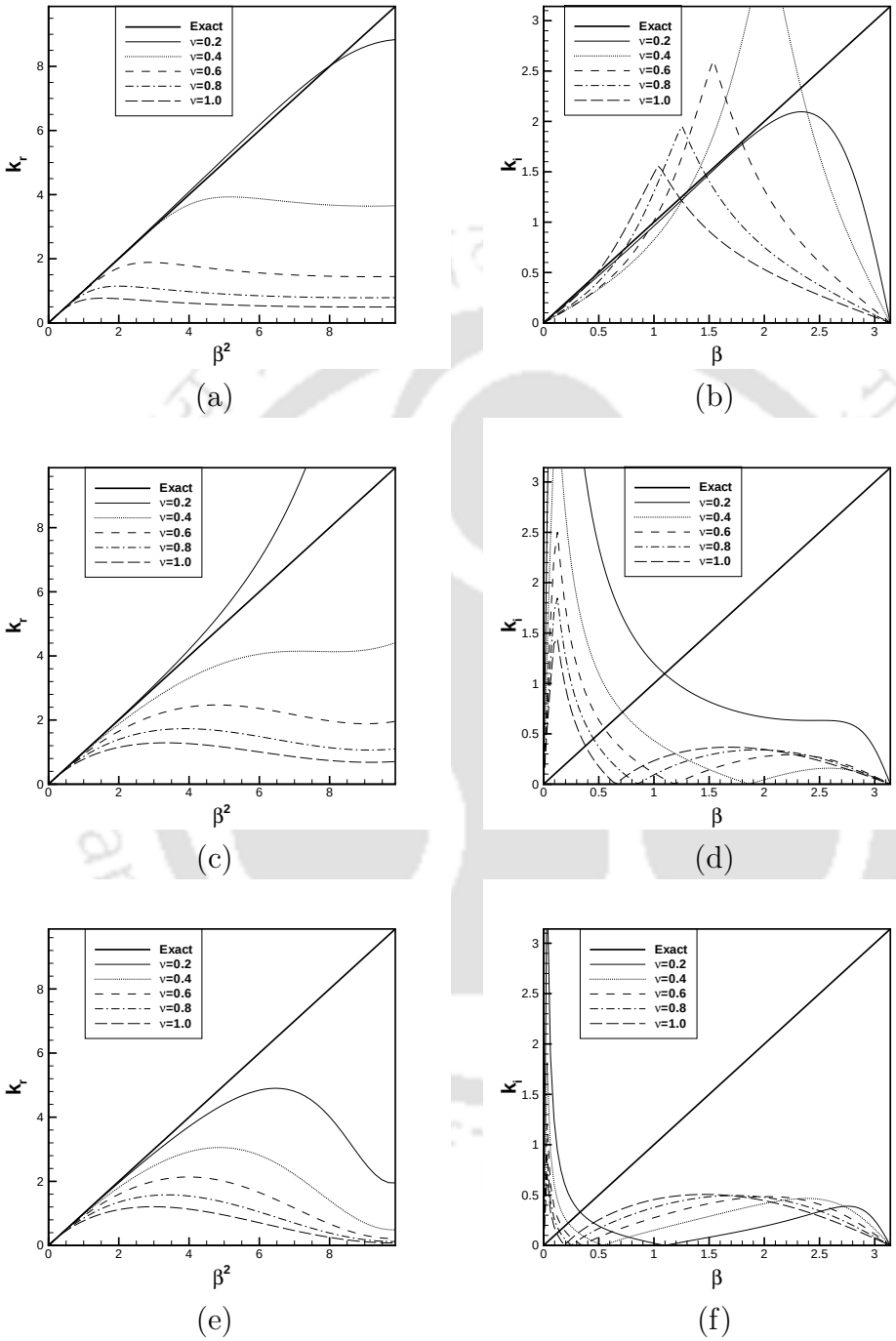

Figure 5.2: *Plots showing k_r and k_i versus β^2 and β for $R = 1$ and : (a)-(b) $Pe = 1$; (c)-(d) $Pe = 100$ and (e)-(f) $Pe = 1000$.*

5.3.3 Stability analysis:

Now, we attempt to carry out a Fourier stbility analysis of our proposed scheme by determining the amplification factor G for different combinations of ν and Pe for $R = 1$. The expression for G may be obtained as $G = \frac{\phi_i^{n+1}}{\phi_i^n} = e^P(cosQ + \mathrm{i}sinQ)$, where the values of P and Q are given by equations (5.46) and (5.47) respectively and $\mathrm{i} = \sqrt{-1}$.

In Figure 5.3, we show the plots of $|G|$ in the $\beta - \nu$ plane for Pe values ranging from $1 - 1000$. From the figures, it is clear that there doesn't exist any region of instability. Hence for $\varsigma = 0.5$, our scheme is unconditionally stable in the range of Peclet numbers considered.

5.4 Numerical test cases.

In order to validate and test the robustness of the proposed schemes, we apply them to two linear and two non-linear test cases. The first linear case deals with constant convective and reactive coefficients while the second one deals with variable convective and reactive coefficients. The first non-linear case is the one provided by Ethier *et al.* [26] while the second non-linear case deals with fluid flows governed by the 3D incompressible N-S equations, namely the famous lid-driven cavity (LDC) flow. As the first two problems have analytical solutions, Dirichlet boundary conditions are used for them, whereas for the third one we use the boundary conditions as obtained from the exact solutions in [26] and for the fourth one, Dirichlet boundary conditions are applied and the results obtained from it are compared with established ones. In all the four cases, although sufficiently accurate numerical results are found with all the proposed schemes, we have shown the results obtained through (19,19) scheme only.

5.4.1 Problem 1

Firstly we consider equation (5.1) with $a = 1$, and constant convective coefficients and reactive coefficients as $p = 2.5$, $q = 3.25$, $r = 5.66$ and $e = 25.0$ in

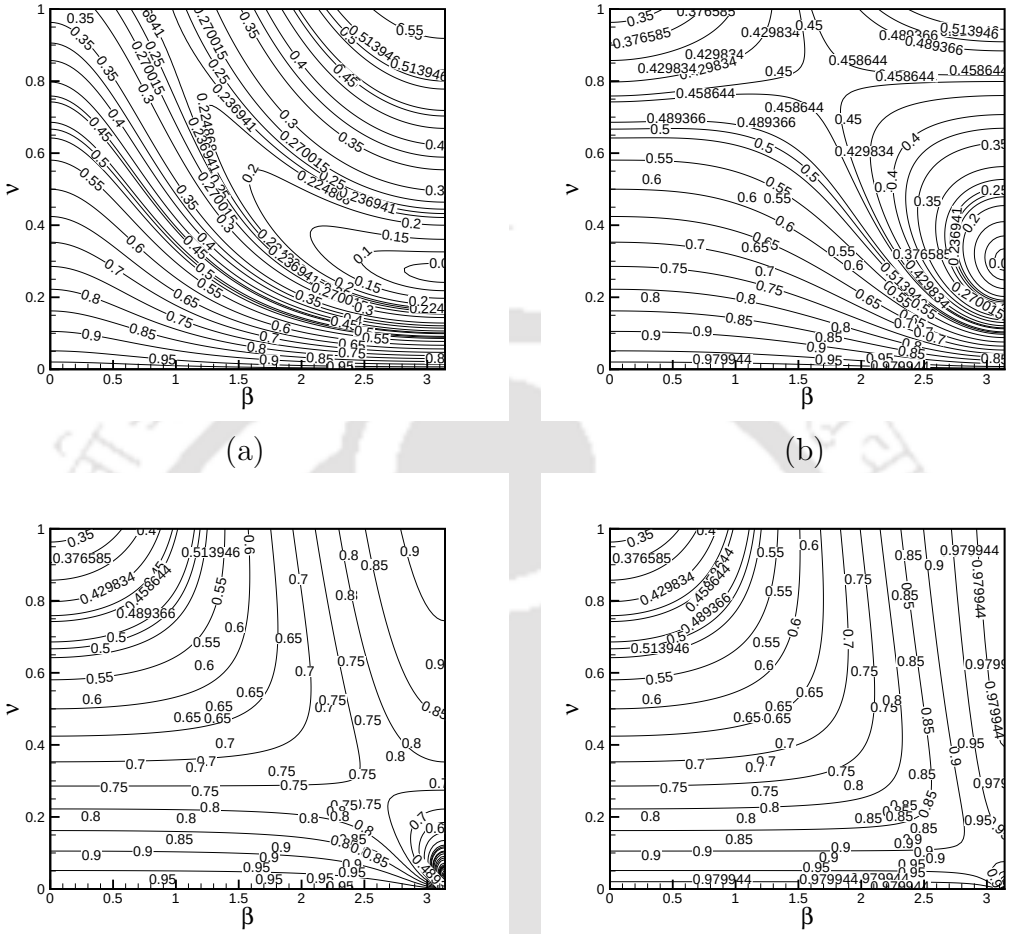

Figure 5.3: *Contours of the magnitude of the amplification factor* $|G|$ *in the* $\beta - \nu$ *plane (a)* $Pe = 1$*, (b)* $Pe = 10$*, (c)* $Pe = 100$ *and (d)* $Pe = 1000$*.*

the cube $[0,1] \times [0,1] \times [0,1]$ with the forcing function f given as

$$f(x,y,z,t) = exp(2t)((e + 3\pi^2)sin(\pi x)sin(\pi y)sin(\pi z) + p\pi cos(\pi x)sin(\pi y)sin(\pi z) + q\pi sin(\pi x)cos(\pi y)sin(\pi z) + r\pi sin(\pi x)sin(\pi y)cos(\pi z)) \tag{5.48}$$

and the initial condition as

$$\phi(x, y, z, 0) = sin(\pi x)sin(\pi y)sin(\pi z) \tag{5.49}$$

An analytical solution to this problem is

$$\phi(x, y, z, t) = exp(2t)sin(\pi x)sin(\pi y)sin(\pi z) \tag{5.50}$$

The boundary conditions have been taken from the analytical solution given by equation (5.50).

In Figure 5.4, we show our computed results with the surface plots of the numerical and analytical solutions on $x = 0.5$ and $y = 0.5$ planes on a $41 \times 41 \times 41$ grid and excellent match is visible from it. The last row of Figure 5.4 shows the corresponding error plots. The computations are carried out with a time step $\triangle t = 0.005$ and the results are recorded at various time stations, $t = 0.1$, 0.5 and 1.0 respectively.

Define the relative error field as

$$error = \frac{\phi_{ana} - \phi_{num}}{\phi_{aveg}} \tag{5.51}$$

where ϕ_{ana} and ϕ_{num} are the analytical and numerical solutions respectively, and $\phi_{aveg} = \left[\frac{1}{N}\sum_{n=1}^{N}\phi_n^2\right]^{\frac{1}{2}}$, with ϕ_n being the value of the analytical solution at the node n, while N is the total number of nodes.
Also define the root mean square (RMS) relative error as

$$E = \frac{RMS(\phi_{ana} - \phi_{num})}{RMS(\phi_{ana})} \tag{5.52}$$

where $RMS(\phi_{ana} - \phi_{num})$ is the root mean square value of the pairwise differences of ϕ_{ana} and ϕ_{num} taken at each node n and $RMS(\phi_{ana})$ is the root mean square value of the analytical solution. In Table 5.1, the convergence rates of the numerical schemes are shown. The average absolute error, average relative error and root mean square (RMS) relative errors have been presented on three different grids of size $11 \times 11 \times 11$, $21 \times 21 \times 21$ and $41 \times 41 \times 41$, which

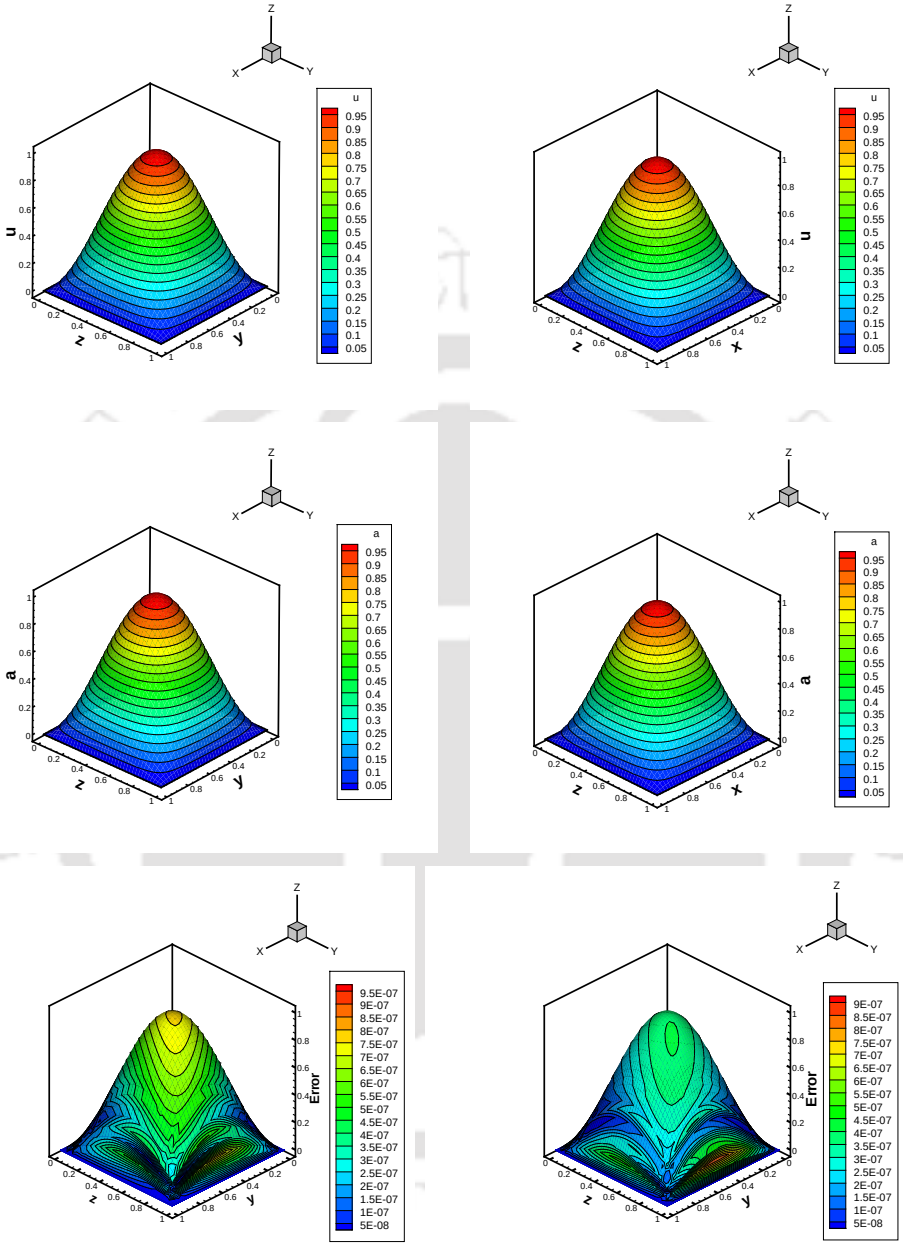

Figure 5.4: *Problem 1 : Numerical solution (top), analytical solution (middle) and error-plot (bottom) on a* $41 \times 41 \times 41$ *grid at time* $t = 1.0$ *: Along* $x = 0.5$ *plane (left) and along* $y = 0.5$ *plane (right).*

in turn measure the rate of convergence (order) of the proposed scheme for this test problem. The columns showing rate represent the estimated orders

of accuracy ($O(A)$), which is calculated by the following formula

$$O(A) = \frac{ln(E_c/E_f)}{ln2}, \tag{5.53}$$

where E_c and E_f stand for the errors on a coarse grid and fine grid respectively; where the coarse grid has half of the numbers of points in each direction respectively than the finer one. The table clearly demonstrates that the rate of convergence is approximately 4.00 which is in accordance with the theoretical rate of convergence.

Table 5.1: *Problem 1: Convergence rates of the numerical scheme: average absolute error e_1, average relative error e_2 and RMS relative error e_3 comparisons on different grid sizes.*

Grid		11^3	Rate	21^3	Rate	41^3
$t = 0.1$	e_1	1.308×10^{-4}	3.839	9.143×10^{-6}	3.824	6.455×10^{-7}
	e_2	3.924×10^{-4}	3.900	2.629×10^{-5}	3.854	1.819×10^{-6}
	e_3	5.771×10^{-4}	4.071	3.434×10^{-5}	3.995	2.156×10^{-6}
$t = 0.5$	e_1	9.827×10^{-4}	3.718	7.469×10^{-5}	3.883	5.064×10^{-6}
	e_2	2.890×10^{-3}	3.814	2.055×10^{-4}	3.928	1.350×10^{-5}
	e_3	6.041×10^{-3}	4.033	3.691×10^{-4}	4.000	2.307×10^{-5}
$t = 1.0$	e_1	2.416×10^{-3}	3.762	1.781×10^{-4}	3.886	1.205×10^{-5}
	e_2	7.885×10^{-3}	3.863	5.421×10^{-4}	3.939	3.536×10^{-5}
	e_3	1.388×10^{-2}	3.999	8.677×10^{-4}	4.000	5.423×10^{-5}

5.4.2 Problem 2

Next we consider the equation (5.1) with $a = 1$, and variable convective coefficients and reactive coefficients as $p = Rx$, $q = Ry$, $r = Rz$ and $e = 5R$ (R is a constant) in the cube $[0, 1] \times [0, 1] \times [0, 1]$ with the forcing function f given as

$$f(x, y, z, t) = exp(t)(11R^2x^2y^2z^2 - 2R(x^2y^2 + y^2z^2 + z^2x^2)) \tag{5.54}$$

and the initial condition as

$$\phi(x, y, z, 0) = Rx^2y^2z^2 \tag{5.55}$$

An analytical solution to this problem is

$$\phi(x, y, z, t) = exp(t)Rx^2y^2z^2 \tag{5.56}$$

Once again, the boundary conditions have been taken from the analytical solution given by equation (5.56).

For $R = 100$, computed results are shown in Figure 5.5, where we show the surface plots of the analytical and numerical solution on $x = 0.2$ plane on a $11 \times 11 \times 11$ grid and on $y = 0.25$ plane on a $41 \times 41 \times 41$ grid respectively. The computations are carried out with a time step $\triangle t = 0.0001$ and at time stations, $t = 0.005$ and $t = 0.01$ respectively.

Table 5.2 shows the numerical and analytical solution at the centroid of the unit cubical domain which clearly reveals the fact that with the increase in grid size the numerical solution approaches the analytical solution more and more closely. However, this convergence towards the analytical solution significantly decreases with the increase in the constant R.

Table 5.2: *Problem 2: Numerical and analytical values of u(mid, mid, mid) for different R at* $t = 0.01$ *for different grid sizes with* $\Delta t = 0.0001$.

R	11^3 grid (numerical)	21^3 grid (numerical)	41^3 grid (numerical)	analytical solution
10	0.15864	0.15801	0.15785	0.15782
50	0.79236	0.79004	0.78932	0.78910
100	1.58847	1.58013	1.57865	1.57820

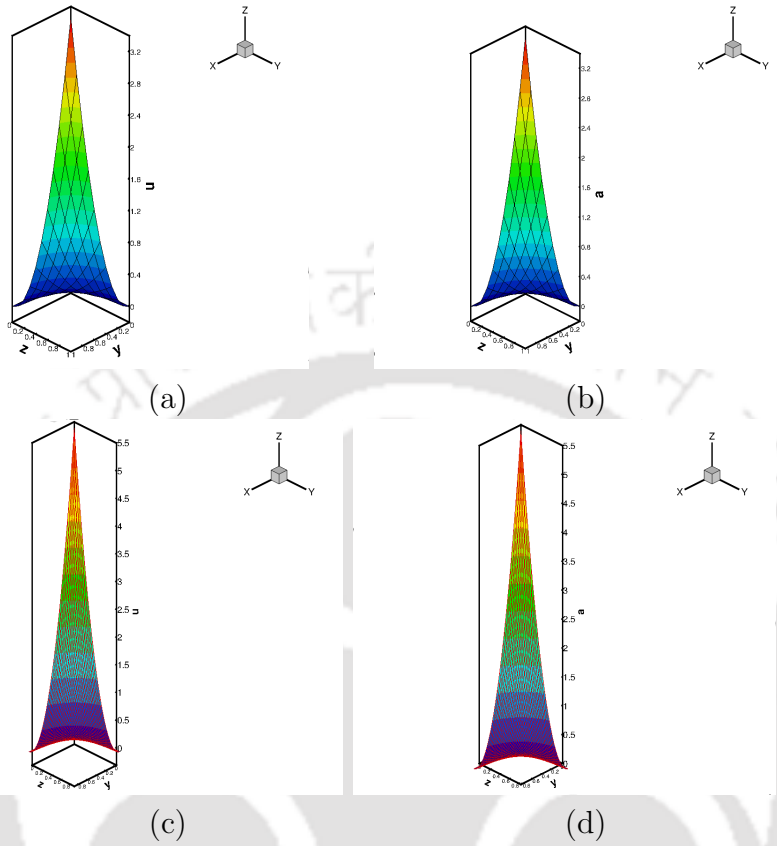

Figure 5.5: *Problem 2 at $R = 100$: (a) Numerical solution (along $x = 0.2$ plane) on a $11\times11\times11$ grid, (b) Analytical solution (along $x = 0.2$ plane) on a $11\times11\times11$ grid, (c) Numerical solution (along $x = 0.25$ plane) on a $41\times41\times41$ grid, (d) Analytical solution (along $x = 0.25$ plane) on a $41 \times 41 \times 41$ grid.*

5.4.3 Problem 3

Next we consider the first non-linear test case, which is the one provided by Ethier *et al.* [26]. The exact solutions to the 3D incompressible N-S equations in primitive variables are given by Ethier as

$$u = -a_2 e^{-a_1^2\left(\frac{t}{Re}\right)} \left[e^{a_2 x}\sin(a_2 y \pm a_1 z) + e^{a_2 z}\cos(a_2 x \pm a_1 y)\right], \tag{5.57}$$

$$v = -a_2 e^{-a_1^2\left(\frac{t}{Re}\right)} \left[e^{a_2 y}\sin(a_2 z \pm a_1 x) + e^{a_2 x}\cos(a_2 y \pm a_1 z)\right], \tag{5.58}$$

$$w = -a_2 e^{-a_1^2\left(\frac{t}{Re}\right)} \left[e^{a_2 z}\sin(a_2 x \pm a_1 y) + e^{a_2 y}\cos(a_2 z \pm a_1 x)\right], \tag{5.59}$$

$$p = \frac{1}{2}(u^2 + v^2 + w^2), \tag{5.60}$$

where a_1 and a_2 are adjustable constants controlling the amplitude and frequency of the solutions. Throughout our computations, we have taken $a_1 = 2\pi$ and $a_2 = 0.1$. Our numerical results have been illustrated in Figures 5.6-5.9.

In Figure 5.6, we have shown the contours of analytical and numerical pressure for $Re = 100$ at time $t = 1.0$ with a time step of $\triangle t = 0.005$ on a $65 \times 65 \times 65$ grid along the cross-sections of planes $x = 0.5$, $y = 0.5$ and $z = 0.5$.

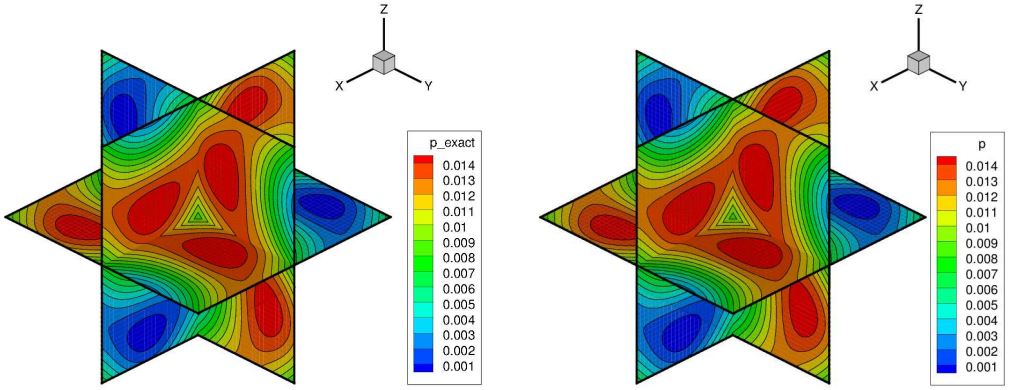

(a) (b)

Figure 5.6: *Problem 3 at* $Re = 100$ *: (a) numerical pressure and (b) exact pressure* ($65 \times 65 \times 65$ *grid).*

Keeping all the parameters same but with a coarse grid $21 \times 21 \times 21$, we again computed the solution and the results are shown in Figures 5.7 and 5.8, which justify that numerical solution of u-, v-, w- velocities and numerical pressure obtained with our method agrees quite excellently with that of the exact solutions.

In Figure 5.9(a), we have shown the u-velocity profiles for $Re = 500$ at the location $x = 0.5, z = 0.5$ on $11 \times 11 \times 11$, $21 \times 21 \times 21$ and $41 \times 41 \times 41$ grids

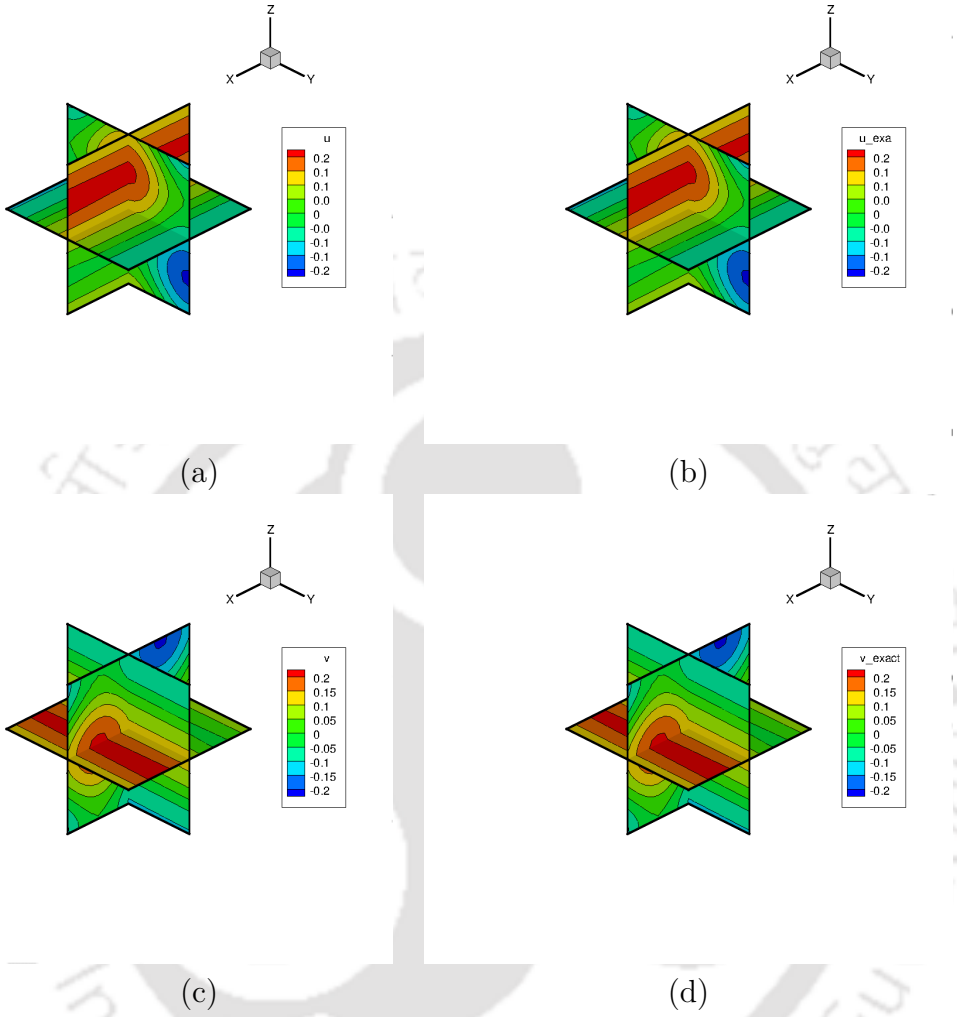

Figure 5.7: *Contour plots for problem 3 ($Re = 100$, $21 \times 21 \times 21$ grid, $\triangle t = 0.005$) at time $t = 1.0$: (a) numerical u velocity and (b) exact u velocity (c) numerical v velocity and (d) exact v velocity.*

which confirmed the grid independence of our computed solutions for this Re.

In Figure 5.9(b), we present the pressure plots for $Re = 1000$ at the location $x = 0.5$ and $z = 0.5$ on a grid of size $41 \times 41 \times 41$ and compare our results with those of Ethier and Steinman [26]. From the figure, it is clear that our solution profiles show an excellent match with theirs.

Next we solve the problem with two other schemes and the average and maxi-

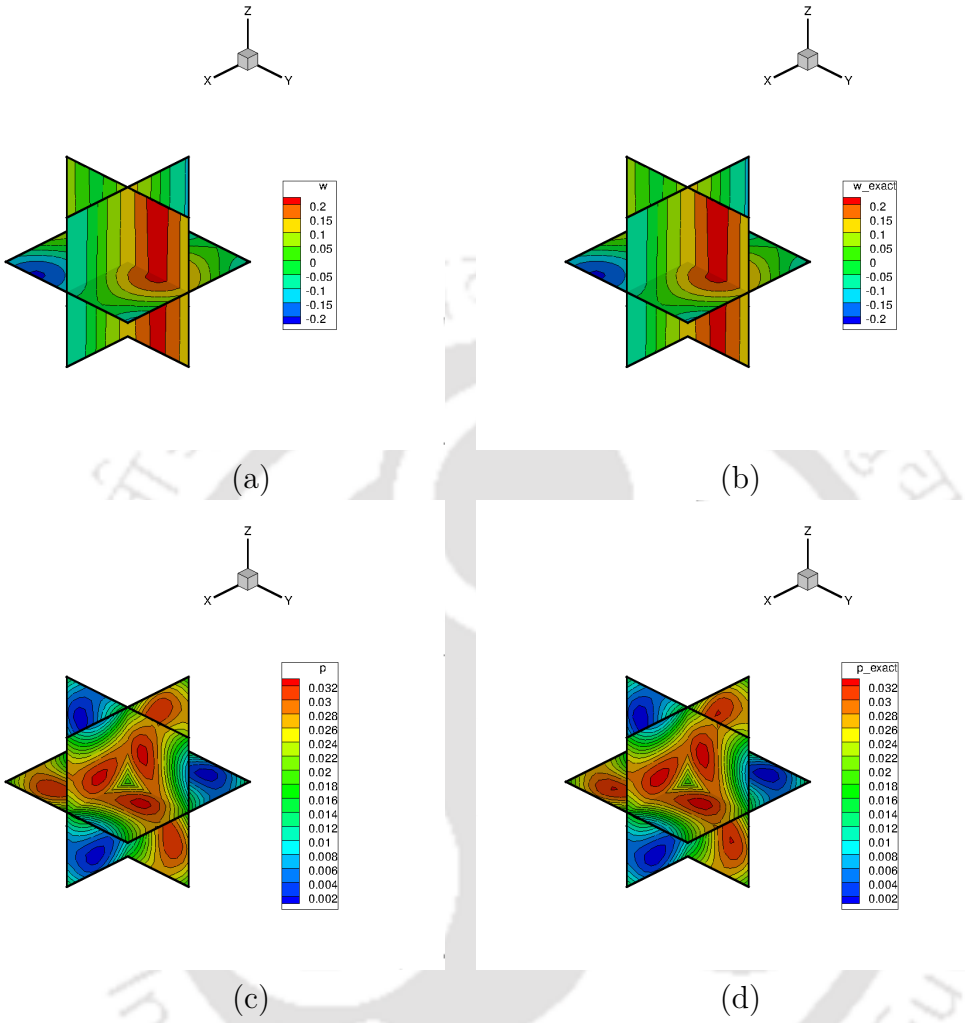

Figure 5.8: *Contour plots for problem 3 ($Re = 100$, $21 \times 21 \times 21$ grid, $\triangle t = 0.005$) at time $t = 0.5$: (e) numerical w velocity and (f) exact w velocity (g) numerical pressure and (h) exact pressure.*

mum absolute errors are presented in Table 5.3 along with the errors obtained by employing our method.

From the table, it is visible that our method (with $\varsigma = 0.5$) has significantly smaller average and maximum absolute errors compared to the other methods.

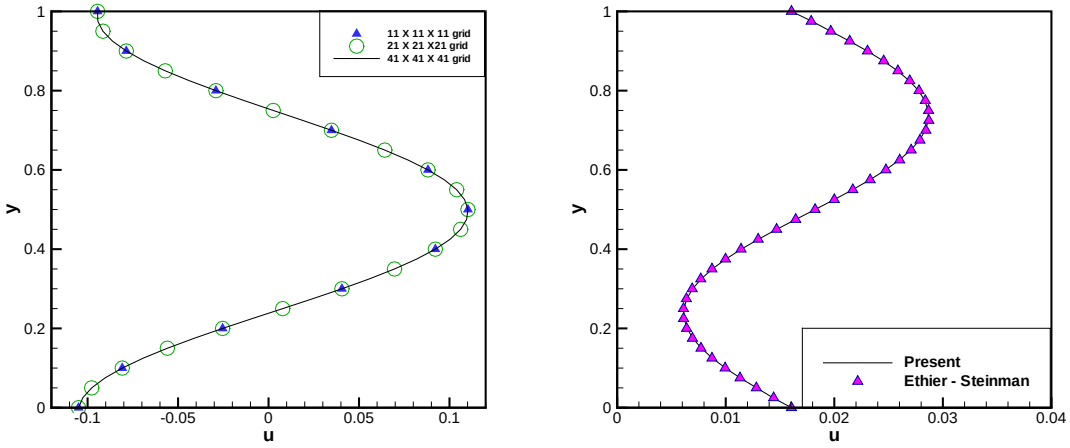

(a) (b)

Figure 5.9: *Problem 3 : (a) Grid independence study for u-velocity at* $Re = 500$ *(at the location* $x = 0.5$ *and* $z = 0.5$*) and (b) Comparison of pressure at* $Re = 1000$ *(at* $x = 0.5$ *and* $z = 0.5$*) with the results of [26].*

Table 5.3: *Average and maximum absolute errors at* $t = 1.0$ *with* $Re = 100$*,* $\triangle t = 0.0025$ *and* $h = k = l = 0.025$*.*

Method	Average |error|	Maximum |error|
FTCS	9.4×10^{-3}	8.3×10^{-1}
SIP	5.7×10^{-4}	1.9×10^{-3}
Present (19, 19)	2.6×10^{-5}	7.7×10^{-4}

5.4.4 Problem 4 : The cubical lid-driven cavity flow

Our last and final test case is the highly non-linear problem : the 3D lid-driven cubical cavity flow. The 2D lid-driven cavity flow is a very popular benchmark problem for solving the 2D incompressible N-S equations because the flow retains many fluid mechanical phenomena demonstrated by multiple counter rotating recirculating regions on the corners of the cavity, albeit on a simple geometry. Researchers used it very frequently in the assessment of their proposed/existing numerical methods and therefore there are abundant

sources of results for the square cavity. However, for the 3D lid-driven cubical cavity, only a meagre amount of numerical results are available in the existing literature. This may be primarily because of its intricate nature arising due to the substantial increase in the memory allocation resulting from the presence of more unknown variables relative to its 2D counterpart.

The flow configuration in the cubic cavity has been shown in Figure 5.10. The velocity boundary conditions may be written as :

$$\begin{aligned} &\text{At } z = 1 : u = 1, v = w = 0 \text{ and} \\ &\text{For } 0 \leq x \leq 1, 0 \leq y \leq 1, 0 \leq z < 1 : u = v = w = 0 \end{aligned} \tag{5.61}$$

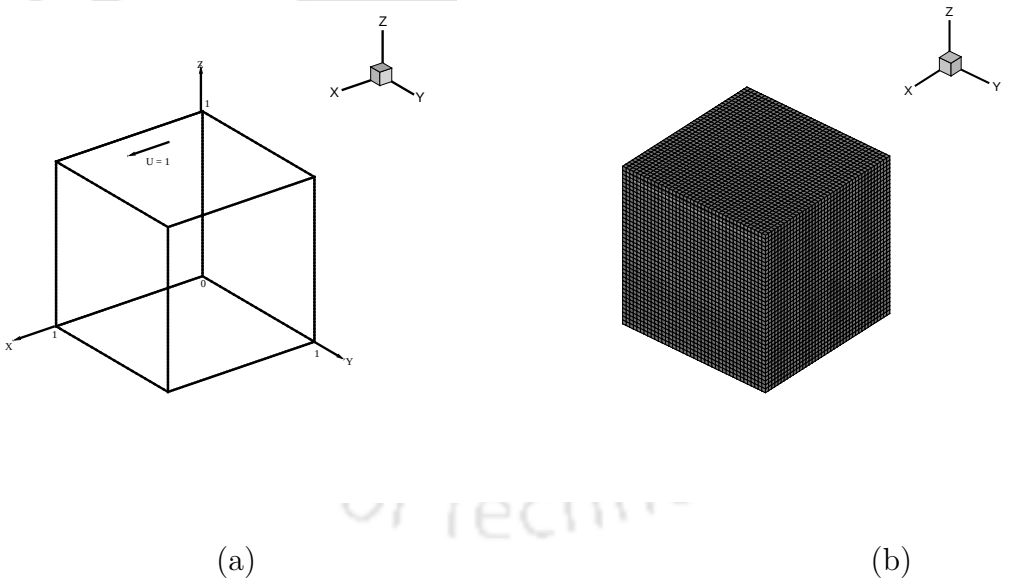

(a) (b)

Figure 5.10: *Problem 4 : (a) The 3D lid-driven cubical cavity configuration and (b) A typical* $65 \times 33 \times 65$ *grid.*

As an initial condition, all the velocity vectors have been initialized to zero at all points, except at location $z = 1$, where the initial value of u-velocity have been taken as 1. Also the pressure field was initialized with a value of zero in

all the cases.

Numerical simulations were performed for Reynolds numbers 10, 100 and 400 on a grid of size $65 \times 33 \times 65$. Our computed steady state solutions have been presented in Figures 5.11-5.13 and in Table 5.4. Steady state is obtained through a time marching strategy and assumed to reach when the maximum ϕ-error (ϕ being u, v or w) between two successive outer temporal iteration steps is smaller than 0.5×10^{-7}; the same tolerance limit was set for the residual fall of the inner BiCGStab iterations as well.

Comparison of u- and w-velocity profiles obtained via 2D simulations and 3D simulations ($y = 0.5$ plane) are shown in Figure 5.11 (top) and Figure 5.11 (bottom) respectively. In the figure, for $Re = 10$ we have shown our computed results along with the two-dimensional results of Gupta and Kalita [41] while for $Re = 100$ and 400, we compare our results with some of the well-established results [31, 50, 65]. From these plots, it is evident that for the cubic cavity, flow motion is reduced even at low Reynolds numbers in contrast to the square cavity. This observation is quite apparent even for Reynolds number as small as 100. However, the plots confirmed that our results are in quite good agreement with those obtained by [50, 65].

In Table 5.4, we have shown the different parameters used in the flow computation and the primary vortex center on the $y = 0.5$ has also been reported. In the table, the first column is for Reynolds number Re, the second column represents the time step-length $\triangle t$, the third column column shows the artificial compressibility parameter λ, the fourth column states the number of iterations taken for pressure corrections and the fifth column represents the primary vortex center.

In Figure 5.12, we have shown the pressure contours for $Re = 100$ and 400 on the $x = 0.5$, $y = 0.5$ and $z = 0.5$ planes. The plots from our figure are in very close agreement with the pressure plots obtained by Jiang *et al.* [50].

Lastly, in Figure 5.13, we have shown our computed results for u- and w-

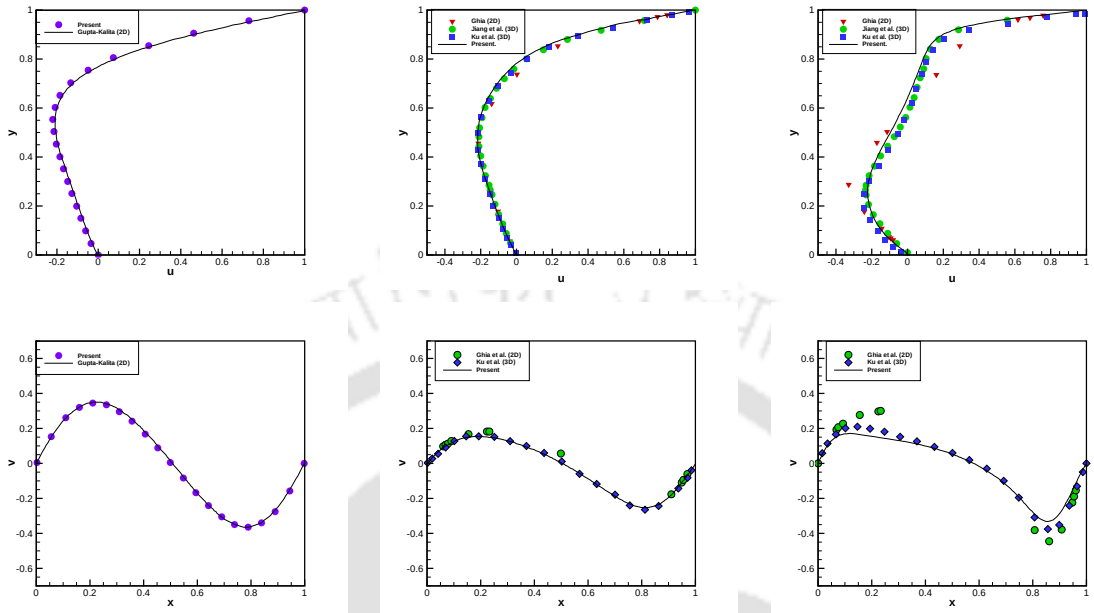

Figure 5.11: *Comparison between the 2D and 3D simulations : horizontal velocity along the vertical centerline (top) for* $Re = 10$ *(left),* $Re = 100$ *(middle),* $Re = 400$ *(right) and vertical velocity along the horizontal centerline (bottom) for* $Re = 10$ *(left),* $Re = 100$ *(middle),* $Re = 400$ *(right).*

Table 5.4: *Problem 4: Different parameters used in the cubical lid-driven cavity problem.*

Re	$\triangle t$	λ	Pressure Iterations	Primary Vortex Center
10	0.01	0.1	15	$(0.5022, 0.7600)$
100	0.01	0.05	25	$(0.5940, 0.7930)$
400	0.005	0.02	40	$(0.6724, 0.7578)$

velocities as functions of z and x respectively and compared our results with the existing literatures [11, 62, 65, 70, 99] for the three-dimensional lid-driven cubic cavity. From the figures, we confirmed that our numerical solutions are in excellent agreement with these established results, unlike the ones seen in the comparison with the 2D lid-driven square cavity.

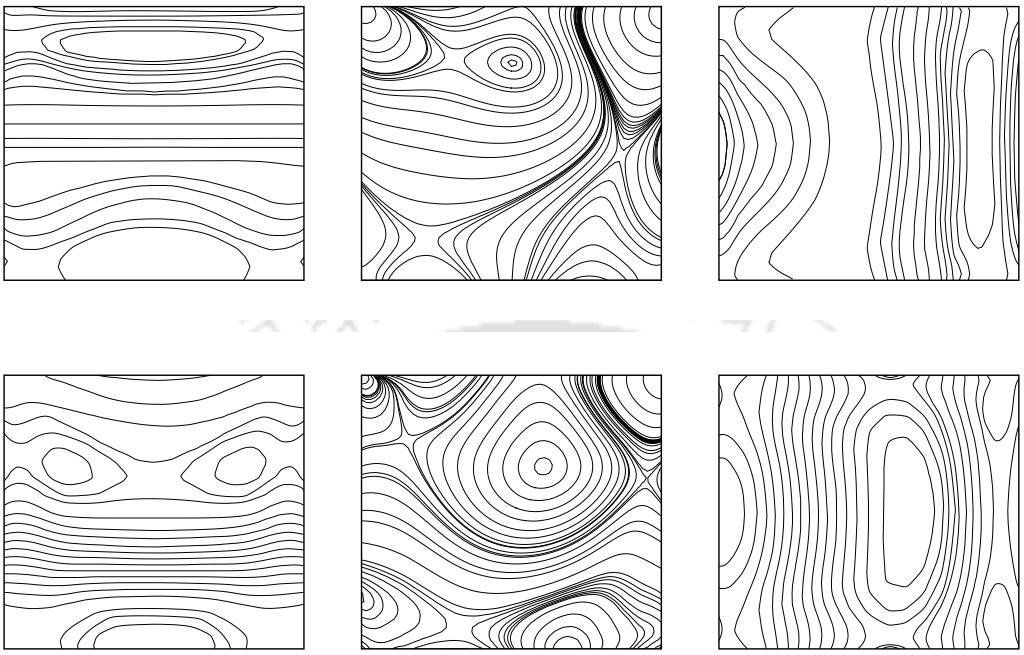

Figure 5.12: *Pressure contours for Problem 4 : $Re = 100$ (top) along $x = 0.5$ (left), $y = 0.5$ (middle) and $z = 0.5$ plane (right) and $Re = 400$ (bottom) along $x = 0.5$ (left), $y = 0.5$ (middle) and $z = 0.5$.*

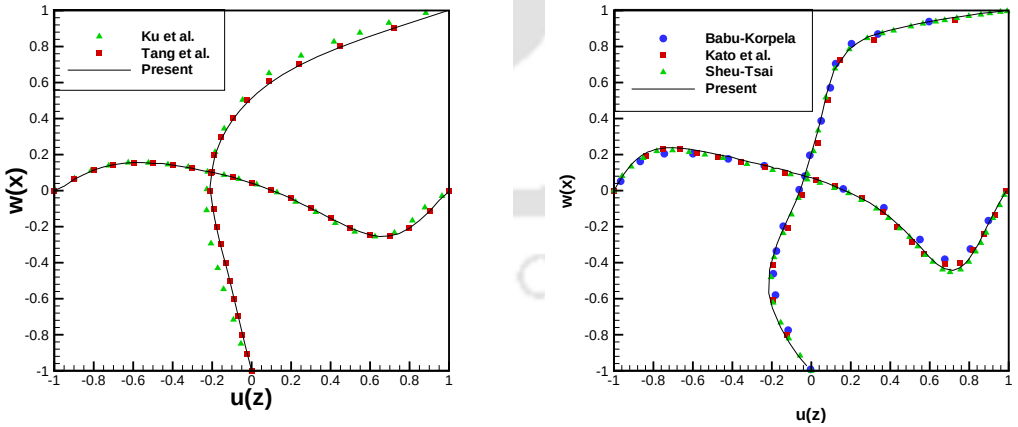

(a) (b)

Figure 5.13: *Change of u- and w-velocities along z and x directions respectively for (a) $Re = 100$, (b) $Re = 400$.*

5.5 Conclusion

In the existing literature, one can find a very limited number of HOC finite difference schemes for the convection-diffusion-reaction equations particularly for the three-dimensional ones. In this chapter, development of a class of implicit HOC finite difference schemes with weighted time discretization to solve the transient 3D variable coefficient convection-diffusion-reaction equation has been discussed. The proposed schemes are fourth order accurate in space and second or lower order accurate in time depending on the choice of the weighted average parameter. A theoretical convergence analysis has been carried out for the proposed schemes confirming their fourth order spatial accuracy in the discrete Euclidean norm (L^2-norm), which has also been established later on by numerical experiments. To compute the flow equations governed by the 3D incompressible Navier-Stokes equations, we use the primitive variable formulation of the 3D N-S equations in conjunction with the modified compressibility technique. In order to highlight the different features of our proposed schemes, we have utilized them to compute the transient solutions of two 3D convection-diffusion-reaction problems whose analytical results are available. Later, we have also applied them to two non-linear 3D convection-diffusion problems, where steady state has been achieved via a time-marching strategy, one of them being the 3D cubical lid-driven cavity flow. Moreover the implicitness of our proposed schemes enable the use of larger time step in contrast to the explicit schemes which have a severe stability limit to the time step. As such, the proposed schemes are very efficient in terms of computational cost and accuracy. The robustness of the schemes are exemplified by their successful implementation on a wide range of problems of varying physical complexities. As a whole, the results obtained in all our test cases are found to be in excellent agreement with the analytical and available benchmark numerical results. Because of being HOC in space, second order accurate in time and implicit in nature, the $(19, 19)$ scheme in particular seems to have good potential for efficient application to many problems of 3D incompressible viscous flows. In the next chapter, we are going to discuss the implementation of the reduced formulation in 2D in simulating pattern formation in Mathematical Biology.

Chapter 6

HIGHER-ORDER COMPACT SIMULATION OF PATTERN FORMATION IN MATHEMATICAL BIOLOGY

6.1 Introduction

The term morphogen is used rigorously to describe a particular type of signaling molecule that acts on cells directly to induce distinct cellular responses in a concentration dependent manner [109]. In nature, various pattern formations occur due to the variation of concentration of morphogens within each cell, which, both react and diffuse within the system owing to instabilities. A variety of species exhibits remarkable types of patterns in their skins, shapes or sizes. Patterns imitating the spots in leopards, spikes in cactus, stripes in zebras etc. has created tremendous interest amongst researchers and biologists. These pattern formation mechanisms are actually governed by simple mathematical models of reaction and diffusion. The signaling molecules involved in the chemical processes spread away from their source to form concentration gradients.

Reaction and diffusion are the two fundamental phenomena which govern the mechanism of morphogenesis. Within a system, reaction and diffusion occur between morphogens resulting in various patterns. Due to instabilities within the system, morphogens react and diffuse to change their cell concentrations which eventually give rise to different pattern formations.

Study on pattern formation dates to 1952, when British mathematician, Alan Turing, in his pioneering work [113] described a reaction-diffusion model for morphogen concentrations. This model hypothesizes the existence of two different molecules, an activator and an inhibitor. Turing's reaction-diffusion model is of the form

$$\begin{aligned} \frac{\partial U}{\partial t} &= D_u \nabla^2 U + F(U,V) \\ \frac{\partial V}{\partial t} &= D_v \nabla^2 V + G(U,V). \end{aligned} \tag{6.1}$$

where U (activator) and V (inhibitor) are the concentrations of the reacting chemicals, D_u and D_v are the diffusion coefficients and F and G are some functions of U and V (generally non-linear).

In his work, Turing showed that the activator and the inhibitor can give rise to spatial patterns starting from a nearly homogenous state. Application of the Turing mechanism to the formation of a given pattern is mainly identified by the specific dynamics of the reaction-diffusion system. This work was followed by numerous researchers which include Newman and Frisch (1979) [81], Bard (1981) [12], Jung *et al.* (1998) [54] etc. In 1993, an alternative mechanism for the spatial patterning was proposed by Murray *et al.* [79]. This mechanism follows a mechanochemical approach where it is assumed that patterns arise due to the physical interaction of cells with their external environment resulting in cell aggregations. With the advent of these models, there has been an immense growth of research in the field of pattern formation. Researchers have continued to carry out their studies on both of these model problems and it has been revealed that these models can simulate many exciting patterns that are observed in nature.

Pattern formation, apart from being studied by researchers to propose numerical methods for simulating those structures and predicting new ones, is also of great importance to science and industry. It is useful in studying pattern formation and regulation in Hydra and other biological patterning processes which include phyllotaxis, veins, spatial ecology, segmentation and colourful pigmentation in sea-shells [75]. Apart from biology, pattern formation is also applicable to microstructure engineering, sputtering and lithography [85]. Spontaneous pattern formation from reaction-diffusion systems reduces certain complications like diffraction and splashing from masks and therefore can be used to obtain higher accuracy [39]. Moreover, sensitiveness of pattern formations to initial conditions and various environmental factors can be utilized in sensing application [39] and in cellular engineering [102]. These features can further be utilized to devices like cameras and in detection of antioxidant [39].

Following the works of Turing, several other reaction-diffusion models have been proposed, notable ones include the Gray-Scott model [35, 36] and the Gierer-Meinhardt model [64]. In recent years, there has been a rapid rise in the field of Mathematical Biology and quite prominent ones include the study of pattern formation. Amongst the recent works worth mentioning are: Turk [114], Pearson [87], Aragon *et al.* [8], Asai *et al.* [9], Barrio *et al.* [13], Fleury [28], Liu *et al.* [72], Wu *et al.* [121] and Zhang *et al.* [128]. Because of non-linearity, these models pose considerable difficulty in direct computation and as such researchers have been driven to adopt novel numerical strategies from time to time. In this chapter, we use the second order time accurate HOC scheme developed in chapter 5 by modifying it so as to fit the equations of the form (6.1). In the process, we carry out the simulation of various patterns, viz. spikes, spots, stripes and labyrinths for varying range of parameters.

The governing unsteady reaction-diffusion model in its two-dimensional (2D) form may be written as

$$\frac{\partial \phi}{\partial t} - \varepsilon \nabla^2 \phi + r(x, y, t)\phi(x, y, t) = f(x, y, t) \tag{6.2}$$

where $\phi(x, y, t)$ is a transport variable in some domain $\Omega \subseteq \mathbb{R}^2$ with bound-

ary $\partial\Omega$, $\varepsilon > 0$ is the diffusion coefficient, $r(x, y, t)$ is the reaction coefficient, $f(x, y, t)$ is the forcing function and ∇^2 is the Laplacian operator.

Considering the HOC formulation (5.8) described in chapter 5, we can approximate Equation (6.2) as follows

$$\left[1 + \overbrace{\frac{h^2}{12\varepsilon}\delta_x^2 + \frac{k^2}{12\varepsilon}\delta_y^2}\right]\delta_t^+\phi_{ij}^n - A_{ij}\delta_x^2\phi_{ij}^n - B_{ij}\delta_y^2\phi_{ij}^n \tag{6.3}$$
$$- \frac{(h^2+k^2)}{12}\varepsilon\delta_x^2\delta_y^2\phi_{ij}^n + G_{ij}\phi_{ij}^n = F_{ij}^n$$

where the coefficients A_{ij}, B_{ij}, G_{ij} and F_{ij} are now as follows:

$$\begin{aligned} A_{ij} &= \varepsilon - \frac{h^2}{12\varepsilon}r_{ijk} \\ B_{ij} &= \varepsilon - \frac{k^2}{12\varepsilon}r_{ijk} \\ F_{ij} &= \left[1 + \frac{h^2}{12\varepsilon}\delta_x^2 + \frac{k^2}{12\varepsilon}\delta_y^2\right] f_{ij} \\ G_{ij} &= \left[1 + \frac{h^2}{12\varepsilon}\delta_x^2 + \frac{k^2}{12\varepsilon}\delta_y^2\right] r_{ij} \end{aligned} \tag{6.4}$$

δ_t^+ is the forward difference operator and the superscript n stands for the n-th time level.

The process of basic discretization and matrix computation follows a similar approach as was adopted in chapter 5 for the computation of 3D flows.

6.2 Code validation:

To lend credibility of our code in problems of pattern formation, we firstly apply it to the example proposed by Zhang *et al.* [128] for the time-dependent Gray-Scott model problem. They considered the following initial-boundary

value problem

$$\frac{\partial u}{\partial t} = d_1 \nabla^2 u + F(1-u) - uv^2, (x,y,t) \in \Omega \times (0,T), \tag{6.5a}$$

$$\frac{\partial v}{\partial t} = d_2 \nabla^2 v - (F+\tilde{k})v + uv^2, (x,y,t) \in \Omega \times (0,T), \tag{6.5b}$$

$$\frac{\partial u}{\partial \boldsymbol{n}} = \frac{\partial v}{\partial \boldsymbol{n}} = 0, (x,y,t) \in \partial\Omega \times (0,T), \tag{6.5c}$$

$$u(x,y,t=0) = u^0(x,y), (x,y) \in \Omega, \tag{6.5d}$$

$$v(x,y,t=0) = v^0(x,y), (x,y) \in \Omega, \tag{6.5e}$$

where u and v represent the reacting chemical species; d_1 and d_2 are the positive diffusion coefficients of chemicals u and v respectively; F is the inflow rate and $\tilde{k}$ is the dimensionless rate constant for the second reaction, $\boldsymbol{n}$ is the outer unit normal of the boundary $\partial\Omega$ and ∇^2 denotes the Laplacian.

In [128], a second order temporally and spatially accurate Galerkin finite element method was proposed with one of the test cases having the following analytical solution

$$u(x,y,t) = cos(2\pi x)cos(\pi y)cos(2t),$$

$$v(x,y,t) = cos(\pi x)cos(2\pi y)cos(2t).$$

Simulations were carried out using $d_1 = d_2 = F = 1$ and $\tilde{k} = 0$ on different uniform meshes of size ranging from 17×17 to 257×257 with a final non-dimensional time of unity. In the present study, we simulate this problem with our proposed scheme on three different grids of size 26×26, 51×51 and 101×101 with the same choice of parameters. To solve this problem with our method, we discretize these equations by setting $\varepsilon = d_1$ or d_2, $c = d = 0$, $r = F + v^2$ or $F + \tilde{k} - uv$ and $f = F$ or 0 respectively. For the Neumann boundary conditions, a fourth order compact scheme [56] has been used and the initial conditions are taken from the analytical solution.

We present our numerical results in Figures 6.1, 6.2 and Table 6.1. Figure 6.1 shows our numerical solution on a 51×51 grid along with the analytical solution and the error plots. From the figure, it is evident that our numerical results are extremely close to the analytical ones. In Table 6.1, we exhibit the average absolute errors of u and v on three different grids of size 26×26, 51×51 and 101×101, which is a measure of the spatial rate of convergence (order) of the proposed scheme for this problem. The last column represents the estimated orders of accuracy ($O(A)$), which is calculated by the formula given in section 5.4 of chapter 5. Table 6.1 clearly demonstrates that the spatial rate of convergence is approximately 4.00 which is in accordance with the theoretical rate of convergence.

Table 6.1: *Average absolute error and convergence rates of the numerical scheme at time $t = 1s$ for the code validating problem.*

Grid	Average absolute error of u	Convergence rate of u	Average absolute error of v	Convergence rate of v
26×26	2.175×10^{-5}		1.7184×10^{-5}	
		3.988		3.999
51×51	1.370×10^{-6}		1.074×10^{-6}	
		4.000		4.002
101×101	8.564×10^{-8}		6.702×10^{-8}	

In Table 6.2, we show the u-error and v-error obtained with our scheme on a grid of size 101×101 in the infinity norm. The errors are determined at time station $t = 1.0$ with time-steps ($\triangle t$) ranging from 0.001 to 0.1.

As the error (E) is proportional to $(\triangle t)^m$ (m is the order of time-accuracy), we have

$$E = C(\triangle t)^m$$

where C is a constant.

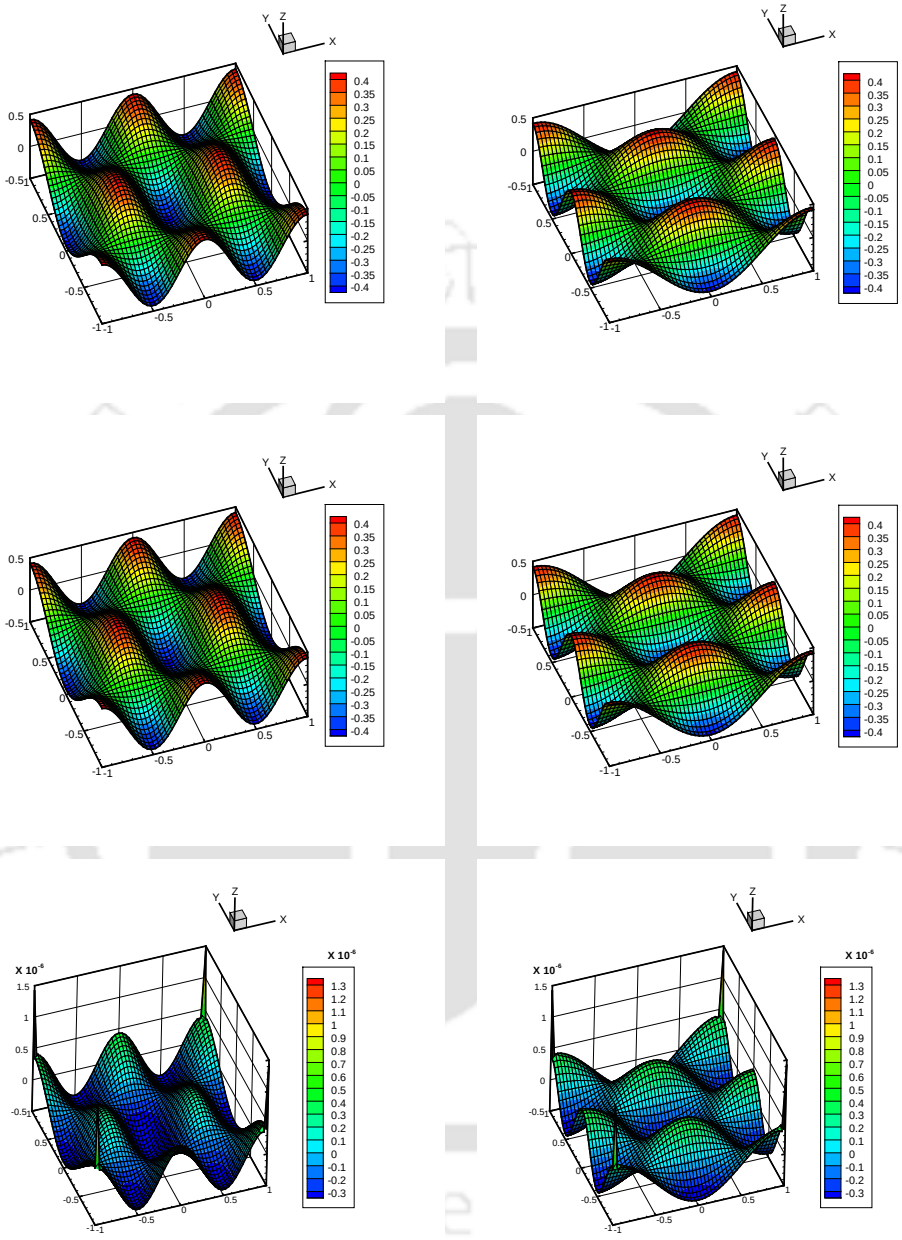

Figure 6.1: *Plots of u-values (left) : Numerical on a* 51×51 *grid (top), Analytical solution (middle), Error plot (bottom) and v- values (right) : Numerical solution on a* 51×51 *grid (top), Analytical solution (middle), Error plot (bottom).*

Table 6.2: *Convergence result of code validating problem at time* $t = 1.0$ *on a* 101×101 *grid.*

Time-step ($\triangle t$)	u-error (infinity norm)	v-error (infinity norm)
0.001	1.5428×10^{-10}	1.4335×10^{-10}
0.0025	9.6857×10^{-10}	8.9852×10^{-10}
0.005	3.8611×10^{-9}	3.5869×10^{-9}
0.01	1.5249×10^{-8}	1.4222×10^{-8}
0.025	9.3172×10^{-8}	8.7321×10^{-8}
0.05	3.5974×10^{-7}	3.4186×10^{-7}
0.1	1.3706×10^{-6}	1.3206×10^{-6}

This gives

$$logE = logC + mlog(\triangle t)$$

Therefore, we have

$$m = log(E_1/E_2)/log((\triangle t)_1/(\triangle t)_2), \quad \text{where}(\triangle t)_1 > (\triangle t)_2$$

In Table 6.3 we show the time rate of convergence of our proposed scheme, (here we consider only the first three rows of Table 6.2, i.e we consider only the three smallest ($\triangle t$) used in our perturbations). From the table, we conclude that the time rate of convergence of our scheme is pretty close to 2.00, which is in agreement with the theoretical rate.

In Figure 6.2, we plot the error norms against different time-steps computed on a grid of size 101×101 at time $t = 1.0$. It is heartening to note from this figure that even for a time-step as large as 0.1, our proposed numerical scheme yields an error norm of approximately 1.37×10^{-6} against the value of 8.151×10^{-3} for the method proposed by Zhang *et al.* [128] for the same time-step. Moreover, the errors resulting from our scheme is much lower than those in [128] and the figure clearly depicts a temporal rate of convergence of

Table 6.3: *Error and convergence rates of the numerical scheme at time* $t = 1s$ *for the code validating problem.*

Time-step ($\triangle t$)	u-error	Convergence rate of u	v-error	Convergence rate of v
0.001	1.5428×10^{-10}		1.4335×10^{-10}	
		2.005		2.003
0.0025	9.6857×10^{-10}		8.9852×10^{-10}	
		1.995		1.997
0.005	3.8611×10^{-9}		3.5869×10^{-9}	

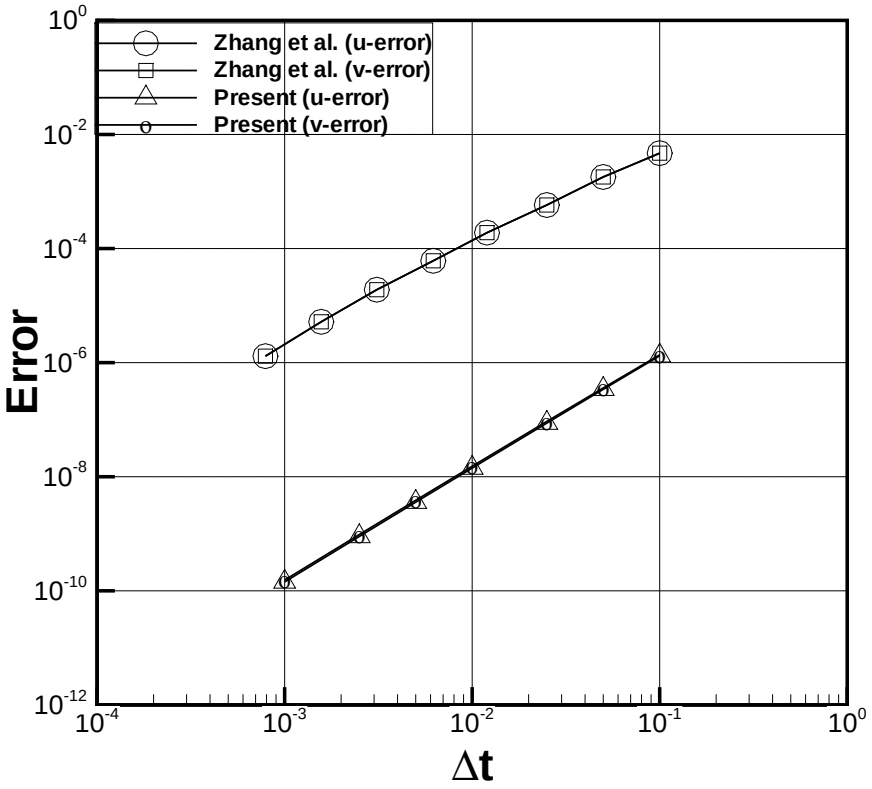

Figure 6.2: *Convergence results for the code validating problem : Error vs time-step size plot.*

two which is exactly the same as the theoretical one.

6.3 Numerical Test Cases:

In this section, we apply our proposed schemes to three different well established two-dimensional model problems, namely, (i) The Gierer-Meinhardt model problem [64], (ii) Barrio *et al.* [13] model problem and the popular (iii) Gray-Scott model problem [35, 36] as was described by Pearson [87]. Throughout the section, the results obtained only through $\varsigma = 0.5$ are presented, although sufficiently accurate results are obtained using the other two approaches as well.

6.3.1 The Gierer-Meinhardt model problem: Formation of spikes

The Gierer-Meinhardt model problem was proposed by A. Gierer and H. Meinhardt in 1972. The model can be formulated as

$$\frac{\partial a}{\partial t} = \frac{\sigma a^2}{b} - \mu_a a + \rho_a + D_a \nabla^2 a \tag{6.6a}$$

$$\frac{\partial b}{\partial t} = \sigma a^2 - \mu_b b + \rho_b + D_b \nabla^2 b \tag{6.6b}$$

where a represents the concentration of a short-range autocatalytic substance called the activator and b denotes the concentration of its long-range antagonist called the inhibitor. σ denotes the production rate coefficient, μ_a and μ_b are the respective decay coefficients describing the rate of decays of the activator and inhibitor, ρ_a and ρ_b represent the constant inflow of activator and inhibitor respectively and D_a and D_b denote the constant diffusion coefficients.

The activator is called so because it catalyzes its own production; either directly or indirectly, while the inhibitor is so called as it promotes the decaying of the activator slowing down its production and therefore inhibiting the reaction diffusion process. If both of them interact with each other in a specific

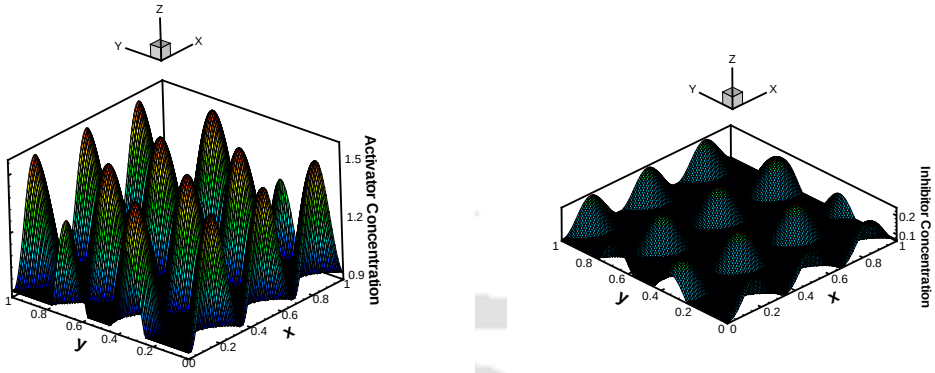

Figure 6.3: *Formation of spikes : activator concentration (left) and inhibitor concentration (right).*

manner, a periodic pattern can be obtained from a initial homogeneous spatial distribution of the activator and the inhibitor.

The system (6.6) can be re-written as

$$\frac{\partial a}{\partial t} - D_a \nabla^2 a + \mu_a a = \frac{\sigma a^2}{b} + \rho_a \tag{6.7a}$$

$$\frac{\partial b}{\partial t} - D_b \nabla^2 b + \mu_b b = \sigma a^2 + \rho_b \tag{6.7b}$$

Considering zero convective effect ($c = d = 0$), we employ our proposed scheme to the above system (6.7) on a grid of size 129×129 with a time-step 0.1 where Ω was chosen to be a unit square. In our computations, we have chosen $\sigma = 0.02$, $\mu_a = 0.01$, $\rho_a = 0$, $\mu_b = 0.02$, $\rho_b = 0$, $D_a = 0.005$ and $D_b = 0.2$. The initial conditions are given by the homogeneous steady state of the system and the boundary conditions are assumed to be periodic.

Simulations were performed till a non-dimensional time $T = 4000$ and results are illustrated in Figure 6.3. From the figure, it is visible that the activator

and inhibitor peaks coincide. The activator peaks are more elevated compared to the inhibitor ones, which are modest. Similar observations were also made by Yamamoto *et al.* [123]. The patterns resulting from the activator concentration at time $t = 900$ and $4,000$ are shown in Figure 6.4.

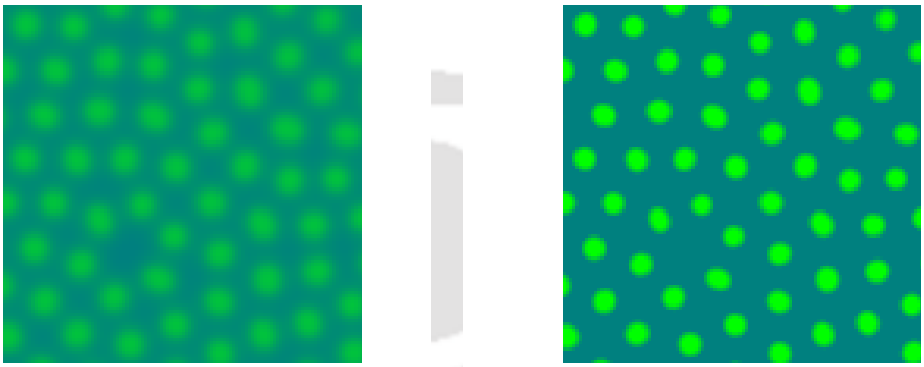

(a) (b)

Figure 6.4: *Contour plots of the activator concentration at time (a)* $t = 900$ *and (b)* $t = 4,000$.

6.3.2 Barrio-Varea-Aragon-Maini model problem: Spots and Stripes Formation

Our next test case is the model problem proposed by R. A Barrio, C. Varea, J. L. Aragon and P. K. Maini in their work [13]. They considered the Turing system to be of the specific form

$$\begin{aligned} \frac{\partial u}{\partial t} &= D\delta\nabla^2 u + \alpha u(1 - r_1 v^2) + v(1 - r_2 u) \\ \frac{\partial v}{\partial t} &= \delta\nabla^2 v + \beta v\left(1 + \frac{\alpha r_1}{\beta} uv\right) + u(\gamma + r_2 v), \end{aligned} \tag{6.8}$$

where $u = U - U_c$ and $v = V - V_c$, so the uniform stationary solution (U_c, V_c) of Equation (6.8) is the point $(0, 0)$. U and V are the actual concentrations of the reacting chemicals and δ is the ratio between the diffusion coefficients of

the two chemicals. r_1 and r_2 are the two interaction parameters, which correspond to the cubic term and quadratic terms respectively. It is remarkable that the cubic interaction produces stripe-like patterns while the quadratic interaction favors spots [25]. Therefore, patterns depend on the values of r_1 and r_2. The quadratic term r_2 produces spots while the cubic term r_1 produces stripes.

In order to solve this system with our proposed scheme for the reaction-diffusion equation (considering a zero convective effect), we reduce the system (6.8) to the following form

$$\begin{aligned} \frac{\partial u}{\partial t} - D\delta\nabla^2 u - \alpha u &= -r_1\alpha u v^2 + v(1 - r_2 u) \\ \frac{\partial v}{\partial t} - \delta\nabla^2 v - \beta v &= r_1\alpha u v^2 + u(\gamma + r_2 v), \end{aligned} \tag{6.9}$$

Considering the domain $[0, 1] \times [0, 1]$ and $[0, 2.5] \times [0, 2.5]$, numerical calculations were performed on a 101×101 grid and 251×251 grid respectively, with a time-step 0.1 with varying range of parameters. Simulations were performed till the spatially-uniform steady state was achieved and we chose the following parameters:

$$D = 0.25,\ \alpha = 0.62,\ \beta = -0.66,\ \gamma = -0.62 \text{ and } \delta = 0.01.$$

Steady state was assumed to reach when the maximum u-error and v-error between two successive outer temporal iteration steps was smaller than the tolerance limit 10^{-8}.

In Figures 6.5 and 6.6, we have shown our results where the initial conditions were randomly chosen and the boundary conditions are the Neumann boundary conditions with zero fluxes. Figure 6.5, shows spot like patterns while Figure 6.6 shows some stripe like patterns.

Except the pattern depicted in Figure 6.5(b), all the other patterns were sim-

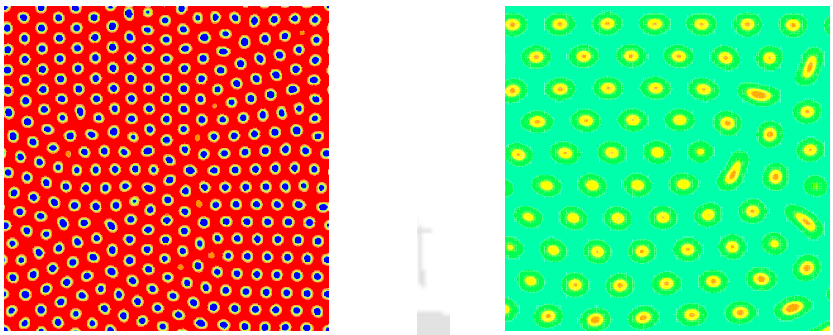

(a) (b)

Figure 6.5: *Barrio-Varea-Aragon-Maini model problem: Spots formation with (a)* $r_1 = 0.056$ *and* $r_2 = 0.3$ *and (b)* $r_1 = 0.009$ *and* $r_2 = 0.25$.

ulated on the square domain $[0, 1] \times [0, 1]$ with a grid of size 101×101. This pattern was obtained on the domain $[0, 2.5] \times [0, 2.5]$ with a grid of size 251×251 and the parameter $D = 0.042$, $\alpha = 0.29$, $\beta = -0.32$, $\gamma = -0.29$ were chosen.

It has been observed that stripe like patterns are revealed only for a very smaller value of r_2 and in all the cases r_1 was considerably larger than r_2. On the contrary, for spot like patterns, the scenario was completely reverse with r_2 greater than r_1.

6.3.3 Gray-Scott model problem (Pearson's form)

6.3.3.1 Formation of Labyrinth and Spot patterns

Our last example is the Gray-Scott model problem which was proposed by P. Gray and S. K. Scott in their works [35, 36].

It may be noted that Alan Turing, in his revolutionary paper [113] prescribed the function F and G in (6.1) to be of the form

$$\begin{aligned} F(u, v) &= \tilde{r}(uv - u - \alpha) \\ G(u, v) &= \tilde{r}(\beta - uv), \end{aligned} \tag{6.10}$$

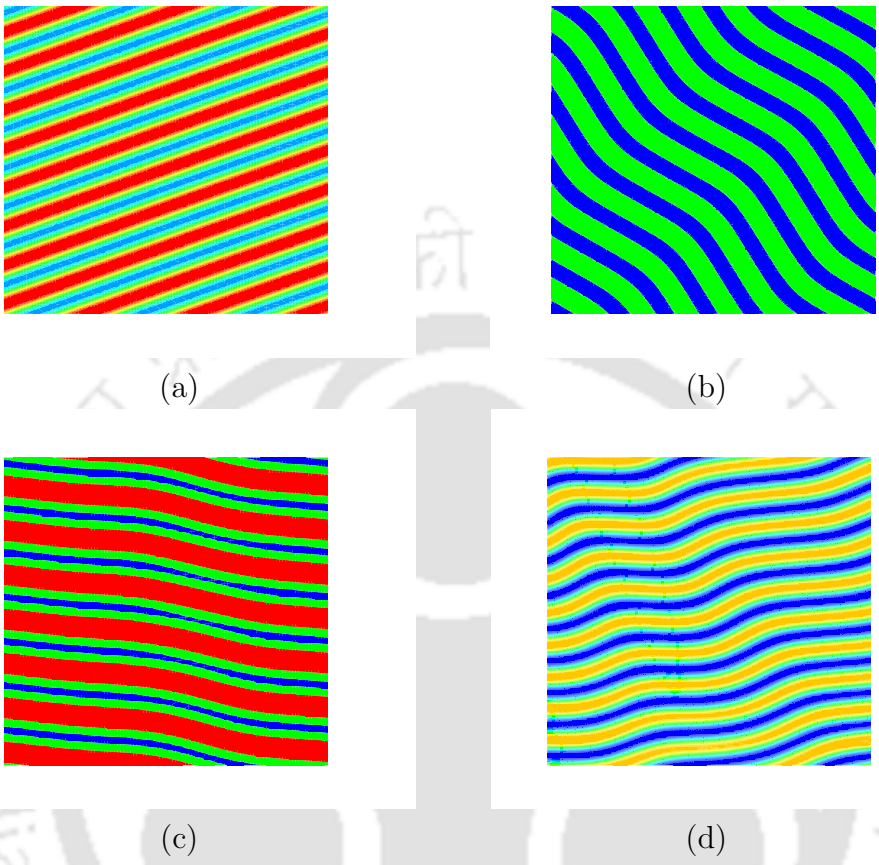

Figure 6.6: *Barrio-Varea-Aragon-Maini model problem: Stripes formation with (a)* $r_1 = 4.20$ *and* $r_2 = 0.005$*, (b)* $r_1 = 2.9$ *and* $r_2 = 0.0035$*, (c)* $r_1 = 3.6$ *and* $r_2 = 0.01$ *and (d)* $r_1 = 6.20$ *and* $r_2 = 0$.

where u and v are the concentrations of the morphogens, $\tilde{r}$ is the reaction rate and α and β are the decay and growth rates of u and v respectively.

In 1993, Pearson [87] described the Gray-Scott reaction model [35, 36] that has the form:

$$\begin{aligned} F(u,v) &= \tilde{r}(u^2 v - (F+\tilde{k})u) \\ G(u,v) &= \tilde{r}(-u^2 v + F(1-v)) \end{aligned} \tag{6.11}$$

where F is the feed rate and $\tilde{k}$ is the degrading rate, $\tilde{r}$ being the same reaction rate.

In this context, we refer to the Turing system (6.1) with the functions F and G given by the system (6.11). The resultant reaction-diffusion equations are the ones considered by Pearson in his work [87]. The equations are of the form:

$$\begin{aligned} \frac{\partial U}{\partial t} &= D_u \nabla^2 U + U^2 V - (F + \tilde{k}) U \\ \frac{\partial V}{\partial t} &= D_v \nabla^2 V - U^2 V + F(1 - V). \end{aligned} \tag{6.12}$$

where the symbols have their usual meaning as described earlier.

To perform our numerical calculations, we consider a system of size 2.5 by 2.5 and the diffusion coefficents are chosen as $D_u = 10^{-5}$ and $D_v = 2.0 \times 10^{-5}$ respectively. Boundary conditions are considered to be periodic and the system was initially placed in the trivial state with $U = 0.0$ and $V = 1.0$.

Following Pearson's work, we perturbed the 20 by 20 grid point area located symmetrically about the center of the domain to $U = 0.25$ and $V = 0.50$ which was further perturbed with $\pm 1\%$ random noise to break the initial square geometry. Simulations were carried out till a non-dimensional time $t = 30,000$, by which steady state has already been achieved. We have employed a grid of size 257×257 and a time step 1.0. Numerical results corresponding to the variable U are illustrated in Figures 6.7 and 6.8. In Figure 6.7, some labyrinth-type patterns were observed while in Figure 6.8, we have shown some of the spot like patterns obtained from our numerical results.

6.3.3.2 Time evolution of spot multiplication:

Next, in order to emulate the time evolution of spots created by Pearson [87] with the Gray-Scott model, we carry out numerical simulations with $D_u = 10^{-5}$, $D_v = 2.0 \times 10^{-5}$, $F = 0.024$ and $k = 0.06$ in the square $0 \leq x \leq 2, \quad 0 \leq y \leq 2$.

Once again, a grid of size 257×257 and a time-step 1.0 were chosen. Analogous to the previous simulations, the entire domian was initially placed in the state

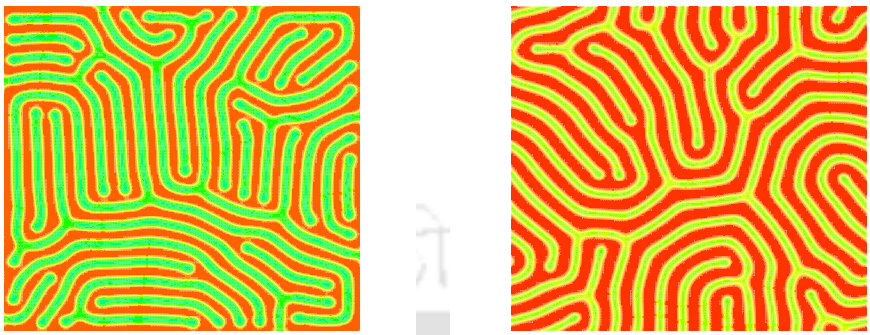

(a) (b)

Figure 6.7: *Gray-Scott model problem: Labyrinth formation with (a)* $F = 0.0355$ *and* $\tilde{k} = 0.0601$*, (b)* $F = 0.0340$ *and* $\tilde{k} = 0.0557$*.*

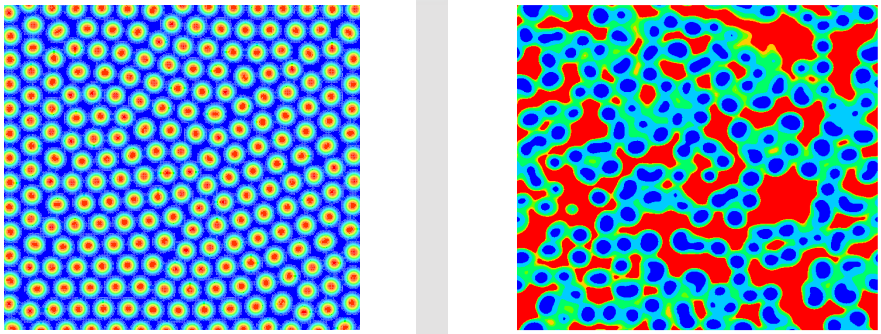

(a) (b)

Figure 6.8: *Gray-Scott model problem: Spots formation with (a)* $F = 0.030$ *and* $\tilde{k} = 0.062$*, (b)* $F = 0.014$ *and* $\tilde{k} = 0.05042$*.*

$U = 0.0, V = 1.0$. A circular area of radius 0.2 and centre at $(1.00, 1.00)$ was then perturbed to

$$U(x,y) = \frac{1}{4} sin^2(4\pi x) sin^2(4\pi y), \quad V(x,y) = 1 - 2U(x,y)$$

Along all boundaries, no-flux boundary condition was used and these Neumann boundary conditions were discretized via a fifth order backward difference formula employed in [96].

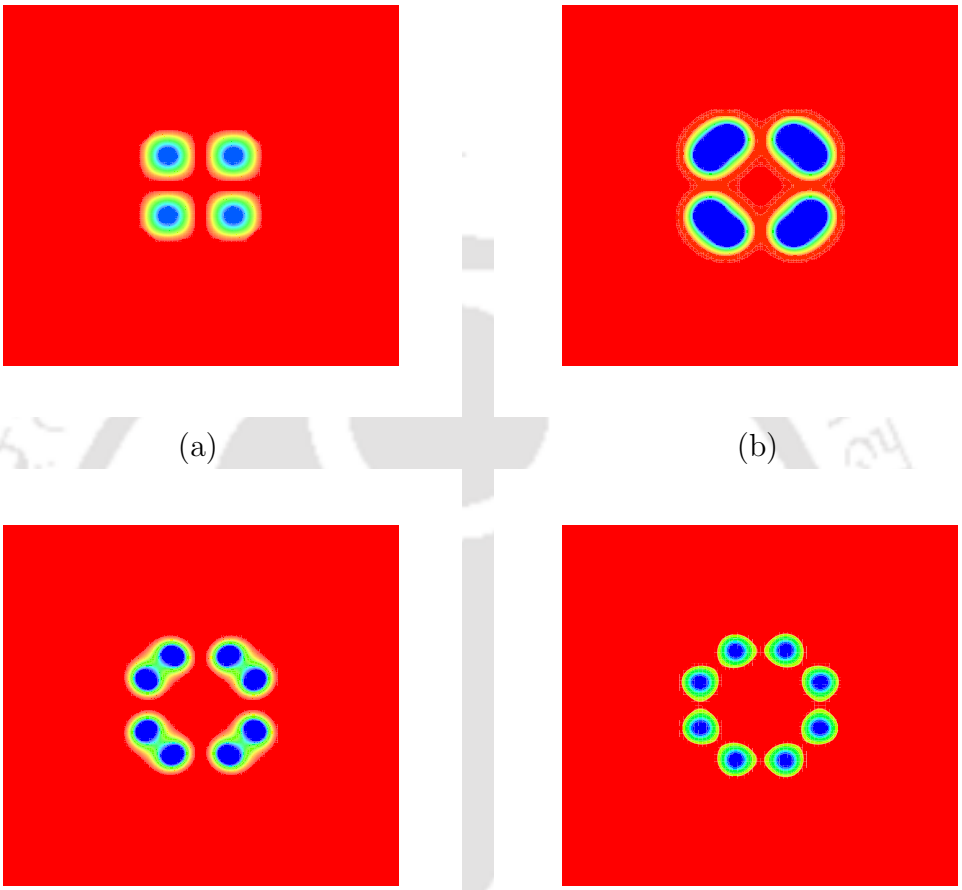

Figure 6.9: *Time evolution of spot multiplication: (a)* $t = 0.0$*, (b)* $t = 350.0$*, (c)* $t = 510.0$ *and (d)* $t = 650.0$*.*

The process of evolution has been shown in Figure 6.9. Initially one can see four spots near the center of the domain (Figure 6.9(a)). Afterwards, these spots move away from each other and get elongated in the direction perpendicular to their motion as in Figure 6.9(b). New spots are clearly visible in Figure 6.9(c) and complete replication of these new spots can be seen in Figure 6.9(d). This replication process is repeated until the entire domain is filled with spots. Once again, the simulated patterns from our computation are in excellent agreement with those obtained by Pearson [87].

6.4 Conclusion:

This chapter details the application of the second order time accurate scheme developed in chapter 5 to problems of pattern formation in nature. Though most of the governing equations in these biological models are of reaction-diffusion type, it poses no problems in implementing our schemes as one requires the switching off the convection term only. A careful undermining into the existing literature reveals that most of the existing numerical methods for solving problems in pattern formation are at most second order accurate in space and time, whereas we have used a scheme which is second order accurate in time and fourth order accurate in space. In the process, the theoretical spatial and temporal accuracies have also been established by applying our scheme to a model problem having analytical solution. Later on, simulations were carried out on more complicated problems of pattern formation and some exciting patterns were observed. The scheme being compact, higher-order accurate and implicit, shows a very good convergence compared to the existing ones. The implicit nature of the scheme has also been exploited in arriving at the steady-state for the Gray-Scott model problem, where time-steps as high as 1.0 has been employed for some of the computations. The robustness of the schemes are exemplified by the efficient transient computation of the spot multiplication in the last numerical test case. This shows that these schemes have very good potential for implementation in more intriguing problems of Mathematical Biology such as vegetation pattern formation, plant morphogenesis and mammals coat patterns etc.

Chapter 7

HOC SCHEMES FOR THE 1D EULER EQUATIONS OF GAS-DYNAMICS

7.1 Introduction

Fluids are classified as incompressible and compressible fluids. The compressible fluid flow phenomena are mainly described by the Euler equations, the study of which in Gas Dynamics gave birth to the theory of hyperbolic conservation laws [19]. Over the decades, numerical computation of nonlinear hyperbolic systems of conservation laws has been an interesting and challenging task amongst the researchers and there have been several attempts on developing numerical schemes for the Euler equations of Gas Dynamics. A majority of these existing numerical methods are lower order accurate in space, for example, the AUSM, HLLC solver, Godunov, Rusanov, Lax-Friedrich, Lax-Wendroff, MacCormack methods etc. In 1988, Saul Abarbanel and Ajay Kumar [1] proposed a higher-order compact method for the simulation of these Euler equations. Later on, several schemes with higher-order accuracy have been proposed for the Euler equations of gas Dynamics [14, 20, 24, 33, 69, 77, 93, 100, 108, 117]. Researchers employed varied formulations to develop higher-order compact schemes for the Euler equations.

HOC schemes developed by Mohamad *et al.* [77] and Shu [100] are based on finite difference formulation. Rezgui *et al.* [93] and Gooch *et al.* [33] developed HOC schemes based on finite volume formulation and the HOC schemes developed by [14, 117] were based on finite element formulation. However, all of these schemes are of only first order accurate in time. In this chapter, we have proposed a new family of HOC schemes for the Euler equations which are fourth-order accurate in space and one of the scheme possesses a second order timewise accuracy [1].

To develop the desired HOC schemes for the Euler equations, we once again utilized the original differential equation to substitute for the leading truncation error terms of the standard central difference approximation as was done earlier for the Navier-Stokes equations. This results in a family of higher order compact schemes for the one dimensional (1D) Euler equations of Gas Dynamics. These schemes are fourth order accurate in space and second or lower order accurate in time depending on the choice of a weighted average parameter. To test the efficiency of our proposed schemes, we first apply it to three shock tube problem of gas dynamics, including the famous SOD shock tube problem. Later on, we apply our proposed schemes to the subsonic-supersonic isentropic flow through a convergent-divergent nozzle (de Laval nozzle). We also compare our solution with the established numerical or analytical solutions and in all the cases our computed numerical results are found to be in excellent match with those of the exact ones.

7.2 1D Euler equations of Gas Dynamics

The 1D Euler equations for inviscid Gas Dynamics are :

$$\frac{\partial \rho}{\partial t} + \nabla \cdot (\rho u) = 0 \quad (\textit{Continuity equation}) \tag{7.1}$$

$$\frac{\partial m}{\partial t} + \nabla \cdot (\rho u^2) + \nabla p = 0 \quad (\textit{Momentum equation}) \tag{7.2}$$

[1] A part of this work has been presented in the *SIAM Annual Meeting, 2014, Chicago, Illinois, USA, Event no. CP15*

$$\frac{\partial E}{\partial t} + \nabla \cdot (u(E+p)) = 0 \quad (\textit{Energy equation}) \tag{7.3}$$

where ρ, u, p and $m = \rho u$ are the density, velocity, pressure and momentum respectively. $E = p/(\gamma - 1) + \frac{1}{2}\rho u^2$ is the internal energy, where γ is the Gas Dynamic constant and $\gamma = 1.4$ for ideal gases.

For entropy we use the relation,

$$\text{Entropy}(S) = \frac{p}{\rho^\gamma}.$$

The above set of Equations (7.1)-(7.3) are together known as the one-dimensional Euler equations of Gas Dynamics.

7.3 Numerical Scheme

Consider the unsteady 1D purely convection equation for a transport variable ϕ in some continuous domain Ω

$$\frac{\partial \phi}{\partial t} + c(x,t)\frac{\partial \phi}{\partial x} = f(x,t) \tag{7.4}$$

where c is the convection coefficient and f is a forcing function such that they are atleast twice differentiable.

The steady-state form of Equation (7.4) may be wriiten as

$$c(x)\frac{\partial \phi}{\partial x} = f(x) \tag{7.5}$$

Considering a uniform mesh of step size h throughout the domain, the standard central difference approximation to Equation (7.5) at the i-th node is given by

$$c\delta_x \phi_i - \tau_i = f_i \tag{7.6}$$

where ϕ_i and δ_x denotes $\phi(x_i)$ and first order central difference operator respectively.

The truncation error τ_i in (7.6) is of the form

$$\tau_i = \left[c\frac{h^2}{6}\frac{\partial^3 \phi}{\partial x^3} \right]_i + O(h^4) \tag{7.7}$$

Now, in order to arrive at a fourth order compact finite difference formulation of (7.5), we differentiate it twice w.r.t. x resulting in the following equation

$$\frac{\partial^2 c}{\partial x^2}\frac{\partial \phi}{\partial x} + 2\frac{\partial c}{\partial x}\frac{\partial^2 \phi}{\partial x^2} + c\frac{\partial^3 \phi}{\partial x^3} = \frac{\partial^2 f}{\partial x^2} \tag{7.8}$$

Transposing the first two terms to the right, equation (7.8) reduces to

$$c\frac{\partial^3 \phi}{\partial x^3} = \frac{\partial^2 f}{\partial x^2} - \frac{\partial^2 c}{\partial x^2}\frac{\partial \phi}{\partial x} - 2\frac{\partial c}{\partial x}\frac{\partial^2 \phi}{\partial x^2} \tag{7.9}$$

Substituting (7.9) in (7.7) and then applying (7.7) on Equation (7.6), we have a fourth order compact approximation for Equation (7.5) on a three-point stencil, which is as follows:

$$\left[A_i \delta_x^2 + B_i \delta_x \right] \phi_i = F_i \tag{7.10}$$

The coefficients A_i, B_i and F_i appearing in Equation (7.10) are of the following forms:

$$A_i = \frac{h^2}{3}\delta_x c_i \tag{7.11a}$$

$$B_i = \left[1 + \frac{h^2}{6}\delta_x^2 \right] c_i \tag{7.11b}$$

$$F_i = \left[1 + \frac{h^2}{6}\delta_x^2 \right] f_i \tag{7.11c}$$

For the unsteady Equation (7.4), the fourth order compact formulation will

be similar to Equation (7.10), but the coefficient c is a function of x and t and the R.H.S. is of the form $f(x,t) - (\partial\phi)/(\partial t)$. Now, if $\triangle t$ is the time-step, then using Equation (7.10) and applying forward differencing for $(\partial\phi)/(\partial t)$, we have the following HOC approximation for the unsteady Equation (7.4).

$$\left[1 + \overbrace{\frac{h^2}{6}\delta_x^2}\right] \delta_t^+ \phi_i + A_i \delta_x^2 \phi_i + B_i \delta_x \phi_i = F_i \tag{7.12}$$

where δ_t^+ is the forward difference operator and the superscript n represents the n-th time level.

Equation (7.12) can be compactly written as

$$\sum\nolimits_{k=-1}^{1} \eta_{i+k} \phi_{i+k}^{n+1} = \sum\nolimits_{k=-1}^{1} \tilde{\eta}_{i+k} \phi_{i+k}^{n} + 6\triangle t F_i \tag{7.13}$$

where $\eta_{i+k} = p_{i+k}$, $\tilde{\eta}_{i+k} = 6q_{i+k} + p_{i+k}$ and

$$\begin{aligned} p_{i-1} = \frac{1}{6};\ \ q_{i-1} &= \triangle t \left(\frac{A_i}{h^2} - \frac{B_i}{2h}\right); \\ p_i = \frac{4}{6};\ \ q_i &= \triangle t \left(\frac{-2A_i}{h^2}\right); \\ p_{i+1} = \frac{1}{6};\ \ q_{i+1} &= \triangle t \left(\frac{A_i}{h^2} + \frac{B_i}{2h}\right). \end{aligned}$$

Now, introduce a weighted average parameter ς such that $t_\varsigma = (1-\varsigma)t^n + \varsigma t^{n+1}$ for $0 \leq \varsigma \leq 1$. Varying ς gives us a family of integrators; forward Euler for $\varsigma = 0$, backward Euler for $\varsigma = 1$ and Crank-Nicholson for $\varsigma = 0.5$. With these, η_{i+k} and $\tilde{\eta}_{i+k}$ can now be written as $\eta_{i+k} = 6\varsigma q_{i+k} + p_{i+k}$ and $\tilde{\eta}_{i+k} = 6(\varsigma - 1)q_{i+k} + p_{i+k}$ respectively, and F_i^n takes the form $\varsigma F_i^{n+1} + (1-\varsigma)F_i^n$. This gives us a family of fourth order compact finite-difference schemes for the unsteady 1D convection equation.

Consequently Equation (7.12) can be written in the matrix form as

$$A\boldsymbol{\phi}^{n+1} = \boldsymbol{g}(\boldsymbol{\phi}^n) + \boldsymbol{F}^n \tag{7.14}$$

where the coefficient matrix A is a tridiagonal sparse matrix and for a grid of size m, A is of size $m \times m$, and ϕ^{n+1}, $g(\phi^n)$ and F^n are m-component vectors.

7.4 Numerical test cases

In order to validate our code and examine the effectiveness of our proposed schemes, we have applied them to three well known 1D shock tube problems and a quasi 1D convergent-divergent nozzle flow.

7.4.1 1D shock tube problem

Figure 7.1 shows a one-dimensional shock tube which is initially filled with a gas (or air) and is divided into two sections by a diaphragm. For the sake of simplicity, we consider a finite domain $-1 \leq x \leq 1$ and the initial discontinuity to be placed at $x = 0$ i.e. the diaphragm is placed at $x = 0$. At time $t = 0$, the two halves of the tube are maintained at different densities, pressures, velocities etc. (state variables). The diaphragm is then broken or removed and gas is allowed to flow and the one-dimensional Euler equations apply.

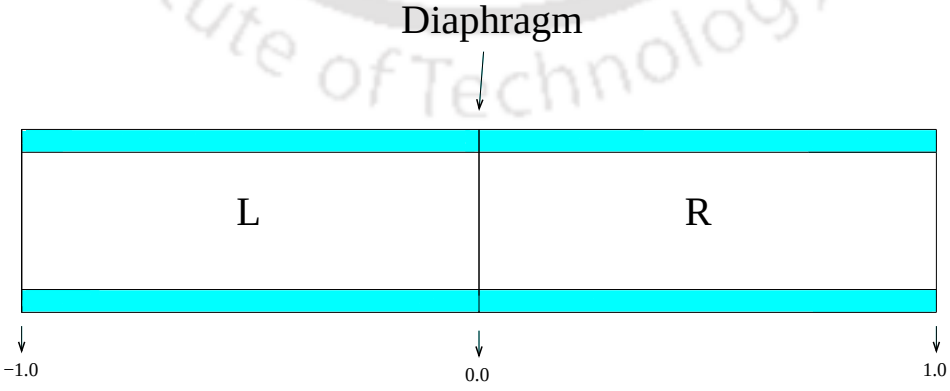

Figure 7.1: 1D Shock Tube Problem in the domain $-1 \leq x \leq 1$ with the initial discontinuity at $x = 0$.

Structure of the flow through the shock tube turns out to be very interesting. The flow structure has been depicted in Figure 7.2. As can be seen from the figure, it gives rise to three distinct wave separating regions in which all the state variables are constant. Across two of these regions there are discontinuities in some of the state variables. A shock wave propagates into the region of lower pressure across which the density and pressure jump to higher values and all of the state variables are discontinuous. This is followed by a contact discontinuity, across which the density is again discontinuous but the velocity and pressure remain constant. The third region of these wave moves in the opposite direction and it has a very different structure. In this region, all of the state variables are continuous and there is a smooth transition. The wave in this region is called an expansion wave. It propagates to the left and decreases the pressure smoothly and continuously as it passes through.

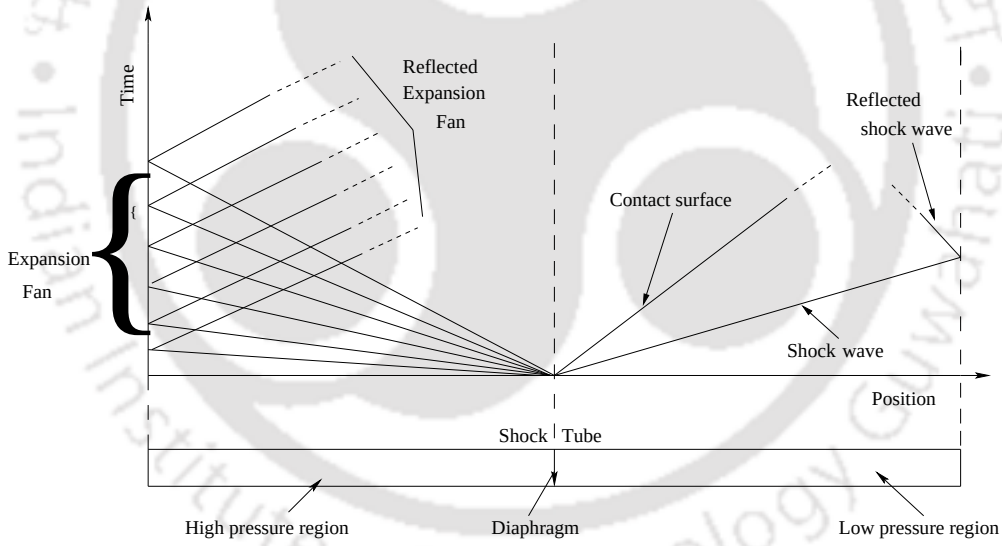

Figure 7.2: Wave Structure of the 1-D Shock Tube Problem in the $x-t$ plane.

The governing set of Equations for the 1D shock tube problem is (7.1)-(7.3), which is not self-contained. So we have to use an equation of state for the closure of the system, which is

$$p = (\gamma - 1)(E - \frac{1}{2}\rho u^2) \tag{7.15}$$

In order to apply our proposed schemes to the shock tube problem, we convert each of the Equations (7.1)-(7.3) to a 1D convection equation as follows:

$$\frac{\partial \rho}{\partial t} + u\frac{\partial \rho}{\partial x} = g_1 \tag{7.16}$$

$$\frac{\partial m}{\partial t} + u\frac{\partial m}{\partial x} = g_2 \tag{7.17}$$

$$\frac{\partial E}{\partial t} + u\frac{\partial E}{\partial x} = g_3 \tag{7.18}$$

where

$$\begin{aligned} m &= \rho u, \\ g_1 &= -\rho\frac{\partial u}{\partial x}, \\ g_2 &= -\frac{\partial p}{\partial x} - m\frac{\partial u}{\partial x} \quad \text{and} \\ g_3 &= -u\frac{\partial p}{\partial x} - p\frac{\partial u}{\partial x} - E\frac{\partial u}{\partial x}. \end{aligned}$$

In the present work, we consider three shock tube problems, namely, Sod's shock tube problem, Lax's shock tube problem and the Strong shock tube problem. In all these computations, the final time-step has been chosen as was considered in Kwatra *et al.* [67].

Computations are carried out on a grid of size 101 with timestep $\triangle t$ is given by the following criteria and we consider, $C_L = \sqrt{(\gamma * p_L/\rho_L)}$ and $C_R = \sqrt{(\gamma * p_R/\rho_R)}$. If $C_L > C_R$, then $\triangle t = (CFL*h)/C_L$; else $\triangle t = (CFL*h)/C_R$, with $\gamma = 1.4$ and $CFL = 0.4$, where C_L and C_R are the speeds of sound in the left and right sections of the shock tube respectively. CFL is the Courant-Friedrichs-Lewy number or Courant number given by $CFL = \frac{u\triangle t}{\triangle x}$, where u is the velocity, $\triangle t$ is the time-step size and $\triangle x$ is the distance between two succesive nodes.

7.4.1.1 SOD Shock Tube problem

The Sod's shock tube problem was introduced by Gary A. Sod in 1978 [103]. It is a shock tube problem with the following initial conditions :

$$x < 0 : p_L = 1.0, \rho_L = 1.0, u_L = 0.0,$$
$$x \geq 0 : p_R = 0.1, \rho_R = 0.125, u_R = 0.0.$$

We compare our computed numerical results with those of the analytical solution and the results obtained are shown in the Figure 7.3.
From the figure, one can see that our results are in very good agreement with the exact solutions and unlike the other available results [1, 24, 77, 67, 108] in the existing literature, our computed results show almost no smearing across all the discontinuities.

7.4.1.2 LAX Shock Tube problem

The Lax's shock tube problem (introduced by P. D. Lax) is similar in nature to Sod's shock tube, except that the initial condition has a discontinuity in the velocity. It's initial conditions are :

$$x < 0 : p_L = 3.528, \rho_L = 0.445, u_L = 0.698,$$
$$x \geq 0 : p_R = 0.571, \rho_R = 0.5, u_R = 0.0.$$

Our simulated results on a 101 grid are depicted in Figure 7.4. From the figure, once again we can see that our results are in very good agreement with the exact solutions with nearly no smearing across all the discontinuities and with very correct propagation of the shocks.

7.4.1.3 Strong Shock Tube problem

The last test case for the shock tube is the Strong shock tube problem. We solve it with the same parameters as was used for the earlier two tests at the

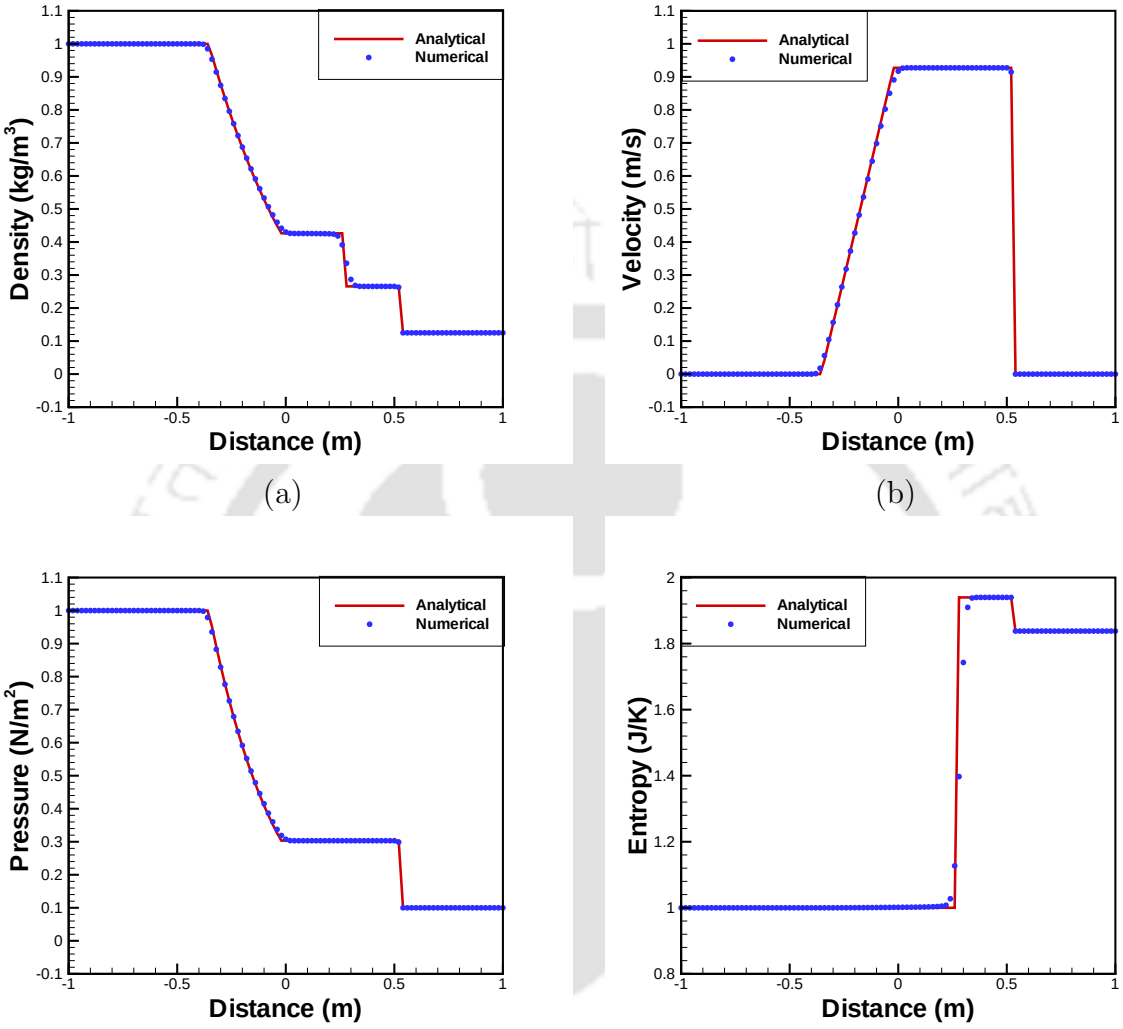

Figure 7.3: *Comparison of numerical and analytical solution of the SOD shock tube problem at non-dimensional time = 0.15 units : (a) density, (b) velocity, (c) pressure and (d) entropy.*

non-dimensional time, $t = 2.5 \times 10^{-6}$. This problem poses initial conditions that generates a supersonic shock :

$$x < 0 : p_L = 10^{10}, \rho_L = 1.0, u_L = 0.0,$$

$$x \geq 0 : p_R = 0.1, \rho_R = 0.125, u_R = 0.0.$$

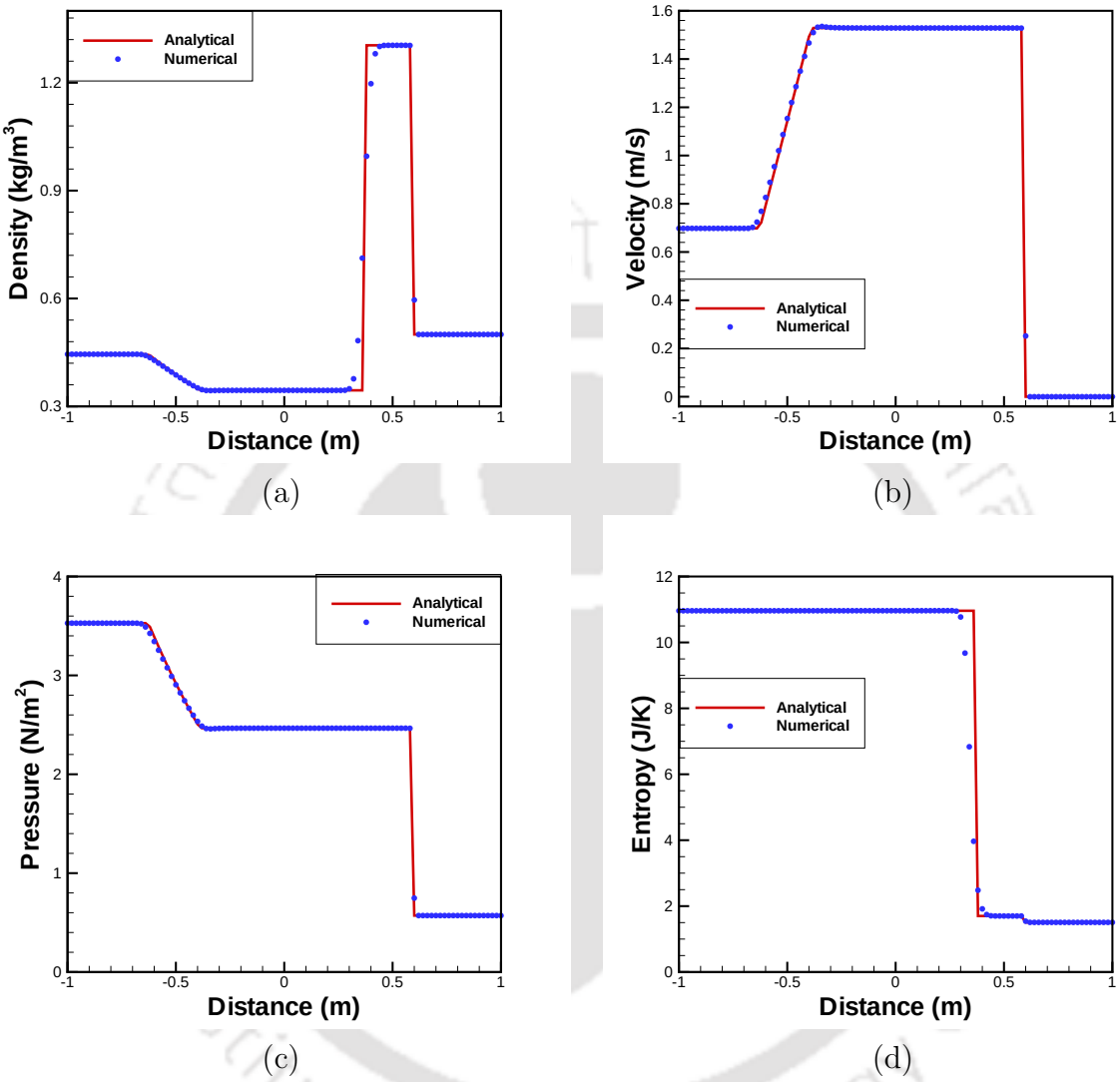

Figure 7.4: *Comparison of numerical and analytical solution of the LAX shock tube problem at non-dimensional time = 0.12 units : (a) density, (b) velocity, (c) pressure and (d) entropy.*

Our computed results for the Strong shock tube problem are shown in Figure 7.5. The figure once again justifies that for a very small grid as coarse as 101, our results are in very good agreement with the analytical ones having almost no smear across all the shocks and discontinuities.

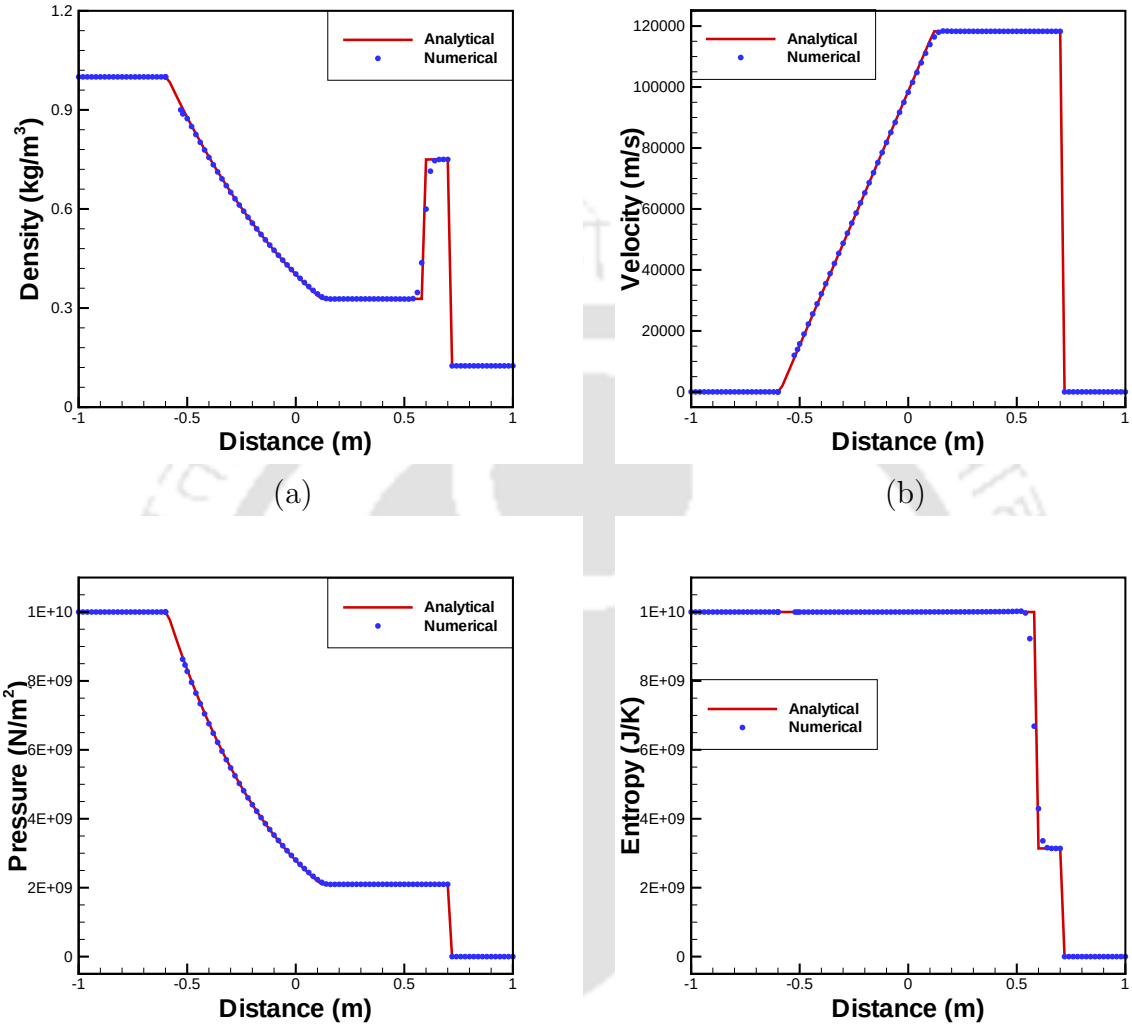

Figure 7.5: *Comparison of numerical and analytical solution of the Strong shock tube problem at non-dimensional time* $= 2.5 \times 10^{-6}$ *units : (a) density, (b) velocity, (c) pressure and (d) entropy.*

7.4.2 The 1D Converging-Diverging Nozzle Flow (de Laval nozzle flow)

Our next test case is the 1D isentropic flow in a convergent-divergent nozzle as shown in the Figure 7.6. The cross section area of the nozzle, A, changes as a function of distance x. It has been assumed that the flow at the inlet to the

nozzle comes from some reservoir of large cross sectional area (theoretically infinite) and hence very small velocity. The pressure and temperature at the inlets are therefore the total pressure and total temperature respectively (say P_0 and T_0, as they are the stagnation values). In the convergent section of the nozzle, the flow is locally subsonic while it is supersonic in the divergent section of the nozzle. At the throat, the flow is sonic i.e. Mach number, $M = 1$, which means that at this location the local velocity is equal to the local speed of sound. We assume a quasi-one-dimensional flow. A brief description of the flow geometry can be found in [53].

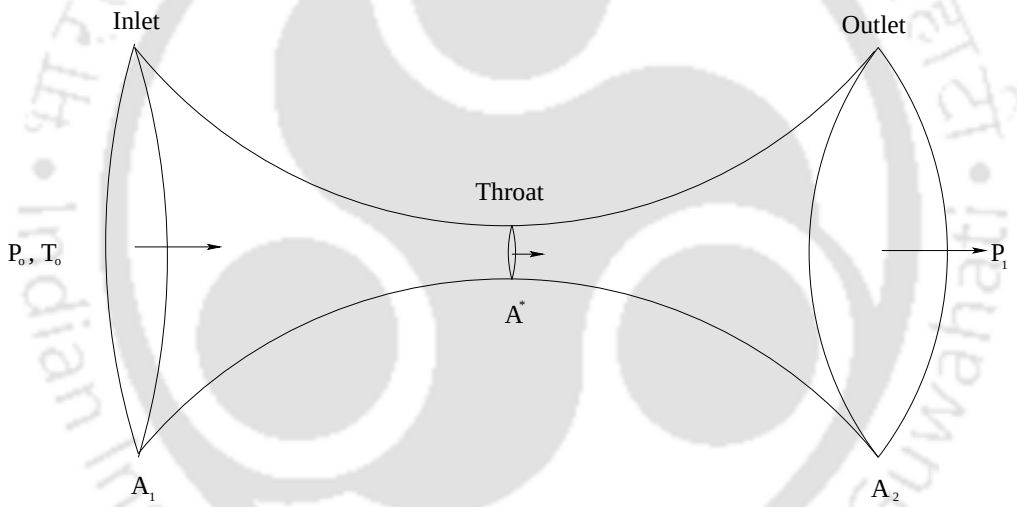

Figure 7.6: A convergent-divergent nozzle.

Let $A(x) = 1 + 2.2(x - 1.5)^2$ for $0 \leq x \leq 3$ be the area of cross-section of the nozzle, where $x = 1.5$ is the throat of the nozzle.

The governing equations of this problem can be derived from the integral form of the continuity, momentum and energy equations as given in [53].

Continuity equation:

$$\frac{\partial \rho}{\partial t} + \rho \frac{\partial V}{\partial x} + \rho V \frac{\partial lnA}{\partial x} + V \frac{\partial \rho}{\partial x} = 0, \tag{7.19}$$

Momentum equation:

$$\frac{\partial V}{\partial t} + V\frac{\partial V}{\partial x} + \frac{1}{\gamma}\left(\frac{\partial T}{\partial x} + \frac{T}{\rho}\frac{\partial \rho}{\partial x}\right) = 0, \tag{7.20}$$

Energy equation:

$$\frac{\partial T}{\partial t} + V\frac{\partial T}{\partial x} + (\gamma - 1)T\left(\frac{\partial V}{\partial x} + V\frac{\partial lnA}{\partial x}\right) = 0, \tag{7.21}$$

where V is the flow velocity, T is the temperature and all the other parameters have usual meanings.

Once again, we convert each of these equations into 1D convection equations, reducing the governing set of equations as follows:

Continuity equation:

$$\frac{\partial \rho}{\partial t} + V\frac{\partial \rho}{\partial x} = h_1, \tag{7.22}$$

Momentum equation:

$$\frac{\partial V}{\partial t} + V\frac{\partial V}{\partial x} = h_2, \tag{7.23}$$

Energy equation:

$$\frac{\partial T}{\partial t} + V\frac{\partial T}{\partial x} = h_3, \tag{7.24}$$

where

$$h_1 = -\left[\rho\frac{\partial V}{\partial x} + \rho V\frac{\partial lnA}{\partial x}\right],$$
$$h_2 = -\left[\frac{1}{\gamma}\left(\frac{\partial T}{\partial x} + \frac{T}{\rho}\frac{\partial \rho}{\partial x}\right)\right] \text{ and}$$
$$h_3 = -\left[(\gamma - 1)T\left(\frac{\partial V}{\partial x} + V\frac{\partial lnA}{\partial x}\right)\right].$$

Boundary and Initial Conditions:

The initial conditions (at time $t = 0$) were chosen as was given in [53], which

are :

$$\rho = 1 - 0.3146x,$$

$$T = 1 - 0.2314x,$$

$$V = (0.1 + 1.09x)T^{\frac{1}{2}}$$

Density boundary conditions :

$$\text{At inlet} : \rho_1 = 1,$$

$$\text{At outlet} : \left(\frac{\partial \rho}{\partial x}\right)_N = \left(\frac{\partial \rho}{\partial x}\right)_{N-1}.$$

Velocity boundary conditions :

$$\text{At inlet} : V_1 = 2V_2 - V_3,$$

$$\text{At outlet} : V_N = 2V_{N-1} - V_{N-2}.$$

Note that the value of V_1 changes with time and is calculated from the information provided by the flow-field solution over the interior points. So, V_1 is calculated by using linear extrapolation from V_2 and V_3 [53].

Temperature boundary conditions :

$$\text{At inlet} : T_1 = 1,$$

$$\text{At outlet} : T_N = 2T_{N-1} - T_{N-2}.$$

We choose a grid of size 31 and $\triangle t$ is chosen as the minimum of dt_i where $dt_i = \text{CFL}\frac{h}{(\sqrt{T_i}+u_i)}$. CFL is chosen as 0.5 and the total time steps is chosen as 1400. Figure 7.7 shows our obtained numerical solutions. From the figure, one can see that our simulated results are in very close agreement with those of [122].

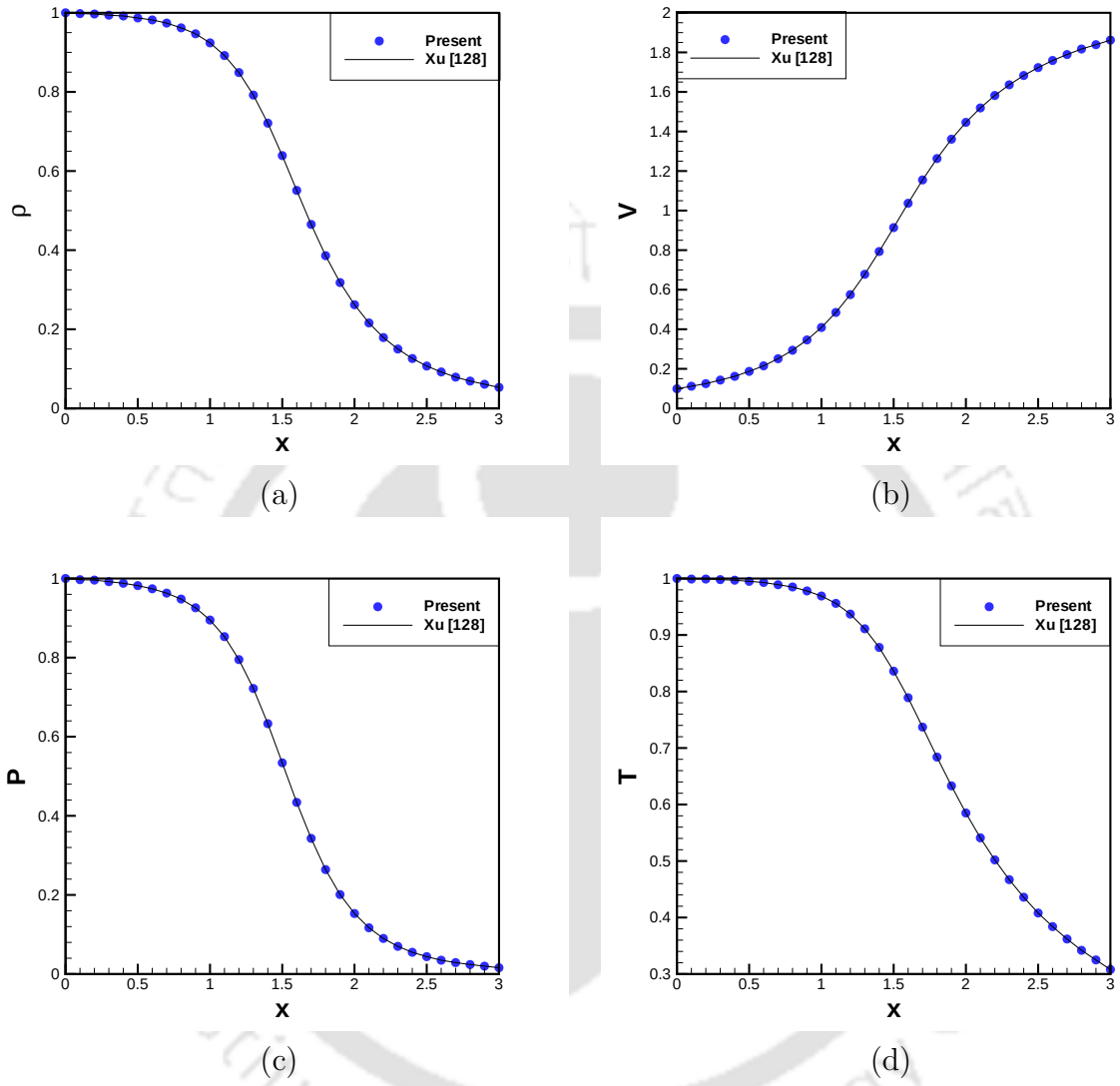

Figure 7.7: *Numerical solution of the de-laval nozzle flow : (a) density, (b) velocity, (c) pressure and (d) temperature.*

7.5 Conclusion

A family of implicit HOC finite difference schemes has been developed with weighted time discretization to solve the one-dimensional Euler equations of Gas Dynamics. The schemes are second or first order accurate in time according as $\varsigma = 0.5$ or otherwise, and fourth order accurate in space. The robustness of the schemes have been illustrated by their application to some famous shock

tube problems and de Laval nozzle problem of Gas Dynamics. In all the shock tube problems, for a grid as coarse as 101, our computed numerical solutions are found to be in excellent match with those of the exact solutions and established solutions. For the shock tube problem, it has been observed that the present schemes can capture the shock front and the contact discontinuity with correct locations and satisfactory sharpness. Unlike the earlier proposed HOC schemes, the numerical results obtained by the present HOC schemes show almost no smearing across all the discontinuities. The schemes are therefore found to be very efficient and accurate. In the de Laval nozzle problem, our numerical results show a very good agreement with existing results even on a much coarser grid of size 31. Overall we consider the present method as an important addition to the existing solution procedures for non-linear hyperbolic conservation laws. These schemes have very good potential for efficient implementation in two-dimensional Euler equations, including the two-dimensional shock tube problems.

Chapter 8

CONCLUDING REMARKS AND SCOPE FOR FUTURE WORK

This chapter is concerned with summing up of the thesis highlighting its major achievements. We will also throw some light on the scopes for future work from the present study.

8.1 Concluding remarks

This dissertation is concerned with the application and development of compact schemes in some diverse fields of computational fluid dynamics research. Application of some existing compact finite difference schemes have been done to examine the global two-dimensional stability of incompressible viscous flows in general and lid-driven cavity flows and flow past an inclined square cylinder in particular. Some new HOC finite difference algorithms are then developed for the 3D nonlinear convection-diffusion-reaction equations. These schemes are first tested on simple convection-diffusion-reaction equations to have an understanding of their mode of working, merits and demerits. They are then applied to problems governed by the 3D Navier-Stokes equations and in particular, the 3D lid-driven cavity flow. One of these schemes is then utilized to simulate the pattern formations in nature. Moreover, a family of implicit HOC schemes has also been developed for the 1D Euler equations of compressible

fluids. These schemes are then applied to the shock tube problem and de Laval nozzle problem. In almost all the cases, one can see an excellent comparison between our computed numerical results and the analytical or established numerical results. In what follows, first the work carried out in the thesis is described briefly so that insightful comments can be made on it later.

Problem 1: An existing HOC Scheme has been applied to analyze the global two-dimensional stability of the two-sided staggered lid-driven cavity flow for both parallel and anti-parallel motions of lids. This approach has been utilized for the first time to construct the generalized eigenvalue problem in order to identify the critical parameters for incompressible viscous flows such as the staggered cavity. Critical parameters have been identified and extensive grid convergence studies are provided including the streamlines corresponding to the eigenmodes over one complete periodic cycle over two grids. Richardson's extrapolation and Lagrange interpolation of the data has also been carried out which confirmed the theoretical rate of convergence and justified the critical Reynolds number. Extensive studies through phase plane and spectral density analysis have also been carried out and results are presented for a wide range of Reynolds number to study the nature of the flow. Qualitative and quantitative results are provided for some Reynolds number for which no results are available in literature.

Problem 2: An earlier existing second order spatially and temporally accurate compact scheme for the biharmonic formulation of the transient Navier-Stokes equations has been employed to investigate the flow stabilities in some more incompressible viscous fluid flow problems, namely, the simple (one-sided) square LDC, the two-sided cross LDC flows and the flow past an inclined square cylinder.This is probably the first time that the ψ-v formulation of the N-S equations has been utilized for the global stability of a flow. A comprehensive study has also been carried out which shows that compared to the streamfunction-vorticity approach, this approach solves the eigenvalue problem with a significantly small CPU time, thus drastically reducing the computational effort. Moreover, it is also notable that, for the cross LDC flow, no global two-dimensional stability analysis is available with any of the numerical

methods in the existing literature. It is therefore, a very first attempt to carry out such analysis.

Problem 3: We have developed a class of fourth order spatially accurate higher order compact schemes for the transient three-dimensional convection-diffusion-reaction equations. The proposed schemes are second or lower order accurate in time depending on the choice of the weighted average parameter. Fundamental studies of these proposed schemes has been carried out which includes the dispersion-dissipation Fundamental studies of these proposed schemes has been carried out which includes the convergence analysis (in the discrete Euclidean norm (L^2-norm)), dispersion-dissipation analysis and Fourier stability analysis. The spatial and temporal accuracy of the schemes have also been numerically verified. It has been observed that our proposed schemes have less dissipative errors and are unconditionally stable. To test the efficiency of the proposed schemes, they are applied to unsteady 3D convection-diffusion-reaction problems with both constant as well as variable convection-reaction coefficients and results obtained are found to be superbly in agreement with the analytical solutions. Further, to check the robustness of the proposed schemes, we apply them to the benchmark problem of 3D lid-driven cubical cavity flow governed by the unsteady Navier-Stokes (N-S) equations and compare our results with established numerical results, which gives us an excellent comparison.

Problem 4: The schemes developed are then reduced to solve the two-dimensional reaction-diffusion problems for pattern formation in nature. Our code has been validated by applying it to well known problems in the existing literature of Mathematical Biology and comparing our results. In the process, spatial and temporal order of accuracy have also been established. The code has been further applied to four well known model problems and excellent simulation of various patterns, viz. spikes, spots, stripes and labyrinths has been observed, exemplifying the robustness of the schemes.

Problem 5: Lastly, we have developed a new family of higher order compact schemes for the solution of unsteady one dimensional (1D) Euler equations of

Gas Dynamics (compressible flows). These schemes are implicit, fourth order accurate in space and at most second order accurate in time depending on a weighted average parameter. To test the efficiency of our proposed schemes, we apply them to three different shock tube problem of gas dynamics, including the famous SOD shock tube problem. In all the cases, for a grid as coarse as 101, our computed numerical solutions are found to be in excellent match with the exact solutions. Later on, we apply it to the quasi one-dimensional convergent-divergent nozzle flow problem (de Laval flow) and observed that our computed numerical results show very accuate results on a very coarse grid of size 31. Our simulted results are then compared with existing numerical results which also shows a very good agreement. Overall the schemes are found to be very efficient and accurate.

The work, therefore achieves with great success of the two major objectives, namely application and development of compact schemes in some diverse directions. Application is mainly confined to the analysis of global two-dimensional stability of some incompressible viscous fluid flow problems. Development of new HOC schemes are done for the 3D transient convection-diffusion-reaction and for the unsteady 1D Euler equations. Modification of the schemes for the 3D transient schemes to simulate pattern formations in Mathematical Biology is a testimony of the potential of these proposed HOC schemes. In what follows the major achievements of the thesis will be highlighted in the form of observations and comments, further substantiating the claim of objectives having been achieved.

(i) The global 2D stability analysis with the HOC scheme for the streamfunction-vorticity formulation of N-S equations reveals the periodic nature of flow for higher Reynolds number which leans towards a chaotic nature with the increase in Reynolds number.

(ii) The global 2D stability analysis with the compact scheme for the streamfunction-velocity formulation of N-S equations shows a very good agreement with the existing literatures for the simple lid-driven cavity and the flow past an inclined square cylinder. Since, the formulation involves only one equation,

which is for the streamfunction only, it drastically reduces the computational effort for solving the linearized eigenvalue problem compared to the other methods. The method has also been utilized for the unconquered problem of cross lid-driven cavity flow which provides us the critical Reynolds number beyond which the flow nature changes. This method has a very good potential for stability analysis of more intriguing problems of computational fluid dynamics research.

(iii) The HOC schemes developed for the transient 3D convection-diffusion-reaction equations involve only 19 points at the current time-level incontrast to the earlier existing HOC schemes. This shows that it requires a small stencil compared to the existing HOC schemes. Moreover, the schemes are unconditionally stable and are of fourth-order accuracy in space and second-order accuracy in time. To demonstrate its high accuracy and efficiency numerical experiments have been performed. Therefore, our proposed schemes inhibit various important features, namely, computationally economical, consumes less memory, highly accurate, compactness and implicitness. Although, HOC finite difference schemes are seen for the three-dimensional convection-diffusion equations, a very few of them are available in the existing literature for the three-dimensional convection-diffusion-reaction equations and there is a distinct void in this area. The HOC schemes developed by us for the transient 3D convection-diffusion-reaction equations (applicable also to 3D Navier-Stokes equations) can be considered a notable step in filling this void. One important factor that determines the merit of an implicit scheme is the time-wise accuracy and one of the proposed schemes is second order accurate in time and is therefore an important development.

(iv) Most of the existing numerical works pertaining to pattern formation revolve around numerical methods which are of atmost second order accurate and mostly explicit in nature. Due to the implicitness, fourth order accuarateness and unconditionally stable, we can use a larger time-step to reach the final time or the steady state. Therefore, we intended to apply this scheme to simulate some biological reaction-diffusion model problems. In order to validate the 2D code for pattern formation in nature, we apply it some existing problems in

the literaure and then to the Gierer-Meinhardt model problem, Barrio-Varea-Aragon-Maini model problem and the Gray-Scott model problem. Overall we consider this procedure as an important addition to the existing solution procedures for problems of pattern formation in Mathematical Biology.

(v) In the field of computational fluid dynamics, many numerical algorithms have been developed to simulate inviscid, compressible flows problems. Among those most famous and relevant are based on flux vector splitting and Godunov-type schemes. However, in the present work, we, develop a new family of implicit high-order compact (HOC) finite difference solver for one-dimensional Euler equation. This method is quite simple as compared to the existing numerical methods in Gas Dynamics. Apart from this, our proposed schemes are very accurate on much coarser grids. The code developed has been implemented on some famous problems like the SOD shock tube problem and the de Laval nozzle problem. For the shock tube problem, our method shows almost no smearing across all the discontinuities while for the quasi 1D convergent-divergent nozzle problem, our method shows a very good agreement with the existing literature for a much coarser grid of size only 31. Overall, our schemes are found to be very accurate, robust and efficient.

8.2 Scope for future work

The work also opens up a host of interesting research possibilities, the major ones of which are listed below.

(i) Although, the two-dimensional staggered lid-driven cavity flow has been an interesting topic amongst the researchers for decades, its 3D counterpart has not been discussed till date. Therefore the numerical simulation of the 3D staggered lid-driven cavity and its stability analysis seems to very good work to be discussed. Moreover, the three-dimensional linear stability analysis of the two-dimensional staggered LDC also seems to be an interesting subject of research.

(ii) The successful implementation of the compact biharmonic formulation on analyzing the global 2D stability analysis of incompressible viscous flows on three different problems involving interesting physics can open the flood gates for examining the stability of more intriguing problems of fluid dynamics.

(iii) One of the transient scheme developed for the 3D convection-diffusion-reaction equations is of fourth accurate in space and second order accurate in time. Whether this scheme in some modified form can be extended to direct numerical simulation (DNS) of turbulent flows seems to be an interesting and important area of research. Moreover, application of our proposed schemes to the problem of natural convection in a box also seems to be a very interesting topic of research.

(iv) Since the application of our schemes to simulate pattern formation in nature shows very good results and patterns. Therefore, it would be interesting to modify our code to simulate patterns in domains beyond rectangular, some of which are the circular, fish-like and tail-like domains. Meanwhile, it also seems to be interesting to examine the implementation of these HOC schemes on Turing pattern formation in problems that include a glucolysis reaction mechanism.

(v) Extension of our code developed for the 1D Euler equations to simulate 2D Euler equations is an interesting arena that could be performed later on. Because of higher order accurateness, the code in 2D extension appears to have good potential for efficient computation of physically meaningful flows in two-dimensional Gas Dynamics. Future work in this direction seems to be fraught with interesting possibilities.

Bibliography

[1] S. Abarbanel and A. Kumar. Compact High-Order Schemes for the Euler Equations. *Journal of Scientific Computing*, 3(3):275–288, 1988.

[2] S. Abdallah. Numerical solutions for the incompressible Navier-Stokes equations in primitie variables using a non-staggered grid ii. *Journal of Computational Physics*, 70:193–202, 1987.

[3] C.K. Aidun, N.G. Triantafillopoulos, and J.D. Benson. Global stability of a lid-driven cavity with through-flow: Flow visualization studies. *Physics of Fluids A*, 3:2081–2091, 1991.

[4] S. Albensoeder, H.C. Kuhlmann, and H.J. Rath. Multiplicity of steady two-dimensional flows in two-sided lid-driven cavities. *Theoretical and Computational Fluid Dynamics*, 14:223–241, 2001.

[5] U. Ananthakrishnaiah, R. Manohar, and J.W. Stephenson. Fourth-order finite difference methods for three-dimensional general linear elliptic problems with variable coefficients. *Numerical Methods for Partial Differential Equations*, 33:229–240, 1987.

[6] D.A. Anderson, J.C. Tannehil, and R.H. Pletcher. *Computational Fluid Mechanics and Heat Transfer*. Hemisphere Publishing Corporation, New York, USA, 1984.

[7] R. Anguelov, J.M.S. Lubuma, and S.K. Mahudu. Qualitatively stable finite difference schemes for advection–reaction equations. *Journal of Computational and Applied Mathematics*, 158(1):19–30, 2003.

[8] J.L. Aragon, C. Varea, R.A. Barrio, and P.K. Maini. Spatial patterning in modified Turing systems: Application to pigmentation patterns in marine fish. *FORMA*, 13(3):213–221, 1998.

[9] R. Asai, E. Taguchi, Y. Kume, M. Saito, and S. Kondo. Zebrafish Leopard gene as a component of the putative reaction-diffusion system. *Mechanism of development*, 89:87–92, 1999.

[10] F. Auteri, N. Parolini, and L. Quartapelle. Numerical investigation on the stability of singular driven cavity flow. *Journal of Computational Physics*, 183:1–25, 2002.

[11] V. Babu and S.A. Korpela. Numerical solution of the incompressible three-dimensional Navier–Stokes equations. *Computers and Fluids*, 23(5):675–691, 1994.

[12] J.B. Bard. DA model for generating aspects of zebra and other mammalian coat patterns. *J Theor Biol*, 93:363–385, 1981.

[13] R.A. Barrio, C. Varea, J.L. Aragon, and P.K. Maini. A Two-dimensional Numerical Study of Spatial Pattern Formation in Interacting Turing Systems. *Bulletin of Mathematical Biology*, 61:483–505, 1999.

[14] F. Bassi and S. Rebay. High-order accurate discontinuous finite element solution of the 2D Euler equations. *Journal of Computational Physics*, 138(2):251–285, 1997.

[15] C.H. Blohm and H.C. Kuhlmann. The two-sided lid-driven cavity: experiments on stationary and time-dependent flows. *Journal of Fluid Mechanics*, 450:67–95, 2002.

[16] V.B.L. Bopanna and J.S.B. Gajjar. Global flow instability in a lid-driven cavity. *International Journal for Numerical Methods in Fluids*, 62(8):1–27, 2010.

[17] J.M. Cadou, M. Potier-Ferry, and B. Cochelin B. A numerical method for the computation of bifurcation point in fluid mechanics. *European Journal of Mechanics Fluids*, 25:234–254, 2006.

[18] A.B. Cortes and J.D. Miller. Numerical experiments with the lid driven cavity flow problem. *Computers and Fluids*, 23(8):1005–1027, 1994.

[19] R. Courant, E. Issacson, and M. Rees. On the solution of nonlinear hyperbolic differential equations by finite differences. *Communications in Pure and Applied Mathematics*, 5:243–255, 1952.

[20] X. Deng and H. Maekawa. Compact High-Order Accurate Nonlinear Schemes. *Journal of Computational Physics*, 130(1):77–91, 1997.

[21] S.C.R. Dennis and J.D. Hudson. Compact h^4 finite difference approximations to operators of Navier-Stokes type. *Journal of Computational Physics*, 85:390–416, 1989.

[22] J. Dieudonne. *Foundations of Modern Analysis*. Academic Press, Inc., New York, USA, 1960.

[23] J.K. Dukowicz and J.D. Ramshaw. Tensor viscosity method for convection in numerical fluid dynamics. *Journal of Computational Physics*, 32:71–79, 1979.

[24] A.M. Elfaghi, W. Asrar, and A.A. Omar. Higher order compact-flowfield dependent variation (HOC-FDV) solution of one-dimensional problems. *Engineering Applications of Computational Fluid Mechanics*, 4(3):434–440, 2010.

[25] B. Ermentrout. Stripes or Spots? Nonlinear Effects in Bifurcation of Reaction-Diffusion Equations on the Square. *In the proceedings of Mathematical and Physical Sciences*, 434(1891):413–417, 1991.

[26] C.R. Ethier and D.A. Steinman. Exact fully 3D Navier-Stokes solutions for benchmarking. *International Journal for Numerical Methods in Fluids*, 19:369–375, 1994.

[27] Y. Feldman and A.Y. Gelfgat. Oscillatory instability of a three-dimensional lid-driven flow in a cube. *Physics of Fluids*, 22:093602, 2010.

[28] V. Fleury. Branching morphogenesis in a reaction-diffusion model. *Physical Review E*, 61(4):41–56, 2000.

[29] A. Fortin, M. Jardak, J.J. Gervais, and R. Pierre. Localization of Hopf bifurcations in fluid flow problems. *International Journal for Numerical Methods in Fluids*, 24(11):1185–1210, 1997.

[30] Y. Ge, Z.F. Tian, and J. Zhang. An exponential high-order compact ADI method for 3D unsteady convection–diffusion problems. *Numerical Methods for Partial Differential Equations*, 29(1):186–205, 2013.

[31] U. Ghia, K.N. Ghia, and C.T. Shin. High-Re solutions for incompressible flow using the navier-stokes equation and a multigrid method. *Journal of Computational Physics*, 48:387–411, 1982.

[32] B.B. Gogoi and J.C. Kalita. On the global instability of square and cross lid-driven cavity flows with a pure stream-function-velocity (ψ-v) approach. *In the Proceedings of the International Conference on Computer Aided Engineering (CAE 2013), IIT Madras, Chennai, India*, pages 314–319, 2013.

[33] C.O. Gooch, A. Nejat, and K. Michalak. Obtaining and Verifying High-Order Unstructured Finite Volume Solutions to the Euler Equations. *AIAA Journal*, 47(9):2105–2120, 2009.

[34] J.W. Goodrich, K. Gustafson, and K. Halasi. Hopf bifurcation in the driven cavity. *Journal of Computational Physics*, 90:219–261, 1990.

[35] P. Gray and S.K. Scott. Sustained oscillations and other exotic patterns of behaviour in isothermal reactions. *Journal of Physical Chemistry*, 89(1):22–32, 1985.

[36] P. Gray and S.K. Scott. *Chemical Oscillations and Inestability: Nonlinear Chemical Kinetics*. Oxford University Press, London, UK, 1990.

[37] P.M. Gresho. Some current cfd issues relevant to the incompressible Navier-Stokes equations. *Computational Methods in Applied Mechanical Engineering*, 87:201–252, 1991.

[38] T.H. Gronwall. Note on the Derivatives with Respect to a Parameter of the Solutions of a System of Differential Equation. *Annals of Mathematics*, 20(4):292–296, 1919.

[39] B.A. Grzybowski, K.J.M. Bishop, C.J. Campbell, M. Fialkowski, and S.K. Smoukov. Micro- and nanotechnology via reaction-diffusion. *Soft Matter*, 1:114–128, 2005.

[40] M.M. Gupta and J.Kouatchou. Symbolic derivation of finite difference approximations for the three-dimensional poisson equation. *Numerical Methods for Partial Differential Equations*, 14(5):593–606, 1998.

[41] M.M. Gupta and J.C. Kalita. A New Paradigm for Solving Navier-Stokes Equations: Streamfunction-Velocity Formulation. *Journal of Computational Physics*, 207(1):52–68, 2005.

[42] M.M. Gupta, R.P. Manohar, and J.W. Stephenson. A single cell high order scheme for the convection-diffusion equation with variable coefficients. *International Journal for Numerical Methods in Fluids*, 4(7):641–651, 1984.

[43] K. Gustafson and K. Halasi. Vortex dynamics of cavity flows. *Journal of Computational Physics*, 64:279–319, 1986.

[44] K. Gustafson and K. Halasi. A study of finite difference approximations to steady-state, convection-dominated flow problems. *Journal of Computational Physics*, 70:271–283, 1987.

[45] I. Harari and T.J.R. Hughes. Finite element methods for the Helmholtz equation in an exterior domain : Model problems. *Computer Methods in Applied Mechanics and Engineering*, 87(1):59–96, 1991.

[46] M. Hinatsu and J.H. Ferziger. Numerical computation of unsteady incompressible flow in complex geometry using a composite multigrid technique. *International Journal for Numerical Methods in Fluids*, 13(8):971–997, 1991.

[47] J.D. Hoffman. *Numerical Methods for Engineers and Scientists*. McGraw-Hill, Inc., Singapore, 1993.

[48] J.D. Hoffmann. *Numerical methods for engineers and scientists*. Marcel Dekker Inc., New York, USA, 2001.

[49] F. Ilinca and D. Pelletier. Positivity preservation and adaptive solution for the k-model of turbulence. *AIAA Journal*, 36(1):44–50, 1998.

[50] B.N. Jiang, T.N. Lin, and L.A. Povinelli. Large-scale computation of incompressible viscous flow by least-squares finite element method. *Computational Methods in Applied Mechanical Engineering*, 114:213–231, 1994.

[51] H. Johnston and J.G. Liu. A finite difference method for incompressible flow based on local pressure boundary conditions. *Journal of Computational Physics*, 180:120–154, 2002.

[52] E.C. Gartland, Jr. Discrete weighted mean approximation of a model convection-diffusion equation. *SIAM Journal on Scientific and Statistical Computing*, 3(4):460–472, 2012.

[53] J.D. Anderson, Jr. *Computational Fluid Dynamics*. McGraw-Hill, Inc., New York, USA, 1995.

[54] H.S. Jung, P.H. Francis-West, and R.B. Widelitz. Local inhibitory action of bmps and their relationships with activators in feather formation: Implications for periodic patterning. *Dev Biol*, 196:11–23, 1998.

[55] J.C. Kalita and P. Chhabra. An improved $(9, 5)$ higher order compact scheme for the transient two-dimensional convection-diffusion equation. *International Journal for Numerical Methods in Fluids*, 51:703–717, 2006.

[56] J.C. Kalita, D.C. Dalal, and A.K. Dass. A class of higher order compact schemes for the unsteady two-dimensional convection-diffusion equation with variable convection coefficients. *International Journal for Numerical Methods in Fluids*, 38:1111–1131, 2002.

[57] J.C. Kalita, A.K. Dass, and D.C. Dalal. A transformation-free HOC scheme for steady convection-diffusion on non-uniform grids. *International Journal for Numerical Methods in Fluids*, 44:33–53, 2004.

[58] J.C. Kalita and B.B. Gogoi. Global two-dimensional stability of the staggered cavity flow with an HOC approach. *Computers and Mathematics with Applications*, 67(3):569–590, 2014.

[59] J.C. Kalita and M.M. Gupta. A streamfunction–velocity approach for 2D transient incompressible viscous flows. *International Journal for Numerical Methods in Fluids*, 62 (3):237–266, 2010.

[60] J.C. Kalita and S. Sen. The $(9, 5)$ HOC formulation for the transient Navier-Stokes equations in primitive variable. *International Journal for Numerical Methods in Fluids*, 55:387–406, 2007.

[61] J.C. Kalita and S. Sen. Triggering asymmetry for flow past circular cylinder at low reynolds numbers. *Computers and Fluids*, 59:44–60, 2012.

[62] Y. Kato, H. Kawai, and T. Tanahashi. Numerical flow analysis in a cubic cavity by the GSMAC finite-element method. *JSME International Journal Series II*, 33:649–658, 1990.

[63] C.T. Kelley. *Iterative Methods for Linear and Nonlinear Equations*. SIAM Publications, Philadelphia, PA, 1995.

[64] A.J. Koch and H. Meinhardt. Biological pattern formation: from basic mechanisms to complex patterns. *Reviews of Modern Physics*, 66(4):1481–1507, 1994.

[65] H.C. Ku, R.S. Hirch, and T.D. Taylor. A pseudospectral method for solution of the three-dimensional incompressible Navier-Stokes equations. *Journal of Computational Physics*, 70:439–462, 1987.

[66] H.C. Kuhlmann, M. Wanschura, and H.J. Rath. Flow in two-sided lid-driven cavities: non-uniqueness, instabilities, and cellular structures. *Journal of Fluid Mechanics*, 336:267–299, 1997.

[67] N. Kwatra, S. Jonathan, J.T. Gretarsson, and R. Fedkiw. A method for avoiding the acoustic time step restriction in compressible flow. *Journal of Computational Physics*, 228:4146–4161, 2009.

[68] R.B. Lehoucq, C. Yang, and D.C. Sorensen. *Solution of Large-scale Eigenvalue Problems with Implicitly Restarted Arnoldi Methods*. ARPACK User's Guide, http://www.caam.rice.edu/software/ARPACK/, 1997.

[69] S. Lele. Compact finite difference schemes with spectral-like resolution. *Journal of Computational Physics*, 103:16–42, 1992.

[70] M. Li, T. Tang, and B. Fornberg. A compact fourth-order finite difference scheme for the steady incompressible Navier-Stokes equations. *International Journal for Numerical Methods in Fluids*, 20:1137–1151, 1995.

[71] W. Liao. A Compact High-Order Finite Difference Method for Unsteady Convection-Diffusion Equation. *International Journal for Computational Methods in Engineering Science and Mechanics*, 13(3):135–145, 2012.

[72] R.T. Liu, S.S. Liaw SS, and P.K. Maini. Two-stage Turing model for generating pigment patterns on the leopard and the jaguar. *Physical Review E*, 74(011914):1–8, 2006.

[73] R.J. Mackinnon and G.F. Carey. Analysis of material interface discontinuities and superconvergent fluxes in finite difference theory. *Journal of Computational Physics*, 75(1):151–167, 1988.

[74] R.J. Mackinnon and R.W. Johnson. Differential equation based representation of truncation errors for accurate numerical simulation. *International Journal for Numerical Methods in Fluids*, 13:739–757, 1991.

[75] H. Meinhardt, P. Prusinkiewicz, and D.R. Fowler. *The Algorithmic Beauty of Sea Shells*. Springer-Verlag, Max-Planck-Institute for Developmental Biology, Tubingen, Germany, 2003.

[76] X. Merle, F. Alizard, and J.H.Robinet. Finite difference methods for viscous incompressible global stability analysis. *Computers and Fluids*, 39:911–925, 2010.

[77] M.A.H. Mohamad, S. Basri, and B. Basuno. One-dimensional high-order compact method for solving Euler's equations. *In the proceedings of the 4th International Meeting of Advances in Thermofluids, Melaka, Malaysia*, page 950–962, 2011.

[78] N. Mohamed, S.A. Mohamed, and L.F. Seddek. Exponential higher-order compact scheme for 3D steady convection–diffusion problem. *Applied Mathematics and Computation*, 232:1046–1061, 2014.

[79] J.D. Murray, G.C. Cruywagen, and P.K. Maini. Pattern formation in tissue interaction models. *Frontiers in Mathematical Biology, S. A. Levin (Ed.), Lecture Notes in Biomathematics*, 100:104–116, 1994.

[80] B.N. Nagorcka and J.R. Mooney. From stripes to spots: prepatterns which can be produced in the skin by a reaction–diffusion system. *IMA J. Math. Appl. Med. Biol*, 9:249–267, 1992.

[81] S.A. Newman and H.L. Frisch. Dynamics of skeletal pattern formation in developing chicklimb. *Science*, 205:662–668, 1979.

[82] P. Nithiarasu and C.B. Liu. Steady and unsteady incompressible flow in a double driven cavity using the artificial compressibility (AC)-based characteristic-based split (CBS) scheme. *International Journal for Numerical Methods in Engineering*, 63:380–397, 2005.

[83] B.J. Noye and H.H. Tan. A third-order semi-implicit finite difference method for solving the one-dimensional convection-diffusion equation. *International Journal for Numerical Methods in Engineering*, 26:1615–1629, 1988.

[84] B.J. Noye and H.H. Tan. Finite difference methods for solving the two-dimensional advection–diffusion equation. *International Journal for Numerical Methods in Fluids*, 9(1):75–98, 1989.

[85] M. Ohring. *Materials Science of Thin Films*. Elsevier, A division of Harcourt, Inc., San Diego, USA, 2009.

[86] S.K. Pandit, J.C. Kalita, and D.C. Dalal. A fourth-order accurate compact scheme for the solution of steady Navier-Stokes equations on non-uniform grids. *Computers and Fluids*, 37(2):121–134, 2007.

[87] J.E. Pearson. Complex patterns in a simple system. *Science 261, (CAA)*, 149:189–192, 1993.

[88] Y.F. Peng, Y.H. Shiau, and R.R. Hwang. Transition in a 2D lid-driven cavity flow. *Computers and Fluids*, 32:337–352, 2003.

[89] M. Poliashenko and C.K. Aidun. A direct method for computation of simple bifurcations. *Journal of Computational Physics*, 121(2):246–260, 1995.

[90] L. Quartapelle. *Numerical Solution of the Incompressible Navier-Stokes Equations*. Birkhauser Verlag, Basel, Switzerland, 1993.

[91] M.M. Rai and P. Moin. Direct simulation of turbulent flows using finite difference methods. *Journal of Computational Physics*, 96:15–53, 1991.

[92] R.K. Ray, J.C. Kalita, and A.K. Dass. An efficient HOC scheme for transient convection-diffusion-reaction equations with discontinuous coefficients and singular source terms. *In the proceedings of Applied Mathematics and Mechanics*, 7:1025603–1025604, 2007.

[93] A. Rezgui, P. Cinnella, and A. Lerat. Third-order accurate finite volume schemes for Euler computations on curvilinear meshes. *Computers and Fluids*, 30:875–901, 2001.

[94] M. Sahin and R.G. Owens. A novel fully-implicit finite volume method applied to the lid-driven cavity problem, part ii, Linear Stability Analysis. *International Journal for Numerical methods in Fluids*, 42:79–88, 2003.

[95] J. Sanchez, F. Marques, and J.M. Lopez. A continuation and bifurcation technique for navier-stokes flows. *Journal of Computational Physics*, 180:78–98, 2002.

[96] S. Sen. A new family of (5,5)CC-4OC schemes applicable for unsteady Navier-Stokes equations. *Journal of Computational Physics*, 251:251–271, 2013.

[97] J. Sesterhenn. A characteristic-type formulation of the Navier–Stokes equations for high order upwind schemes. *Computers and Fluids*, 30(1):37–67, 2000.

[98] T.W.H. Sheu, T.N. Lin, and R.K. Lin. On the equal fourth-order accurate temporal/spatial scheme for the convection-diffusion equation. *Numerical Heat Transfer, Part B.*, 51:67–96, 2007.

[99] T.W.H. Sheu and S.F. Tsai. Flow topology in a steady three-dimensional lid-driven cavity. *Computers and Fluids*, 31:911–934, 2002.

[100] C.W. Shu. High-order Finite Difference and Finite Volume WENO Schemes and Discontinuous Galerkin Methods for CFD. *International Journal of Computational Fluid Dynamics*, 17(2):107–118, 2003.

[101] G.L.G. Sleijpen and H.A. van der Vorst. *Hybrid bi-conjugate gradient methods for CFD problems.* In: M. Hafez and K. Oshima (Eds.), Computational Fluid Dynamics, 1995.

[102] S.K. Smoukov, A. Bitner, C.J. Campbell, K.K. Grzybowska, and B.A. Grzybowski. Nano- and microscopic surface wrinkles of linearly increasing heights prepared by periodic precipitation. *Journal of the American Chemical Society*, 127(50):17803–17807, 2005.

[103] G.A. Sod. A survey of several finite difference methods for systems of nonlinear hyperbolic conservation laws. *Journal of Computational Physics*, 27:1–31, 1978.

[104] A. Sohankar, C. Norberg, and L. Davidson. Low-Reynolds-number flow around a square cylinder at incidence: study of blockage, onset of vortex shedding and outlet boundary condition. *International Journal for Numerical Methods in Fluids*, 26(1):39–56, 1998.

[105] W.F. Spotz and G.F. Carey. *High Order Compact Finite Difference Methods with Applications to Viscous Flows. Technical Report 94-03.*

Texas insititute of computational and applied mechanics, The university of Texas at Austin, 1994.

[106] W.F. Spotz and G.F. Carey. High-order compact scheme for the steady stream-function vorticity equations. *International Journal for Numerical Methods in Engineering*, 38:3497–3512, 1995.

[107] W.F. Spotz and G.F. Carey. A high-order compact formulation for the 3D Poisson equation. *Numerical Methods for Partial Differential Equations*, 12:235–243, 1996.

[108] G. Stipcich and C. Liu. High-order mixed weighted compact and non-compact scheme for shock and small length scale interaction. *International Journal of Computer Mathematics*, 90(2):376–407, 2013.

[109] T. Tabata and Y. Takei. Morphogens, their identification and regulation. *Development*, 131:703–712, 2004.

[110] D. Tafti. Alternate formulations for the pressure equation Laplacian on a collocated grid for solving unsteady incompressible Navier-Stokes equations. *Journal of Computational Physics*, 116:143–153, 1995.

[111] P.M. Tekic, J.B. Radenovic, N.L. Lukic, and S.S. Popovic. Lattice Boltzmann simulation of two-sided lid-driven flow in a staggered cavity. *International Journal of Computational Fluid Dynamics*, 24:383–390, 2010.

[112] G. Tiesinga, F.W. Wubs, and A.E.P. Veldmen. Bifurcation analysis of incompressible flow in a driven cavity by the newton-picard method. *Journal of computational and Applied Mathematics*, 140:751–772, 2002.

[113] A.M. Turing. The chemical basis of morphogenesis. *Phil. Trans. R. Soc. Lond.*, B237:37–72, 1952.

[114] G. Turk. Generating textures on arbitrary surface using reaction-diffusion. *SIGGRAPH '91 Proceedings of the 18th annual conference on Computer graphics and interactive techniques*, pages 289–298, 1991.

[115] E. Turkel, D. Gordon, R. Gordon, and S. Tsynkov. Compact 2D and 3D Sixth Order Schemes for the Helmholtz Equation with Variable Wave Number. *Journal of Computational Physics*, 232(1):272–287, 2013.

[116] J.de. Vicente, D. Rodríguez, V. Theofilis, and E. Valero. Stability analysis in spanwise-periodic double-sided lid-driven cavity flows with complex cross-sectional profiles. *Computers and Fluids*, 43:143–153, 2011.

[117] L. Wang and D.J. Mavriplis. Implicit solution of the unsteady Euler equations for high-order accurate discontinuous Galerkin discretizations. *Journal of Computational Physics*, 225(2):1994–2015, 2007.

[118] M.D. Warren. The solution of a convection–diffusion–reaction equation arising from cathodic reduction in a pulsating crack. *International Journal for Numerical Methods in Fluids*, 3(3):217–225, 1983.

[119] J.O. Wilkes and C.P. Thomson. An evaluation of higher-order upwind differencing for elliptic flow problems. *In proceedings of the Third International Conference on Numerical Methods for Laminar and Turbulent Flows*, pages 248–247, 1983.

[120] H.H. Wong and G.D. Raithby. Improved finite-difference methods based on a critical evaluation of the approximation errors. *Numerical Heat Transfer*, 2(2):139–163, 2007.

[121] Y.N. Wu, P.J. Wang, C.J. Hou, C.S. Liu, and Z.C. Zhu. Turing patterns in a reaction-diffusion system. *Communications in Theoretical Physics*, 44:761–764, 2006.

[122] A. Xu. Numerical solutions of quasi-one-dimensional nozzle flows. *In the Proceedings of the 23rd International Congress of Theoretical and Applied Mechanics (ICTAM - 2012), Beijing, China*, pages CFD PB09005054, pp 1–10, 2012.

[123] L. Yamamoto and D. Miorandi. Evaluating the Robustness of Activator-Inhibitor Models for Cluster Head Computation. *Swarm Intelligence, Lecture Notes in Computer Science*, 6234:143–154, 2010.

[124] M. Yanwen, F. Dexun, T. Kobayashi, and N. Taniguchi. Numerical solution of the incompressible Navier–Stokes equations with an upwind compact difference scheme. *International Journal for Numerical Methods in Fluids*, 30(5):509–521, 1999.

[125] D.H. Yoon, K.S. Yang, and C.B. Choi. Flow past a square cylinder with an angle of incidence. *Physics of Fluids*, 22), YEAR = 2010, PAGES = 043603 (1-12),.

[126] S. Zhai, X. Feng, and Y.He. A new high-order compact ADI method for 3D unsteady convection-diffusion problems with discontinuous coefficients. *Numerical Heat Transfer, Part B: Fundamentals: An International Journal of Computation and Methodology*, 65(4):376–391, 2014.

[127] J. Zhang. An explicit fourth-order compact finite difference scheme for three-dimensional convection–diffusion equation. *International Journal for Numerical Methods in Biomedical Engineering*, 14(3):209–218, 1998.

[128] K. Zhang, J.C.F. Wong, and R. Zhang. Second-order implicit-explicit scheme for the Gray-Scott model. *Journal of Computational and Applied Mathematics*, 213:559–581, 2008.

[129] Y.C. Zhou, B.S.V. Patnaik, D.C. Wan, and W. Wei. DSC solution for flow in a staggered double lid driven cavity. *International Journal for Numerical Methods in Engineering*, 57:211–234, 2003.

Publications:

Based on the work in this thesis, the following research articles are published or communicated.

List of Papers Published/Accepted.

1. Kalita JC and Gogoi BB, Global two-dimensional stability of the staggered cavity flow with an HOC approach, *Computers and Mathematics with Applications*, 67(3): 569-590, 2014.

2. Gogoi BB and Kalita JC, On the Global Instability of Square and Cross Lid-Driven Cavity flows with a pure streamfunction-velocity (ψ-v) approach, *proceedings of the International Conference on Computer Aided Engineering*, (CAE) 2013, IIT Madras, 19-21 Dec 2013, pp-314-319.

3. Kalita JC and Gogoi BB, Fourth order compact simulation of the one dimensional Euler Equations of Gas Dynamics, in the book of Abstracts in *SIAM Annual Meeting, 2014*.

List of Papers Communicated/Under Preparation.

1. Gogoi BB and Kalita JC, Compact High-Order Simulation of Pattern Formation in Nature, *Mathematics and Computers in Simulation*, under review.

2. Kalita JC and Gogoi BB, A Biharmonic Approach for the Global Stability Analysis of 2D Incompressible Viscous Flows, *Applied Mathematical Modelling*, under review.

3. Gogoi BB and Kalita JC, An efficient class of HOC solver for the transient three-dimensional convection-diffusion-reaction equations, *Indian Journal of Pure and Applied Mathematics*, under review.

4. Kalita JC and Gogoi BB, Fourth order compact simulation of the one dimensional Euler Equations of Gas Dynamics, *SIAM Journal of Scentific Computing*, communicated.